Degassing and Vesiculation Mechanisms in Hydrous Volcanic Systems: Insights from Rhyolitic, Phonolitic, and Basaltic Melts

Dissertation

der Mathematisch-Naturwissenschaftlichen Fakultät

der Eberhard Karls Universität Tübingen

zur Erlangung des Grades eines

Doktors der Naturwissenschaften

(Dr. rer. nat.)

vorgelegt von

Patricia Louisa Marks, geb. Petri

aus Nagold

Tübingen

2025

Gedruckt mit Genehmigung der Mathematisch-Naturwissenschaftlichen Fakultät der Eberhard Karls Universität Tübingen.

Tag der mündlichen Qualifikation: 21.07.2025

Dekan:	Prof. Dr. Thilo Stehle
1. Berichterstatter:	Prof. Dr. Marcus Nowak
2. Berichterstatter:	Dr. Christoph Berthold
3. Berichterstatter:	Prof. Dr. James Gardner

Acknowledgements

This work was funded by the German Science Foundation (NO378/15-1).

My special thanks goes to **Marcus Nowak**, for his unwavering support, trust, and encouragement throughout the past decade. His enthusiasm, constant interest, and openness to discussing results, challenges, and plans created an exceptional working atmosphere. His open-door policy, patience, and belief in my abilities helped me to navigate the many challenges of my doctorate and to develop into an independent scientist. I am grateful for his kindness and understanding, not just as an academic mentor, but also as a confidant beyond work.

I am grateful to **Christoph Berthold**, not only for his willingness to serve as my second reviewer, but also for his dedication in keeping the LMB running smoothly and addressing the challenges and problems that regularly arise.

I would like to thank **Anja Allabar** for guiding and supporting me in all the essential aspects at the start of my studies. Her warmth and friendship had a profound influence on me, and she has been a role model throughout, both personally and academically.

Special thanks goes to **Dennis Eul**, whose immense helpfulness in the lab, along with his unwavering support and encouragement through all the ups and downs, was invaluable to me throughout my PhD journey. The last years wouldn't have been the same without Dennis and our unique way of communicating.

I would like to thank **Annette Flicker** for her technical expertise, all-round support and for our wonderful encounters throughout, even beyond the university. I would especially like to thank **Barbara Maier** for her excellent work, which made precise and efficient experimental work possible. Her cheerful and humorous nature always lifted the spirits and brightened every day. Not forgetting **Simone Schafflick**, whose perfect sample preparation is irreplaceable.

Many thanks to all my colleagues in the working group and other departments, as well as my wonderful friends, including my Mädels, my old and new friends, and my family, who always supported and believed in me. Very special thanks goes to my friend **Rebekka Reich**, who consistently demonstrated a deep understanding for challenging situations and who always found a way to motivate and encourage me.

My heartfelt thanks go to my parents, **Brigitta** and **Christoph Petri**, and my brother, **Christian Petri** who have always supported and motivated me in any manner during my whole studies. I would also like to thank my best friend, **Lydia Papkalla**, and of course, my love, **Peter Marks**, whose unwavering belief in me and pride in my abilities have been invaluable.

Thanks to all of you!

TABLE OF CONTENTS

Abstract

Volcanic eruptions are among the most hazardous natural catastrophes on Earth, profoundly affecting human societies and ecosystems. These eruptions originate from dynamic processes within the Earth's interior, where silicate melts in magmatic systems contain dissolved volatile components, primarily water (H_2O). Dissolved H_2O significantly influences key physical and chemical properties of magmas, including viscosity, density, liquidus temperature, and phase equilibria. The solubility of H_2O in silicate melts is strongly dependent on pressure and, to a lesser extent, on temperature and chemical composition. During magma ascent, pressure decreases, leading to degassing and vesicle formation, which play a critical role in eruption dynamics. Rapid vesicle formation reduces magma density, increases buoyancy, accelerates magma ascent, and can trigger explosive eruptions. However, variations in volcanic settings, melt compositions, and volatile contents result in different eruption behaviors.

The studies presented here experimentally examine degassing behavior of magma in two volcanic settings, focusing on the influence of pressure, temperature, and chemical composition on H_2O solubility and degassing in silicate melts.

Study I and II examine the degassing behavior of the Lower Laacher See Phonolite melt, with focus on the initial formation and growth of vesicles, as well as the onset and progression of vesicle coalescence during decompression. Systematic solubility and decompression experiments with hydrous phonolite melts were conducted at superliquidus temperatures to analyze degassing mechanisms in detail. Upon reaching sufficient supersaturation pressures, all melts exhibited homogeneous vesiculation with high vesicle number densities (logVND) of 5.1–5.7, facilitating near-equilibrium H_2O concentration adjustments through further degassing. The decompression rate independent initial VND appears inconsistent with nucleation theory but may align with the theory of spinodal decomposition, a phenomenon notably observed in alkali-rich melts (*Study I*).

While the initial logVNDs remained constant across different decompression rates, the coalesced vesicle volumes formed during further decompression exhibited a significant decrease in logVNDs, dropping by 1.2 to 4.1 log units depending on the decompression rate. This behavior mimics a decompression rate dependent VND predicted by nucleation theory (*Study II*). This shift reflects the transition from high VND during initial

degassing to coalescence-driven processes, which can significantly alter eruption dynamics.

Study III explores the H_2O solubility in peralkaline haplogranitic melts as a function of pressure and temperature. Melt compositions based on haplogranitic melts with 2, 4, and 8 wt% excess Na_2O were used. The H_2O solubility was found to decrease with temperature and increase with pressure and peralkalinity. A linear relationship between Na_2O excess and H_2O solubility was established, enabling predictions of H_2O solubility in peralkaline rhyolitic melts based on excess alkali content.

Study IV investigates the interaction of basaltic and mildly peralkaline hydrous rhyolitic melts under decompression, simulating the injection of a mafic melt into a hydrous felsic magma chamber. Bimodal decompression experiments using contacted pre-hydrated rhyolite and basalt cylinders revealed an enhanced vesiculated zone in the alkali-depleted rhyolitic part of the hybrid zone. This zone formed due to rapid diffusional loss of alkalis from the rhyolitic melt into the basaltic melt, significantly reducing H_2O solubility and enhancing H_2O supersaturation. This process accelerates vesicle formation, buoyancy-driven magma ascent, and magma mingling, which can intensify degassing and potentially trigger explosive eruptions.

Zusammenfassung

Vulkanische Eruptionen gehören zu den gefährlichsten Naturkatastrophen der Erde und haben tiefgreifende Auswirkungen auf menschliche Gesellschaften und Ökosysteme. Diese Eruptionen entstehen aus dynamischen Prozessen im Erdinneren, bei denen silikatische Schmelzen in magmatischen Systemen gelöste flüchtige Komponenten, vor allem Wasser (H_2O), enthalten. Gelöstes H_2O beeinflusst wesentlich die physikalischen und chemischen Eigenschaften von Magmen, darunter Viskosität, Dichte, Liquidustemperatur und Phasengleichgewicht. Die Löslichkeit von H_2O in silikatischen Schmelzen hängt stark vom Druck und in geringerem Maße von der Temperatur und chemischen Zusammensetzung ab. Während des Magmaaufstiegs nimmt der Druck ab, was zu Entgasung und Vesikelbildung führt, die eine zentrale Rolle in der Dynamik von Eruptionen spielen. Schnelle Vesikelbildung verringert die Schmelzdichte, erhöht die Auftriebskraft, beschleunigt den Magmenaufstieg und kann explosive Eruptionen auslösen. Variationen in vulkanischen Umgebungen, Schmelzzusammensetzungen und Gehalten an flüchtigen Komponenten führen jedoch zu unterschiedlichem Eruptionsverhalten.

Die hier vorgestellten Studien untersuchen experimentell das Entgasungsverhalten von Magmen in zwei vulkanischen Systemen, wobei der Einfluss von Druck, Temperatur und chemischer Zusammensetzung auf die H_2O-Löslichkeit und Entgasung in silikatischen Schmelzen im Fokus steht.

Die *Studien I und II* untersuchen das Entgasungsverhalten der Phonolithschmelze der Unteren Laacher See Zusammensetzung mit Schwerpunkt auf der initialen Vesikelbildung, dem Wachstum sowie dem Beginn und Fortschreiten der Vesikelkoaleszenz während der Dekompression. Systematische Löslichkeits- und Dekompressionsexperimente mit wasserhaltiger Phonolith-Schmelze wurden bei Superliquidustemperaturen durchgeführt, um Entgasungsmechanismen im Detail zu analysieren. Bei ausreichendem Übersättigungsdruck zeigten alle Schmelzen homogene Vesikulation mit hohen Vesikelanzahl-Dichten (logVND) von 5.1–5.7, was durch weitere Entgasung eine nahezu gleichgewichtige Anpassung der H_2O-Konzentrationen ermöglichte. Die initiale, von der Dekompressionsrate unabhängige logVND scheint nicht mit der Nukleationstheorie übereinzustimmen, könnte jedoch mit

der Theorie der Spinodalen Entmischung in Einklang stehen, einem Phänomen, das insbesondere in alkalireichen Schmelzen beobachtet wird (*Studie I*).

Während die initialen logVNDs bei unterschiedlichen Dekompressionsraten konstant blieben, zeigten die durch Koaleszenz gebildeten Vesikelvolumina während der weiteren Dekompression einen signifikanten Rückgang der logVNDs, der je nach Dekompressionsrate um 1.2 bis 4.1 Logeinheiten sank. Dieses Verhalten ähnelt einer dekompressionsratenabhängigen VND, wie sie von der Nukleationstheorie vorhergesagt wird (*Studie II*). Dieser Übergang von hoher VND während der initialen Entgasung zu koaleszenzgetriebenen Prozessen kann die Dynamik von Eruptionen erheblich verändern.

Studie III untersucht die H_2O-Löslichkeit in peralkalinen haplogranitischen Schmelzen als Funktion von Druck und Temperatur. Schmelzzusammensetzungen basierend auf haplogranitischen Schmelzen mit 2, 4 und 8 wt% überschüssigem Na_2O wurden verwendet. Es wurde festgestellt, dass die H_2O-Löslichkeit mit der Temperatur abnimmt, während sie mit Druck und Peralkalinität zunimmt. Eine lineare Beziehung zwischen Na_2O-Überschuss und H_2O-Löslichkeit wurde nachgewiesen, die Vorhersagen der H_2O-Löslichkeit in peralkalischen rhyolithischen Schmelzen auf Basis des Überschusses an Alkalien ermöglicht.

Studie IV untersucht die Wechselwirkung von basaltischen und mild peralkalinen H_2O-haltigen rhyolithischen Schmelzen unter Dekompression und simuliert die Injektion einer mafischen Schmelze in eine wasserhaltige felsische Magmenkammer. Bimodale Dekompressionsexperimente mit kontaktierten, vorhydrierten Rhyolith- und Basaltzylindern zeigten eine verstärkte Vesikulationszone im alkaliverarmten rhyolithischen Teil der Hybridzone. Diese Zone entstand durch den schnellen diffusionsbedingten Verlust von Alkalien aus der rhyolithischen Schmelze in die basaltische Schmelze, was die H_2O-Löslichkeit signifikant verringerte und die H_2O-Übersättigung verstärkte. Dieser Prozess beschleunigt die Vesikelbildung, den auftriebsgetriebenen Magmenaufstieg und die Magmenvermischung, was die Entgasung intensivieren und potenziell explosive Eruptionen auslösen kann.

List of Publications with Author Contributions

Study I: **Marks, P.L.** and Nowak, M.: Vesiculation dynamics – Part 1: Decompression-induced H_2O vesicle formation in the Lower Laacher See phonolitic melt. European Journal of Mineralogy, 37, 385–412, https://doi.org/10.5194/ejm-37-385-2025, 2025.

Study II: **Marks, P.L.** and Nowak, M.: Vesiculation dynamics – Part 2: Decompression-induced H_2O vesicle growth, onset, and progression of coalescence. European Journal of Mineralogy, 37, 413–435, https://doi.org/10.5194/ejm-37-413-2025, 2025.

Study III: Allabar, A., **Petri, P.L.**, Eul, D., and Nowak, M.: An empirical H_2O solubility model for peralkaline rhyolitic melts. Contributions to Mineralogy and Petrology, 177, 52, https://doi.org/10.1007/s00410-022-01915-8, 2022.

Study IV: **Marks, P.L.**, Allabar, A., and Nowak, M.: H_2O degassing triggered by alkali depletion in bimodal magma injection processes – a new experimental approach. European Journal of Mineralogy, 35, 613–633, https://doi.org/10.5194/ejm-35-613-2023, 2023.

Table 1: List of Publications with Author Contributions. Numbers are related to the work of Patricia Marks. Data in brackets for *Study IV* indicate the proportion conducted during the master's thesis.

Nr.	Status of publication	List of authors	Position in list of authors	Scientific ideas (%)	Data generation (%)	Analysis and interpretation (%)	Paper writing (%)
I	published	2	1	80	100	90	90
II	published	2	1	90	100	90	90
III	published	4	2	5	10	10	5
IV	published	3	1	50 (25)	90 (60)	50 (25)	60

List of Abbreviations

A_{H2Om}	absorbance of molecular H_2O	
A_{OH}	absorbance of OH	
AOQ	$Ab_{38}Or_{34}Qz_{28}$ composition in wt% (Ab: $NaAlSi_3O_8$; Or: $KAlSi_3O_8$; Qz: SiO_2)	
AOQ2	$Ab_{38}Or_{34}Qz_{28}$ composition + 2 wt% Na_2O	
AOQ4	$Ab_{38}Or_{34}Qz_{28}$ composition + 4 wt% Na_2O	
AOQ8	$Ab_{38}Or_{34}Qz_{28}$ composition + 8 wt% Na_2O	
b	intercept of the DRM line on the logVND y-axis	
c_{H2Oeq}	equilibrium H_2O concentration	[wt%]
c_{H2Oi}	initial H_2O concentration prior to decompression	[wt%]
c_{H2Ot}	total H_2O concentration	[wt%]
c_{SiO2}	SiO_2 concentration	[wt%]
CSPV	Cold Seal Pressure Vessel	
d	thickness	[cm]
D_{H2O}	diffusivity of H_2O in silicate melt	[mm^2/s]
dP/dt	decompression rate	[MPa/s]
DRM	Decompression Rate Meter	
EPMA	Electron Probe Micro Analysis	
FTIR	Fourier Transform Infrared Spectroscopy	
H_2O_m	molecular H_2O	
IHPV	Internally Heated Pressure Vessel	
k	Boltzmann constant ($1.38 \cdot 10^{-23}$)	[J/K]
KFT	Karl Fischer Titration	
LLST	Lower Laacher See Tephra Phonolite composition	
MI	Magma Injection	
MLST	Middle Laacher See Tephra Phonolite composition	
OH	hydroxyl groups	
P	pressure	[MPa]
P_f	final pressure where samples were quenched	[MPa]
P_{sat}	saturation pressure	[MPa]
P_{SS}	supersaturation pressure	[MPa]

Rt	Rhyolite	
SEM	Scanning Electron Microscopy	
T	temperature	[K]
t	time	[s]
ULST	Upper Laacher See Tephra Phonolite composition	
VAD79	Vesuvius "white pumice" AD79 eruption composition	
V_m	molar volume of H_2O fluid	[m^3]
VND	Vesicle Number Density	[mm^{-3}]
x	inter-vesicle distance	[µm]
x_{ex}	excess alkali ($Na_2O+K_2O–Al_2O_3$)/100)	
ε_{H2Om}	molar absorption coefficient of H_2O_m	[$L \cdot mol^{-1} \cdot cm^{-1}$]
ε_{OH}	molar absorption coefficient of OH	[$L \cdot mol^{-1} \cdot cm^{-1}$]
η	melt viscosity	[Pa/s]
ρ	glass density	[g/L]
ρ_{melt}	melt density	[g/cm^3]
σ	surface tension	[N/m]
τ_d	decompression timescale	[s]
τ_{diff}	diffusion timescale	[s]

List of Figures and Tables

Introduction

Studies I and II

Study III

Study IV

Introduction

Vesiculation mechanisms

Explosive volcanic eruptions are driven by the formation and growth of volatile vesicles within hydrous silicic melts, primarily composed of H_2O along with minor amounts of CO_2, Cl, F, and sulfur species (e.g., De Vivo et al., 2005). The solubility of H_2O in silicate melts is highly dependent on pressure (*P*) and, to a lesser extent, on temperature (*T*) and melt composition (e.g., Holtz et al., 1995; Moore et al., 1998). As magma rises, decompression causes a reduction in H_2O solubility (e.g., Iacono-Marziano et al., 2007), leading to an increased H_2O supersaturation within the melt. Upon reaching a critical threshold, the melt degasses, releasing H_2O through vesicle formation. With further decompression, the concomitant H_2O supersaturation can be reduced by H_2O diffusion from the melt into the vesicles. This vesiculation process reduces magma density, accelerates its ascent, and rapid expansion of vesicles can finally lead to magma fragmentation and explosive volcanic eruptions (e.g., Kueppers et al., 2006; Genareau et al., 2012).

The initial stage of vesicle formation, which marks the onset of degassing, is crucial for understanding the degassing behavior in silicate melts and the mechanisms influencing volcanic eruptions. The number of fluid vesicles per unit volume of silicate melt (VND) is a key parameter for assessing the efficiency of fluid-melt separation and the acceleration of magma ascent, both of which significantly influence eruption style.

In experimental studies evaluating degassing behavior in silicate melts, nucleation theory is often used to explain vesicle formation and the observed VND (e.g., Navon and Lyakhovsky, 1998). Vesicles can nucleate heterogeneously on crystal surfaces or homogeneously within a crystal-free melt. In both cases, a threshold level of supersaturation is needed to overcome the surface tension energy barrier and form new H_2O vesicle interfaces within the silicate melt. Critically sized H_2O clusters (nuclei) at the nanometer scale emerge within the metastable state of hydrous rhyolitic melt (e.g., Hurwitz and Navon, 1994; Navon and Lyakhovsky, 1998). When H_2O clusters reach a critical radius, they either shrink or grow spontaneously due to diffusional loss or addition of H_2O molecules at the fluid-melt interface, respectively. With continued decompression, existing vesicles expand by diffusional H_2O uptake and by increasing

molar volume, while simultaneously new vesicles continue to nucleate. This process persists until the number of vesicles in the melt volume is sufficient for H_2O supersaturation to decrease solely through diffusion into existing vesicles. When vesicles form on crystals, the required energy can be lower due to the reduced surface area (e.g., Hurwitz and Navon 1994). Nucleation theory generally predicts that VND rises significantly with increased decompression rates (d*P*/d*t*) and reduced surface tension (Navon and Lyakhovsky, 1998). Building on this concept, Toramaru (2006) developed a decompression rate meter (DRM), which calculates magma ascent velocity based on the VND of volcanic ejecta (Eq. 1). These dependencies are crucial for determining the decompression rates at which vesicles nucleate in natural volcanic ejecta (e.g., Toramaru, 2006).

$$\mathrm{VND} = 34 \cdot c_{\mathrm{H2Oi}} \cdot \left(\frac{16 \cdot \pi \cdot \sigma^3}{3 \cdot k \cdot T \cdot P_{\mathrm{sat}}^2}\right)^{-2} \cdot \left(\frac{V_{\mathrm{m}} \cdot P_{\mathrm{sat}}}{k \cdot T}\right)^{-\frac{1}{4}} \cdot \left(\frac{P_{\mathrm{sat}}^2 \cdot k \cdot T \cdot C \cdot D_{\mathrm{H2O}}}{4 \cdot \sigma^2 \cdot (dP/dt)}\right)^{-\frac{3}{2}} \quad (1)$$

Alternatively, a phase separation of hydrous melt into H_2O fluid vesicles and less hydrous melt may proceed through spinodal decomposition (Cahn, 1965), suggested for alkali-rich hydrous melts (Allabar and Nowak, 2018; Gardner et al., 2023; *Study I*). In this process, the initially formed VND remains unaffected by decompression rates (Allabar and Nowak, 2018; Sahagian and Carley, 2020; *Study I*). As decompression leads to sufficiently high H_2O supersaturation, the melt may enter an instable state, susceptible to compositional fluctuations with wavelengths exceeding a critical threshold (Cahn, 1965). Initially, small fluctuations in composition within small volumes lead to the formation of H_2O-enriched and H_2O-depleted melt regions through uphill diffusion without sharply defined boundaries (Allabar and Nowak, 2018; Sahagian and Carley, 2020). The progressive amplification of the concentration gradients leads to the formation of vesicles throughout the melt during decompression.

Even though high melt porosities may form at ambient pressures, many volcanic products exhibit lower porosities than anticipated based on their pre-eruptive volatile content, suggesting extensive outgassing enabled by vesicle coalescence and percolation (Jaupart and Allègre, 1991; Gardner et al., 1996; Giachetti et al., 2019; *Study II*). Vesicle coalescence is key to the permeability of vesiculated melts and influences eruption behavior. Retained volatiles can lead to explosive eruptions, while volatile escape during magma ascent supports effusive activity (Eichelberger et al., 1986; Jaupart, 1998). As an interconnected vesicle network expands, magma can

reach a percolation threshold that enables high permeability, allowing fluids to move through the porous structure and escape from the magma (Klug and Cashman, 1996; Sahimi, 1994; Saar and Manga, 1999). Understanding the relationship between porosity and permeability, which is critical to magma degassing and eruption dynamics, requires considering not only VND but also vesicle sizes, shapes, and connectivity (Saar and Manga, 1999; Gardner et al., 2006).

Degassing of the Lower Laacher See Phonolite

The objectives of *Studies I and II* were to explore the entire vesiculation process within the phonolitic Lower Laacher See melt (LLST), focusing on initial H_2O vesicle formation and growth (*Study I*) and the onset and progression of vesicle coalescence (*Study II*) under continuous decompression conditions. The LLST composition is particularly well suited for investigating vesiculation dynamics, given its extensive prior examination (Wörner and Schmincke, 1984; Schmincke et al., 1999; Harms and Schmincke, 2000; Larsen and Gardner, 2004; Schmidt and Behrens, 2008; Schmidt et al., 2013).

The Laacher See volcano, located in the East Eifel volcanic field in western Germany, is one of Central Europe's youngest volcanoes, with its most recent eruption occurring ~13,006 ± 9 years BP (relative to AD 1950) (Reinig et al., 2021). This eruption, among the largest in Europe during the late Pleistocene, had a volcanic explosivity index of 6, comparable in magnitude to the 1991 eruption of Mount Pinatubo (Holasek et al., 1996). In less than 10 days, the Laacher See volcano explosively released around 6.3 km^3 of phonolitic magma, or 20 km^3 of tephra in a series of phreatomagmatic and Plinian eruptions (Wörner and Schmincke, 1984; Schmincke et al., 1999; Harms and Schmincke, 2000). This eruption injected at least 1.9 Tg of sulfur, 6.6 Tg of chlorine, and 403 Tg of water vapor into the atmosphere, with a significant portion reaching the stratosphere, likely impacting climate and environmental conditions (Harms and Schmincke, 2000; Harms et al., 2004). For comparison, the 1991 Mount Pinatubo eruption led to an estimated global temperature drop of 0.4 K during the following five years (McCormick et al., 1995).

Within the Laacher See magma chamber, temperatures and pressures ranged from 1023 to 1033 K and 115 to 145 MPa at the chamber's uppermost section, increasing to 1113 to 1133 K and 200 MPa in the mafic, more crystalline magma at its base.

Volatile-saturation barometry places the upper boundary of the magma chamber at a depth of 5–6 km. Based on the geometry of the volcanic depression and the erupted volumes, the magma body's overall height is estimated at 1–2 km (Fig. 1; Harms et al., 2004).

Laacher See tephra layers, dispersed across central Europe, reveal a chemically and mineralogically stratified magma chamber (Van den Bogaard and Schmincke, 1984, 1985; Wörner and Schmincke, 1984). Initial Plinian eruptions produced the Lower Laacher See Tephra (LLST), which consists of highly differentiated, water-saturated, and extremely crystal-poor (<2 vol%) phonolites, originating from the chamber's uppermost region. Later Plinian eruptions released the Middle Laacher See Tephra (MLST), comprising less differentiated phonolitic magma with slightly lower alkali content and crystal contents up to 15 vol%. In the final eruption stages, phreatomagmatic activity generated a crystal-rich mafic phonolite (ULST) with phenocryst concentrations up to 55 vol%, attributed to occasional injections of hot basanite melt and mixing with the resident melt at the chamber's base (Tomlinson et al., 2020).

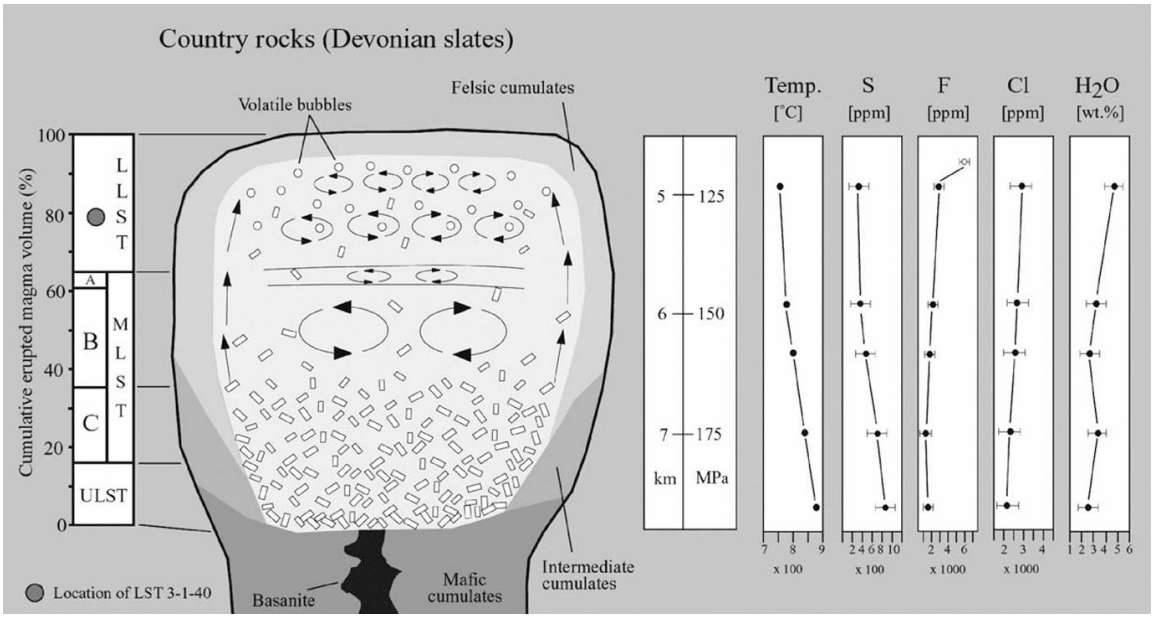

Fig.1: Simplified model of the Laacher See magma reservoir, illustrating chemical and mineralogical zonation (Harms et al., 2004). Bubbles (vesicles) indicate the volatile-enriched, fluid-saturated, differentiated phonolitic melt. The magma chamber is estimated to have been stored at a depth of ~ 5–8 km, under pressures of 115–200 MPa. Average concentrations of S, F, Cl, and H_2O in glass inclusions, reported by Harms and Schmincke (2000), reveal pre-eruptive volatile gradients from the base to the top of the reservoir.

The influence of peralkalinity on H_2O solubility and degassing in rhyolitic melts

While *Studies I and II* primarily investigate decompression-induced vesiculation within a homogeneous melt, *Studies III and IV* focus on the influence of bulk composition of rhyolitic melts on H_2O solubility and on decompression-induced vesiculation within a bimodal rhyolite-basalt melt system.

For haplogranite melts, a minimum in H_2O solubility has been observed near metaluminous compositions, where the molar ratio $M_2O/Al_2O_3 = 1$, with *M* representing Li, Na, K, Rb, Cs (Behrens, 1995; Dingwell et al., 1997). Behrens and Jantos (2001) describe how H_2O solubility increases toward both peraluminous ($M_2O/Al_2O_3 < 1$) and peralkaline ($M_2O/Al_2O_3 > 1$) melts, following a parabolic trend. However, Dingwell et al. (1997) demonstrated a linear relationship between molar H_2O solubility and excess alkali (x_{ex} = the difference between the mole fraction of alkalis and that of Al) at 50 MPa, with their data suggesting this relationship holds up to pressures of 500 MPa.

Building on this understanding, *Study III* systematically examines H_2O solubility in peralkaline rhyolitic melts as a function of pressure, temperature, and peralkalinity. From the newly obtained data, an empirical model was developed to predict H_2O solubility in peralkaline rhyolitic melts based on their excess alkali content.

The injection of mafic magma into a hydrous felsic magma chamber can potentially trigger bimodal explosive volcanism, involving both mechanical mingling and chemical mixing processes (e.g., Miller and Wark, 2008; Perugini et al., 2012; Tomlinson et al., 2020). Bimodal basaltic–rhyolitic volcanism in Iceland was first described by Bunsen (1851). Partially crystallized mafic streaks, glass fragments, blebs, and enclaves (Fig. 2) are described as common features in products of explosive felsic volcanic eruptions (e.g., Sparks et al., 1977; Miller and Wark, 2008; Paredes-Marino et al., 2017; Jarvis et al., 2021). When hot basaltic magma intrudes a rhyolitic magma chamber, local temperature differences of up to 500 K can occur, pushing the system out of equilibrium (e.g., Sparks et al., 1977; Snyder, 2000; Miller and Wark, 2008). Mechanical mingling increases the contact surface between the two melts (e.g., Perugini et al., 2012; Jarvis et al., 2021), promoting heat transfer and enhancing chemical mixing via diffusion.

This heat transfer potentially initiates two major effects: (1) the volatile-bearing basaltic magma cools, partially crystallizes and enriches the residual melt in volatiles, which may exceed saturation and trigger vesicle formation and growth; and (2) the volatile-rich silicic magma may become superheated, leading to vesicle formation as H_2O solubility decreases with temperature at pressures below 300 MPa (Holtz et al., 1995). In both cases, vesicle formation significantly decreases magma density, potentially inducing buoyancy-driven convection and large-scale overturning of a stratified magma chamber (e.g., Sparks et al., 1977). Continued vesicle formation and expansion accelerate magma ascent, contributing to explosive volcanic eruptions.

Study IV focuses on H_2O degassing by simulating the injection of volatile-bearing basaltic melt into an H_2O-saturated, slightly peralkaline rhyolitic melt, with compositions similar to the Askja volcanic complex (Sparks et al., 1977), using decompression experiments. Specifically, it examines how interdiffusion between the rhyolitic and basaltic melts influences H_2O solubility in the resulting intermediate melt composition, with focus on how these compositional changes—especially the depletion of Na_2O concentration in the rhyolitic melt—affect vesicle formation. The study also assesses which regions of the bulk melts are affected by mixing and degassing processes, considering variables such as time and decompression rate.

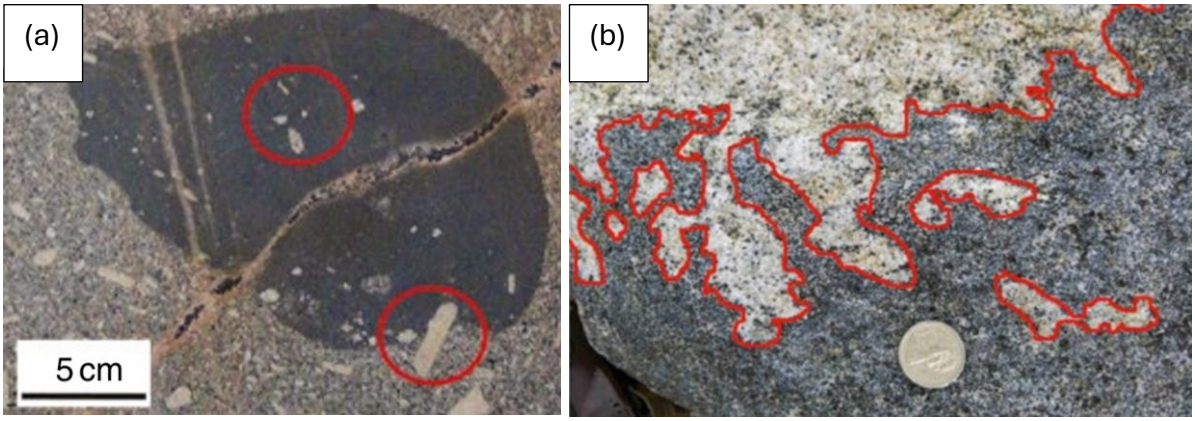

Fig. 2: Common features of bimodal explosive volcanic eruptions (Jarvis et al., 2021): (a) Large fine-grained enclave within alkali feldspar granite from Blackenstone Quarry, Dartmoor, England. These enclaves are typically finer grained than their host rock but contain occasional large crystals (circled in red), which are xenocrysts mechanically transferred from the host. (b) Examples of mingling textures between felsic and mafic magma (outlined in red) from the layered intrusions of the Northern Igneous Complex, Guernsey.

H_2O solubility, hydration, and decompression experiments

The initial steps of the experimental procedure are consistent across all studies, and all specific research questions. To conduct decompression experiments as best as possible, silicate glasses were synthesized by mixing, milling, and melting analytical-grade oxide and carbonate powders, following the protocol of Marxer et al. (2015) with improvements described by Allabar and Nowak (2018).

For *Studies I and II*, a homogeneous phonolitic LLST glass was synthesized, matching the LLST G140 composition described by Harms et al. (2004). *Study III* required the synthesis of peralkaline haplogranitic glasses based on the AOQ composition ($Ab_{38}Or_{34}Qz_{28}$ in wt%; Holtz et al., 1995; Nowak and Behrens, 1997). For this study, glasses with 2, 4, and 8 wt% excess Na_2O were prepared and are referred to as AOQ2, AOQ4, and AOQ8, respectively (Table 2). The AOQ2 glass composition corresponds to the rhyolitic component of the bimodal magma compositions based on the Askja volcanic complex (Sparks et al., 1977), as utilized in *Study IV*. Additionally, the basaltic composition was synthesized according to the composition given in Philpotts and Ague (2009). The glass compositions from several syntheses were then verified using electron probe microanalysis (EPMA) and are given as mean values in Table 2.

For the LLST, AOQ2, AOQ4, and AOQ8 glass compositions standard samples were produced. Crushed glass pieces sieved to a particle size of <500 µm were filled into Au80Pd20 capsules and synthesized with varying amounts of dissolved H_2O (0.5–7 wt%) to determine the near-infrared linear molar absorption coefficients for hydrous species (molecular H_2O (H_2O_m) and hydroxyl (OH)), for subsequent H_2O concentration analyses by infrared spectroscopy. For the basaltic composition, no absorption measurements were possible as the basaltic glass was opaque to near-infrared radiation.

The hydration of the standard samples was conducted in pairs at ~1523 K within an internally heated argon pressure vessel (IHPV), operating at an intrinsic oxygen fugacity close to ΔlogQFM + 3.5 (Berndt et al., 2002). The same apparatus was used for subsequent hydration and decompression experiments. Pressure conditions of 200–300 MPa were chosen to ensure H_2O-undersaturated conditions (Schmidt and Behrens, 2008; Liu et al., 2005). After 24 h, the capsules were isobarically quenched to glass at a rate of 16 K/s by switching off the furnace (Allabar et al., 2020a).

Glass densities of the hydrated standard samples were determined via the buoyancy method using a Sartorius Archimedes precision balance. Total H_2O concentrations in the hydrous standard glasses were measured by Karl Fischer Titration (KFT) at the Institute of Mineralogy, Leibniz University Hannover, Germany (Behrens et al., 1996).

For the H_2O-solubility, hydration, and decompression experiments, glass cylinders (3.6 or 5 mm in diameter) were drilled from homogeneous glass charges. The H_2O-solubility and hydration experiments followed the same procedure across all studies to achieve saturation conditions of the melts at specific pressures and temperatures. Excess water was added with the cylinders to the capsules, which were then sealed. Capsule integrity was tested by heating to 383 K and pressurizing to 200 MPa at ambient temperature followed by re-weighing.

In the LLST solubility experiments (*Study I*), samples were hydrated under pressures matching final pressures (P_f) of the subsequent decompression experiments (200–30 MPa). All samples were hydrated in the IHPV at 1523 K for 96 h, then cooled to 1323 K at 10 K/min and held for an additional 30 min. One sample was also hydrated at 200 MPa at 1523 K and quenched immediately. These durations ensured homogeneous H_2O distribution in the melt. Samples were rapidly quenched either at ~97 K/s or ~150 K/s by melting the suspension wire of the capsule, causing it to drop into the cool section of the sample holder (*Study I*; Berndt et al., 2002). In three cases where the suspension wire failed to melt, samples were quenched at ~16 K/s by turning off the electric furnace (Allabar et al., 2020a). The quench rate prevented quench crystal formation, as confirmed by optical microscopy and backscattered electron imaging. All capsules of the solubility experiments were pierced before preparation, with water escaping out of the hole, which confirmed H_2O saturation during hydration.

For LLST decompression experiments (*Studies I and II*), glass cylinders (~ 5–7 mm in length and 5 mm in diameter) were placed in Au80Pd20 capsules. Two hydration conditions were achieved by adding 5.7 or 5.0 wt% H_2O to adjust H_2O-saturated or slightly undersaturated conditions before decompression, respectively. Samples were hydrated in the IHPV at 200 MPa and 1523 K for 96 h, then isobarically reduced at 10 K/min to 1323 K for 30 min of thermal equilibration. The hydrous melts were then isothermally decompressed at 1.7, 0.17, or 0.064 MPa/s to P_f of 110, 90, 80, 70, 60,

50, 40, and 30 MPa. Upon reaching P_f, samples were quenched isobarically at ~150 K/s or ~97 K/s to room temperature.

In *Study III*, H_2O-solubility experiments were conducted in the IHPV at temperatures above 1123 K. Experiments at ~1123 K were performed in a rapid-quench cold-seal pressure vessel (CSPV) with H_2O as the pressure medium. Solubility experiments were conducted at pressures of 200, 150, 100, 50, and 27 MPa and at temperatures of 1523, 1323, and 1123 K. Experiments above 1123 K were held for at least 72 h, while those at 1123 K ran for at least 264 h to ensure homogeneous H_2O dissolution in the melt. In the IHPV, experiments were quenched isobarically at 16 K/s by switching off the furnace. CSPV experiments were quenched by releasing the external magnet, dropping the sample from the hot zone into the water-cooled section of the autoclave within ~30 s. Water release upon piercing the samples post-experiment confirmed that H_2O was still present as a free fluid phase, essential for successful solubility experiments.

In *Study IV*, preparatory hydration and bimodal magma decompression experiments, as well as reference experiments, were performed in the IHPV. Excess water and either rhyolite or basalt glass cylinders were sealed in capsules to maintain saturation conditions at 200 MPa and 1523 K during the 96 h hydration process. After hydration, the glass cylinders were removed from the capsules, halved, and one cylinder face of each half was ground and polished to enable perfect contact of two cylinders in the bimodal decompression experiments.

For each bimodal magma injection (MI) experiment, a hydrated rhyolite cylinder and a hydrated basalt cylinder were placed in a new Au80Pd20 capsule, with their polished faces horizontally aligned (rhyolite atop basalt or vice versa) to prevent air entrapment, which could otherwise form pre-existing vesicles and impact degassing behavior (Wiesmaier et al., 2015). A reference sample was also prepared with two rhyolite cylinders in contact within a capsule. The experiments were heated isobarically at 25 K/s to an initial pressure of 210 MPa, reaching the run temperature of either 1348 K or 1403 K. These conditions maintained H_2O undersaturation to prevent H_2O loss during the 10 min temperature equilibration. Except for the bimodal reference experiment, all hydrous bimodal and rhyolite-rhyolite (Rt–Rt) assemblages were isothermally decompressed at 0.17 or 1.7 MPa/s to P_f of 100 MPa. To minimize

crystallization in the basaltic melt and to maintain the integrity of the quenched vitreous samples, all MI samples were quenched at a moderate rate of 44 K/s (Allabar et al., 2020a). The Rt-Rt sample, less prone to quench-crystal formation, was quenched at 16 K/s by switching off the furnace. Each sample was checked for H_2O loss due to leakage.

For Fourier Transform Infrared (FTIR) spectroscopy, glass samples from *Studies I and III*, as well as hydration samples from *Study IV*, were sliced perpendicularly to the cylinder axis and prepared as thin sections polished on both sides. Depending on the total H_2O concentration (c_{H2Ot}), sample thickness ranged from 200 to 800 µm. In the solubility and decompression experiments (*Studies I, II, III, and IV*), samples were halved along the cylinder axis, with one half prepared as a ~200 µm thin section for FTIR spectroscopy and transmitted light microscopy. Thin-section thickness was measured using a Mitutoyo digital micrometer (±3 µm). The other half was embedded in epoxy, polished, and double-sputtered with 5 nm carbon for EPMA and scanning electron microscopy (SEM) imaging.

Table 2: Mean glass compositions of LLST (*Studies I and II*), AOQ, AOQ2, AOQ4, and AOQ8 (*Study III*), as well as Rhyolite, Basalt, and the mean hybrid melt from samples MI_T_3, MI_7, and MI_6 (*Study IV*), determined by EPMA. Total Fe concentrations are given as FeO. Totals are <100 wt% due to the H_2O content in the hydrated hybrid glass. x_{ex} represents the difference between the mole fractions of alkalis and alumina (($Na_2O + K_2O - Al_2O_3$) × 100) (*Study III*).

Composition/ Oxides	LLST [wt%]	AOQ [wt%]	AOQ2 /Rhyolite [wt%]	AOQ4 [wt%]	AOQ8 [wt%]	Basalt [wt%]	Hybrid Melt [wt%]
SiO_2	59.61	76.14	75.16	74.16	70.66	54.75	71.43
TiO_2	0.20					1.97	0.02
Al_2O_3	23.60	13.53	12.76	12.09	11.95	13.87	12.17
FeO	1.80					11.84	1.70
MnO	0.41					0.20	0.06
MgO	0.08					4.05	0.66
CaO	0.73					7.93	1.44
Na_2O	9.60	4.65	6.54	8.37	12.18	3.16	4.60
K_2O	4.77	5.68	5.50	5.39	5.21	1.46	4.34
total	100.79	100.00	99.96	100.04	100.00	99.23	96.42
x_{ex}		0.00	0.03	0.05	0.09	-0.04	0.001

Aim of the Studies

Studies I and II examine the H_2O degassing behavior in synthetic hydrous Lower Laacher See phonolite melt (LLST).

Study I investigates fundamental degassing mechanisms through systematic solubility and decompression experiments at superliquidus temperatures, with varying H_2O concentrations and decompression rates. The primary objective is to determine whether H_2O phase separation from the phonolitic melt occurs via vesicle nucleation (Navon and Lyakhovsky, 1998) or spinodal decomposition (Cahn, 1965; Debenedetti, 2000). Vesicle nucleation is expected to produce decompression rate dependent VNDs with a large vesicle size distribution (Toramaru, 2006), while spinodal decomposition would result in decompression rate independent high VNDs and uniformly sized vesicles, as observed in supersaturated phonolitic and phono-tephritic melts (Allabar and Nowak, 2018; Gardner et al., 2023).

Study II builds on the findings from *Study I*, extending decompression experiments to lower pressures to induce and analyze vesicle coalescence in LLST melt. This study focuses on vesicle growth through diffusional H_2O uptake, as well as the onset and progression of vesicle coalescence during decompression. This process is expected to result in a rapid transition from initially high VNDs to a coalescence stage, characterized by significantly reduced VNDs. This shift has important implications for understanding magma dynamics during ascent in volcanic conduits.

The solubility of H_2O in haplogranitic melts increases with increasing pressure, decreasing temperature, and increasing peralkalinity (Holtz et al., 1995; Dingwell et al., 1997). *Study III* investigates the relationship between Na_2O excess (wt%) and H_2O solubility (wt%) in peralkaline haplogranitic and rhyolitic melts as a function of pressure and temperature. The objective is to predict the H_2O solubility in peralkaline rhyolitic melts based on excess alkali content.

In *Study IV*, basaltic and mildly peralkaline rhyolitic melts are used for decompression experiments to simulate the magma injection process of a basaltic melt into a hydrous rhyolitic magma chamber. Alkali transfer at the interface from the mildly peralkaline rhyolitic melt into the basaltic melt is hypothesized to trigger extensive degassing. The

reduced Na_2O concentration is suggested to significantly lower the H_2O solubility in the rhyolite, promoting H_2O supersaturation in the alkali-depleted rhyolitic melt near the contact zone during decompression. Such interactions can lead to substantial degassing and vesicle nucleation at the interface between volatile-bearing mafic and felsic melts, which can notably reduce the magma's density, accelerate buoyancy-driven magma ascent, and intensify magma mingling. This mingling enlarges the contact zone and enhances chemical mixing processes (Wiesmaier et al., 2015; Huppert et al., 1982). Therefore, the injection of a mafic melt into a felsic magma chamber might be considered a potential trigger for explosive volcanic eruptions.

Results and Discussion

Degassing of hydrous Lower Laacher See phonolite (*Studies I and II*)

LLST density, molar absorption coefficients, and H_2O solubility

EPMA measurements (Table 2) confirm the homogeneous glass composition of each synthetic batch, closely matching the LLST composition G140 as reported by Harms et al. (2004). The glass density of hydrous standard glasses decreases linearly with increasing H_2O content. A linear regression of the measured densities yields the following density function for LLST [g/L] as a function of c_{H2Ot} [wt%]:

$$\rho_{LLST} = (2485 \pm 11) - (21.9 \pm 2.8) \cdot c_{H2Ot} \quad (2)$$

Linear molar absorption coefficients for LLST were determined from the H_2O_m (~5210 cm^{-1}) and OH (~4470 cm^{-1}) absorbances measured via FTIR spectroscopy. After baseline correction, the near infrared (NIR) band intensities of OH and H_2O_m were obtained (Behrens et al., 1996). A weighted least-squares regression of normalized absorbances yielded molar absorption coefficients of ε_{H2Om} = 1.27 ± 0.04 and ε_{OH} = 1.15 ± 0.07 $L \cdot mol^{-1} \cdot cm^{-1}$.

FTIR spectroscopy results obtained from quenched samples that run at different temperatures under 200 MPa indicate an increase in H_2O solubility with decreasing temperature, consistent with findings by Schmidt and Behrens (2008) for phonolitic melts from the Laacher See volcano and Montana Blanca volcano, Tenerife, Spain. From the solubility series at 1323 K, an empirical equation for pressure dependent H_2O solubility (in wt%) was derived:

$$c_{H2Oeq} = 0.2403 \cdot P^{0.5988} \quad (3)$$

Applying the solubility equation, H_2O saturation pressures (P_{sat}) of 198 MPa for the initial H_2O concentration (c_{H2Oi}) = 5.7 wt% and 156 MPa for c_{H2Oi} = 5.0 wt% were determined for the decompression series. These values correspond to two distinct starting conditions at the beginning of decompression at 1323 K: one at H_2O saturation with 5.7 wt%, and the other H_2O-undersaturated with 5.0 wt%. Consequently, while melt supersaturation occurs immediately for the 5.7 wt% series upon the onset of decompression, a pressure reduction of ~ 40 MPa is required to reach saturation at 156 MPa for the 5.0 wt% series.

Decompression experiments: vesiculation stages

Combined hydration and decompression experiments with the LLST melts were conducted in the IHPV to investigate the effect of decompression rate on the vesicle formation, the subsequent vesicle growth, and the onset of vesicle coalescence during decompression. The melts were hydrated with 5.7 or 5.0 wt% H_2O at 200 MPa and 1523 K for 96 h. Following hydration, the temperature was isobarically reduced at a controlled rate of 10 K/min to 1323 K, and the melts were thermally equilibrated for 30 min. Subsequently, the hydrous melts underwent isothermal decompression at rates of 1.7, 0.17, or 0.064 MPa/s to final pressures of 110, 90, 80, 70, 60, 50, 40, and 30 MPa. Upon reaching P_f, the samples were quenched isobarically to room temperature at rates of 150 K/s (Berndt et al., 2002) or 97 K/s (*Study I*).

All decompressed samples were free of microlites. Notably, all samples exhibited fringe zones characterized by the presence of large vesicles at the melt-capsule interface. The size of these vesicles increased with decreasing decompression rates and lower P_f.

The quenched samples of decompression series generally undergo three stages as P_f decreases:

- the first observable vesicle formation (*Study I*),
- complete vesiculation of the central sample volume accompanied by vesicle growth (*Studies I and II*),
- the onset and progression of vesicle coalescence (*Study II*).

The pressure difference between P_{sat} and the pressure at which vesicles first appear in the glass defines the supersaturation pressure (P_{SS}). Within the analyzed 10 MPa intervals for the two c_{H2Oi} series, the initial P_{sat} and P_{SS} differences do not significantly influence the onset of vesicle formation. At slower decompression rates (0.064 and 0.17 MPa/s), vesicles first appear in the glass at a P_f of 80 MPa (Fig. 3). At faster decompression rates (1.7 MPa/s), lower P_f values are required: 70 MPa for the 5.7 wt% series and 60–50 MPa for the 5.0 wt% series. Consequently, the P_{SS} increases with decompression rate, from 120 MPa to 130 MPa for the 5.7 wt% series and from 80 MPa to 100–110 MPa for the 5.0 wt% series. This indicates that the initially saturated melt requires a higher P_{SS} (~40 MPa) than the initially slightly undersaturated melt at slower decompression rates. However, faster decompression rates necessitate an

even higher P_{SS}, corresponding to lower P_f values of 10 to 20 or 30 MPa, depending on c_{H2Oi} (Fig. 3).

Vesicle formation is initially observed in localized regions of the quenched samples, with high densities of small vesicles (2–4 µm) in the upper, middle, or lower sample areas. The stage of complete vesiculation and vesicle growth across the sample volume follows, spanning a wide pressure range of 20–40 MPa at faster decompression rates (0.17 and 1.7 MPa/s). At the slowest rate (0.064 MPa/s), coalescence occurs after complete vesiculation, over a narrower pressure range of ~10 MPa. Comparing the pressure range of uniform vesicles, coalescence starts at higher P_f for initially H_2O saturated melts (~30 MPa) than for undersaturated melts, correlating with P_{sat} differences of 198 MPa and 156 MPa for the 5.7 wt% and 5.0 wt% series, respectively.

The onset of vesicle coalescence is decompression rate dependent, occurring at higher P_f with slower decompression. In the 5.7 wt% series, coalescence starts at a P_f of 70 MPa at 0.064 MPa/s, and at 60 MPa for faster rates (0.17 and 1.7 MPa/s). In the 5.0 wt% series, coalescence starts at 40 MPa at 0.064 MPa/s and at 30 MPa for faster rates. Samples quenched at the onset of coalescence exhibit pristine vesiculated volumes alongside the first coalesced vesicles. Notably, the logVND of pristine vesicles decreases at the onset of coalescence, particularly at slower decompression rates (0.064 and 0.17 MPa/s).

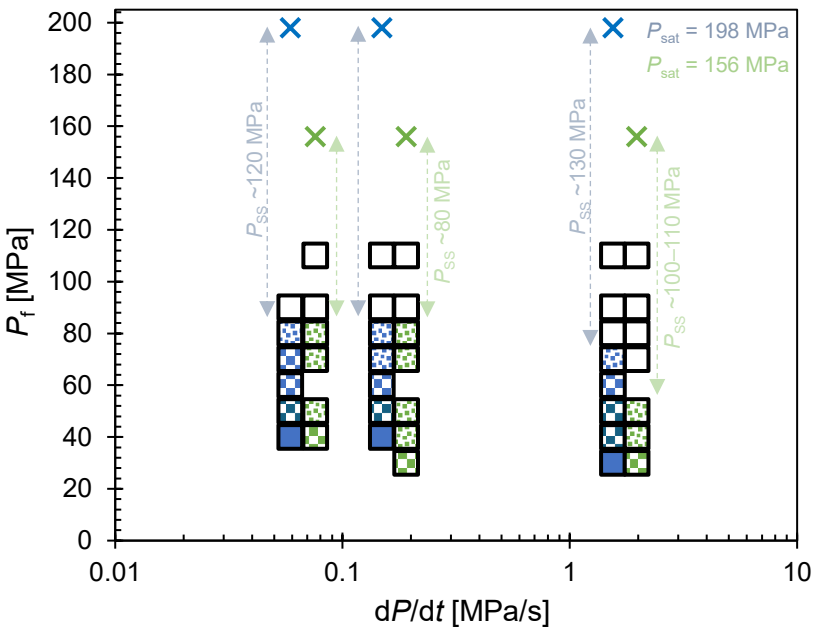

Fig. 3: Vesicle occurrence in decompressed LLST samples: Open symbols indicate no vesicles after decompression and quenching. Dotted symbols show homogeneous vesicle formation at P_f, while crossed filled symbols indicate both coalesced and pristine vesiculated volumes. Filled symbols denote only coalesced vesicles. Blue and green symbols represent c_{H2Oi} of 5.7 wt% and 5.0 wt%, respectively. P_{sat} refers to the saturation pressure of 5.7 wt% and 5.0 wt% H_2O, and P_{SS} is the ΔP from P_{sat} to the pressure of first observed vesicles.

P_f [MPa]	0.064 MPa/s	0.17 MPa/s	1.7 MPa/s
70	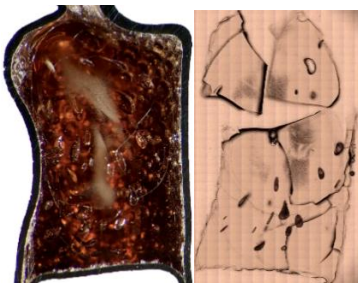 LLST_37D	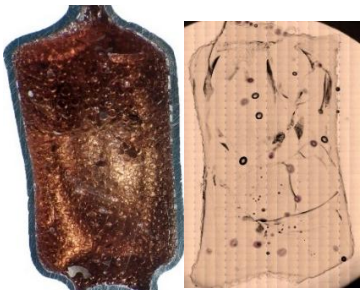 LLST_3D	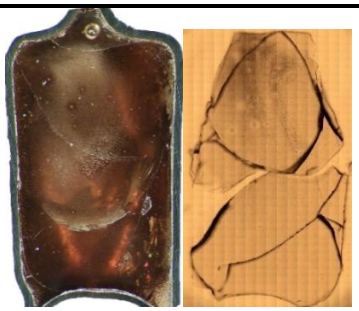 LLST_5D
60	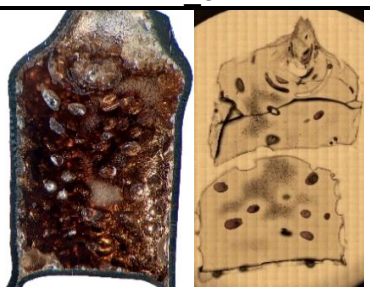 LLST_48D	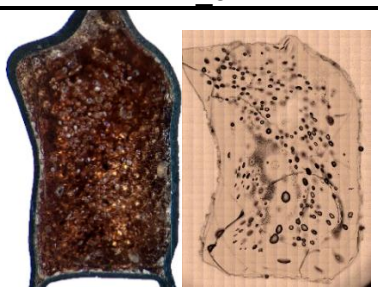 LLST_49D	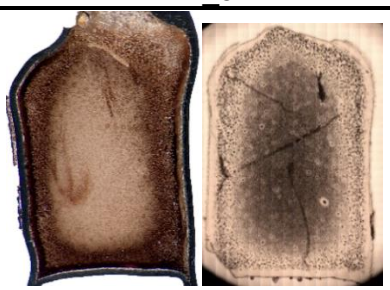 LLST_50D
50	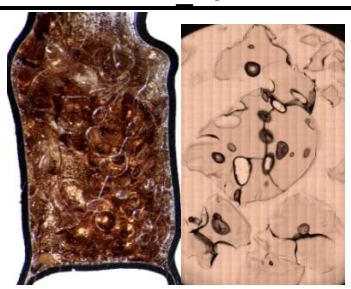 LLST_38D	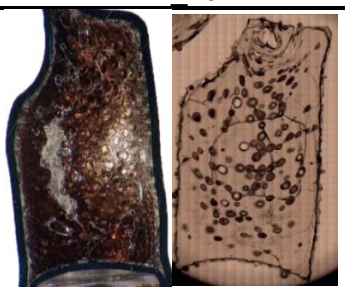 LLST_4D	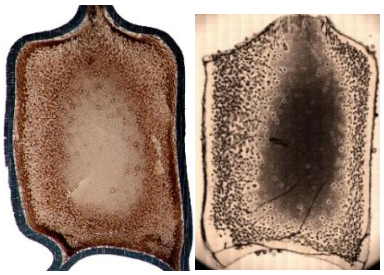 LLST_13D
40	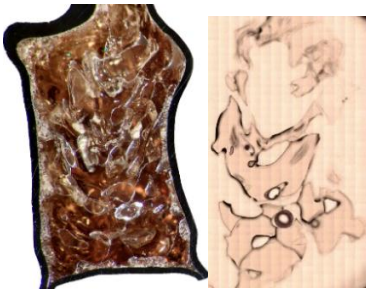 LLST_39D	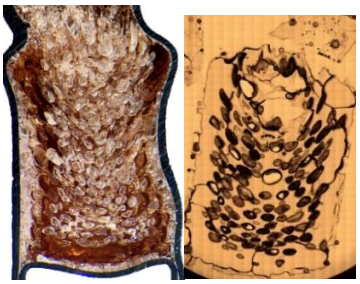 LLST_26D	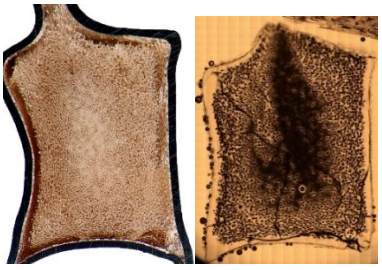 LLST_25D
30			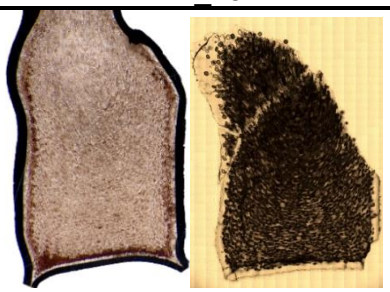 LLST_44D

Fig. 4: Decompression samples of LLST with initially 5.7 wt% dissolved H_2O. Hydrous melts were decompressed from 200 MPa with 0.064, 0.17 or 1.7 MPa/s to P_f of 70, 60, 50, 40 and 30 MPa. Left image of each sample shows the in epoxy embedded sample half, the right image shows the thin section of ~200 µm thickness. Each sample had an original diameter of 5 mm.

Fig. 5: Decompressed LLST samples with initially 5.0 wt% dissolved H_2O. Decompressed from 200 MPa with 1.7, 0.17 or 0.064 MPa/s to P_f of 80, 70, 50, 40 and 30 MPa. Left image of each sample shows the in epoxy embedded sample half, the right image shows the thin section of ~200 µm thickness. Each sample had an original capsule inner diameter of 5 mm.

Vesicle number density

The VND was analyzed in volumes of the samples exhibiting a uniform vesicle distribution and was determined to logVNDs of 4–5.7. The stage of maximum vesiculation is characterized by high logVNDs of 5.1–5.7, visible as milky white opacity in reflection mode under the optical microscope for embedded sample halves, and as opaque dark areas in thin sections under transmission mode (Fig. 4, 5). As P_f decreases, highly vesiculated volumes diminish, and vesicle coalescence becomes evident. At slower decompression rates, large coalesced vesicles form within the sample volume while small uniformly sized vesicles persist in the glass interstices. In contrast, at the fast decompression rate, vesicle coalescence initiates from the outer sample margins and progresses inward toward the sample center.

Within each sample, vesicles are uniformly sized, with diameters increasing from ~2 µm to ~15 µm as P_f decreases, consistent across the different decompression rates. Notably, the VND is independent of c_{H2Oi} prior to decompression, as both H_2O series display the same range of logVND. However, VND does exhibit an apparent dependence on the onset of observable vesicle formation. The P_f associated with the highest logVNDs shifts towards lower pressures at faster decompression rates. For example, at 5.0 wt% dissolved H_2O and a decompression rate of 0.064 MPa/s, the highest logVND is observed at a P_f of 50 MPa. In contrast, P_f decreases to 40 MPa at 0.17 MPa/s and further to 30 MPa at 1.7 MPa/s. However, the samples show uniformly distributed vesicles, spanning from the initial vesicle formation stage to the maximum vesiculation stage. The onset and progression of coalescence are characterized by larger vesicles, ranging from ~37 µm to ~500 µm, accompanied by significantly reduced logVNDs between 3.7 and 0.5.

Resorption of H_2O during quench

Slight variations in logVND of 4–5.7 are observed in quenched glasses showing initial vesiculation. We expect that phase separation at higher P_f and lower P_{SS} may result in H_2O resorption during cooling, leading to the complete dissolution of earlier-formed smallest vesicles. H_2O resorption from vesicles back into the melt during quenching, as described by McIntosh et al. (2014) and Allabar et al. (2020a), is driven by the increasing solubility of H_2O in phonolitic melt as temperature decreases (Schmidt and Behrens, 2008). This effect is more pronounced in the 5.7 wt% series due to higher

H_2O diffusivity and lower melt viscosity, which decreases with increasing residual c_{H2Ot} (Giordano et al., 2008).

LogVND values of 4–5, determined in glass samples exhibiting uniform vesicle distributions, reflect the early stages of vesiculation, particularly at high P_f (80–70 MPa) (Fig. 6). In these samples, a small number of vesicles persist through quenching due to slight size variations, while the majority of smaller vesicles dissolve during cooling (stage 1). Vesicle sizes in these glasses range between 2 and 5 µm. Subsequently, the increase in logVND to maximum values of 5.1–5.7 with decreasing P_f corresponds to the true initial VND of formed vesicles, as a sufficiently large vesicle population survives quenching (stage 2). The initial gradual decline in VND during progressive decompression (stage 3) marks the onset of coalescence. This stage is characterized by a coexistence of pristine vesicle populations with high VND and regions containing larger, coalesced vesicles. This process continues until complete coalescence is achieved (stage 4). During coalescence, logVND decreases sharply by 1.2–4.1 log units, reaching low values of 3.7–0.5, depending on the decompression rate.

The data show clustering of logVND values (4.8–5.4) across all samples decompressed at 1.7 MPa/s, while slower decompression rates (0.17–0.064 MPa/s) result in a broader range (4.0–5.7). This trend may be influenced by decompression time, which increases significantly with slower rates. For example, decompression from 200 to 70 MPa requires 1 min at 1.7 MPa/s, 13 min at 0.17 MPa/s, and 34 min at 0.064 MPa/s. Longer decompression times at slower rates facilitate vesicle growth. At the fastest decompression rate, the onset of vesicle formation is not resolvable due to rapid decompression within seconds, followed by resorption and shrinkage during quenching, which may erase small vesicles formed during this process.

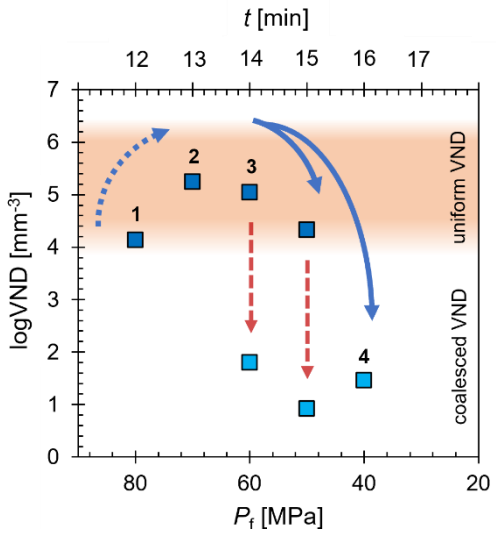

Fig. 6: LogVND evolution vs. P_f and t during decompression for c_{H2Oi} 5.7 wt% at 0.17 MPa/s. Stages of vesicle textures:

1. Initial vesicle formation, influenced by shrinkage and resorption. 2. Vesiculated volumes with maximal logVND. 3. LogVND decreases with the onset of coalescence. 4. Complete coalescence, erasing pristine vesicle volumes.

(Dis)equilibrium degassing

High logVND values during the maximum vesicle stage (5.1–5.7) suggest near-equilibrium melt degassing, driven by the rapid reduction of H_2O supersaturation during decompression. Using Hertz's equation (1908) for random vesicle distribution ($x = 5/9 \cdot VND^{-1/3}$), the mean inter-vesicle distance (x) is calculated to be ~7–9 µm. This small distance allows near-equilibrium c_{H2Ot} and porosity to develop within seconds via H_2O diffusion during decompression, as estimated from H_2O diffusivity data (Schmidt et al., 2013). Consequently, near-equilibrium degassing is inferred at high logVNDs of ~5.5, with c_{H2Oeq} achieved in the melt.

However, FTIR measurements of samples with reduced VNDs reveal residual glass c_{H2Ot} values exceeding c_{H2Oeq} by 1–2 wt%, indicating disequilibrium degassing at the onset and during progression of coalescence. Disequilibrium is predicted when the diffusion timescale (τ_{diff}) is significantly longer than the decompression timescale (τ_d), i.e., $\tau_{diff}/\tau_d >> 1$ (Hajimiaza et al., 2019). Under such conditions, H_2O diffusion from the melt into vesicles is too slow to maintain near equilibrium conditions throughout the sample, leading to degassing controlled by diffusion rather than decompression rate.

In coalesced samples, high τ_{diff}/τ_d ratios indicate disequilibrium degassing (*Study II*). This corresponds to increasing inter vesicle distances due to an ongoing decrease in logVND and c_{H2Ot}, correlated with the H_2O diffusion (D_{H2O}) dependence on c_{H2Ot} in the melt (Schmidt et al., 2013). As coalescence progresses, supersaturation between vesicles increases, potentially triggering secondary vesicle formation in the interstitial melt (Allabar et al., 2020b). The H_2O diffusion from the interstitial melt into the large vesicles will not be fast enough to reduce the H_2O supersaturation effectively that builds up during further continuous decompression. This may result in a secondary vesicle formation event at $c_{H2Ot} < c_{H2Oi}$ and lower P_f compared to the initial vesicle population. However, no evidence of secondary vesicle formation was observed in this study, indicating that the achieved P_f values were still too high for additional vesicle formation.

Therefore, in addition to the resorption of H_2O from fluid vesicles back into the melt during quenching, the increasing inter-vesicle distance associated with progressing coalescence and decreasing VND contributes to the elevated c_{H2Ot} values measured in glasses between coalesced vesicles. This reflects the transition from equilibrium degassing to disequilibrium degassing as coalescence advances.

Initial vesicle formation with decompression rate independent VND: an indicator for spinodal decomposition?

To determine the degassing mechanism of the LLST melt, VNDs were quantified in vesiculated samples. This analysis distinguishes between decompression rate dependent behavior, where VND increases with increasing decompression rate, and decompression rate independent behavior, where VND remains constant across varying decompression rates. The decompression rate dependent VND can be explained by nucleation theory, which suggests that vesicles form only to the extent required to reduce supersaturation. This results in a range of vesicle sizes within a single sample as new vesicles nucleate when the existing ones are insufficient during decompression (Navon and Lyakhovsky, 1998).

In contrast, the maximum logVND values of 5.1–5.7, associated with uniformly sized vesicles with diameters increasing as P_f decreases for each decompression rate and c_{H2Oi} series, show decompression rate independent behavior for the LLST melt. This behavior may be explained by the model of spinodal decomposition, where the H_2O supersaturated melt becomes unstable to compositional fluctuations (Cahn, 1965). Similar observations were found in supersaturated K-phonolitic melt from the Vesuvius "white pumice" AD79 eruption (VAD79) (Allabar and Nowak, 2018; Allabar et al., 2020a, b). They observed vesicle formation in the hydrous VAD79 composition with c_{H2Oi} of 5.3 wt% H_2O at P_f of ≤ 100 MPa, showing homogeneously distributed vesicles with logVNDs of 4.8–5.4, irrespective of decompression rates ranging from 0.024 to 1.7 MPa/s. Further decompression to 70 MPa did not change the VND but only led to vesicle growth, mirroring the behavior observed in the LLST melt.

These results demonstrate that both Na_2O-rich (LLST) and K_2O-rich (VAD79) phonolite melts exhibit the same decompression rate independent vesicle formation process, aligning with spinodal decomposition (Allabar and Nowak, 2018; Sahagian and Carley, 2020; Gardner et al., 2023). This suggests that other alkali-rich melt compositions may also follow a similar degassing mechanism.

VND adjusted by coalescence follows the DRM of Toramaru (2006)

The VND of the initially formed (logVND of 5.1–5.7) and partially extinct (logVND of 4.0–5.0) vesicles remains constant across all decompression rates, suggesting spinodal decomposition as the degassing mechanism (Allabar and Nowak, 2018; Allabar et al., 2020a, b; Sahagian and Carley, 2020; Gardner et al., 2023). Upon the onset of coalescence, the VND decreases significantly by 1–2 log units below the predicted VND using the DRM, (Fig. 7), calculated by Eq. 1 (Toramaru, 2006).

Assuming vesicle nucleation, the DRM estimates VND as a function of dP/dt, incorporating surface tension (σ), H_2O content, and diffusivity determined by H_2O saturation pressure. Surface tension, calculated via Eq. 4, is 0.053 N/m (Shea, 2017). Given reference parameters from Shea (2017) are σ_{ref} = 0.06 N/m, T_{ref} = 900 °C, P_{ref} = 200 MPa, and SiO_{2ref} = 66.5 wt%. H_2O diffusivity ($\log D_{H2O}$ in m^2/s) was calculated using Eq. 5 (Schmidt et al., 2013) with c_{H2Ot} in wt% and T in Kelvin.

$$\sigma = \sigma_{ref} \cdot \exp[(-2.2 \cdot 10^{-2}) \cdot (SiO_{2ref} - SiO_2)] - 5 \cdot 10^{-6} \cdot (T_{ref} - T) + 2 \cdot 10^{-5} \cdot (P_{ref} - P_{sat}) \quad (4)$$

$$\log D_{H2O} = (-6.001 - 0.277 \cdot c_{H2Ot}) - (6281 - 565.6 \cdot c_{H2Ot})/T \quad (5)$$

While the maximum logVND of the homogeneous vesicles remains independent of decompression rates, the logVND of coalesced samples follows the DRM trend, ranging from 0.5–0.8 at the lowest decompression rate (0.064 MPa/s) to 3.1–3.7 at the highest rate (1.7 MPa/s), with decreasing VND with P_f. Nonetheless, experimental design can mimic this dependency, as seen in prior decompression studies with phonolitic and trachytic melts that show both rate independent and rate dependent VND behavior (Fig. 7).

For example, VAD79 experiments by Iacono-Marziano et al. (2007) and Marxer et al. (2015) revealed that small capsule diameters (2.4–2.5 mm) inhibited uniform vesicle formation due to H_2O diffusional loss towards fringe vesicles at the capsule walls, compounded by coalescence at low P_f. Only the highest decompression rate of 1.7 MPa/s, presented in the study of Marxer et al. (2015), produced uniformly distributed small vesicles (logVND ~4.3) due to shorter diffusion times. In contrast, Preuss et al. (2016) used larger glass cylinders (5 mm) of Campi Flegrei trachytic and VAD79 phonolitic melts, achieving high logVNDs of ~5.6 with decompression rate

independent VNDs. However, using powdered starting material at the same experimental conditions reduced VNDs significantly due to pre-existing H_2O-N_2 vesicles and degassing by diffusive growth of these pre-existing vesicles. The samples with powder used as starting material are therefore not included in Fig. 7. Allabar and Nowak (2018) and Allabar et al. (2020a, b) also observed decompression rate independent behavior in hydrous VAD79 melts, with high logVNDs (4.6–6.4) consistent with spinodal decomposition and deviating from the DRM trend (Fig. 7). This underscores that sample geometry, initial starting material and experimental conditions can critically influence VNDs, specifically if the sample size is too small, powder is used as the starting material, or the decompression rate is too slow, significantly lowering VND by orders of magnitude.

Fitting the DRM to coalesced data (this *Study II* and Marxer et al., 2015) yields surface tension values of 0.09 N/m and 0.035 N/m, respectively. According to Eq. 1, the DRM slope remains constant at 3/2, as dictated by the used simplified H_2O diffusivity model $x^2 = 2 \cdot D_{H2O} \cdot t$ (with x as diffusion distance), (Toramaru, 2006), allowing simplification of Eq. 1 to Eq. 6.

$$\log\mathrm{VND} = 3/2 \cdot \log(\mathrm{d}P/\mathrm{d}t) + b \qquad (6)$$

The y-axis intercept b of the DRM line (Fig. 7) depends on surface tension, which varies with H_2O content and melt composition, shifting the DRM line vertically.

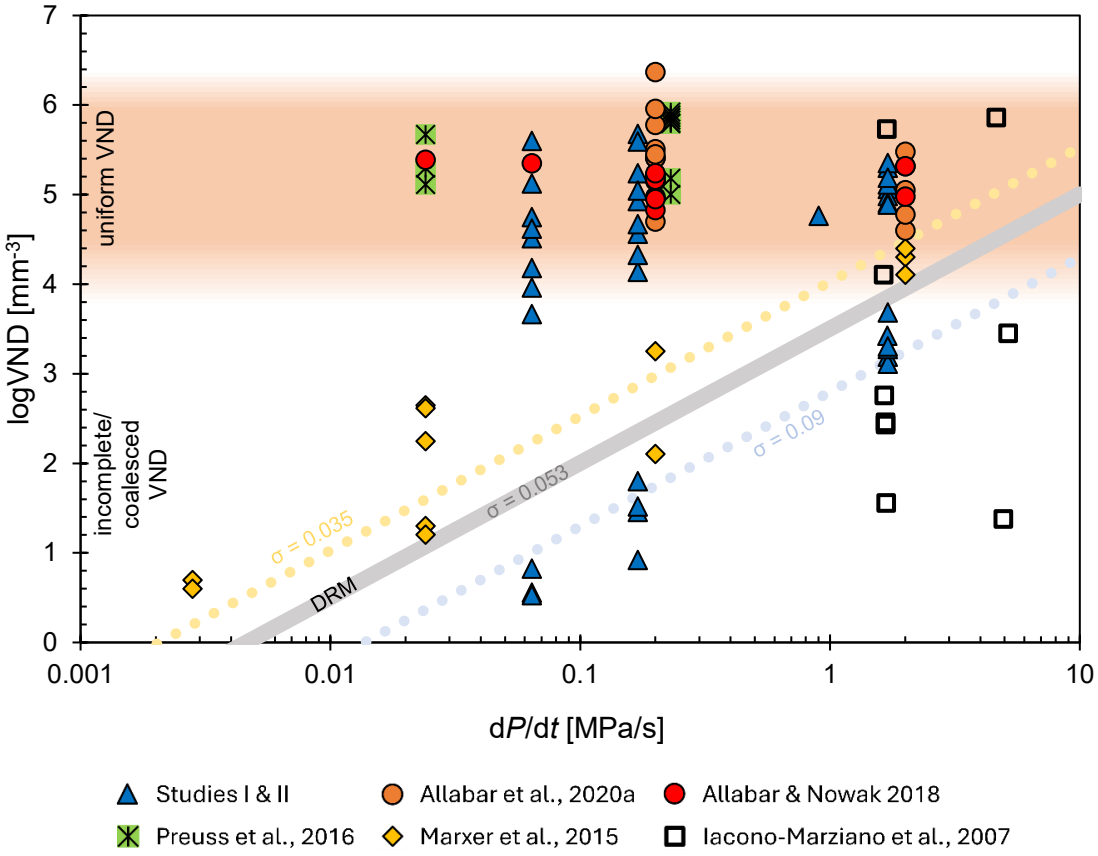

Fig. 7: VND vs. d*P*/d*t* plot with data for hydrous phonolitic and trachytic melts. To minimize overlap, data from other studies are slightly shifted at 0.17 MPa/s and 1.7 MPa/s. The DRM line is calculated for LLST composition (σ = 0.053 N/m (Shea, 2017); Toramaru, 2006). Successful decompression experiments are plotted in the uniform VND region, indicating degassing via spinodal decomposition. Data aligning with the DRM line reflects the results of experiments affected by coalescence, pre-existing bubbles, or unsuitable capsule design.

Vesicle coalescence generally proceeds through three primary stages: (1) the approach of vesicles, driven by external and/or internal forces such as vesicle growth (e.g., Maruishi and Toramaru, 2022); (2) the drainage of the melt film between vesicles until it reaches a critical thickness and ruptures; and (3) the relaxation of the coalesced vesicles to a spherical shape due to surface tension forces (e.g., Eri and Okumura, 2010). Various forces contribute to film drainage in magmas, including gravitational forces (Proussevitch et al., 1993), capillary forces (Nguyen et al., 2013; Proussevitch et al., 1993), vesicle growth (Castro et al., 2012), and shear deformation in conduit flow (e.g., Caricchi et al., 2011).

In our samples, only the initial and final stages of vesicle coalescence were observed. In uniformly vesiculated regions, vesicles appeared spherical and remained separated (Maruishi and Toramaru, 2022), while coalesced vesicles displayed the final stage of relaxation to spherical shapes (Eri and Okumura, 2010).

The volatile content and bulk composition of magma significantly influence its bulk density (e.g., Wilson et al., 1980) and viscosity (e.g., Mader et al., 2013). Consequently, the magma composition and the timescales of H_2O diffusion and viscous deformation play critical roles in determining the effects of H_2O diffusivity and melt viscosity on vesicle growth and coalescence (Navon and Lyakhovsky, 1998). Depending on the respective timescales, vesicle growth is governed by the diffusion of H_2O molecules from the bulk supersaturated melt to the vesicle-melt interface, or the expansion of vesicles through viscous deformation of the surrounding melt (Navon and Lyakhovsky, 1998).

Additionally, the c_{H2Ot} strongly affects vesicle surface tension (Shea, 2017), a parameter critical in determining the work required for the formation of critically sized vesicles within the framework of the DRM model proposed by Toramaru (2006). Notably, the DRM model assumes a single, constant value for surface tension to predict VND across varying decompression rates.

To predict VND during decompression and its dependence on decompression rate, a model incorporating dynamically evolving parameters such as H_2O content, surface tension, melt viscosity, vesicle size, and growth rates is essential. While several models exist to simulate vesicle growth during decompression or equilibration at specific pressures (e.g., Gardner, 2007; Castro et al., 2012; Huber et al., 2014; Mancini et al., 2016; Giachetti et al., 2019; Coumans et al., 2020; Ohashi et al., 2022), no existing equations or models can predict the specific VND at which vesicle coalescence begins or determine the extent to which it will progress.

We propose that extensive experimental work, incorporating variable melt compositions, decompression rates, and H_2O contents, is necessary to develop a comprehensive predictive model for vesicle coalescence during decompression. Such efforts would clarify why coalescence appears to depend on decompression rate, while the initial vesicle number density remains independent of this rate.

Conclusion of LLST degassing

This study identifies a rapid transformation of the initial VND, characterized by high logVND values and decompression rate independence, to the coalescence stage with significantly lower VNDs as a function of decompression rate which is consistent with the VND predictions of the DRM (Toramaru, 2006) related to vesicle nucleation. During the initial vesiculation stage, high logVNDs ranging from 5.1 to 5.7 were observed. These values are consistent with previously reported logVNDs of 4–6 in both experimental and natural phonolitic and trachytic samples from Vesuvius and Campi Flegrei (Marxer et al., 2015; Allabar et al., 2018; Gurioli et al., 2005; Mastrolorenzo et al., 2001). At these high VND levels, near-equilibrium degassing from the melt into nearby adjacent vesicles is expected during decompression.

Vesicle expansion during magma ascent is driven by ongoing H_2O diffusion into vesicles, promoted by reduced H_2O solubility in the silicate melt and the increase of the molar volume of the fluid phase. As vesiculation advances, decompression rates may increase due to buoyancy forces acting on the magma and the reduction in magma density as vesicles expand (e.g., Wilson et al., 1980). Additionally, vesicle rise relative to the surrounding magma, influenced by vesicle size and melt viscosity, promotes coalescence and further decompressive expansion (Proussevitch et al., 1993).

At higher decompression rates, the time available for vesicle coalescence is reduced, potentially preserving the initially high VND up to the surface. Consequently, VND values in natural pumice may not directly correlate with decompression rates, as VND can vary significantly throughout magma ascent. This highlights the substantial influence of viscosity, controlled by the melt bulk composition, on the vesiculation process during decompression and, in turn, on magma ascent dynamics within volcanic conduits.

An empirical H_2O solubility model for peralkaline rhyolitic melts (*Study III*)

Glass densities

In the H_2O solubility experiments of the peralkaline rhyolitic melts, H_2O was uniformly dissolved within the corresponding quenched glasses. For all investigated glass compositions (Table 2), the density exhibited a linear decrease with increasing H_2O content. The linear correlations between density (in g/L) and c_{H2Ot} were fitted through regression analysis for the hydrous glasses of each composition (Eqs. 7–10), where the AOQ density relationship (ρ_{AOQ}) is from Nowak and Behrens (1997). The increase in density with higher peralkalinity is attributed to enhanced depolymerization caused by the incorporation of Na_2O, which leads to a reduction in molar volume of the glass (Bottinga and Richet, 1995).

$$\rho_{AOQ} = (2362) - (14.5) \cdot c_{H2Ot} \quad (7)$$

$$\rho_{AOQ2} = (2351 \pm 2) - (12.30 \pm 0.6) \cdot c_{H2Ot} \quad (8)$$

$$\rho_{AOQ4} = (2362 \pm 4) - (9.90 \pm 1.2) \cdot c_{H2Ot} \quad (9)$$

$$\rho_{AOQ8} = (2392 \pm 3) - (7.96 \pm 0.9) \cdot c_{H2Ot} \quad (10)$$

Linear molar absorption coefficients

Linear molar absorption coefficients of the NIR absorption bands related to OH at ~4470 cm^{-1} and molecular H_2O at ~5210 cm^{-1} were determined by applying a linear tangent baseline correction, consistent with the method described by Behrens et al. (1996), to measure peak heights for the AOQ2, AOQ4, and AOQ8 compositions. This baseline correction was chosen as it was also employed for AOQ compositions (Behrens and Nowak, 2003), enabling direct comparison of the linear molar absorption coefficients obtained in this study. The absorption coefficients for each glass composition were determined using the NIR absorbances of hydrous glasses with known total H_2O concentrations from KFT analysis. According to Eq. 11 the normalized absorbances (shown in parentheses) were calculated:

$$\left(\frac{1802 \cdot A_{H_2O}}{d \cdot \rho \cdot c_{H_2O_t\,(KFT)}}\right) = \varepsilon_{H_2O} - \frac{\varepsilon_{H_2O}}{\varepsilon_{OH}} \left(\frac{1802 \cdot A_{OH}}{d \cdot \rho \cdot c_{H_2O_t(KFT)}}\right) \quad (11)$$

A straight line is obtained by plotting the normalized absorbances, where the absorption coefficients of OH and H_2O_m correspond to the intercepts with the x-axis and y-axis, respectively. The absorption coefficients, determined using weighted linear least-squares regression, are as follows:

AOQ2: ε_{OH} =1.59 ± 0.04 and ε_{H2Om} = 1.50 ± 0.02 L·mol^{-1}·cm^{-1}

AOQ4: ε_{OH} =1.50 ± 0.04 and ε_{H2Om} = 1.20 ± 0.02 L·mol^{-1}·cm^{-1}

AOQ8: ε_{OH} =1.03 ± 0.05 and ε_{H2Om} = 0.96 ± 0.02 L·mol^{-1}·cm^{-1}.

Compared to the AOQ absorption coefficients (ε_{OH}: 1.56 ± 0.021 L·mol^{-1}·cm^{-1} and ε_{H2Om}: 1.79 ± 0.021 L·mol^{-1}·cm^{-1}; Behrens and Nowak, 2003), ε_{H2Om} decreases significantly with increasing excess alkali content (x_{ex} = (Na_2O+K_2O–Al_2O_3)/100). While ε_{OH} increases slightly from AOQ to AOQ2, it subsequently decreases at higher excess alkali levels, following a parabolic trend as illustrated in Fig. 8.

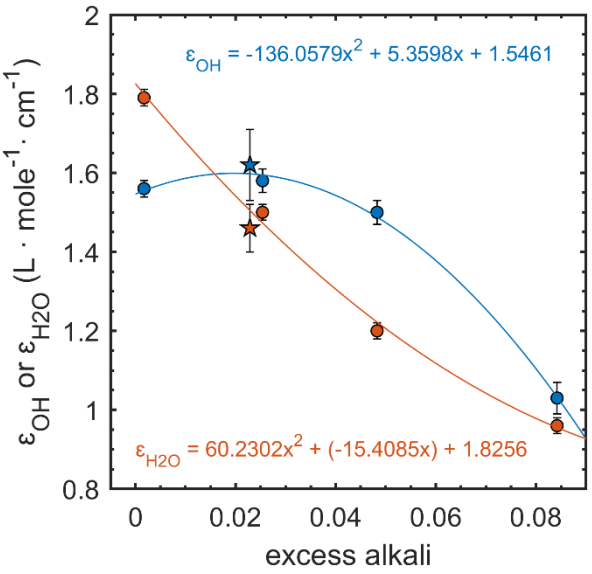

Fig. 8: Dependence of linear molar absorption coefficients with excess alkali content. The lines represent the fits to the data obtained in this study (circles), while the stars denote the absorption coefficients for a natural peralkaline rhyolite composition (NSL) from Behrens et al., (2009).

The observed decrease in absorption coefficients with increasing excess alkali and peralkalinity is consistent with previous studies (Acocella et al., 1984; Behrens et al., 1996). Behrens et al. (1996) attributed this effect to the strong hydrogen bonding of H_2O species to non-bridging oxygens, where only a portion of the water contributes to the absorption bands. The slight increase in ε_{OH} with moderate excess alkali additions is not fully understood and lies beyond the scope of this study. However, the dependence of absorption coefficients shown in Fig. 8 is supported by data from Behrens et al. (2009), who determined absorption coefficients using the same baseline procedure for a natural peralkaline rhyolite (NSL) glass from New Zealand. This glass

exhibited a similar excess alkali content and an identical molar Na/(Na + K) ratio of 0.64 as AOQ2.

Behrens et al. (1996) also demonstrated that alkali substitution (e.g., Na, K, Li) affects absorption coefficients in hydrous alkali feldspar glasses. It is possible that a similar effect occurs in peralkaline rhyolitic glasses. Consequently, the trends observed in Fig. 8 may also reflect changes in the Na/(Na + K) ratio, which increases from 0.55 in AOQ to 0.78 in AOQ8.

H_2O solubility of AOQ4 and AOQ8

In accordance with the Lambert-Beer law, the NIR band intensities of OH and H_2O_m were used to calculate their respective concentrations in the glass samples. Similar to other silicate melt compositions, the solubility of H_2O in both AOQ4 and AOQ8 melts increases with pressure at a constant temperature and decreases with temperature at a constant pressure. The empirical solubility equation for rhyolitic melts proposed by Liu et al. (2005) (Eq. 12) effectively describes H_2O solubility as a function of pressure and temperature for AOQ melts. Based on this, the functional form of the equation was adapted to derive solubility equations for AOQ4 and AOQ8.

The resulting H_2O solubility equations as a function of pressure and temperature are presented in Eqs. 13 and 14. These equations are valid within the specified pressure and temperature ranges. Both fits yield an R^2 value of 0.99, with root-mean-square errors of 0.07 wt% and 0.06 wt% for AOQ4 and AOQ8, respectively.

$$\text{AOQ: } c_{\mathrm{H_2O_t}}(\text{wt\%}) = \frac{354.94P^{0.5} + 9.623P - 1.5223P^{1.5}}{T} + 0.001244P^{1.5}$$

[0.1–500 MPa, 825–1423 K] (12)

$$\text{AOQ4: } c_{\mathrm{H_2O_t}}(\text{wt\%}) = \frac{337.9P^{0.5} + 28.33P - 2.217P^{1.5}}{T} + 0.001271P^{1.5}$$

[27–200 MPa, 1123–1523 K] (13)

$$\text{AOQ8: } c_{\mathrm{H_2O_t}}(\text{wt\%}) = \frac{536.4P^{0.5} + 5.125P - 1.091P^{1.5}}{T} + 0.001323P^{1.5}$$

[50–200 MPa, 1123–1523 K] (14)

Results derived from Eqs. 12–14 show that H_2O solubility increases linearly with increasing Na_2O excess, from AOQ to AOQ8, at constant pressure and temperature (Fig. 9). Given this linear relationship, the solubility for any Na_2O excess value can be calculated via linear interpolation between the AOQ and AOQ8 compositions at a given pressure and temperature.

This approach was validated through an additional solubility experiment conducted with the AOQ2 melt composition (100 MPa and 1123 K) and data from Dingwell et al. (1997) for haplogranitic melts (HPG8; compositionally similar to AOQ) containing 5 wt% Na_2O excess (+5 Na) and 10 wt% Na_2O excess (+10 Na) at 50 MPa and 1273 K. The interpolated and moderately extrapolated H_2O solubility values (in the case of the 10 wt% Na_2O experiment) agree with the experimentally determined H_2O solubilities, with a relative deviation of no more than 6%.

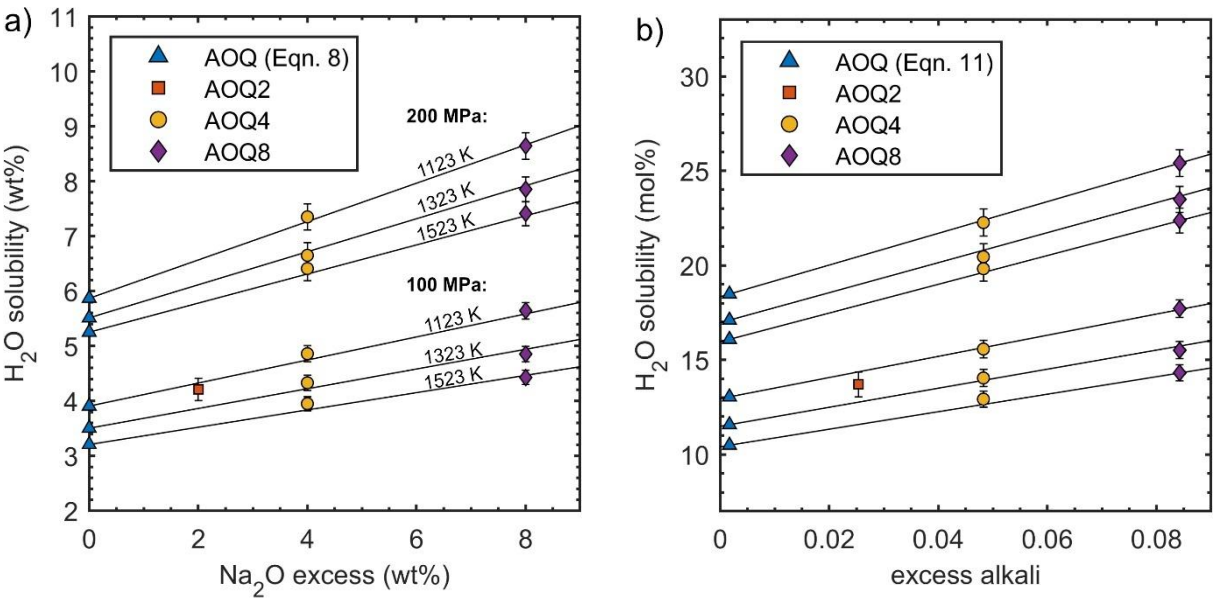

Fig. 9: (a) Linear relationship between H_2O solubility (wt%) and increasing Na_2O excess relative to the AOQ composition. AOQ data are derived from Eq. 12, and the solid lines represent linear interpolations between results from Eq. 14 (for AOQ8) and Eq. 12. (b) Linear relationship between H_2O solubility (mol%) and excess alkali (defined as the difference between alkali mole fractions and that of alumina) under identical *P* and *T* conditions. H_2O solubility for AOQ is calculated using Eq. 15, while the solid lines correspond to calculations based on Eq. 18.

A general H_2O solubility model for peralkaline rhyolitic melts

Dingwell et al. (1997) demonstrated that, for peralkaline haplogranitic melts at 50 MPa and 1273 K, the increase in H_2O solubility with peralkalinity on a molar basis is identical for Na_2O, K_2O, Rb_2O, and Cs_2O. They further suggested that this behavior is likely consistent at pressures up to 500 MPa. However, the addition of Li_2O had a comparatively smaller effect on H_2O solubility, which they attributed to Li_2O's potential inability to form non-bridging oxygens that could interact with hydrous species.

Based on these findings, it can be inferred that, on a molar basis, the dependence of H_2O solubility on peralkalinity observed between AOQ and AOQ8 as a function of pressure and temperature may be extended to haplogranitic compositions with general excess alkali, excluding lithium. Consequently, the H_2O solubilities from AOQ experiments (data from Holtz et al., 1995, and Liu et al., 2005), as well as AOQ4 and AOQ8 experiments, were recalculated in mol%, and new fit parameters were obtained:

$$\mathrm{AOQ}:\ c_{\mathrm{H_2O_t}}(mol\%) = \frac{1440P^{0.5} + 3.689P - 3.839P^{1.5}}{T} + 0.003308P^{1.5}$$

[0.1–500 MPa, 825–1423 K] (15)

$$\mathrm{AOQ4}:\ c_{\mathrm{H_2O_t}}(mol\%) = \frac{1249P^{0.5} + 83.59P - 8.523P^{1.5}}{T} + 0.004575P^{1.5}$$

[27–200 MPa, 1123–1523 K] (16)

$$\mathrm{AOQ8}:\ c_{\mathrm{H_2O_t}}(mol\%) = \frac{1896P^{0.5} + 9.01P - 5.518P^{1.5}}{T} + 0.004884P^{1.5}$$

[50–200 MPa, 1123–1523] (17)

The equations are constrained to the pressure and temperature ranges specified in brackets. These equations reproduce both the AOQ data and the results of this study. Additionally, the linear dependence of H_2O solubility on increasing excess alkali at constant pressure and temperature is also observed on a molar basis. Interpolation between AOQ and AOQ8 solubilities at given *P* and *T* enables the calculation of H_2O solubility as a function of excess alkali, regardless of the specific alkali type, except in the case of lithium.

$$c_{\mathrm{H2Ot}}\,(\mathrm{mol\%}) = c_{\mathrm{AOQ8}} - ((c_{\mathrm{AOQ8}} - c_{\mathrm{AOQ}})/0.0825) \cdot (0.0842 - x_{\mathrm{ex}}) \quad (18)$$

Where c_{AOQ} and c_{AOQ8} are the results of Eqs. 15 and 17, respectively, under the desired P and T conditions, while x_{ex} represents the excess alkali of the desired composition.

The solubility model was validated against several natural peralkaline rhyolitic melt compositions (Scaillet and Macdonald, 2001, 2006; Moore et al., 1998; Behrens and Jantos, 2001; Gaillard et al., 2001; Stabile et al., 2018), yielding very good agreement with relative deviations of 5–10%. The consistency between observed and predicted H_2O solubility, based on a single chemical parameter (excess alkali), for both Fe-free haplogranites and Fe-bearing peralkaline rhyolitic melts indicates that Fe does not significantly influence H_2O solubility in peralkaline melts. This conclusion is further supported by Gaillard et al. (2001), who reported no measurable effect of the Fe^{2+}/Fe^{3+} ratio on H_2O solubility, as well as by the data of Scaillet and Macdonald (2001), where similar H_2O concentrations were observed under both reduced and oxidized conditions in iron-bearing melts.

This study demonstrates that H_2O solubility can be reliably calculated as a function of excess alkali for melts containing any alkali element except lithium. The model is valid within the experimental conditions of 27–500 MPa, 976–1523 K, and excess alkali values up to 0.0825. Accurate prediction of H_2O solubility in peralkaline melts contributes to a better understanding of the largely unknown eruption styles of peralkaline rhyolites (Clarke et al., 2019) and improves reconstructions of magmatic and volcanic processes related to peralkaline melts, such as those in the East African Rift, Kenyan Rift, Gran Canaria, Turkey, and Pantelleria (Lowenstern and Mahood, 1991; Neave et al., 2012; McDonald et al., 2015; Clarke et al., 2019).

Calculation scripts (MS Excel and Matlab (“SolModel_peralk_rhyolite”)) are provided in the supplementary material at https://doi.org/10.1007/s00410-022-01915-8 for calculating the excess alkali and H_2O solubility (in mol% and wt%) based on input values of P, T, and the anhydrous composition (in wt%).

H_2O degassing triggered by alkali depletion during bimodal magma injection processes *(Study IV)*

Validation of experimental setup

The novel experimental procedure, involving the contact of two hydrous glass cylinders without air entrapment, was validated using a reference decompression experiment with two contacted hydrous rhyolitic glass cylinders. The results showed homogeneously distributed vesicles throughout the sample's central volume. The former interface between the two cylinders was no longer visible, and no enhanced vesicle formation was observed at the former interface. These findings confirm the suitability of the experimental setup for subsequent magma injection experiments with different bulk compositions.

Vesiculation in bimodal magma injection experiments

The bimodal magma injection (MI) reference experiment established the initial melt conditions after heating and thermal equilibration for 10 min at 1348 K and 210 MPa prior to decompression to the final pressure of 100 MPa (MI_T_3, MI_7, MI_6). No vesicles formed during the experiment in either the rhyolitic or basaltic sections of the sample. The basalt exhibited partial crystallization, characterized by 1–3 µm sized magnetite crystals as identified through EPMA analysis.

In decompressed MI samples, the rhyolitic glasses showed a homogeneously vesiculated central volume (Fig. 10). All decompressed MI samples demonstrated an increase in VND or larger vesicle sizes near the contact zone between the initial rhyolitic and basaltic melts. This contact zone, marked by a color gradient transitioning from colorless (rhyolitic) to brownish or black (basaltic), corresponds to the hybrid zone formed by diffusion-controlled mixing during the experiment (Fig. 10d). The onset of magnetite crystal occurrence correlates with the black coloration in the optical images. Notably, the enhanced VND region consistently appeared within the rhyolite-dominated part of the hybrid zone across all bimodal decompressed samples.

Textural analysis of the decompressed samples revealed four distinct zones:

1. Peripheral zone: Fringe vesicles at the capsule wall-melt interface (Navon and Lyakhovsky, 1998; Iacono-Marziano et al., 2007).

2. Partially crystallized basaltic glass: Central volume containing vesicles.

3. Rhyolitic glass: Central volume with vesicles (Navon and Lyakhovsky, 1998).

4. Hybrid zone: Enhanced VND compared to the rhyolitic volume.

These zones likely result from different nucleation mechanisms. Fringe vesicles in zones (1) and vesicles in (2) were attributed to heterogeneous nucleation at crystal-melt interfaces.

In the peripheral rhyolitic melt, vesicles formed heterogeneously at the capsule melt interface due to a low wettability of the capsule material with hydrous rhyolitic melt. This reduced the required energy for vesicle formation under low supersaturation during decompression (e.g., Mangan and Sisson, 2000; Iacono-Marziano et al., 2007). In the basaltic melt, magnetite crystals formed during hydration likely acted as nucleation sites for H_2O vesicles during reheating and decompression within the stability field of magnetite (Hurwitz and Navon, 1994; Mangan and Sisson, 2000, 2005; Gardner and Denis, 2004; Gardner, 2007; Edmonds et al., 2015).

In contrast, zone (3) exhibited homogeneous vesicle nucleation in rhyolitic melt, which lacked pre-existing crystals. According to nucleation theory, VND increases with the decompression rate (Toramaru, 2006). This is consistent with the VND data of the MI samples, where MI_6, decompressed at 1.7 MPa/s, showed the highest VND with $1.2 \cdot 10^3$ cm^{-3} compared to MI_T_3 and MI_7, decompressed at 0.17 MPa/s and VNDs of $1.9 \cdot 10^2$ and $2.2 \cdot 10^2$ cm^{-3}, respectively.

The hybrid zone's vesicle textures and VNDs differed significantly from those of the central rhyolitic melt. It was confirmed that vesicles nucleated heterogeneously at magnetite crystals did not migrate from the basalt to the hybrid zone. This conclusion was supported by MI_7, where the basalt overlays the rhyolite. Despite the basalt sinking into the rhyolite due to density differences, the enhanced VND zone remained confined to the lower rhyolite-dominated region of the hybrid zone, positioned beneath the partially crystallized basalt (Fig. 10b, d).

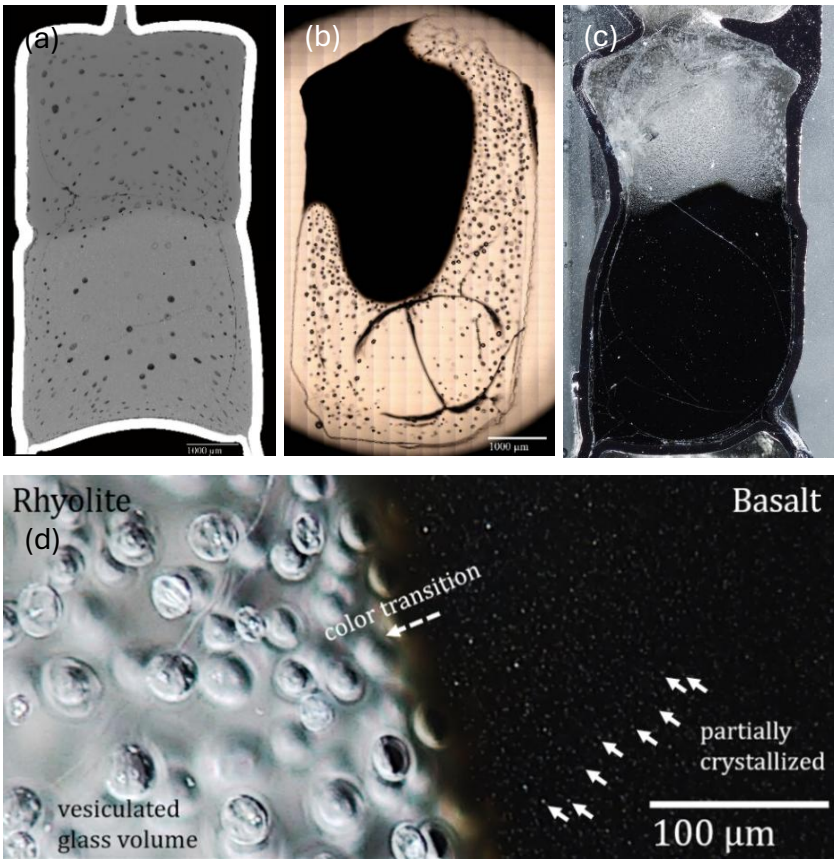

Fig. 10: (a) SEM image of sample MI_T_3 (d*P*/d*t* = 0.17 MPa/s);
(b) Microscope image in transmission mode of sample MI_7 (d*P*/d*t* = 0.17 MPa/s);
(c) Microscope image of sample MI_6 (d*P*/d*t* = 1.7 MPa/s);
(d) Microscope image of sample MI_7, showing partially crystallized basaltic glass with magnetite (indicated by arrows). The hybrid zone displays a color gradient, transitioning from opaque black (basalt) to semitransparent brownish and finally to transparent colorless (rhyolite).

All samples are cut and polished along the cylinder axis, with image alignment matching the capsule orientation during the experiment. Increased vesicle formation is observed at the former interface.

Magma mixing

The melt between rhyolite and basalt developed as intermediate composition through multicomponent interdiffusion processes of ions, depending on their concentrations, charges, specific diffusion coefficients, and the requirement to maintain charge neutrality over the sample. The alkali ions Na and K diffuse several orders of magnitude faster than other network-modifying cations, including Ca, Mg, Fe, and Ti, as well as network-forming ions like Si and Al, which exhibit the lowest mobilities due to their coupling with O-diffusion (e.g., Watson, 1982; Baker, 1992; Johnston and Wyllie, 1988; Zhang et al., 2010).

Notably, Na and K exhibited significantly faster diffusion rates than Si toward the basaltic region, leading to a pronounced depletion of measured Na_2O and K_2O in the rhyolite-dominated hybrid zone. In contrast, cations such as Ca, Mg, Fe, Ti and Al diffused toward the rhyolitic melt as a counter flux. The concentration profiles of oxide components illustrate these interdiffusion processes (Fig. 11). Specifically, the asymmetric profile of Na_2O, with a greater length extending into the rhyolitic side, suggests varying diffusion coefficients of Na in basaltic versus rhyolitic melts, with Na

exhibiting higher diffusivity in the rhyolitic composition (Zhang et al., 2010). This effect is further amplified by the increased H_2O content in the rhyolite, as higher H_2O content increases ion mobility in the melt (Watson, 1982).

In contrast to the alkalis, other oxide components display symmetric concentration profiles within the hybrid zone (Fig. 11). For further evaluation, SiO_2 concentration profiles were analyzed across all samples to determine the extent of the mixed hybrid zone.

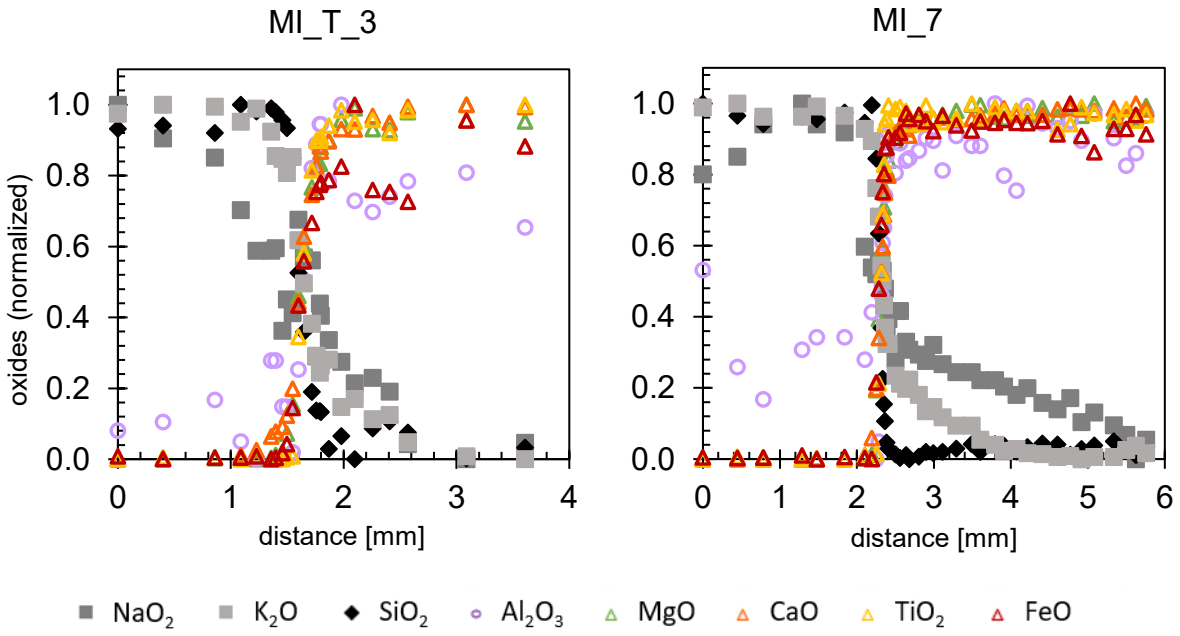

Fig. 11: EPMA measured concentration-distance profiles of oxide components between initial rhyolitic composition (left) and initial basaltic composition (right) of MI_T_3 and MI_7. The concentrations of the individual oxides were normalized to a range from 0 to 1.

c_{H2Ot} profiles along the hybrid zones

The c_{SiO2} concentration profiles align with the c_{H2Ot} profiles (Fig. 12), as the inflection point of the c_{SiO2} profile corresponds to the first measurement within the color transition from brownish to transparent glass (referred to the "midpoint"). To calculate the c_{H2Ot} from FTIR-measured profiles across the hybrid zone, each measurement point was assigned the corresponding SiO_2 concentration obtained from EPMA measurements.

For the determination of the c_{H2Ot} concentration profile across the hybrid zone, FTIR absorption spectra were baseline-corrected following the method of Ohlhorst et al. (2001). Straight lines were fitted through the minima on both sides of the NIR

combination bands corresponding to H_2O_m and OH to measure peak heights. The linear molar absorption coefficients (ε) were calculated using the parabolic equation from Ohlhorst et al. (2001), which predicts ε as a function of the c_{SiO2} (wt%) content of the glass, applicable for compositions ranging from rhyolite to basalt:

$$\varepsilon = a + b \cdot c_{SiO2}{}^2 \quad (19)$$

The baseline-dependent parameters a = −0.13 and b = 0.000257 were used, resulting in absorption coefficients for rhyolite (ε_{H2Om} = 1.57 and ε_{OH} = 1.32 L·mol^{-1}·cm^{-1}) and basalt (ε_{H2Om} = 0.76 and ε_{OH} = 0.64 L·mol^{-1}·cm^{-1}).

Glass density [g/L], required for the calculation of c_{H2Ot} via the Lambert-Beer law, was determined at each measurement point using equations from Allabar et al. (2022; *Study III*; Eq. 8), Yamashita (1997, composition no. 43gm, Eq. 20), and Ohlhorst et al., (2001, Eq. 21) for rhyolite, dacite, and basalt, respectively. For the hybrid composition, density values were interpolated iteratively between dacite density (at the midpoint) and rhyolite or basalt densities.

$$\rho_D = (2515 \pm 6) - (11.8 \pm 2.0) \cdot c_{H2Ot} \quad (20)$$

$$\rho_B = (2819 \pm 13.5) - (20.8 \pm 6.6) \cdot c_{H2Ot} \quad (21)$$

Applying this procedure, c_{H2Ot} profiles across the hybrid zone reveal an increase in H_2O concentrations transitioning from rhyolitic to basaltic compositions (Fig. 12). Within the high VND zones, c_{H2Ot} was generally higher than c_{H2Oeq} predicted for P_f. This discrepancy might be attributed to the increased solubility of H_2O with decreasing temperature at pressures below 300 MPa (Holtz et al., 1995), causing H_2O diffusion from vesicles back into the melt during quenching. This process led to vesicle shrinkage and the formation of resorption halos, with elevated H_2O concentrations surrounding the vesicles (McIntosh et al., 2014; Allabar et al., 2020a). Higher VNDs accelerated H_2O resorption due to the larger number of H_2O fluid sources per unit melt volume, particularly in the hybrid zones.

Based on EPMA data, the hybrid melt evolved to a dacitic composition, similar to Unzen dacite (Chen et al., 1993). The elevated c_{H2Ot} in dacitic hybrid zones may also result from vesicle resorption. Assuming similar temperature dependence of H_2O solubility in dacite, vesicles nucleated in basaltic-dominated hybrid regions during decompression could have dissolved during cooling, increasing c_{H2Ot} in the glass. Therefore, hybrid

melt that resorbed H_2O indicates a much higher c_{H2Ot} in the glass than in the rhyolite-dominated vesiculated hybrid regions (Fig. 12). Experimental results from Sato et al. (1999) demonstrated that at 98 MPa and 1303 K, 5.7 wt% H_2O is soluble, comparable to the experimental final conditions here (100 MPa, 1348 K). Therefore, dacitic melts show higher H_2O solubility (5.7 wt%) than rhyolitic (3.8 wt%) or basaltic (3.3 wt%) melts under similar conditions (*Study III*; Berndt et al., 2002). This solubility difference may explain the ~1 wt% increase in c_{H2Ot} across hybrid zones.

Despite possible uncertainties in absorption coefficients, baseline corrections, and the influence of H_2O resorption during quenching, the observed increase in c_{H2Ot} toward the basaltic hybrid zone is plausible. However, the high c_{H2Ot} values (~6 wt%) in dacitic hybrid regions warrant further investigation. Improving H_2O quantification via NIR spectroscopy could involve synthesizing hydrous glass standards with intermediate compositions to match the hybrid zone's bulk composition through controlled mixing of rhyolite and basalt.

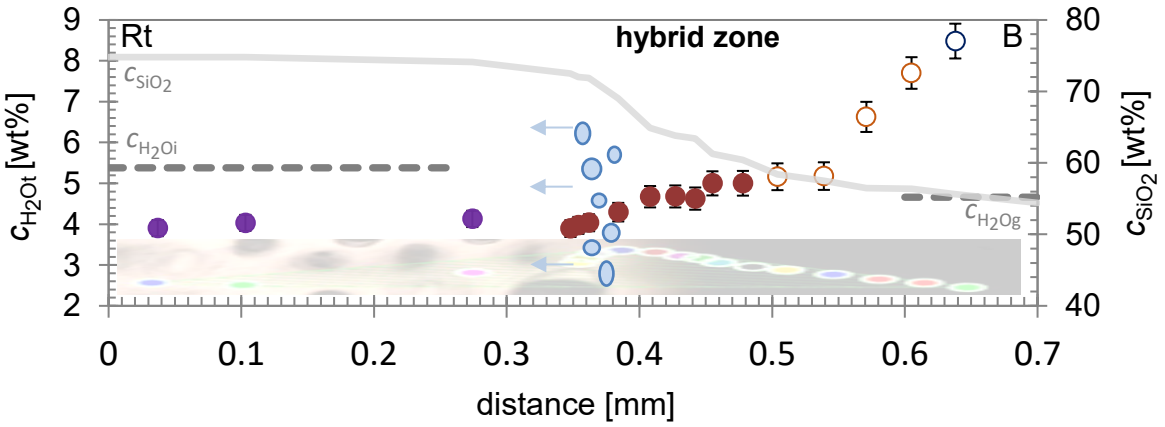

Fig. 12: A c_{H2Ot}-distance profile from rhyolite (violet) to basalt (blue) through the hybrid melt zone (red) of bimodal sample MI_T_3. Open circles represent excluded NIR measurements. Shaded transmission microscope image shows data points, with dashed lines marking c_{H2Oi} in rhyolite and basalt. Grey solid lines indicate the SiO_2 concentration profile, and blue ellipsoids highlight the vesiculated rhyolite zone.

Alkali depletion responsible for enhanced vesicle formation in the hybrid zone

Enhanced VND is consistently observed in the rhyolite-dominated regions of the hybrid zones across all decompressed bimodal samples (Figs. 10, 12). As a novel approach to understanding vesicle nucleation, this section discusses the role of alkali diffusion and the resulting alkali depletion in the rhyolite-dominated region of the hybrid zone formed between rhyolite and the injected basalt.

The enhanced vesiculated zone likely forms due to the rapid diffusive loss of alkalis from the mildly peralkaline rhyolitic melt into the basaltic melt. The significant reduction in Na_2O concentration in the rhyolitic melt reduces its H_2O solubility, promoting H_2O supersaturation near the contact zone during decompression. Dingwell et al. (1997) demonstrated that H_2O solubility in silicate melts is influenced by alkali excess (x_{ex} = (Na_2O+K_2O–Al_2O_3)/100). This relationship was confirmed in *Study III*, where a linear increase in H_2O solubility with increasing Na_2O excess, or alkali excess in general was reported.

The initial x_{ex} in the mildly peralkaline rhyolite was 0.03. However, during the decompression experiments, x_{ex} decreased by more than 90%, approaching the H_2O solubility minimum at x_{ex} = 0. This reduction in alkali excess led to a decrease in H_2O solubility by ~ 0.4 wt%, thereby lowering ΔP required to initiate vesicle formation in the alkali-depleted rhyolitic melt near the contact zone. In contrast, vesicle nucleation and growth in pristine rhyolitic melt occurred at higher ΔP values, resulting in VNDs approximately half of those of the hybrid melt zones. These findings indicate that, in addition to pressure and temperature, the alkali concentration is a critical parameter influencing H_2O solubility and, consequently, vesicle formation in rhyolitic silicate melts.

References

Acocella, J., Tomozowa, M., Watson, E.B.: The nature of dissolved water in sodium silicate glasses and its effect on various properties. J. Non. Cryst. Solids, 65, 355–372, https://doi.org/10.1016/0022-3093(84)90058-9, 1984.

Allabar, A. and Nowak, M.: Message in a bottle: Spontaneous phase separation of hydrous Vesuvius melt even at low decompression rates, Earth Planet. Sc. Lett., 501, 192–201, https://doi.org/10.1016/j.epsl.2018.08.047, 2018.

Allabar, A., Salis Gross, E., Nowak, M.: The effect of initial H_2O concentration on decompression-induced phase separation and degassing of hydrous phonolitic melt. Contrib. Mineral. Petrol., 175, 22, 10.1007/s00410-020-1659-2, 2020a.

Allabar, A., Dobson, K. J., Bauer, C. C., Nowak, M.: Vesicle shrinkage in hydrous phonolitic melt during cooling, Contrib. Mineral. Petr. 175, 21, https://doi.org/10.1007/s00410-020-1658-3, 2020b.

Allabar, A., Petri, P. L., Eul, D., and Nowak, M.: An empirical H_2O solubility model for peralkaline rhyolitic melts, Contrib. Mineral. Petr., 177, 52, https://doi.org/10.1007/s00410-022-01915-8, 2022.

Baker, D. R.: Estimation of diffusion coefficients during interdiffusion of geologic melts: Application of transition state theory, Chem. Geol., 98, 11–21, https://doi.org/10.1016/00092541(92)90089-N, 1992.

Behrens, H.: Determination of water solubilities in high-viscosity melts: an experimental study on $NaAlSi_3O_8$ and $KAlSi_3O_8$ melts. Eur. J. Mineral., 7, 905–920, 10.1127/ejm/7/4/0905, 1995.

Behrens, H. and Jantos, N.: The effect of anhydrous composition on water solubility in granitic melts. Am. Mineral., 86, 14–20, https://doi.org/10.2138/am-2001-0102, 2001.

Behrens, H., Romano, C., Nowak, M., Holtz, F., Dingwell, D. B.: Near-infrared spectroscopic determination of water species in glasses of the system $MAlSi_3O_8$ (M = Li, Na, K): an interlaboratory study, Chem. Geol., 128, 41–63, https://doi.org/10.1016/0009-2541(95)00162-X, 1996.

Behrens, H. and Nowak, B.: Quantification of H_2O speciation in silicate glasses and melts by IR Spectroscopy – in situ versus quench techniques. Phase Transitions 76, 45–61, 10.1080/0141159031000076048, 2003.

Behrens, H., Misiti, V., Freda, C., Vetere, F., Botcharnikov, R.E., Scarlato, P.: Solubility of H_2O and CO_2 in ultrapotassic melts at 1200 and 1250 °C and pressure from 50 to 500 MPa. Am. Mineral., 94, 105–120, https://doi.org/10.2138/am.2009.2796, 2009.

Berndt, J., Liebske, C., Holtz, F., Freise, M., Nowak, M., Ziegenbein, D., Hurkuck, W., and Koepke, J.: A combined rapid-quench and H_2-membrane setup for internally heated pressure vessels: Description and application for water solubility in basaltic melts, Am. Mineral., 87, 1717–1726, https://doi.org/10.2138/am-200211-1222, 2002.

Bottinga, Y. and Richet, P.: Silicate melts: The “anomalous” pressure dependence of the viscosity. Geochim. Cosmochim. Acta, 59, 2725–2731, https://doi.org/10.1016/0016-7037(95)00168-Y, 1995.

Bunsen, R. W.: Ueber die Processe der vulkanischen Gesteinsbildung Islands, Annu. Rev. Phys. Chem., 83, 197–272, https://doi.org/10.1002/andp.18511590602, 1851.

Cahn, J.W.: Phase separation by spinodal decomposition in isotropic systems. J. Chem. Phys., 42, 93–99, https://doi.org/10.1063/1.1695731, 1965.

Caricchi, L., Pommier, A., Pistone, M., Castro, J., Burgisser, A., Perugini, D.: Strain-induced magma degassing: Insights from simple-shear experiments on bubble bearing melts. Bull. Volcanol., 73(9), 1245–1257, https://doi.org/10.1007/s00445-011-0471-2, 2011.

Castro, J. M., Burgisser, A., Schipper, C. I., Mancini, S.: Mechanisms of bubble coalescence in silicic magmas. Bull. Volcanol., 74, 10, 2339–2352, https://doi.org/10.1007/s00445-012-0666-1, 2012.

Coumans, J.P., Llewellin, E.W., Wadsworth, F.B., Humphreys, M.C.S., Mathias, S.A., Yelverton, B.M., Gardner, J.E.: An experimentally validated numerical model for bubble growth in magma. J. Volcanol. Geotherm. Res., 402, https://doi.org/10.1016/j.jvolgeores.2020.107002, 2020.

Chen, C. H., DePaolo, D. J., Nakada, S., and Shieh, Y. N.: Relationship between eruption volume and neodymium isotopic composition at Unzen volcano, Nature, 362, 831–834, https://doi.org/10.1016/j.jvolgeores.2008.03.042, 1993.

Clarke, B., Calder, E.S., Dessalegn, D., Fontijn, K., Cortés, J.A., Naylor, M., Hutchinson, W., Yirgu, G.: Fluidal pyroclasts reveal the intensity of peralkaline rhyolite pumice cone eruptions. Nat. Commun., 10, 2010, 10.1038/s41467-019-09947-8, 2019.

De Vivo, B., Lima, A., Webster, J.D.: Volatiles in Magmatic-Volcanic Systems. Elements, 1, 19–24, 10.2113/gselements.1.1.19, 2005.

Debenedetti, P.G.: Phase separation by nucleation and by spinodal decomposition: fundamentals. In: Kiran, E., Debenedetti, P.G., Peters, C.J. (Eds.), Supercritical Fluids. In: Nato Science Series E, 366, 123–166, 10.1007/978-94-011-3929-8_5, 2000.

Dingwell, D. B., Holtz, F., and Behrens, H.: The solubility of H_2O in peralkaline and peraluminous granitic melts, Am. Mineral., 82, 434–437, https://doi.org/10.2138/AM-1997-3-421, 1997.

Edmonds, M., Brett, A., Herd, R. A., Humphreys, M. C. S., and Woods, A.: Magnetite-bubble aggregated at mixing interfaces in andesite magma bodies, in: The Role of Volatiles in the Genesis, Evolution and Eruption of Arc Magmas, Geol. Soc. Sp., 410, 95, https://doi.org/10.1144/SP410.7, 2015.

Eichelberger, J.C., Carrigan, C.R., Westrich, H.R., Price, R.H.: Non-explosive silicic volcanism. Nature, 323, 598–602, https://doi.org/10.1038/323598a0, 1986.

Eri, A. and Okumura, K.: Bursting of a thin film in a confined geometry: Rimless and constant-velocity dewetting. Phys. Rev. E - Statistical, Nonlinear and Soft Matter Physics, 8, 3, 1–4, https://doi.org/10.1103/ PhysRevE.82.030601, 2010.

Gaillard, F., Scaillet, B., Pichavant, M., Bény, J.M.: The effect of water and f_{O2} on the ferric-ferrous ratio of silicic melts. Chem. Geol., 174, 255–273, https://doi.org/10.1016/S0009-2541(00)00319-3, 2001.

Gardner, J., Thomas, R.M.E., Jaupart, C., Tait, S.: Fragmentation of magma during Plinian volcanic eruptions. Bull. Volcanol., 58, 144–162, https://doi.org/10.1007/s004450050132, 1996.

Gardner, J. E. and Denis, M.-H.: Heterogeneous bubble nucleation on Fe-Ti oxide crystals in high-silicia rhyolitic melt, Geochim. Cosmochim. Ac., 68, 3587–3597, https://doi.org/10.1016/j.gca.2004.02.021, 2004.

Gardner, J.E., Burgisser, A., Hort, M., Rutherford, M.: Experimental and model constraints on degassing of magma during ascent and eruption. Geol. Soc. Am. Bull. Spec. Pap., 402, 99–114, DOI: 10.1130/2006.2402(04), 2006.

Gardner, J. E.: Heterogeneous bubble nucleation in highly viscous silicate melts during instantaneous decompression from high pressure, Chem. Geol., 236, 1–12, https://doi.org/10.1016/j.chemgeo.2006.08.006, 2007.

Gardner, J. E., Wadsworth, F. B., Carley, T. L., Llewellin, E. W., Kusumaatmaja, H., & Sahagian, D.: Bubble Formation in Magma. Annual Review of Earth and Planetary Sciences, 51(1), 131–154. https://doi.org/10.1146/annurev-earth-031621-080308, 2023.

Genareau, K., Proussevitch, A.A., Durant, A.J., Mulukutla, G., Sahagian, D.L.: Sizing up the bubbles that produce very fine ash during explosive volcanic eruptions. Geophys. Res. Lett., 39, L15306, doi:10.1029/2012GL052471, 2012.

Giachetti, T., Gonnermann, H. M., Gardner, J. E., Burgisser, A., Hajimirza, S., Earley, T. C., Truong, N., Toledo, P.: Bubble coalescence and percolation threshold in expanding rhyolitic magma. Geochemistry, Geophysics, Geosystems, 20, 1054–1074. 10.1029/2018GC008006, 2019.

Giordano, D., Potuzak, M., Romano, C., Dingwell, D.B., Nowak, M.: (2008) Viscosity and glass transition temperature of hydrous melts in the system CaAl2Si2O8-CaMgSi2O6. Chem. Geol., 256, 203–215, 10.1016/j.chemgeo.2008.06.027, 2008.

Gurioli, L., Houghton, B.F., Cashman, K.V., Cioni, R.: Complex changes in eruption dynamics during the 79 AD eruption of Vesuvius. Bull. Volcanol. 67, 144–159, 10.1007/s00445-004-0368-4, 2005.

Hajimirza, S., Gonnermann, H.M., Gardner, J.E., Giachetti, T.: Predicting homogeneous bubble nucleation in rhyolite. J. Geophys. Res. Solid Earth, 124, 2395–2416, https://doi.org/10.1029/2018JB015891, 2019.

Harms, E. and Schmincke, H.U.: Volatile composition of the phonolitic Laacher See magma (12,900 yr BP): implications for syn-eruptive degassing of S, F, Cl and H_2O. Contrib. Mineral. Petrol., 138, 84–98, 10.1007/PL00007665, 2000.

Harms, E., Gardner, JE., Schmincke, H.U.: Phase equilibria of the Lower Laacher See Tephra (East Eifel, Germany): constraints on pre-eruptive storage conditions of a

phonolitic magma reservoir. J. Volcanol. Geotherm. Res., 134, 135-148, https://doi.org/10.1016/j.jvolgeores.2004.01.009, 2004.

Hertz, P.: Über den gegenseitigen durchschnittlichen Abstand von Punkten, die mit bekannter mittlerer Dichte im Raume angeordnet sind. Math. Ann., 67, 387–398, https://doi.org/10.1007/BF01450410, 1908.

Holasek, R. E., Self, S., Woods, A. W.: Satellite observations and interpretation of the 1991 Mount Pinatubo eruption plumes. J. Geophys. Res., 101, 27635–27655, https://doi.org/10.1029/96JB01179, 1996.

Holtz, F., Behrens, H., Dingwell, D.B., Johannes, W.: H_2O solubility in haplogranitic melts: Compositional, pressure, and temperature dependence. Am. Mineral., 80, 94–108, https://doi.org/10.2138/am-1995-1-210, 1995.

Huber, C., Su, Y., Nguyen, C.T., Parmigiani, A., Gonnermann, H. M., Dufek, J.: A new bubble dynamics model to study bubble growth, deformation, and coalescence, J. Geophys. Res. Solid Earth, 119, 216–239, doi:10.1002/2013JB010419, 2014.

Huppert, H. E., Sparks, R. S. J., and Turner, J. S.: Effects of volatiles on mixing in calc-alkaline magma systems, Nature, 297, 554–557, https://doi.org/10.1038/297554a0, 1982.

Hurwitz, S. and Navon, O.: Bubble nucleation in rhyolitic melts: experiments at high pressure, temperature, and water content. Earth Planet. Sci. Lett., 122, 267–80, https://doi.org/10.1016/0012-821X(94)90001-9, 1994.

Iacono-Marziano, G., Schmidt, B. C., Dolfi, D.: Equilibrium and disequilibrium degassing of a phonolitic melt (Vesuvius AD 79 “white pumice”) simulated by decompression experiments, J. Volcanol. Geoth. Res., 161, 151–164, https://doi.org/10.1016/j.jvolgeores.2006.12.001, 2007.

Jarvis, P. A., Pistone, M., Secretan, A., Blundy, J. D., Cashman, K. V., Mader, H. M., and Baumgartner, L. P.: Crystal and Volatile Controls on the Mixing and Mingling of Magmas, Geoph. Monog. Ser., 264, 125–150, https://doi.org/10.1002/9781119564485.ch6, 2021.

Jaupart, C. and Allègre, C.J.: Gas content, eruption rate and instabilities of eruption regime in silicic volcanoes. Earth Planet. Sci. Lett., 102, 413–429, https://doi.org/10.1016/0012-821X(91)90032-D, 1991.

Jaupart, C.: Gas loss from magmas through conduit walls during eruption. The physics of explosive volcanic eruptions. Geol. Soc. Lond. Spec. Pub., 145, 73–90, DOI:10.1144/GSL.SP.1996.145.01.05, 1998.

Johnston, A. D. and Wyllie, P. J.: Interaction of granitic and basic magmas: experimental observations on contamination processes at 10 kbar with H_2O, Contrib. Mineral. Petr., 98, 352–362, https://doi.org/10.1007/BF00375185, 1988.

Klug, C., and Cashman, K. V.: Permeability development in vesiculating magmas: Implications for fragmentation. Bull. Volcanol., 58, 87–100, https://doi.org/10.1007/s004450050128, 1996.

Kueppers, U., Scheu, B., Spieler, O., Dingwell, D.B.: Fragmentation efficiency of explosive volcanic eruptions: a study of experimentally generated pyroclasts. J. Volcanol. Geotherm. Res., 153, 125–135, https://doi.org/10.1016/j.jvolgeores.2005.08.006, 2006.

Larsen, J.F. and Gardner, J.E.: Experimental study of water degassing from phonolitic melts: implications for volatile oversaturation during magmatic ascent. J. Volcanol. Geotherm. Res., 134, 109–124, 10.1016/j.jvolgeores.2004.01.004, 2004.

Liu, Y., Zhang, Y., Behrens, H.: Solubility of H_2O in rhyolitic melts at low pressures and a new empirical model for mixed H_2O–CO_2 solubility in rhyolitic melts. J. Volcanol. Geotherm. Res., 143, 219–235, https://doi.org/10.1016/j.jvolgeores.2004.09.019, 2005.

Lowenstern, J. and Mahood, G.A.: New data on magmatic H_2O contents of pantellerites, with implications for petrogenesis and eruptive dynamics at Pantelleria. Bull Volcanol, 54, 78–83, https://doi.org/10.1007/BF00278208, 1991.

Mader, H. M., Llewellin, E. W., Mueller, S. P.: The rheology of two-phase magmas: A review and analysis. J. Volcanol. Geotherm. Res., 257, 135–158, https://doi.org/10.1016/j.jvolgeores.2013.02.014, 2013.

Marks, P.L., Allabar, A., Nowak, M.: H_2O degassing triggered by alkali depletion in bimodal magma injection processes – a new experimental approach. Eur. J. Mineral., 35, 613–633, https://doi.org/10.5194/ejm-35-613-2023, 2023.

Mangan, M. and Sisson, T.: Delayed, disequilibrium degassing in rhyolite magma: decompression experiments and implications for explosive volcanism. Earth Planet. Sci. Lett., 183, 441–55, 10.1016/S0012-821X(00)00299-5, 2000.

Mangan, M. and Sisson, T.: Evolution of melt-vapor surface tension in silicic volcanic systems: Experiments with hydrous melts, J. Geophys. Res., 110, B01202, https://doi.org/10.1029/2004JB003215, 2005.

Mancini, S., Forestier-Coste, L., Burgisser, A., James, F., Castro, J.: An expansion-coalescence model to track gas bubble populations in magmas. J. Volcanol. Geotherm. Res., 313, 44–58, https://doi.org/10.1016/ j.jvolgeores.2016.01.016, 2016.

Maruishi, T. and Toramaru, A.: Effect of bubble deformation on the coalescence of two ascending bubbles in a viscous liquid. Physics of Fluids, 34(4), 043302. https://doi.org/10.1063/5.0082506, 2022.

Marxer, H., Bellucci, P., Nowak, M.: Degassing of H2O in a phonolitic melt: A closer look at decompression experiments, J. Volcanol. Geoth. Res., 297, 109–124, https://doi.org/10.1016/j.jvolgeores.2014.11.017, 2015.

Mastrolorenzo, G., Brachi, L., Canzanella, A.: Vesicularity of various types of pyroclastic deposits of Campi Flegrei volcanic field: Evidence of analogies in magma rise and vesiculation mechanisms. J. Volcanol. Geotherm. Res., 109, 41–53, 10.1016/S0377-0273(00)00303-6, 2001.

McCormick, M.P., Thomason, L.W., Trepte, C.R.: Atmospheric effects of the Mt. Pinatubo 1991 eruption. Nature, 373, 399–404, https://doi.org/10.1038/373399a0, 1995.

McDonald, R., Sumita, M., Schmincke, H.U., Baginski, B., White, J.C., Ilnicki, S.S.: Peralkaline felsic magmatism at the Nemrut volcano, Turkey: impact of volcanism on the evolution of Lake Van (Anatolia) IV. Contrib. Mineral. Petrol., 169, 34, 10.1007/s00410-015-1127-6, 2015.

McIntosh, I. M., Llewellin, E. W., Humphreys, M. C. S., Nichols, A. R. L., Burgisser, A., Schipper, C. I., and Larsen, J. F.: Distribution of dissolved water in magmatic glass records growth and resorption of bubbles, Earth Planet. Sc. Lett., 401, 1–11, https://doi.org/10.1016/j.epsl.2014.05.037, 2014.

Miller, C. F. and Wark, D. A.: Supervolcanoes and their supereruptions, Elements, 4, 11–15, https://doi.org/10.2113/GSELEMENTS.4.1.11, 2008.

Moore, G., Vennemann, T., Carmichael, ISE.: An empirical model for the solubility of H_2O in magmas to 3 kilobars. Am. Min., 83, 36–42, 10.2138/am-1998-1-203, 1998.

Navon, O. and Lyakhovsky, V.: Vesiculation processes in silicic magmas. In: Gilbert, J.S., Sparks, R.S.J. (Eds.), The Physics of Explosive Volcanic Eruptions. In: Geological Society, London, Special Publications, 145, 27–50, ISBN 1-86239-020-7, 1998.

Neave, D.A., Fabbro, G., Herd, R.A., Petrone, C.M., Edmonds, M.: Melting, differentiation and degassing at the Pantelleria Volcano, Italy. J. Petrol., 53, 637–663, https://doi.org/10.1093/petrology/egr074, 2012.

Nguyen, C. T., Gonnermann, H. M., Chen, Y., Huber, C., Maiorano, A. A., Gouldstone, A., Dufek, J.: Film drainage and the lifetime of bubbles. Geochem., Geophys., Geosyst., 14(9), 3616–3631, https://doi.org/10.1002/ggge.20198, 2013.

Nowak, M. and Behrens, H.: An experimental investigation on diffusion of water in haplogranitic melts. Contrib. Mineral. Petrol., 126, 365–376, https://doi.org/10.1007/s004100050256, 1997.

Ohashi, M., Maruishi, T., Toramaru, A.: Coalescence of growing bubbles in highly viscous liquids. Geochem., Geophys., Geosyst., 23, e2022GC010618, https://doi.org/10.1029/2022GC010618, 2022.

Ohlhorst, S., Behrens, H., and Holtz, F.: Compositional dependence of molar absorptivities of near-infrared OH- and H2O bands in rhyolitic to basaltic glasses, Chem. Geol., 174, 5–20, https://doi.org/10.1016/S0009-2541(00)00303-X, 2001.

Paredes-Marino, J., Dobson, K. J., Ortenzi, G., Kueppers, U., Morgavi, D., Petrelli, M., Hess, K.-U., Laeger, K., Porreca, M., Pimentel, A., and Perugini, D.: Enhancement of eruption explosivity by heterogeneous bubble nucleation triggered by magma mingling, Sci. Rep.-UK, 7, 16897, https://doi.org/10.1038/s41598-017-17098-3, 2017.

Perugini, D., De Campos, C.P., Ertel-Ingrisch, W., and Dingwell, D. B.: The space and time complexity of chaotic mixing of silicate melts: Implications for igneous petrology, Lithos, 155, 326–340, https://doi.org/10.1016/j.lithos.2012.09.010, 2012.

Philpotts, A. R. and Ague, J. J.: Principles of Igneous and Metamorphic Petrology, Cambridge University Press, 700 pp., https://doi.org/10.1017/9781108631419, 2009.

Preuss, O., Marxer, H., Ulmer, S., Wolf, J., Nowak, M.: Degassing of hydrous trachytic Campi Flegrei and phonolitic Vesuvius melts: Experimental limitations and chances to study homogeneous bubble nucleation. Am. Mineral., 101, 859–875, https://doi.org/10.2138/am-2016-5480, 2016.

Proussevitch, A.A., Sahagian, D.L., Kutolin, V.A.: Stability of foams in silicate melts. J. Volcanol. Geotherm. Res., 59, 161–178, https://doi.org/10.1016/0377-0273(93)90084-5, 1993.

Reinig, F., Wacker, L., Jöris, O., Oppenheimer, C., Guidobaldi, G., Nievergelt, D., Adolphi, F., Cherubini, P., Engels, S., Esper, J., Land, A., Lane, C., Pfanz, H., Remmele, S., Sigl, M., Sookdeo, A., Büntgen, U.: Precise date for the Laacher See eruption synchronizes the Younger Dryas. Nature 595, 66–69, https://doi.org/10.1038/s41586-021-03608-x, 2021.

Saar, M. and Manga, M.: Permeability-porosity relationship in vesicular basalts. Geophysical Research Letters, 26, 111–114, https://doi.org/10.1029/1998GL900256, 1999.

Sahagian, D. and Carley, T.L.: Explosive volcanic eruptions and spinodal decomposition: A different approach to deciphering the tiny bubble paradox. Geochem. Geophys. Geosys., 21, 1–9, 10.1029/2019GC008898, 2020.

Sahimi, M.: Applications of percolation theory. London Taylor and Francis, ISBN 0-203-22153-2, https://doi.org/10.1201/9781482272444, 1994.

Sato, H., Nakada, S., Fujii, T., Nakamura, M., and SuzukiKamata, K.: Groundmass pargasite in the 1991–1995 dacite of Unzen volcano: phase stability experiments and volcanological implications, J. Volcanol. Geoth. Res., 89, 197–212, https://doi.org/10.1016/S0377-0273(98)00132-2, 1999.

Scaillet, B. and Macdonald, R.: Phase relations of peralkaline silicic magmas and petrogenetic implications. J. Petrol., 42, 825–845, https://doi.org/10.1093/petrology/42.4.825, 2001.

Scaillet, B. and Macdonald, R.: Experimental constraints on pre-eruption conditions of pantelleritic magmas: Evidence from the Eburru complex, Kenyan Rift. Lithos 91, 95–108, 10.1016/j.lithos.2006.03.010, 2006.

Schmidt, B.C. and Behrens, H.: Water solubility in phonolite melts: Influence of melt composition and temperature. Chem. Geol., 256, 259–268, doi:10.1016/j.chemgeo.2008.06.043, 2008.

Schmidt, B.C., Blum-Oeste, N., Flagmeier, J.: Water diffusion in phonolite melts. Geochim. Cosmochim. Acta, 107, 220–230, http://dx.doi.org/10.1016/j.gca.2012.12.044, 2013.

Schmincke, H.U., Park, C., Harms, E.: Evolution and environmental impacts of the eruption of Laacher See Volcano (Germany) 12,900 a BP. Quaternary International, 61, 61–72, https://doi.org/10.1016/S1040-6182(99)00017-8, 1999.

Shea, T.: Bubble nucleation in magmas: a dominantly heterogeneous process? J. Volcanol. Geotherm. Res., 343, 155–170, https://doi.org/10.1016/j.jvolgeores.2017.06.025, 2017.

Snyder, D.: Thermal effects of the intrusion of basaltic magma into a more silicic magma chamber and implications for eruption triggering, Earth Planet. Sc. Lett., 175, 257–273, https://doi.org/10.1016/S0012-821X(99)00301-5, 2000.

Sparks, R. S. J., Sigurdsson, H., and Wilson, L.: Magma mixing: a mechanism for triggering acid explosive eruptions, Nature, 267, 315–318, https://doi.org/10.1038/267315a0, 1977.

Stabile, P., Radica, F., Bello, M., Behrens, H., Carroll, M.R., Paris, E., Giuli, G.: H_2O solubility in pantelleritic melts: pressure and alkali effects. J. Min. Geochem., 195, 1, 1–9, 10.1127/njma/2017/0060, 2018.

Tomlinson, E.L., Smith, V.C., Menzies, M.A.: Chemical zoning and open system processes in the Laacher See magmatic system. Contrib. Mineral. Petrol., 175, 19, https://link.springer.com/ article/10.1007/s00410-020-1657-4, 2020.

Toramaru, A.: BND (bubble number density) decompression rate meter for explosive volcanic eruptions. J. Volcanol. Geoth. Res., 154, 303–316, https://doi.org/10.1016/j.jvolgeores.2006.03.027, 2006.

Van den Bogaard, P. and Schmincke, H.U.: The Eruptive Center of the Late Quaternary Laacher See Tephra. Geologische Rundschau, 73, 3, 933–980, 10.1007/BF01820883, 1984.

Van den Bogaard, P. and Schmincke, H.U.: Laacher See Tephra: A widespread isochronous late Quaternary tephra layer in Central and Northern Europe. Geol. Soc. Am. Bull., 96, 12, 1554–1571, 10.1130/0016-7606(1985)96<1554:LSTAWI>2.0.CO;2, 1985.

Watson, B.: Basalt Contamination by Continental Crust: Some Experiments and Models, Contrib. Mineral. Petr., 80, 73–87, https://doi.org/10.1007/BF00376736, 1982.

Wiesmaier, S., Morgavi, D., Renggli, C. J., Perugini, D., De Campos, C. P., Hess, K.-U., Ertel-Ingrisch, W., Lavallée, Y., and Dingwell, D. B.: Magma mixing enhanced by bubble segregation, Solid Earth, 6, 1007–1023, https://doi.org/10.5194/se-6-1007-2015, 2015.

Wilson, L., Sparks, R. S. J., Walker, G. P. L.: Explosive volcanic eruptions—IV. The control of magma properties and conduit geometry on eruption column behaviour. Geophys. J. Int., 63, 1, 117–148. https://doi.org/10.1111/j.1365-246x.1980.tb02613.x, 1980.

Wörner, G. and Schmincke, H.U.: Mineralogical and chemical zonation of the Laacher see tephra sequence. J. Petrol., 25, 805-835, 10.1093/petrology/25.4.805, 1984.

Yamashita, S., Kitamura, T., and Kusakabe, M.: Infrared spectroscopy of hydrous glasses of arc magma compositions, Geochem. J., 31, 169–174, https://doi.org/10.2343/geochemj.31.169, 1997.

Zhang, Y., Ni, H., and Chen, Y: Diffusion Data in Silicate Melts, Rev. Mineral. Geochem., 72, 311–408, https://doi.org/10.2138/rmg.2010.72.8, 2010.

Appendix

Manuscript Study I

Titel: Vesiculation dynamics – Part 1: Decompression-induced H_2O vesicle formation in the Lower Laacher See phonolitic melt

Authors: Patricia Louisa Marks and Marcus Nowak

Published online on July 04, 2025, in European Journal of Mineralogy; special issue: Probing the Earth: experiments on and for our planet, 37, 385–412, https://doi.org/10.5194/ejm-37-385-2025.

Eur. J. Mineral., 37, 385–412, 2025
https://doi.org/10.5194/ejm-37-385-2025

European Journal of Mineralogy
Open Access

Vesiculation dynamics – Part 1: Decompression-induced H_2O vesicle formation in the Lower Laacher See phonolitic melt

Patricia Louisa Marks and Marcus Nowak

Department of Geosciences, Eberhard Karls University of Tübingen, Tübingen 72074, Germany

Correspondence: Patricia Louisa Marks (patricia.marks@uni-tuebingen.de)

Received: 15 August 2024 – Revised: 26 March 2025 – Accepted: 1 April 2025 – Published: 4 July 2025

Abstract. The Laacher See volcano is located in the East Eifel region of Germany, an area that remains volcanologically active, indicated by ongoing degassing and low-frequency seismic activities. Its last eruption, ~ 13 000 years ago, was one of the most significant volcanic events in central Europe, characterized by explosive Plinian and phreatomagmatic eruptions with devastating environmental consequences. To contribute to understanding the eruption behavior of the Laacher See volcano, this experimental study focuses on the degassing behavior of the sodium-rich Lower Laacher See Tephra, part of the first highly differentiated melt ejected.

Systematic solubility and decompression experiments were conducted at superliquidus temperatures of 1323 K and at starting pressures of 200 MPa in an internally heated pressure vessel. H_2O concentrations of 5.7 wt % and 5.0 wt % revealed saturation pressures of 198 and 156 MPa, respectively, resulting in saturation and slightly undersaturation conditions prior to decompression. The hydrated melts were then continuously decompressed at rates ranging from 0.064–1.7 MPa s^{-1} to final pressures between 110 and 30 MPa.

H_2O concentrations in the residual glasses were measured using FTIR spectroscopy, for which the absorption coefficients for the synthesized glass composition were determined ($\varepsilon_{H_2Om} = 1.27 \pm 0.04$ and $\varepsilon_{OH} = 1.15 \pm 0.07$), as well as the H_2O-dependent density equation $\rho_{LLST} = (2485 \pm 11) - (21.9 \pm 2.8) \cdot c_{H_2Ot}$. Upon reaching a sufficient supersaturation pressure of 80–130 MPa, all samples exhibited homogeneously dispersed and micrometer-sized vesicles in the sample volume. Each series showed maximal logVNDs (where VND is vesicle number density) of 5.1–5.7, irrespective of decompression rate, which seems difficult to reconcile with nucleation theory. The observed high VNDs are supposed to cause very fast near-equilibrium adjustment of H_2O concentration in the melt by degassing.

Under the investigated experimental conditions, the results align with recent studies indicating that the decompression rate does not significantly affect potassium-rich phonolitic and phono-tephritic melts. These findings suggest that off-critical spinodal decomposition might be responsible in the rapid phase separation of hydrous, alkali-rich intermediate melts into H_2O fluid and less hydrous melt, potentially enhancing the explosive eruption behavior.

1 Introduction

1.1 Laacher See setting

The Laacher See volcano, located in the East Eifel volcanic field in western Germany, stands as one of central Europe's youngest volcanoes, with its most recent eruption occurring ~ 13 006 ± 9 years BP (relative to 1950 CE) (Reinig et al., 2021). This eruption ranks among the largest in Europe during the upper Pleistocene, with a volcanic explosivity index (VEI) of 6, comparable in magnitude to the 1991 eruption of Mount Pinatubo (Holasek et al., 1996). Over a span of fewer than 10 d, approximately 6.3 km^3 of phonolitic magma, equivalent to 20 km^3 of tephra, was explosively ejected through phreatomagmatic and Plinian eruptions (Wörner and Schmincke, 1984a; Schmincke et al.,

Published by Copernicus Publications on behalf of the European mineralogical societies DMG, SEM, SIMP & SFMC.

1999; Harms and Schmincke, 2000). This eruption unleashed a minimum of around 1.9 Tg of sulfur, 6.6 Tg of chlorine, and 403 Tg of water vapor into the atmosphere, with a substantial portion reaching the stratosphere, likely exerting a significant influence on climate and the environment (Harms and Schmincke, 2000). For context, the mentioned 1991 eruption of Mt. Pinatubo resulted in an estimated global temperature decrease of 0.4 K (McCormick et al., 1995).

The temperatures and pressures within the Laacher See magma chamber were estimated to range from 1023 to 1033 K (750 to 760 °C) and 115 to 145 MPa at the uppermost section of the chamber, increasing to 1113 to 1133 K (840 to 860 °C) and 200 MPa at the mafic, more crystalline magma at the chamber's base. The upper boundary of the magma chamber was positioned at a depth of 5–6 km. Considering the volcanic depression's geometry and the volumes of erupted material, the overall height of the magma body was approximated to be 1–2 km (Wörner and Schmincke, 1984b; Harms et al., 2004).

The Laacher See tephra layers were dispersed across central Europe, embodying a chemically and mineralogically stratified magma chamber (Van den Bogaard and Schmincke, 1984, 1985; Wörner and Schmincke, 1984a). Initially, Plinian eruptions ejected the Lower Laacher See Tephra (LLST), characterized by highly differentiated, water-saturated, and exceptionally crystal-poor (< 2 vol %) phonolites, representing the uppermost segment of the magma chamber. Highly evolved LLST glass inclusions were estimated to contain ∼ 5.7 wt % H_2O using secondary ion mass spectrometry and the by-difference method, suggesting that the LLST magma was near water saturation at depth (Harms and Schmincke, 2000). Subsequent Plinian eruptions ejected less differentiated phonolitic magma, featuring a slightly reduced alkali content and crystal contents of up to 15 vol %, leading to the deposition of the Middle Laacher See Tephra (MLST). In the later stages of the eruption, phreatomagmatic activity produced a crystal-rich mafic phonolite (ULST, Upper Laacher See Tephra) with phenocryst concentrations of up to 55 vol %, attributed to occasional replenishment of hot basanite melt and mixing with the resident melt at the base of the magma chamber (Tomlinson et al., 2020).

Beyond analyzing natural volcanic products, experimental work is crucial for investigating and understanding the physicochemical processes within the magma chamber. While the study of erupted products yields information about the initial conditions of the magma chamber, it does not provide insights into the behavior of the magma during ascent. Experimental simulations of ascending magma, undergoing degassing and/or crystallization, offer valuable insights into the dynamic magma behavior under various conditions. Numerous studies about the Laacher See eruption at ∼ 13 ka have delved into pressure and temperature conditions, melt composition, volatile content, phase relations, fluid inclusion, crystal analysis, and other factors (e.g., Wörner and Schmincke, 1984a, b; Harms and Schmincke, 2000; Harms et al., 2004; Schmidt and Behrens, 2008; Schmidt et al., 2013; Tomlinson et al., 2020). However, the question of the actual phase separation behavior of the initial hydrous melt into fluid and less hydrous melt (terminated as degassing in this publication), which reveals the explosive potential of the volcano, has remained unanswered. Therefore, this study focuses on investigating the H_2O degassing behavior of hydrous melt with LLST composition through systematic decompression experiments conducted under superliquidus conditions. Superliquidus conditions were chosen as it is crucial to start with relatively simple conditions before progressing to more complex systems. Accordingly, our initial focus is on the phase separation of the pure melt (homogeneous phase separation), prior to studying more complex systems, such as melts containing crystals. We selected the Laacher See composition as the melt composition as the Laacher See volcano has a history of explosive eruptions and continues to exhibit frequent seismic activity.

1.2 Cavitation: formation of gas vesicles in a liquid

The eruption dynamics of volcanic systems are dominated by the phase separation mechanism of H_2O fluid from a hydrous silicate melt, the primary volatile component dissolved in magma. As magma ascends, the solubility of H_2O decreases with decreasing pressure (e.g. Iacono-Marziano et al., 2007; Schmidt and Behrens, 2008), leading to progressive H_2O supersaturation within the melt. Upon reaching a critical threshold, the melt degasses, forming H_2O fluid vesicles within it or, in other more general words, small vapor-filled cavities form within the melt by exceeding its tensile strength, resulting in the rupturing of the melt structure (Brennen, 1995). This process of vesicle formation during decompression at constant temperatures is known as cavitation, which is widely used in other areas of natural science, particularly in the physicochemical literature, and was initially described by Reynolds in 1873 and further specified by Parsons in 1906. Cavitation involves the formation, growth, and collapse of vapor-filled cavities within a liquid.

The rupturing of the melt is strongly influenced by its tensile strength, defined by the intermolecular forces that hold the molecules together, preventing the formation of large cavities. This tensile strength measures the extent of pulling force the melt can withstand before breaking and is determined by the difference between the saturated vapor pressure and the melt pressure. When the tensile strength is exceeded, the melt ruptures, forming cavities. In the context of cavitation, the tensile strength and elasticity of the melt set the threshold for the pressure drop required to initiate vesicle formation. If the tensile stress surpasses the melt's elasticity, bonds break, forming cavities where H_2O molecules assemble into vesicles. Consequently, tensile strength is a critical factor in cavitation, significantly influencing the formation and growth of vesicles and, subsequently, the melt's integrity

and behavior. High tensile strength implies that the melt can withstand greater tension before failing, potentially delaying the onset, growth, and coalescence of vesicles, which may lead to abrupt and violent eruptions, such as those for rhyolitic compositions. Conversely, in melts with lower tensile strength, vesicles can grow and coalesce more readily, resulting in more constant and less-explosive eruptions, as is often observed for basaltic compositions.

While cavitation describes the process of the vesicle formation during depressurization, the mechanisms of homogeneous vesicle formation can be described by nucleation or spinodal decomposition. These two established homogeneous formation mechanisms will be briefly presented as an overview. These mechanisms are of great interest, as the number of fluid vesicles per unit volume of silicate melt (VND, vesicle number density) serves as a key parameter for quantifying the efficiency of fluid–melt separation and, consequently, the acceleration of magma ascent.

1.2.1 Homogeneous vesicle nucleation

Phase separation in supersaturated hydrous silicate melt is conventionally explained using nucleation theory (Navon and Lyakhovsky, 1998), where vesicles uniformly form throughout the melt. Homogeneous nucleation theory predicts that the nucleation rate, defined as the number of vesicles formed per unit volume per second, increases exponentially with the degree of supersaturation. Exceeding the H_2O solubility limit of the homogeneous melt, which is characterized by the binode, leads to supersaturation of the melt. Further decompression into the metastable state leads to the onset of vesicle nucleation (e.g. Sahagian and Carley, 2020). According to the mechanical equilibrium approach of homogeneous nucleation, energy is required to create new interfaces of H_2O vesicles within the silicate melt. Critically sized H_2O clusters at the nanometer scale emerge within the metastable state of the hydrous melt (e.g., Hurwitz and Navon, 1994; Navon and Lyakhovsky, 1998). When H_2O clusters (or nuclei) reach a critical radius, they either shrink or grow spontaneously due to diffusional loss or addition of an H_2O molecule at the fluid–melt interface, respectively. Because clustering makes the formation of critical nuclei a statistical process, the spatial positions of nuclei in the melt also follow a statistical distribution, resulting in variable inter-nuclei distances. The exponential increase of the nucleation rate of surviving vesicles is influenced by factors such as surface tension, viscosity, supersaturation pressure (difference between internal vesicle pressure and ambient melt pressure), temperature through kinetic energy of molecules, H_2O diffusivity, and the rate of decompression (e.g., Toramaru, 2006). Upon further decompression, existing vesicles expand by diffusional H_2O uptake and decreasing external pressure, while simultaneously nucleation continues by the formation of new vesicles. This process persists until the number of vesicles in the melt volume is sufficient for H_2O supersaturation to decrease solely through diffusion into the vesicles.

The nucleation theory suggests that VNDs should depend on decompression rate, with faster decompressions resulting in greater supersaturation pressures by exceeding the rate of volatile diffusion to newly formed vesicles (Hurwitz and Navon, 1994; Navon and Lyakhovsky, 1998; Gardner et al., 2023). The necessary H_2O supersaturation pressure for homogeneous vesicle nucleation was experimentally determined by several studies to exceed 60–100 MPa for a range of silicate melt compositions (e.g. Hurwitz and Navon, 1994; Mourtada-Bonnefoi and Laporte, 1999, 2002; Mangan and Sisson, 2000; Iacono-Marziano et al., 2007; Hamada et al., 2010; Gardner and Ketcham, 2011; Gondé et al., 2011; Gardner et al., 2013; Gonnermann and Gardner, 2013; Fiege et al., 2014; Le Gall and Pichavant, 2016; Preuss et al., 2016; Hajimirza et al., 2019, 2021). However, nucleation theory tends to underestimate the vesicle nucleation rate to achieve high VNDs of $\sim 10^5$ mm^{-3} observed in samples of phonolitic and phono-tephritic melts at moderate to low decompression rates (Allabar and Nowak, 2018; Allabar et al., 2020a, b; Gardner et al., 2023) and is not able to explain decompression-rate-independent VNDs. Therefore, off-critical spinodal decompositions has been proposed as an explanation for the high and constant VNDs across several orders of magnitude.

1.2.2 Spinodal decomposition

In contrast to nucleation, off-critical spinodal decomposition is a spontaneous phase separation process that occurs when a homogeneous hydrous melt becomes thermodynamically unstable at the lower limit of metastability, known as the spinodal region (Cahn, 1965; Debenedetti, 2000). When a hydrous silicate melt is decompressed through the metastable region, it may enter the off-critical spinodal region of the phase diagram. During this decompression, the melt traverses the metastable state, where supersaturation gradually increases. However, upon crossing the spinodal boundary, the melt reaches a state of extreme supersaturation, marking the onset of spinodal decomposition. Below the spinode, the H_2O supersaturated melt becomes thermodynamically unstable to compositional fluctuations with wavelengths greater than a critical wavelength (Cahn, 1965). In this regime, the system no longer requires nucleation to phase separate; instead, it undergoes spontaneous and rapid decomposition driven by extreme supersaturation, leading to the growth of compositional fluctuations without an energy barrier. As phase separation is now characterized by the wavelength of these fluctuations, the concept of a critical nucleus radius, as in homogeneous nucleation, becomes irrelevant. Following the model of Cahn (1965), small compositional fluctuations with significant concentration differences in small volumes occur and amplify spontaneously, leading to the formation of H_2O-rich and H_2O-poor regions by uphill diffusion (Allabar

and Nowak, 2018; Sahagian and Carley, 2020). This process creates a gradient in H_2O concentration, transitioning from H_2O-rich melt to nearly H_2O-free melt without a sharp initial boundary. The critical wavelength of the H_2O concentration fluctuations, which increase through uphill diffusion, determines the number of vesicles formed uniformly and spontaneously throughout the melt during decompression. This process results in a decompression-rate-independent high VND and uniformly sized vesicles, as observed in supersaturated phonolitic and phono-tephritic melts (Preuss et al., 2016; Allabar and Nowak, 2018; Allabar et al., 2020b; Sahagian and Carley, 2020; Gardner et al., 2023).

To determine whether the degassing behavior of phonolitic melt with LLST composition corresponds to homogeneous nucleation or off-critical spinodal decomposition, experiments were conducted in an internally heated pressure vessel (IHPV) at the University of Tübingen. These experiments included hydration and subsequent decompression, under both H_2O-saturated and slightly H_2O-undersaturated starting conditions.

2 Experimental techniques

2.1 Glass synthesis

Phonolitic glasses were synthesized according to the LLST G140 composition by Harms et al. (2004) (Table B1). To receive homogeneous starting glasses, the synthesis was conducted by mixing, milling, and melting analytical-grade oxide and carbonate powders following the experimental protocol of Marxer et al. (2015) and the improvement described in Allabar and Nowak (2018). Powder batches of 25 g of the LLST composition were loaded into Pt90Rh10 crucibles and heated at 1873 K for 6 h to decarbonize and melt the mixture. The melt was then rapidly quenched in water to induce tension cracks and fracturing of the glass. The shattered glass shards were then ground, mixed, and remelted at 1873 K for 1 h. The melt was air-cooled to the approximate glass transition temperature of ~ 950 K, calculated with the model of Giordano et al. (2008), and transferred into a preheated furnace at ~ 900 K. The furnace was then shut down to provide a cooling rate of $\sim 5\,\mathrm{K\,min^{-1}}$ until room temperature was reached. This procedure ensured crystal- and tension-free homogeneous glasses that are nearly free of air bubbles. Four syntheses with multiple batches (LLST_1a/b, LLST_2a/b/c, LLST_3a/b/c, and LLST_4a/b/c/d) were conducted to receive enough sample material for all experiments. The glass compositions were confirmed with electron probe microanalysis (EPMA) (Table B1). Cylinders of 3.6 or 5 mm in diameter were drilled from the homogeneous batches for the H_2O solubility and decompression experiments.

2.2 Standard glass samples

Hydrated standard glass samples were prepared for the determination of near-infrared (NIR) linear molar absorption coefficients of dissolved hydrous species (molecular H_2O (H_2O_m) and hydroxyl (OH)). The samples were synthesized using glass chips of 250–500 µm in diameter of LLST_1a. The 20 mm long cleaned and annealed Au80Pd20 tubes (4.0 mm o.d., 3.6 mm i.d.) were crimped on one side and welded shut. The tubes were then filled with glass chips and densified with a steel piston. An Eppendorf micropipette was used to insert water into the capsules. Seven samples were prepared to obtain glasses with 0.5 wt %, 1 wt %, 2 wt %, 3.24 wt %, 4 wt %, 5.5 wt %, and 7 wt % dissolved H_2O. To control the amount of H_2O added, the capsules were weighed after each preparation step to determine gravimetrically the H_2O content (c_{H_2Og}). After filling, the upper part of the capsule was crimped shut and welded. The capsules were heated in a compartment drier at 383 K for at least 1 h, then compressed to 200 MPa at room temperature and reheated to 383 K, and reweighed after each step to ensure tightness. Two samples each were hydrated together in the IHPV at 1523 K and 300 or 200 MPa (Table S1) at an intrinsic oxygen fugacity close to $\Delta\log\mathrm{QFM} \approx +3.5$ (Berndt et al., 2002). Pressure conditions were chosen to ensure H_2O undersaturation (Schmidt and Behrens, 2008) to dissolve the complete amount of H_2O in the melt and to avoid the formation of hydration bubbles that could affect the determination of H_2O (c_{H_2Ot}) dissolved in the quenched glasses with Karl Fischer titration (KFT; Preuss et al., 2016; Allabar et al., 2022). After 24 h, the capsules were quenched isobarically with about $16\,\mathrm{K\,s^{-1}}$ by switching off the furnace (Allabar et al., 2020b).

2.3 H_2O solubility experiments

For the H_2O solubility experiments, glass chips of 250–500 µm grain size as well as solid glass cylinders of 3.6 mm in diameter were used. To ensure H_2O saturation of the melt, excess water of 8 wt % to 4 wt % H_2O, dependent on the pressure conditions, was welded together with the LLST glass in 3.6 mm diameter Au80Pd20 capsules (Table 1). The capsule material was crimped and welded on both sides to seal the samples. Possible leakage of the capsules was tested by heating to 383 K and pressurizing to 200 MPa at ambient temperature as for the standard samples. The samples were hydrated under the same final pressure conditions as the subsequent decompression experiments (110–30 MPa). All samples were hydrated in the IHPV at 1523 K, then lowered to 1323 K with $10\,\mathrm{K\,min^{-1}}$, and held there for a further 30 min. Additionally, one sample was hydrated at 200 MPa and 1523 K and quenched immediately to validate the initial melt conditions at the hydration temperature. For the 200 MPa runs, the 110 MPa run, and the 30 MPa run, a sample with a glass cylinder and a sample with glass chips were

both hydrated simultaneously in the IHPV for comparison. Only glass chip samples were used for the solubility experiments at 90, 80, 70, 50, and 40 MPa. The combined glass cylinder and glass chip samples were hydrated for 96 h, while the other glass chip samples were hydrated for 24 h due to the shorter diffusion distance of H_2O initially distributed between the glass chips. These hydration times ensured homogeneous distribution and dissolution of H_2O in the melt. One additional cylinder sample was hydrated at 200 MPa for 96 h at 1523 K, lowered with 10 K s^{-1} to 1123 K, and equilibrated there for another 24 h before quenching, to investigate the temperature-dependent solubility of H_2O.

After hydration, the samples were isobarically and rapidly quenched at $\sim 97\,K\,s^{-1}$ (MQ, medium quenching) or $\sim 150\,K\,s^{-1}$ (RQ, rapid quenching) by melting the suspension wire of the capsule, which caused the capsule to fall into the cold part of the sample holder (Table 1; Berndt et al., 2002). Three hydration experiments (LLST_11H/Hg, LLST_12Hg, and LLST_13H/Hg) failed to melt the suspension wire, so they were quenched at $\sim 16\,K\,s^{-1}$ (NQ, normal quenching) by switching off the electric furnace. Nevertheless, the quenching rate was sufficient to prevent the formation of quenching crystals, confirmed by optical microscopy and backscattered electron (BSE) imaging. All capsules of the solubility experiments were pierced before preparation with water bubbling out of the hole. This ensured that H_2O still coexisted with the saturated melt during the hydration. The pierced capsules were then stored in a drying cabinet for 1 h at 383 K. This drying time was confirmed to be sufficient based on previous experiments, which were weighed for 3 h every 30 min after piercing and placement in the drying cabinet. The weight loss was then used to gravimetrically calculate the dissolved H_2O content in the glass for each sample.

2.4 Decompression experiments

For the decompression experiments, glass cylinders of 5.3–7.5 mm in length and 5 mm in diameter were inserted into Au80Pd20 capsules (outer diameter: 5.4 mm, inner diameter: 5.0 mm). Two series of hydration melt conditions were performed by adding 5.7 wt % or 5.0 wt % H_2O to the capsule, adjusting to H_2O-saturated or slightly undersaturated conditions prior to decompression, respectively. The bottom of the capsules was closed with Au80Pd20 lids, and the upper capsule side was pressed into a three-sided star and welded. The tightness of the samples was tested by the same procedure as for the hydration of the glass standards and the H_2O solubility experiments.

The samples were hydrated in the IHPV at 200 MPa and 1523 K for 96 h. After hydration, the temperature was isobarically reduced at 10 K min^{-1} to 1323 K, where the samples were thermally equilibrated for 0.5 h. The hydrous melts were then isothermally decompressed at 1.7, 0.17, and 0.064 MPa s^{-1} to final pressures (P_f) of 110, 90, 80, 70, 60, 50, 40, and 30 MPa. By reaching P_f, the samples were quenched isobarically with $\sim 150\,K\,s^{-1}$ (Berndt et al., 2002) or $97\,K\,s^{-1}$ to room temperature. During quenching, a further pressure drop of a few MPa may occur due to the drop of the sample into the cold zone of the sample holder. For this reason, the minimum recorded pressure (P_{min}) is also listed in addition to the desired P_f (Table 2). The capsules were reweighed to ensure tightness and then punctured to determine the degassed H_2O content gravimetrically as a first approximation.

2.5 Quantification of cooling rate

The rapid cooling from 1323 K to room temperature within a few seconds, corresponding to an average cooling rate of $\sim 150\,K\,s^{-1}$ (Berndt et al., 2002), induces tension stress in the supercooled sample material. This often leads to tension cracks in the glass, which can cause further breakage and shattering during subsequent sample preparation. For this reason, we achieved a medium-quenching (MQ) rate that largely prevents stress-induced glass cracking but captures as close as possible the melt state in the quenched glass. Therefore, a 35 mm long brass cylinder was inserted at the bottom of the sample holder to keep the sample slightly closer to the hot zone of the furnace during cooling. This technique has already been described by Allabar et al. (2020a), who, additionally, placed a 1 cm long piece of platinum between the brass cylinder and the capsule and determined a quenching rate of $44 \pm 11\,K\,s^{-1}$. To quantify the quenching rate of the actual setup, a glass cylinder with haplogranitic composition (AOQ = $Ab_{38}Or_{34}Qz_{28}$; Holtz et al., 1995; Nowak and Behrens, 1997) was used as starting material for a hydration reference experiment under the same conditions as the LLST samples. Dependent on the H_2O solubility, the sample was hydrated with 5.3 wt % H_2O at 200 MPa and 1523 K for 96 h. The sample was then isobarically quenched by melting the suspension wire. To determine the quenching rate, the hydrous species geospeedometer of Zhang et al. (2000) was used, which is based on the homogeneous interconversion reaction between molecular H_2O species and OH species in haplogranitic glass. For this purpose, a double-polished thin section of 200 µm thickness was prepared from the hydrated glass sample. The linear near-infrared absorption band intensities (A_{5230} and A_{4520}) located at $\sim$ 5230 and 4520 cm^{-1} were determined by Fourier transform infrared (FTIR) spectroscopy with a spectral resolution of 4 cm^{-1}, 32 scans per measurement cycle, and the application of a linear baseline correction according to Behrens et al. (1996). In total, 35 measurements across the sample resulted in a mean $A_{5230} = 0.155 \pm 0.003$ and $A_{4520} = 0.072 \pm 0.002\,cm^{-1}$. Normalization of A to 1 mm sample thickness results in $A'_{5230} = 0.76$ and $A'_{4520} = 0.35$, giving a MQ cooling rate of 97 $(-1/+22)\,K\,s^{-1}$.

2.6 Sample preparation

For FTIR spectroscopy, a glass slice was cut perpendicular to the cylinder axis from both ends of the glass standard samples. Each slice was then prepared as a thin section and polished on both sides. The residual sample material was used for the glass density determination and absolute H_2O concentration measurements by KFT. For the H_2O solubility and decompression experiments, the samples were sectioned through the middle of each sample parallel to the cylinder axis. One half of the sample was prepared as a thin section ($\sim 200\,\mu m$) for FTIR spectroscopy and transmitted light microscopy. The thickness of each thin section was measured with a Mitutoyo digital micrometer ($\pm 3\,\mu m$). The other half was embedded in epoxy with subsequent polishing and double sputtering with 5 nm carbon for EPMA and scanning electron microscopy (SEM) image analysis.

3 Analytical techniques

3.1 Electron microprobe analysis

The bulk compositions of the nominally dry starting glasses were analyzed with a JEOL JXA 8230 electron microprobe. Wavelength-dispersive X-ray spectroscopy analyses were conducted using an acceleration voltage of 15 kV, a beam current of 10 nA, and a defocused beam with a diameter of 10 µm on the sample surface to optimize for Na analysis (e.g., Morgan and London, 2005; Stelling et al., 2008). Beam counting times were set to 10 s (Na), 16 s (K, Si, Ca, Al, Mg, Fe), and 30 s (Mn, Ti). Additional energy-dispersive X-ray spectroscopy (EDX) analyses were conducted using a focused beam with a diameter of 1 µm. Calibration standards were albite for Si, Al, and Na; strontium titanite for Ti; hematite for Fe; bustamite for Mn; diopside for Mg and Ca; and sanidine for K. To test the homogeneity of the glasses and the agreement with the desired glass composition, 15 points were measured across an entire glass cylinder section of each glass batch. A focused beam with a spot size of 1 µm was used to measure the crystal composition of the partially crystallized sample LLST_12Hg (Table B1).

3.2 Glass density determination

Glass densities of the hydrated standard glass samples were determined by the buoyancy method using a Sartorius Archimedes precision balance (± 0.02 mg). For this purpose, the glass pieces of 43–208 mg were weighed in air and in water. The glass density was determined by the buoyancy, dependent on the weight difference.

3.3 Karl Fischer titration

Total H_2O concentrations of the seven hydrous standard glasses were measured by KFT at the Institute of Mineralogy of the Leibniz University Hannover, Germany. A detailed description of this method is given by Behrens et al. (1996). Two to four KFT-derived H_2O concentration results for the standard samples are given in Table S1.

3.4 FTIR spectroscopy

All thin sections were analyzed in the near-infrared range for the H_2O concentrations with a Bruker Vertex 80v FTIR spectrometer, coupled with a Hyperion 3000 IR microscope. A halogen light source, a CaF_2 beam splitter, a liquid-nitrogen-cooled InSb single-element detector, and a 15× Cassegrain objective were used for measurements, as well as the software OPUS 7 for evaluation. Homogeneous glasses were measured with the knife aperture set to 50 µm × 50 µm, while for extremely vesiculated samples the measuring range was set to 25 µm × 25 µm to still be able to determine the H_2O content of the vesicle-free glass. Each measurement was tested to ensure that it was free of fluid vesicles by focusing through the thin section. Additionally, in highly vesiculated samples, the volumes of glass containing vesicles were measured with the knife aperture set to 50 µm × 50 µm. The samples were measured in transmission mode with 32 scans per spectrum at a spectral resolution of $4\,cm^{-1}$. Air was measured as a reference for each new sample. Across each standard sample, 20 measurements were conducted to confirm the homogeneous distribution of H_2O in the glasses. For the hydration samples, 15–24 measurements were taken along the longitudinal and transverse cylinder axes for each sample to confirm a homogeneous H_2O concentration distribution throughout the sample. Decompression samples were also measured for their H_2O content in horizontal and vertical profiles to detect a possible H_2O concentration gradient throughout the cylinder. H_2O_m ($\sim 5210\,cm^{-1}$) and OH ($\sim 4470\,cm^{-1}$) absorbances were determined after applying a linear tangential baseline correction according to Behrens et al. (1996). Following the Lambert–Beer law, the concentrations of H_2O_m (c_{H_2Om}) and OH (c_{OH}) were calculated using the glass density, linear molar absorption coefficients, and thickness of the samples. The sum of both H_2O species gives the total dissolved H_2O content (c_{H_2Ot}) in the glass (Tables 1, 2).

3.5 Raman spectroscopy

Raman micro-spectroscopy was used to identify possible iron oxide nanolites, which range in size from less than 1 µm down to the nanometer scale and potentially influence vesiculation during decompression, if present (Di Genova et al., 2017a, b, 2018, 2020; Dubosq et al., 2022). While optical microscopy and SEM-BSE imaging can detect microlites in quenched glasses (between 1 and 100 µm in size, as defined by Murphy et al., 2000, and Mujin et al., 2017), they are unable to detect nanolites. Therefore, several hydration and decompression experiments quenched at 1523 or 1323 K

were examined for the presence of nanolites or quenching phases. Raman scattering at 660–690 cm^{-1} is indicative for the most common nanolite phase of magnetite (Di Genova et al., 2017b, 2020; Scarani et al., 2022). Additionally, the microlites in sample LLST_12Hg, quenched at 1123 K, were measured for identification.

A Renishaw inVia confocal Raman micro-spectrometer was equipped with a 532 nm laser and a Peltier-cooled CCD detector. A 50× objective with a numerical aperture of 0.75 was used to collect spectra from 100–4500 cm^{-1} in a high confocality setting with three accumulations and an acquisition time of 10 s each. The laser was focused on the sample surface, while the intensity was set to 10 % (corresponding to ∼ 2.5 mW). The laser penetration depth in hydrous silicate glass can be up to ∼ 20 µm (Allabar et al., 2020b).

3.6 Quantitative image analysis

Overview and detailed surface images of the epoxy-embedded samples were acquired as BSE images using a Phenom XL microscope and a laser-scanning microscope for quantitative image analysis and determination of the VND. BSE images were acquired under vacuum conditions using the Phenom XL microscope equipped with a CeB_6 source. Imaging was performed at an acceleration voltage of 10 kV and magnifications of up to 500× to resolve the appearance and size of vesicles. Images acquired with the VK-X120K confocal laser scanning microscope were taken at 20× or 50× magnification. Image stitching was performed with the appropriate microscope software that allowed for detailed overview images. The specific detailed image sections were selected from central parts of the samples to be analyzed by quantitative image analysis for the VND with ImageJ and CSDcorrections (Higgins, 2000), as described in Marxer et al. (2015) and Preuss et al. (2016).

3.7 Transmission light microscopy

Vesicles in each thin section were quantified using the Zeiss Axio Image M2M microscope and the TrackWorks software. Each measurement was performed by focusing through the sample in a predefined area, counting each vesicle, and measuring the vesicle diameter in this area, resulting in an analyzed sample volume that was used to normalize the number of vesicles to 1 mm^3 of vesicle-free glass. The errors of the transmitted light microscopy (TLM) analyses are calculated using error propagation, assuming errors of 5 % for vesicle size and vesicle number as well as ±3 µm for sample thickness.

4 Results

4.1 LLST standard glasses

EPMA measurements confirm the homogeneous glass composition of each synthetic batch close to the Lower Laacher See Tuff composition G140 reported in Harms et al. (2004) (Table B1). The glasses are free of crystals, pre-existing bubbles, or cracks. The glass density of hydrous standard glasses decreases linearly with increasing H_2O content (Fig. 1a). However, the density of the nominally dry glass (2442 ± 5.9 g L^{-1}) is slightly lower than the linear trend of the hydrous glasses predicts. This is attributed to a pressure dependence on density, as the dry glasses were synthesized at 1 bar (Behrens et al., 1996; Balzer et al., 2020; Allabar et al., 2022) and were therefore not included for the linear regression calculation. Fitting a linear regression line through the measured densities of hydrous glasses yields a linear density function of LLST [g L^{-1}] as a function of $c_{H_2O_t}$ [wt %]:

$$\rho_{LLST} = (2485 \pm 11) - (21.9 \pm 2.8) \cdot c_{H_2O_t}. \quad (1)$$

Linear molar absorption coefficients for LLST were calculated from the H_2O_m and OH absorbances, measured by FTIR spectroscopy (Table S1). The spectra were baseline corrected to determine the peak heights at ∼ 5210 and ∼ 4470 cm^{-1}. Mean absorptions of these spectra show increasing absorbances with increasing H_2O content. With the known $c_{H_2O_t}$ from KFT analysis of each sample, the normalized absorbances were obtained by rearranging the Lambert–Beer law:

$$c_{H_2O_m} = \frac{1802 \cdot A_{H_2O_m}}{d \cdot \rho \cdot \varepsilon_{H_2O_m}}, \quad (2)$$

$$c_{OH} = \frac{1802 \cdot A_{OH}}{d \cdot \rho \cdot \varepsilon_{OH}}, \quad (3)$$

$$\left(\frac{1802 \cdot A_{H_2O}}{d \cdot \rho \cdot c_{H_2O_t(KFT)}}\right) = \varepsilon_{H_2O} - \frac{\varepsilon_{H_2O}}{\varepsilon_{OH}}\left(\frac{1802 \cdot A_{OH}}{d \cdot \rho \cdot c_{H_2O_t(KFT)}}\right). \quad (4)$$

The $c_{H_2O_m}$ and c_{OH} are the species concentrations of dissolved H_2O in wt %, A is the height of the respective absorbance band, d is the sample thickness (in cm), ρ is the density (in g L^{-1}), and ε is the absorption coefficient (in L (mol cm)$^{-1}$). Plotting the normalized absorbances against each other with the weighted least-square regression yields a straight line whose intersections with the y and x axes obtain the absorption coefficients of H_2O_m and OH, respectively. The molar absorption coefficients are $\varepsilon_{H_2O_m} = 1.27 \pm 0.04$ and $\varepsilon_{OH} = 1.15 \pm 0.07$ (Fig. 1b).

A comprehensive description and classification of the molar absorption coefficients, including comparisons with related studies (Carroll and Blank, 1997; Larsen and Gardner, 2004; Iacono-Marziano et al., 2007; Schmidt and Behrens, 2008; Schmidt et al., 2013; Fanara et al., 2013; Table C1) and determinations of the coefficients, have been provided in Appendix C.

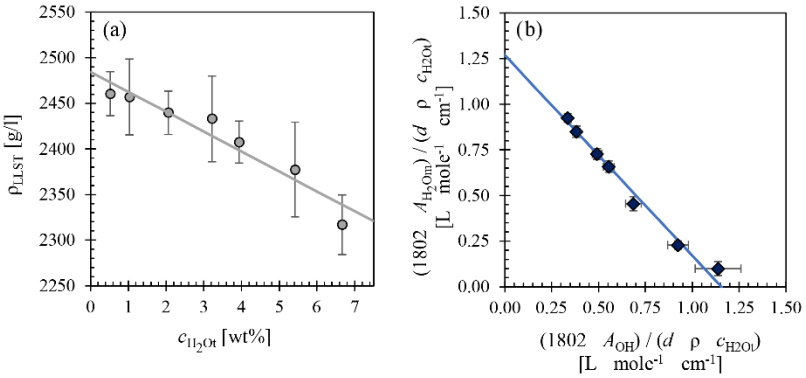

Figure 1. **(a)** LLST glass density as a function of $c_{H_2O_t}$ (i.e., $\rho_{LLST} = (2485 \pm 11) - (21.9 \pm 2.8) \cdot c_{H_2O_t}$) determined from hydrous glasses only. **(b)** Normalized absorbances of H_2O_m and OH from NIR measurements of the hydrous standard glasses. The weighted least-squares regression calculated from these data provides the molar absorption coefficients of H_2O_m in the y-axis intercept ($\varepsilon_{H_2O_m} = 1.27 \pm 0.04$) and OH in the x-axis intercept ($\varepsilon_{OH} = 1.15 \pm 0.07$).

4.2 Quenched glasses

Examination of synthesized dry starting glasses using EMPA, TLM, and Raman spectroscopy result in crystal and vesicle-free glasses (Fig. 2a). The microscopic analyses with a Zeiss Axio Image M2M microscope at 1000× magnification of quenched hydrated glass samples with H_2O contents > 2 wt % show tiny light-diffraction rings, indicative of objects with sizes of ≤ 0.5 µm (Airy, 1834; Fig. 2b–f). No differences in the size and object number density (OND, in mm^{-3}) were found, regardless of the quenching rate, $c_{H_2O_t}$ of 2.2 wt %–5.7 wt %, dP/dt, or P_f. The size of the objects seems to remain constant at ≤ 0.5 µm as well as the logOND, ranging between 5.2 to 5.6. The appearance of the small objects observed in the quenched hydrous glasses is independent of the experimental conditions and is not influenced by the presence of H_2O vesicles (Fig. 2c). No direct contact between objects and vesicles was detected. However, the absence of the small objects in the boundary region of the glass to the capsule walls of the hydrated samples is striking (Fig. 2c). The width of the object-free zones ranges from ∼ 10 to ∼ 100 µm, depending on the respective position in the sample. In all samples, the glass above the bottom of the capsule has a particularly large object-free zone. The identification of the small objects with the SEM, up to 7700× magnification, and the Raman micro-spectroscopy were not successful, which might be due to the small object size and minimal intersection probability. Also, no Raman signal at ∼ 660–690 cm^{-1} indicative of iron oxides (Di Genova et al., 2017b; Scarani et al., 2022) was detected. However, several EDX measurements using the EPMA revealed that the objects are AuPd particles. This is surprising, as the melting point of Au80Pd20 is ∼ 1603 K at ambient pressure, well above the hydration and equilibration temperature. Similar objects were also found in experimental products of other compositions, such as the 39 ka Campanian Ignimbrite (CI) melt composition (Preuss et al., 2016). Quenched melt samples with platinum as capsule material exhibit the same behavior with the appearance of small Pt particles. Such precious metal particles (Au, Pt, Pd, Re, Rh) have already been observed in several studies, both in geological samples and synthetic silicate glasses, and are described in the literature as micronuggets (Ertel et al., 2001; Mallmann and O'Neill, 2007; Lorand et al., 2010; Blaine et al., 2011; Bondar et al., 2022). Although this phenomenon is well known, its origin has not yet been clarified. It could reflect redox reactions occurring during the experimental runs and may also be responsible for the diffusion of Fe from the silicate melt into the metal capsules (Bondar et al., 2022). We assume that the objects precipitated during the quenching of the melt, as no objects are found in each sample in the outer area of the glass volume with the fastest cooling rate. However, the investigation of their occurrence is beyond the scope of this study and will not be examined further here.

4.3 H_2O solubility

The H_2O solubility ($c_{H_2O_{eq}}$) at various conditions, including 1523 K and 200 MPa; 1323 K at 200, 110, 90, 80, 70, 50, 40, and 30 MPa; and 1123 K at 200 MPa, was determined using FTIR micro-spectroscopy and is presented in Fig. 3. The analysis of several different measuring positions through each glass sample revealed a homogeneous distribution of H_2O. Comparison of solubility data between samples with glass cylinders and glass shards used as starting material showed agreement within analytical error, with the glass shard samples consistently exhibiting a slightly higher H_2O content of 1.2 %–3.6 % relative. The H_2O solubility equation (Eq. 5) was derived from a least-squares regression of the obtained solubility data (Table 1). In the

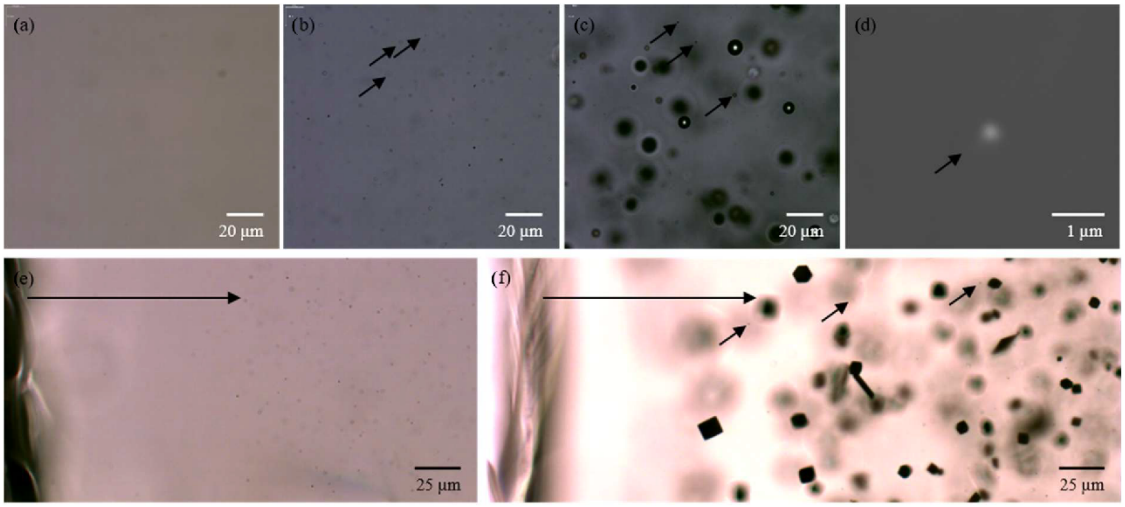

Figure 2. **(a)** Starting glass of the glass synthesis batch LLST_4b, no discernible objects with optical microscopy, SEM, EPMA, and Raman spectroscopy. **(b)** Solubility sample LLST_4Hg with marked objects ≤ 0.5 µm ($c_{H_2Oeq} = 3.88 \pm 0.3$ wt %, 1323 K, $P_{eq} = 110$ MPa, RQ). **(c)** decompression sample LLST_7D with marked objects ($c_{H_2Oi} = 5.0$ wt %, 1323 K, $dP/dt = 0.17$ MPa s^{-1}, $P_f = 50$ MPa, MQ). **(d)** BSE image of LLST_4Hg; marked object was identified as a AuPd micronugget by EDX measurements using the EPMA. **(e)** LLST_32D: The object-free zone from the capsule rim is marked by the arrow ($c_{H_2Oi} = 5.0$ wt %, 1323 K, $dP/dt = 0.064$ MPa s^{-1}, $P_f = 110$ MPa, MQ). **(f)** LLST_12Hg: The object-free zone from the capsule rim is marked by the arrow, while small arrows indicate objects in the glass partially crystallized with hematite ($c_{H_2Oeq} = 6.16 \pm 0.27$ wt %, 1123 K, $P_f = 200$ MPa, NQ).

case of double determination of the H_2O concentrations, the values of the glass cylinder samples were used. Generally, c_{H_2Oeq} increases with pressure at constant temperature. Furthermore, the results obtained at different temperatures at 200 MPa show an increase in H_2O solubility with decreasing temperature. The measured H_2O concentration at 1523 K is 5.45±0.26 wt %, at 1323 K is 5.83±0.27 wt %, and at 1123 K is 6.16 ± 0.27 wt % (Table 1). This observation aligns with findings by Schmidt and Behrens (2008) regarding phonolitic melts of the Laacher See volcano and the Montaña Blanca volcano from Tenerife, Spain (Fig. C1). From the solubility series at 1323 K, a pressure-dependent (in MPa) H_2O solubility (in wt %) equation was derived:

$$c_{H_2Oeq} = 0.2403 \cdot P^{0.5988}. \quad (5)$$

From this, an H_2O saturation pressure (P_{sat}) of 156 MPa for c_{H_2Oi} of 5.0 wt % and 198 MPa for c_{H_2Oi} of 5.7 wt % was obtained for the decompression series. This leads to two distinct starting conditions at the beginning of decompression at 1323 K: one with H_2O saturation at 5.7 wt % and the other H_2O undersaturated at 5.0 wt %.

In addition to the H_2O concentration, homogeneously dispersed crystals of 5–10 µm in size were measured in LLST_12Hg (Fig. 2f). The crystallization is attributed to the subliquidus conditions at 1123 K. Raman spectroscopy and EPMA identified these crystals as magnetite, with an average composition of 78.2 wt % FeO, 6.5 wt % MnO, 5.1 wt % Al_2O_3, 1.3 wt % TiO_2, and 0.8 wt % MgO (Table B1).

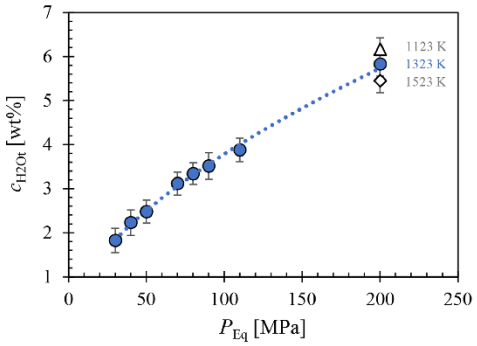

Figure 3. Measured c_{H_2Ot} of LLST glass hydrated at 200, 110, 90, 80, 70, 50, 40, and 30 MPa and at 1323 K (blue circles), 1523 K (open diamond), and 1123 K (open triangle), determined by FTIR spectroscopic analysis. A pressure-dependent c_{H_2Oeq} equation was derived from the data for 1323 K: $c_{H_2Ot} = 0.2403 \cdot P^{0.5988}$.

4.4 Decompression experiments

All decompression samples are free of microlites. Consistently present across all samples are fringe zones. These are represented by large fringe vesicles at the interface between the capsule and the melt (Fig. S1). The size of those vesicles increases with decreasing decompression rate and P_f. Next to the fringe vesicles is the fringe zone, characterized by a vesicle-free area due to the depletion of H_2O from the melt into the fringe vesicles during decompression. The size of the fringe zone expands with decreasing decompression rate, explaining the necessity of a large sample diameter for slow decompression rates. In addition to exhibiting fringe vesicles, decompression samples might also show growth of pre-existing air bubbles originally present within the glass (Fig. S1). These bubbles form H_2O-rich vesicles during hydration prior to decompression and remain easily distinguishable from the surrounding smaller and uniform vesicles due to their significantly larger size after decompression and quenching (50–100 times the size of the uniform tiny vesicles; samples: 3D, 7D, 17D, 20D, 27D, 35D, 36D, 47D; Fig. 4). A comprehensive overview of all decompression samples is included in the Supplement (Figs. S2 and S3).

Generally, all decompression series undergo three stages from the highest to the lowest P_f: (i) the first occurrence of observable vesicle formation, (ii) complete vesiculation of the entire central sample volume and vesicle growth, and (iii) the onset of vesicle coalescence (companion paper Part 2, Marks and Nowak, 2025). The required pressure interval between P_{sat} and the pressure at which the first vesicles can be observed in glass is given by the supersaturation pressure (P_{SS}). Hydrous melts decompressed at a rate of 0.064 MPa s^{-1} exhibit the first occurrence of homogeneously formed vesicles at a P_f of 80 MPa, regardless of an initial H_2O concentration (c_{H_2Oi}) of either 5.7 wt % or 5.0 wt % (Table 2). The same applies to melts decompressed at a rate of 0.17 MPa s^{-1}. However, a significant difference in P_f is observed in melts decompressed at the fastest rate of 1.7 MPa s^{-1}. Here, the appearance of the first vesicles decreases to a P_f of 70 MPa for a c_{H_2Oi} of 5.7 wt % and further down to 50 MPa for a c_{H_2Oi} of 5.0 wt % (Table 2, Figs. S2, S3). A consistent observation across all samples is that the initial vesicle-containing regions at the highest P_f are not vesiculated throughout the entire central sample volume. Instead, small localized areas, positioned variably in the upper, middle, or lower regions, exhibit a high number of tiny vesicles, measuring 2–4 µm. The following stage of complete vesiculation and vesicle growth within the central sample volume is observed across all decompression series. At faster decompression rates of 0.17 and 1.7 MPa s^{-1}, this stage spans a broad pressure interval of 20–40 MPa. In contrast, at the slowest decompression rate of 0.064 MPa s^{-1}, vesicle coalescence is observable after complete vesiculation, corresponding to a pressure decrease of 10 MPa.

4.4.1 Decompression rate

The importance of the influence of decompression rate on vesicle formation is demonstrated by the comparison between samples LLST_34D and LLST_43D. Both samples contained a c_{H_2Oi} of 5 wt %, were hydrated under identical conditions, and decompressed to the same desired P_f of 50 MPa, whereby the recorded data of LLST_34D showed a P_{min} of 50 MPa and that of 43D showed a P_{min} of 46 MPa. After decompression, both samples underwent medium quenching with 97 K s^{-1}. The samples are identical except for one key difference: sample LLST_43D was continuously decompressed at a rate of 1.7 MPa s^{-1}, whereas sample LLST_34D experienced a reduction in decompression rate to $\sim$ 0.9 MPa s^{-1} towards the end of decompression (Fig. D1). This resulted in an increased decompression time of 11 s for sample LLST_34D compared to sample LLST_43D. This deceleration in decompression rate resulted in complete vesiculation of the melt throughout the volume of the slightly slower decompressed sample LLST_34D (Fig. D1), in contrast to sample LLST_43D, which, at the higher and constant decompression rate, exhibited vesiculation only in the central part of the melt volume.

Various parameters have been quantified in all samples, including the VND, vesicle size, glass porosity, melt porosity, and c_{H_2Ot} of the quenched glasses. All these parameters depend on each other. At a first step, they are described independently of each other for characterization purposes. Sample areas displaying incipient coalescence were intentionally excluded from analysis, as these constitute the primary focus within an extended dataset of the second companion paper (Marks and Nowak, 2025).

4.4.2 Vesicle number density

The VND was determined by TLM in areas of the samples exhibiting a homogeneous distribution of vesicles (Fig. S1). The logVNDs range from 4.0 up to 5.7 across all c_{H_2Oi} and decompression rates (Fig. 5). However, there is a slight trend towards an increase in logVND with decreasing P_f. The logVND increases on average by 1 log unit, from 4.5 at P_f of 80 MPa to 5.5 at P_f of 30 MPa. Comparative analysis using TLM and surface imaging via the laser-scanning microscope, combined with CSDcorrections for sample LLST_17D, yielded consistent results (TLM: logVND = 5.68, CSD: logVND = 5.59). Samples decompressed with 1.7 MPa s^{-1} show logVND values clustering between 4.8 and 5.4, while logVND of slower-decompressed samples (0.17–0.064 MPa s^{-1}) range from 4.0 to 5.7. This indicates that a discernible dependence of VND on the decompression rate could not be verified.

4.4.3 Vesicle size

The vesicles in the quenched glasses are uniformly sized within each sample, with diameters steadily increasing from

~ 2 to $\sim 14\,\mu m$ as P_f decreases for each decompression and c_{H_2Oi} series (Fig. 5). The optical transparency of the glasses diminishes with increasing vesicle size and number, finally becoming opaque, as observed in samples 20D, 17D, and 42D. In reflected light images, this opacity is seen as white, milky glass, whereas in TLM images the highly vesiculated sample areas appear black (see the Supplement).

4.4.4 Porosities

Glass porosities (Φ_{glass}) of vesiculated samples were calculated based on the number and sizes of vesicles per mm^{-3} of silicate glass (Table 2, Fig. 5). These porosities range from 0.1 vol % to a maximum of 10 vol %. Additional, equilibrium melt porosities (Φ_{eq}) at P_f were calculated according to Gardner et al. (1999), using the melt density ρ_{melt} (Ochs and Lange, 1999) and the molar volume of H_2O fluid V_{mH_2O} (Duan and Zhang, 2006; Table 2):

$$\Phi_{cq} = \left[\frac{\frac{\rho_{melt}}{M_{H_2O}} \cdot V_{mH_2O} \cdot \left(c_{H_2Oi} - c_{H_2Ocq}\right)}{1 + \left(\frac{\rho_{melt}}{M_{H_2O}} \cdot V_{mH_2O} \cdot \left(c_{H_2Oi} - c_{H_2Oeq}\right)\right)} \right]. \quad (6)$$

Equilibrium porosities were added to the same diagram as the glass porosities, with the c_{H_2Oi} series of 5.0 wt % and 5.7 wt % indicated by yellow and red colors, respectively (Fig. 5). The calculated Φ_{cq} range from 18 vol % to 56 vol % with decreasing P_f. High P_f values of 80 or 70 MPa correspond to melt porosities of 18 vol %–22 vol %, while lower P_f values of 40 or 30 MPa result in melt porosities of 42 vol %–56 vol %.

4.4.5 H_2O concentrations

H_2O concentrations of decompressed LLST samples are presented in Fig. 6. Additionally, c_{H_2Oi} of 5.7 wt % and 5.0 wt % were plotted, along with c_{H_2Oeq} calculated from the solubility data (Eq. 5, Fig. 3). Samples that contained vesicles in the beam path could not be evaluated, because they yielded unrealistically high virtual c_{H_2Ot} values, reaching up to 10 wt %. This is particularly relevant for samples that reached the stage of complete vesiculation. At this stage, the VND is so high that the size of glass areas is insufficient for the beam to pass through without interference from the vesicles (Table 2). Consequently, only c_{H_2Ot} values from samples where the IR beam exclusively penetrated glass were included in the plot. Figure 6 displays c_{H_2Ot} of samples from the 5.0 wt % series data which are related to depleted glass regions around pre-existing bubbles or fringe zones. Therefore, they do not represent the residual c_{H_2Ot} values of glass in vesiculated areas and are marked as unfilled symbols.

In general, the c_{H_2Ot} values of decompressed samples are consistently far above the expected equilibrium concentrations at P_f (Fig. 6). Both 5.7 wt % and 5.0 wt % c_{H_2Oi} series share a common characteristic: the difference in c_{H_2Ot} between the non-vesiculated samples and c_{H_2Ocq} rises from 1 wt % at the highest P_f to 2 wt % until vesicle formation initiates. Subsequently, irrespective of the P_f, all analyzable glass sample areas consistently exhibit a difference of approximately 2 wt %.

Despite the absence of observable vesicles in the glass samples decompressed to P_f of 100 and 90 MPa, the measured c_{H_2Ot} is systematically 0.1 wt % to 0.2 wt % lower than the originally measured amount of H_2O, related to supersaturation and reduced pressure. This observed reduction may be attributed to different structural states of the melts before quenching. The molar absorption coefficients of the H_2O and OH absorption bands were determined in glasses quenched from H_2O undersaturated melts, whereas the melts decompressed to 110–90 MPa were significantly supersaturated with H_2O. Consequently, a lower density compared to the melts at higher pressure before quenching could be expected. However, adjusting the density to slightly lower values would yield a higher calculated H_2O content. We suggest that the apparent reduction in H_2O contents in non-degassed supersaturated samples is related to slightly different melt structures and H_2O species concentrations before quenching, causing minor changes in the absorption coefficients of the glasses compared to the standard glasses quenched from higher pressures. Therefore, it is likely that the actual c_{H_2Oi} remains constant within the sample volume of decompressed and non-degassed samples.

The decompression series with c_{H_2Oi} of 5.7 wt % and a rate of 1.7 MPa s^{-1} shows only a minor decrease in c_{H_2Ot} from P_f of 110 to 80 MPa, where the first vesicles appear in glass (5.52 wt % to 5.43 wt %, respectively). The decompression series at the slower rate of 0.17 MPa s^{-1} exhibits a significantly faster drop in c_{H_2Ot} from 5.52 wt % at 110 MPa to 4.99 wt % at 90 MPa. Due to the high number of vesicles, undisturbed measurements were no longer possible below 80 MPa. The samples decompressed at the slowest rate of 0.064 MPa s^{-1} show an increased decline in c_{H_2Ot} from 90 to 70 MPa, with c_{H_2Ot} measured around large pre-existing or already coalesced vesicles. There is a strong reduction in the residual H_2O content of the glass, from 5.43 wt % at 90 MPa to 4.86 wt % at 70 MPa.

It seems that samples of all decompression series at c_{H_2Oi} of 5.0 wt % maintain a constant c_{H_2Ot} down to 70 MPa, regardless of decompression rate. However, this observation holds true only for the highest decompression rate of 1.7 MPa s^{-1}. Vesicle formation can be observed in samples decompressed with 1.7 MPa s^{-1} at a P_f of 50 MPa. Consequently, all samples with a higher P_f remain vesicle-free and are therefore suitable for FTIR measurements. The rapid decompression rate results in a very short decompression time (total ~ 1 min, ~ 35 s from P_{sat}), insufficient for significant diffusion of dissolved H_2O into the fringe vesicles at the capsule walls. A decrease in c_{H_2Ot} of 0.6 wt % is observed at 50 MPa, attributed to vesicle formation within the melt volume. Glass volumes between vesicles of samples decom-

pressed to 40 and 30 MPa could not be measured due to the high VNDs.

In the samples of the experimental series at $c_{H_2O_i}$ of 5.0 wt % with a decompression rate of 0.17 MPa s^{-1}, $c_{H_2O_i}$ values were maintained down to a P_f of 90 MPa. Vesicle formation commenced at 80 MPa, but the number and size of the vesicles at this pressure prevented the acquisition of sufficient glass volumes for undisturbed measurements. Consequently, there is a data gap for P_f values of 80, 70, and 50 MPa. In the sample decompressed to 40 MPa, tiny pre-existing air-bubbles were already present in the glass. Similar to fringe vesicles, a fringe zone formed around these vesicles, where H_2O was previously depleted during decompression. Therefore, the $c_{H_2O_t}$ value related to a P_f of 40 MPa does not reflect the equilibrium H_2O content in the melt but is expected to be higher than the $c_{H_2O_t}$ in the glass interstices of the homogeneous vesicles volume. Due to early H_2O depletion in the fringe zone surrounding the pre-existing vesicles, the remaining H_2O supersaturation was insufficient in the fringe zone to enable further vesicle formation during decompression to P_f. Consequently, the actual $c_{H_2O_t}$ values in the glass interstices of the uniform vesicle volumes are expected to be below the plotted concentration of 4.25 wt %.

The samples of the series with the slowest decompression rate of 0.064 MPa s^{-1} exhibit the same behavior as the samples decompressed with 0.17 MPa s^{-1}. Down to a P_f of 90 MPa, $c_{H_2O_t}$ is close to $c_{H_2O_i}$ and remains nearly constant. Due to the high VND, a data gap exists in the P_f range of 80 to 60 MPa. H_2O concentrations could only be measured again at P_f starting from 50 MPa. In this case as well, $c_{H_2O_t}$ was determined in H_2O-depleted fringe zones around pre-existing vesicles due to the lack of sufficiently large glass areas in the uniformly vesiculated sample volume. Consequently, at a P_f of 50 MPa the $c_{H_2O_t}$ of the interstitial glass should be lower than 4.47 wt %.

5 Discussion

5.1 Decompression samples

5.1.1 Onset of vesicle formation, P_{SS} determination, and its problem

To investigate the homogeneous vesicle formation of the LLST melt, decompression series with two different initial H_2O concentrations were conducted. Regarding the solubility experiments, H_2O saturation prior to decompression was nearly achieved for the 5.7 wt % series, as the determined P_{sat} at 1323 K was 198 MPa, which closely matches the hydration pressure of 200 MPa. For the series with a $c_{H_2O_i}$ of 5.0 wt %, P_{sat} was calculated to be 156 MPa (Eq. 5). Consequently, while supersaturation of the melt occurs immediately at 5.7 wt % after the start of decompression, a pressure decrease of $\sim$ 40 MPa must first be achieved before supersaturation begins at $\sim$ 156 MPa for the 5.0 wt % series.

This initial P_{sat} difference and the associated P_{SS}, determined as the pressure difference between P_{sat} and the pressure at which vesicles are first observed, do not influence the observed onset of vesicle formation within the frame of the analyzed 10 MPa intervals for the two $c_{H_2O_i}$ series. At slower decompression rates (0.064 and 0.17 MPa s^{-1}) and a P_f of 80 MPa, the first vesicles appear in the glass. However, at a faster decompression rate of 1.7 MPa s^{-1}, lower P_f values are required: 70 MPa for the 5.7 wt % series and 60–50 MPa for the 5.0 wt % series. Consequently, the P_{SS} necessary for vesicle formation in the 5.7 wt % series is 120 MPa at the slower decompression rates, increasing to 130 MPa at 1.7 MPa s^{-1}. In contrast, the P_{SS} for the 5.0 wt % series is 80 MPa at 0.064 and 0.17 MPa s^{-1}, rising to 100–110 MPa at the fast decompression rate. Therefore, the observable onset of vesicle formation necessitates a higher P_{SS} of $\sim$ 40 MPa for the initially saturated melt compared to the initially slightly undersaturated melt at slower decompression rates. Nonetheless, faster decompression rates demand an even higher P_{SS}, corresponding to a lower P_f of 10 to 20–30 MPa, depending on $c_{H_2O_i}$.

To date, we are unable to fully explain this behavior. However, we propose that phase separation may have occurred at higher P_f and lower P_{SS}, but the H_2O resorption process during cooling might have resulted in the complete dissolution of the already formed vesicles. Resorption of H_2O from the fluid vesicles into the melt during quenching (McIntosh et al., 2014; Allabar and Nowak, 2020) is driven by the increasing solubility of H_2O in phonolitic melt with decreasing temperature at pressures < 300 MPa (Schmidt and Behrens, 2008). This effect is more pronounced for the 5.7 wt % series, due to the higher diffusivity with greater $c_{H_2O_t}$, as well as the low melt viscosity, which decreases with higher residual $c_{H_2O_t}$ (Giordano et al., 2008). The resorption of H_2O from vesicles back into the melt was demonstrated by Allabar and Nowak (2020) for samples containing 4 wt %–5 wt % residual $c_{H_2O_t}$ in the glass. The effect was quantifiable due to the large vesicle size of $\sim$ 20 µm. Resorption halos of 3 and 10 µm were detected around the vesicles, depending on the quenching rate (> 100 and 44 K s^{-1}, respectively). The high quenching rate of > 100 K s^{-1} is comparable to the quenching rate determined in these experiments, which was 97 K s^{-1}, although slightly slower, thereby enhancing the effect of greater resorption. Therefore, if we assume vesicles of $\sim$ 1 µm in diameter at high P_f of 90 or 110 MPa, these vesicles would have dissolved completely. The effect of resorption is particularly pronounced in the samples of the 5.7 wt % series, as evidenced by a comparison of vesicle sizes. While the vesicle diameters in the glasses of the 5.0 wt % series are initially very small, measuring 2.2, 3.0, and 5.0 µm for decompression rates of 0.064, 0.17, and 1.7 MPa s^{-1}, respectively, the first analyzable vesicle diameters in the 5.7 wt % series are significantly larger at 4.3, 3.8, and 6.8 µm, which is roughly double the size. However, the molar volume of H_2O increases sharply with decreasing pressure, causing expansion to have

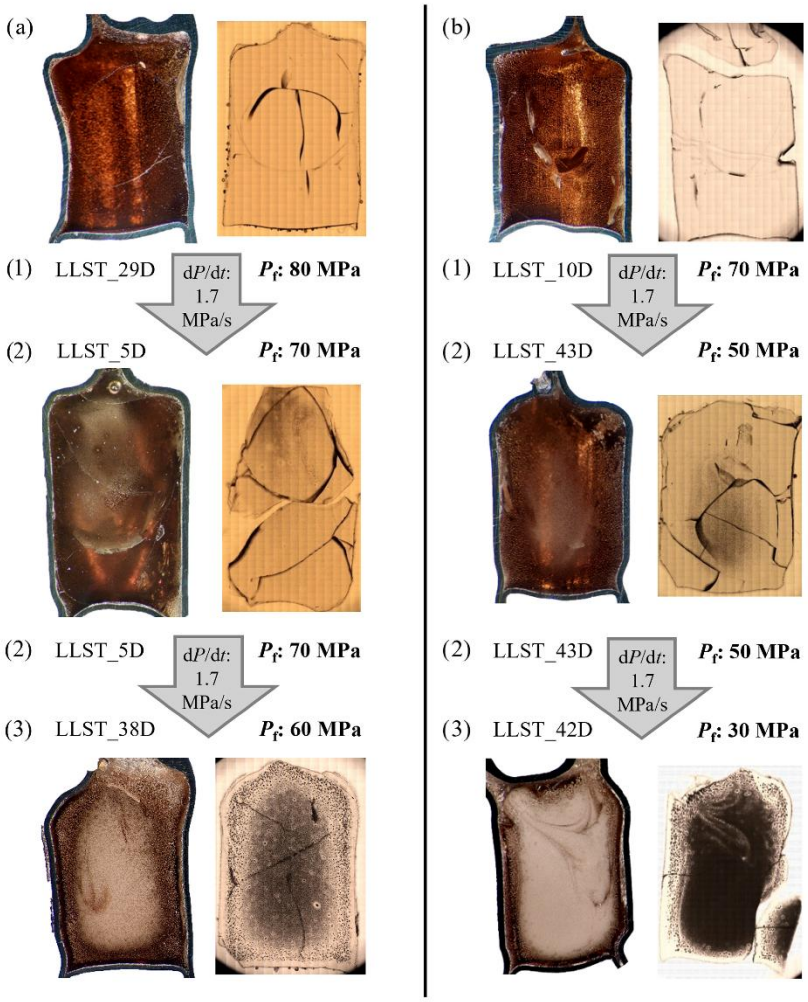

Figure 4. Decompression series illustrating vesicle formation during pressure decrease. Samples were initially hydrated with ~ 5.7 wt % or 5.0 wt % H_2O (corresponding to **a** and **b**) at 200 MPa, then decompressed to P_f of 80–30 MPa. An overview of all series with decompression rates of 1.7, 0.17, or 0.064 MPa s^{-1} is provided in Figs. S2 and S3. All series follow the same progression: (1) No visible vesicle formation due to insufficient P_{SS}; (2) vesicle formation observable, primarily in specific regions of the sample; and (3) vesicle formation throughout the sample, reaching maximum VND. In both displayed samples, partial vesicle coalescence is observed in the intermediate regions between the sample center and the capsule wall. Each sample originally had a capsule inner diameter of 5 mm.

an increasingly significant role at lower pressures. This effect is more pronounced in the 5.0 wt % series, where vesicle formation occurs at lower P_f, favoring the appearance of the first analyzable vesicle sizes. Therefore, it is reasonable to infer that smaller vesicles were initially present in the decompressed melts of the 5.7 wt % series at higher P_f. However, these vesicles likely dissolved completely due to resorption during the quenching process.

5.1.2 Glass vs. melt porosities

The vesicles in each individual sample are of uniform size within the resolution range. Following the onset of vesicle formation, subsequent decompression led to vesicle growth without significant change in VND (Fig. 5). For maximal logVNDs ranging from 5.1 to 5.7, a mean-vesicle distance (x) of ~ 7 to 9 µm was calculated based on Hertz (1908) ($x = 5/9 \cdot \mathrm{VND}^{-1/3}$) for a random vesicle distribution. This inter-vesicle distance is sufficiently small to enable near-equilibrium c_{H_2Ot} and near-equilibrium porosity to be

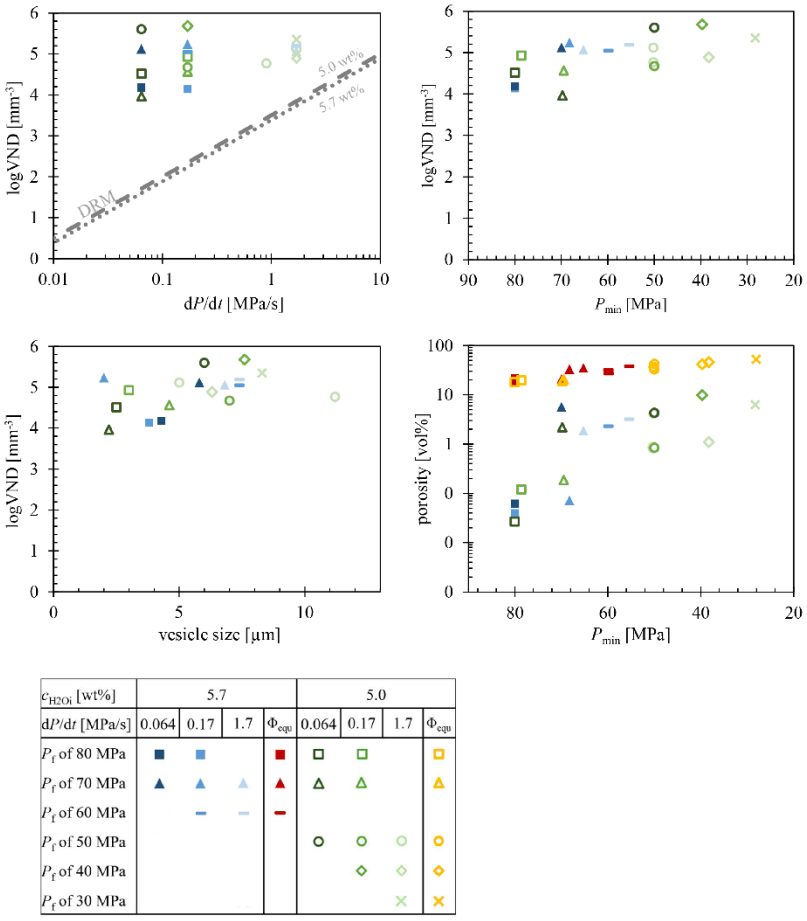

Figure 5. The logVND data plots of decompressed LLST samples. In conjunction with the glass porosity plotted in standard colors, the calculated equilibrium melt porosity has been included in the logVND–porosity diagram. Red data points denote a c_{H_2O}i of 5.7 wt %, while yellow data points represent a c_{H_2O}i of 5.0 wt %.

achieved within seconds through H_2O diffusion during further decompression, as can be estimated using the H_2O diffusivity reported by Schmidt et al. (2013). However, for all samples, the glass porosities are with 0.01 %–10 % significantly lower than the calculated equilibrium porosities prior to quenching, yielding values between 18 %–56 % (Table 2, Fig. 5). These equilibrium porosities exceed the measured glass porosities by a factor of 10 to 100. This discrepancy can be attributed to vesicle shrinkage resulting from the reduction in the molar volume of H_2O (Marxer et al., 2015) and the resorption of H_2O from the fluid vesicles into the melt during quenching (McIntosh et al., 2014; Allabar et al., 2020a). Allabar et al. (2020b) determined a fictive temperature (T_f) at which vesicle shrinkage stops, up to 200 K above the glass transition temperature (T_g) for a cooling rate of 44 K s^{-1}. To calculate T_f, T_g was first calculated according to Giordano et al. (2008), which is dependent on c_{H_2O}t in the melt. Lower c_{H_2O}t increases T_g (Giordano et al., 2008), and the temperature where vesicles are preserved in the glass is higher at the same quenching rate. Based on the expected near-equilibrium degassing with near-equilibrium c_{H_2O}t, we can assume that c_{H_2O}eq was reached in the melt at a high logVND of ∼ 5.5. The T_g was calculated for the determined P_f where vesicles are preserved in the glass after quenching, ranging from 745 to 787 K at the specific observable onset of vesicle formation at the cooling rate of 97 K s^{-1}. Adding 200 K to reach T_f yields ∼ 965 ± 20 K, covering all samples. This results in temperature differences from the degassing temperature (1323 K) of 350 K. Considering the more than double the cooling rate (97 K s^{-1} compared to 44 K s^{-1}) reduces the shrinkage and resorption time to 3–4 s instead of ∼ 9 s as valid for Allabar et al. (2020b). Therefore, the resorption

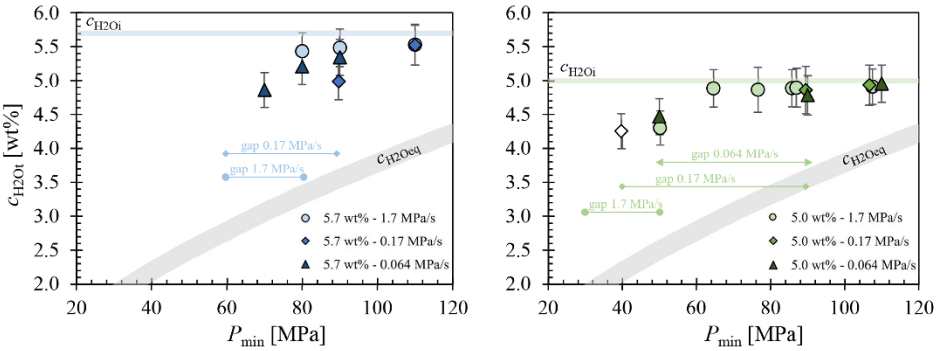

Figure 6. The residual $c_{H_2O_t}$ of the glasses is plotted against P_{min} of the decompressed samples. Only $c_{H_2O_t}$ of samples that were able to be measured undisturbed by vesicles in the near-infrared beam path are shown. Blue symbols indicate samples with $c_{H_2O_i}$ of 5.7 wt %, while green symbols show samples with $c_{H_2O_i}$ of 5.0 wt %. The legend corresponding to the decompression rates is provided in the lower right corner. The $c_{H_2O_{eq}}$ curve was calculated according to Eq. (5). Symbols without fill color represent $c_{H_2O_t}$ of vesicle-free and H_2O-depleted glass regions around pre-existing bubbles or fringe zones and do not represent residual $c_{H_2O_t}$ of vesiculated glass regions.

Table 1. Conditions and results of solubility experiments. In the solubility section, samples labeled with an "H" were produced using glass pieces, whereas those labeled with "Hg" were derived from an initial glass cylinder. Decompression experiments were hydrated at 200 MPa for 96 h at 1523 K and thermally equilibrated for 0.5 h at 1323 K prior to decompression. Quenching rates: RQ: ~ 150 K s^{-1} (Berndt et al., 2002), MQ: ~ 97 K s^{-1}, NQ: ~ 16 K s^{-1} (Allabar et al., 2020b).

Sample	T [K] quench	P_f [MPa]	P_{min} [MPa]	Quenching rate [K s^{-1}]	$c_{H_2O_i}$ [wt %]	$c_{H_2O_{eq}}$ at P_f [wt %]	c_{H_2O} in glass without vesicles [wt %]	T_g [K]
H_2O solubility experiments								
10H	1523	200	200	MQ	8.13	–	5.52 ± 0.26	652
10Hg	1523	200	200	MQ	7.99	–	5.45 ± 0.26	655
11H	1323	200	200	NQ	7.89	5.74	5.92 ± 0.27	608
11Hg	1323	200	200	NQ	8.13	5.74	5.83 ± 0.27	611
12Hg*	1123	200	200	NQ	9.02	–	6.16 ± 0.27	596
4H	1323	110	110	RQ	6.05	4.01	4.04 ± 0.32	719
4Hg	1323	110	110	RQ	5.93	4.01	3.88 ± 0.30	726
5H	1323	90	90	RQ	6.04	3.56	3.52 ± 0.26	743
8H	1323	80	80	RQ	5.98	3.31	3.34 ± 0.29	752
6H	1323	70	70	RQ	5.14	3.06	3.12 ± 0.26	763
7H	1323	50	50	RQ	4.98	2.50	2.46 ± 0.25	799
9H	1323	40	40	RQ	5.06	2.19	2.23 ± 0.28	813
13H	1323	30	30	NQ	3.94	1.84	1.87 ± 0.21	792
13Hg	1323	30	30	NQ	3.95	1.84	1.83 ± 0.21	794

* 24 h at 1123 K

halos around the vesicles in our samples should be smaller than the 3 to 10 µm determined by the authors, yet the effect remains observable in the measured $c_{H_2O_t}$. However, we suggest that during decompression near-equilibrium conditions were established at the maximum logVNDs, where homogeneous vesicle formation occurred. A more detailed discussion of porosity including an extended dataset is addressed in the associated coalescence companion paper (Marks and Nowak, 2025).

5.1.3 Total H_2O content

The high logVND of ~ 5.5 and inter-vesicle distances of 7–9 µm should enable near equilibrium degassing. However, the $c_{H_2O_t}$ in the residual glass are 1 wt %–2 wt % higher than $c_{H_2O_{eq}}$ at P_f. The $c_{H_2O_t}$ values close to $c_{H_2O_i}$ at higher P_f correlate with the absence of vesicles or with the lowest logVNDs of ~ 4, related to resorption.

The effect of resorption of H_2O back into the melt during quenching, has already mentioned in vesicle formation, as well as in glass porosity, and plays also in analyzing $c_{H_2O_t}$ a

https://doi.org/10.5194/ejm-37-385-2025

Table 2. Decompression samples were hydrated at 200 MPa for 96 h at 1523 K and thermally equilibrated for 0.5 h at 1323 K prior to decompression. Quenching rates: RQ: ~ 150 K s^{-1} (Berndt et al., 2002); MQ: ~ 97 K s^{-1}; NQ: ~ 16 K s^{-1} (Allabar et al., 2020b).

Sample	P_f [MPa]	P_{min} [MPa]	Quenching rate [K s^{-1}]	$c_{H_2O}i$ [wt %]	$c_{H_2O}eq$ at P_f [wt %]	$c_{H_2O}t$ in glass without vesicles [wt %]	c_{H_2O} in glass through vesicles [wt %]	T_g [K]	Number of analyzed vesicles	Vesicle size [µm]	Volume [mm^3]	Φ_{glass} [vol %]	Φ_{equ} [vol %]	logVND [mm^{-3}]
Decompression experiments 1.7 MPa s^{-1}														
$c_{H_2O}i$: 5.7 wt %														
28D	110	95	MQ	5.72	3.68	5.53 ± 0.30		652						
24D	90	86	MQ	5.70	3.46	5.48 ± 0.28		653						
29D	80	79	MQ	5.73	3.30	5.43 ± 0.28		655						
5D	70	65	MQ	5.73	2.93		5.33 ± 0.28		202	6.8	1.8×10^{-3}	1.9	35.5	5.07
50D	60	55	MQ	5.72	2.66		5.26 ± 0.26		191	7.4	1.3×10^{-3}	3.2	38.0	5.19
$c_{H_2O}i$: 5.0 wt %														
33D	110	108	MQ	5.00	3.96	4.91 ± 0.26		675						
15D	90	86	MQ	4.99	3.46	4.89 ± 0.27		676						
31D	90	87	MQ	5.00	3.48	4.90 ± 0.28		675						
11D	80	77	RQ	5.02	3.23	4.87 ± 0.33		684						
10D	70	65	MQ	5.06	2.92	4.89 ± 0.27		676						
34D[a]	50	50	MQ	5.01	2.51	4.30 ± 0.25	4.82 ± 0.26	699	168	11.2	3.0×10^{-3}	4.1	36.6	4.77
43D	50	46	MQ	4.99	2.37		4.99 ± 0.26		232	5.0	1.8×10^{-3}	0.8	34.7	5.12
16D	40	38	MQ	5.02	2.13		4.79 ± 0.26		125	6.3	1.5×10^{-3}	1.1	46.3	4.89
42D	30	28	MQ	5.01	1.78		7.98 ± 0.33		78	8.3	3.7×10^{-4}	6.3	55.8	5.35
Decompression experiments 0.17 MPa s^{-1}														
$c_{H_2O}i$: 5.7 wt %														
14D	110	110	MQ	5.78	4.01	5.52 ± 0.29		652						
2D	90	90	MQ	5.70	3.55	4.99 ± 0.27		658	18	78.7	3.6×10^{-1}	1.3	23.7	1.70[b]
27D	80	80	MQ	5.71	3.31		5.37 ± 0.33		144	3.8	1.0×10^{-2}	0.0	21.7	4.14
3D	70	68	MQ	5.68	3.01		4.95 ± 0.27		309	2.0	1.8×10^{-3}	0.1	33.5	5.24
49D	60	60	MQ	5.73	2.79		5.08 ± 0.26		356	7.4	3.3×10^{-3}	2.3	32.0	5.05
$c_{H_2O}i$: 5.0 wt %														
30D	110	107	MQ	5.01	3.94	4.93 ± 0.30		674						
12D	90	90	RQ	4.93	3.54	4.86 ± 0.35		692						
23D	80	79	MQ	5.01	3.28		4.94 ± 0.28		297	3	3.5×10^{-3}	0.1	19.8	4.93
35D	70	70	MQ	5.00	3.05		4.76 ± 0.26		148	4.6	4.0×10^{-3}	0.2	20.4	4.56
7D	50	50	MQ	4.99	2.50		5.12 ± 0.27		81	7.0	1.7×10^{-3}	0.8	42.3	4.67
17D	40	40	MQ	5.03	2.18	4.25 ± 0.26[c]	7.67 ± 0.34	702	151	7.6	3.5×10^{-4}	9.9	41.9	5.68
17D	40	40	MQ	5.03	2.18	4.25 ± 0.26[c]	7.67 ± 0.34	702	571	10.8		25.3	41.9	5.59[d]
Decompression experiments 0.064 MPa s^{-1}														
$c_{H_2O}i$: 5.7 wt %														
46D	90	90	MQ	5.71	3.56	5.34 ± 0.27		659						
36D	80	80	MQ	5.71	3.31	5.21 ± 0.26		664	118	4.3	7.8×10^{-3}	0.1	17.8	4.18
37D	70	70	MQ	5.71	3.06	4.86 ± 0.26	5.14 ± 0.26	677	266	5.8	2.0×10^{-3}	1.3	21.1	5.12
$c_{H_2O}i$: 5.0 wt %														
32D	110	110	MQ	5.00	4.01	4.95 ± 0.28		673						
19D	90	90	MQ	4.97	3.56	4.78 ± 0.29		680						
22D	80	80	MQ	5.00	3.31		4.93 ± 0.28		124	2.5	3.8×10^{-3}	0.03	18.0	4.51
47D	70	70	MQ	5.06	3.06		4.82 ± 0.26		39	2.2	4.2×10^{-3}	0.01	20.9	3.96
20D	50	50	MQ	5.01	2.50	4.47 ± 0.27[c]	5.34 ± 0.28	692	269	6.0	2.4×10^{-3}	4.3	19.0	5.60

[a] dP/dt of 0.9 MPa s^{-1} in the end of decompression; see Fig. D1. [b] pre-existing bubbles; [c] $c_{H_2O}t$ determined in depleted areas; [d] determined by CSDcorrections.

crucial role. The c_{H_2Ot} of the glass between vesicles does not represent c_{H_2Ot} dissolved in the melt at P_f prior to quenching due to H_2O resorption from the fluid phase back into the melt (McIntosh et al., 2014; Allabar et al., 2020b). During all stages where vesicles were present, resorption took place and increased the c_{H_2Ot} in the residual melt, and therefore in the measured glass areas. A simplified calculation illustrates the absorption effect during quenching. During the assumed cooling duration of 4 s within the quenching process, H_2O diffusion distances were calculated according to the diffusion equation of Schmidt et al. (2013), assuming c_{H_2Oeq} for 1323 K as well as T_f of 965 K. Covering all samples at different P_f and their corresponding c_{H_2Oeq}, H_2O diffusion distances of 22–19 µm for 1323 K and 5–3 µm for 965 K were calculated. Therefore, even with the decreasing diffusion coefficient at decreasing temperature, at least a resorption distance of 3 µm can be achieved, which is responsible for the high c_{H_2Ot} in the residual glasses. Importantly, the interstitial glass of the samples, where equilibrium degassing is expected due to the short inter-vesicle distance, was not measurable due to the high VND, preventing FTIR measurements of glass without vesicles in the measured volume. These stages are marked in Fig. 6 by the gaps, according to each decompression series. The subsequent stages of beginning coalescence again allowed measurements in the residual glass, although between large vesicles. Disequilibrium is expected again in these cases, due to the increased vesicle distances, explaining the high c_{H_2Ot}. The H_2O content in the residual glass is analyzed in detail in Marks and Nowak (2025), incorporating an extended dataset that examines the transition of c_{H_2Ot} during maximum VND to the onset and progression of coalescence.

These observations are similar to those of Allabar et al. (2020b) on K-phonolite melt of the Vesuvius AD79 eruption (VAD79). Their decompressed samples also exhibited high residual c_{H_2Ot} of about 2 wt % above c_{H_2Oeq}, despite calculations indicating near-equilibrium conditions in all experiments due to sufficiently high H_2O diffusivity and small inter-vesicle distances at a 10 µm scale at high logVNDs of 4.6 to 6.3, which are quite similar to the VNDs of this study.

The parameters measured in the glass, such as c_{H_2Ot} and porosity, do not reflect the melt conditions during decompression. Vesicles form at a sufficiently high P_{SS}, grow during continuous decompression, and shrink during quenching with simultaneous resorption of H_2O from the fluid vesicles back into the melt, potentially to the extent of complete dissolution. These factors are enhanced by depolymerized melt structures due to the lower viscosity as well as increased diffusivity resulting from high c_{H_2Ot}. To minimize these effects, it is essential to quench the melt as quickly as possible when analyzing and quantifying these parameters, while also considering the potential cost of sample breakage.

5.1.4 Decompression-rate-independent VND

To determine the degassing mechanism of the LLST melt, VNDs were quantified in vesiculated samples. This allowed us to distinguish between a decompression-rate-dependent behavior (where VND increases with increasing decompression rate and thus a significant increase of VND with P_f) and a decompression-rate-independent behavior (where VND remains constant across different decompression rates). The decompression-rate-dependent VND can be explained by nucleation theory, where vesicles form only to the extent necessary to reduce supersaturation, resulting in a range of vesicle sizes within a single sample as new vesicles form when the existing ones are insufficient (Navon and Lyakhovsky, 1998). Based on this theory, Toramaru (2006) established a decompression rate meter (DRM) that derives magma ascent velocity using VNDs of volcanic ejecta. For comparison, the DRM was applied to hydrous LLST melt used in our study considering the physicochemical key parameters.

$$\mathrm{VND} = 34 \cdot C \cdot \left(\frac{16 \cdot \pi \cdot \sigma^3}{3 \cdot k \cdot T \cdot P_{sat}^2}\right)^{-2} \cdot \left(\frac{V_m \cdot P_{sat}}{k \cdot T}\right)^{-\frac{1}{4}} \cdot \left(\frac{P_{sat}^2 \cdot kT \cdot C \cdot D}{4 \cdot \sigma^2 \cdot (\mathrm{d}P/\mathrm{d}t)}\right)^{-\frac{3}{2}} \quad (7)$$

C: initial total H_2O concentration (number of molecules per cubic meters [m^{-3}]); σ: surface tension of the vesicle–melt interface [$N\,m^{-1}$]; k: Boltzmann constant (1.38×10^{-23} [$J\,K^{-1}$]); T: temperature [K]; P_{sat}: H_2O saturation pressure [Pa]; D: H_2O diffusivity in the silicate melt [$m^2\,s^{-1}$]; V_m: volume of an H_2O molecule in the melt $= 3 \times 10^{-29}\,m^3$ (Burnham and Davis, 1971); $\mathrm{d}P/\mathrm{d}t$: decompression rate [$Pa\,s^{-1}$]

The model assumes that each H_2O molecule is a potential vesicle nucleation site and that nucleation ceases during decompression when the VND reaches a level where vesicle distances are sufficiently small for a diffusion-controlled decrease in H_2O concentration below a supersaturation threshold needed for further vesicle nucleation (Toramaru, 2006). Using the DRM, the logVND as a function of $\mathrm{d}P/\mathrm{d}t$ can be calculated by considering diffusivity, surface tension, and the H_2O content via the saturation pressure (P_{sat}). The required H_2O diffusivity ($\log D$) was calculated by Eq. (8), according to Schmidt et al. (2013):

$$\log D\,[\mathrm{m^2\,s^{-1}}] = (-6.001 - 0.277 \cdot c_{H_2Ot}) - (6281 - 565.6 \cdot c_{H_2Ot})/T. \quad (8)$$

The surface tension was calculated according to Shea (2017) and was predicted to be $0.1231\,N\,m^{-1}$ for 5.7 wt % H_2O and $0.1411\,N\,m^{-1}$ for 5.0 wt %. Applying these values in the DRM, the linear logVND trend with the fixed slope of 3/2 would match our experimentally determined maximum logVND of 5.7 at an unrealistically high decompression rate of $\sim 30\,MPa\,s^{-1}$.

In contrast to nucleation theory, the determined maximum logVNDs of 5.1–5.7 with uniformly sized vesicles across all decompression rates indicate a decompression-rate-independent behavior for the LLST melt. This behavior might indicate an off-critical spinodal decomposition process, which has been observed in supersaturated K-phonolitic melts (Allabar and Nowak, 2018; Allabar et al., 2020b).

Slight variations in the logVND of 4–5.7 determined in quenched glasses are likely related to resorption processes. Glass samples with logVNDs of 4–5 indicate the early stages of degassing, primarily seen in samples with high P_f of 80 and 70 MPa. In these cases, a small number of vesicles formed during decompression appear to have survived the quenching, potentially due to slight differences in vesicle size. It is also plausible that smaller vesicles with numerous neighboring vesicles underwent resorption, thereby favoring the growth of larger vesicles. The vesicles that underwent resorption would have continued to grow if the melt had been subjected to further decompression, as observed in samples quenched at lower P_f, showing high logVNDs with 5.1–5.7. However, such minor variations in vesicle size could not be resolved within the scope of this study and with the analytical methods employed. Consequently, it is expected that the majority of minimally smaller vesicles dissolved during the quenching process. This is also reflected in the vesicle sizes in the glass, generally ranging between 2 and 5 µm for samples with P_f of 80 and 70 MPa. Increased vesicle sizes related to vesicle growth are observed for samples at lower P_f, which also correspond to the highest logVNDs, with values of 5.1–5.7 representing the VND of the vesicle formation process unaffected by extinction related to resorption. The VND keeps constant down to a P_f of 70–60 MPa for samples with $c_{H_2O_i}$ of 5.7 wt % and P_f of 50–30 MPa for samples with $c_{H_2O_i}$ of 5.0 wt %, caused by the different ΔP_{SS} values. These samples also correspond to the highest porosities, measured in glass with up to 10 vol %. However, in the series with 0.17 and 0.064 MPa s^{-1}, a third stage of vesiculation was observed. The VNDs of all series show a slight decrease in logVND by 0.1 to 0.2 at 0.17 MPa s^{-1} and even 0.5 to 0.8 at 0.064 MPa s^{-1}, which is correlated to the observed onset of coalescence. A detailed analysis of the coalescence behavior in the LLST melt, based on an extended dataset, is presented in the corresponding coalescence paper (Marks and Nowak, 2025).

The data from Allabar and Nowak (2018) and Allabar et al. (2020a, b) are particularly comparable to this study due to a similar experimental design and bulk composition. Allabar and Nowak (2018) observed vesicle formation in the hydrous VAD79 composition with 5.3 wt % H_2O at P_f of $\leq$ 100 MPa, showing homogeneously distributed vesicles with logVNDs of 4.8–5.4, irrespective of decompression rates ranging from 0.024 to 1.7 MPa s^{-1}. Further decompression to 70 MPa did not change VND but only led to vesicle growth, similar to the behavior of LLST melt. Thus, the results of VAD79 and LLST show a decompression-rate-independent behavior. A decompression-rate-dependent behavior would follow the DRM line, as calculated using the Toramaru (2006) model (Fig. 5).

Despite the suggested independence of the initial VND on the decompression rate, an apparent dependence of VND on the onset of the observable vesicle formation was observed. The P_f of the highest logVNDs shifted towards faster decompression rates. While at 5.0 wt % H_2O and 0.064 MPa s^{-1} the highest logVND is measured at a P_f of 50 MPa, P_f decreased to 40 MPa at 0.17 MPa s^{-1} and even to 30 MPa at 1.7 MPa s^{-1} (Table 2). Partially, there is a correlation between the observable onset of vesicle formation in the glass and the vesicle formation in the melt, which is evident when comparing the respective P_{SS} values (see Sect. 5.1.1 "Onset of vesicle formation").

However, the data show an apparent clustering of logVNDs between 4.8 and 5.4 covering all samples at 1.7 MPa s^{-1}, while slower-decompressed samples at 0.17–0.064 MPa s^{-1} range from logVNDs of 4.0 to 5.7. This might be an artifact of the decompression time. With decreasing decompression rate, the decompression time increases significantly. For comparison, decompression from 200 to 70 MPa requires 76 s (1.2 min) at 1.7 MPa s^{-1}, 765 s (13 min) at 0.17 MPa s^{-1}, and 2031 s (34 min) at 0.064 MPa s^{-1}. This longer decompression time at slower rates leads to increased vesicle growth. Thus, the beginning of vesicle formation at the fast decompression rate is not resolvable due to the rapid decompression within a few seconds and subsequent resorption and shrinkage during quenching, as this process may effectively erase already formed vesicles if they are particularly small.

Besides the decompression rate independence in VND, we want to highlight the independence of VND on $c_{H_2O_i}$ prior to decompression, as both H_2O series cover the same range of logVND (Fig. 5). This observation differs slightly from the data of Allabar and Nowak (2018) and Allabar et al. (2020a). They conducted a set of decompression experiments at a constant temperature of 1323 K and a decompression rate of 0.17 MPa s^{-1}, while varying the initial H_2O content. The experimental set from Allabar and Nowak (2018) with a $c_{H_2O_i}$ of 5.3 wt % H_2O was extended to include experiments with higher ($\sim$ 6.3 wt %) and lower $c_{H_2O_i}$ ($\sim$ 3.3 and $\sim$ 4.3 wt %). While our data show a VND independent of $c_{H_2O_i}$, Allabar et al. (2020a) showed a $c_{H_2O_i}$-dependent ($\sim$ 3.3 wt %–6.3 wt %) logVND with minimum numbers of formed vesicles around logVNDs of $\sim$ 5 for $c_{H_2O_i}$ of 5 wt %. They observed that logVND increases significantly towards both lower and higher $c_{H_2O_i}$ values by an order of magnitude.

However, there are some notable features in the dataset from Allabar et al. (2020a). Although the influence of $c_{H_2O_i}$ on logVND is emphasized, some samples with almost identical initial conditions exhibit different VNDs. For example, sample CD83 has a logVND of 5.78, while sample CD42 has a logVND of 4.98, a difference of 0.8 log units. CD83 had a $c_{H_2O_i}$ of 5.46 wt % and was decompressed at 0.17 MPa s^{-1}

to P_f of 80 MPa. CD42 had a c_{H_2Oi} of 5.20 wt % and was decompressed at the same rate to a P_f of 90 MPa. Although c_{H_2Oi} remained almost the same, the sample with the lower P_f (CD83) had a significantly higher VND. This observation aligns with our findings for the LLST samples. Further samples from Allabar et al. (2020a) confirm this trend. Their lowest logVND of 4.60 corresponds to the sample with the highest P_f of 100 MPa. Although this P_f is 20 MPa above the pressure determined here for the onset of vesicle observation, it supports the observation of partial extinction of the smallest vesicles during quenching at early stages of degassing.

However, their observation that c_{H_2Oi} determines the VND of initial phase separation and the evolution of vesiculation during decompression cannot be confirmed for the LLST composition. Still, our observation of the increasing VND towards lower P_f is supported by their experiments with VAD79, albeit not as clearly as with LLST. Nonetheless, an effect of c_{H_2Oi} on the VND for LLST composition cannot be entirely ruled out. Further decompression experiments with significantly different c_{H_2Oi} values would be necessary for such an analysis.

We can state that both Na_2O-rich and K_2O-rich phonolitic melt compositions result in the same decompression-rate-independent vesicle formation process. There is evidence that the enrichment of alkalis, especially in phonolites, allows off-critical spinodal decomposition to occur at crustal pressures (Allabar and Nowak, 2018), whereas spinodal decomposition of critical compositions like hydrous rhyolites would require high pressures of > 1 GPa (Bureau and Keppler, 1999). During further decompression of the system, recurring supersaturation of the melt is prevented by downhill diffusion of H_2O into existing vesicles, as demonstrated by increasing vesicles sizes with decreasing P_f (Fig. 5). This is consistent with our observations of increasing vesicle size with decreasing pressure while the VND remains constant. Hence, off-critical spinodal decomposition could explain the high VNDs in decompressed hydrous silicate melts by enabling the spontaneous phase separation of H_2O without relying on the nucleation process.

6 Conclusion

The experimental results in this study offer critical parameters of the phonolite melt, such as equilibrium H_2O solubility, ΔP_{SS}, VND, and melt porosity, that can improve melt degassing simulations. Our findings show that high VNDs are consistently observed under both H_2O-saturated and H_2O-undersaturated conditions, independent of the decompression rate. During vesiculation, logVND values ranging from 5.1 to 5.7 were recorded, with uniform vesicle sizes across samples, suggesting that degassing is potentially driven by spinodal decomposition rather than by classical nucleation theory. At these high VND levels, near-equilibrium degassing from the melt into adjacent vesicles is expected during decompression. Further decompression experiments at lower final pressures are presented in Marks and Nowak (2025) to trace the subsequent degassing pathway potentially triggering explosive eruptions through rapid vesicle expansion and increased buoyancy or, alternatively, promote effusive behavior through coalescence and the formation of percolation channels.

Appendix A: Experimental setting

In recent decades, optimal experimental conditions – from starting material to sample preparation – have been developed to study H_2O vesicle formation in hydrous silicate melt during decompression. The following outlines the key components of the successful experimental protocol.

Starting material. Previous research has utilized natural porous volcanic rock or glass powders as the starting material for experiments. Adjusting conditions to create H_2O supersaturation during the synthesis of hydrous melt (e.g., Larsen and Gardner, 2004; Gardner and Denis, 2004; Gardner, 2007; Larsen, 2008; Mongrain et al., 2008; Shea et al., 2010; Cichy et al., 2011) can result in the formation of hydration vesicles in the sample volume before decompression (e.g., Gardner et al., 1999; Larsen and Gardner, 2004; Iacono-Marziano et al., 2007). Likewise, even under H_2O-undersaturated conditions, the synthesis process induces the formation of N_2–H_2O vesicles due to entrapped air in the pores of the glass powder used (Preuss et al., 2016), resulting from the very low solubility of N_2 even at high pressures and temperatures (Keppler et al., 2022). These pre-existing fluid vesicles within the melt volume experience growth during subsequent decompression, leading to a reduction in the H_2O content of the melt. Consequently, the supersaturation of the melt, necessary for the formation of new vesicles, may be decreased before extensive homogeneous vesicle formation can occur (Preuss et al., 2016; Allabar and Nowak, 2018; Allabar et al., 2020b). Therefore, for observing homogeneous vesicle formation the initial glass porosity should be below a critical value of ~ 6 vol % (Preuss et al., 2016).

Sample size and decompression time. A crucial factor influencing vesiculation is the decompression timescale, which is determined by factors such as the initial pressure, saturation pressure, decompression rate, and the final pressure (e.g., Mangan and Sisson, 2000; Preuss et al., 2016). The diffusion-controlled loss of volatiles into vesicles, which are nucleated heterogeneously and early at the interface between the capsule and melt, dictates the diameter of the sample necessary to maintain a sufficiently sized unaffected melt volume at the center of the sample (Fig. S1; Preuss et al., 2016; Allabar and Nowak, 2018; Allabar et al., 2020a, b). Additionally, for low-viscosity hydrous melts, the ascent of vesicles formed heterogeneously at the bottom of the capsule into the melt volume imposes a constraint on the available time for decompression (Allabar and Nowak, 2018). These con-

straints necessitate the use of the largest technically feasible sample capsule diameter and length for investigating vesicle formation.

Continuous decompression. In previous studies, vesicle formation has been observed to vary significantly depending on the decompression strategies employed (Nowak et al., 2011; Marxer et al., 2015). Rapid decompression to a final pressure followed by annealing for a specified duration (Larsen and Gardner, 2004; Gardner, 2012), as well as multistep decompression involving high rates of 2.5–10 MPa s^{-1} to the final pressure, followed by periods of isobaric annealing (Gardner et al., 1999; Larsen and Gardner, 2004), do not constitute true continuous decompression of the melt, making it challenging to determine vesicle formation. The assumption of continuous decompression during the annealing period at the final pressure is erroneous. On the other hand, this method can assess nucleation rates in hydrous melts showing vesicle nucleation by rapid decompression and annealing at different times at a constant reduced pressure (Gardner, 2012; Hajimirza et al., 2019). If the phase separation mechanism is unknown, we suggest true continuous decompression achievable through a fine-dosing decompression valve (Nowak et al., 2011; Marxer et al., 2015; Preuss et al., 2016; Allabar and Nowak, 2018).

Quenching rate. To analyze the vesiculation process at different decompression rates and final pressures, the melts have to be quenched to glass as fast as possible. During isobaric cooling of the vesiculated melt, vesicle shrinkage occurs (Allabar et al., 2020a), especially in low-viscosity melts like hydrous phonolitic compositions. This shrinkage is related to the decrease in the molar volume of H_2O (Marxer et al., 2015) and H_2O resorption from the vesicles back into the melt, driven by the increased solubility of H_2O with decreasing temperature (McIntosh et al., 2014). Therefore, to account for vesicle shrinkage and H_2O resorption, the determination of porosities and residual H_2O concentrations in melts requires back-calculation based on the vesiculated glasses. The cooling of decompressed vesiculated melts as rapidly as possible minimizes vesicle shrinkage (Allabar et al., 2020b). However, it is important to note that rapidly quenched glass samples contain tension cracks and therefore tend to shatter during sample preparation. In this study, it was determined that cooling rates of up to ~ 100 K s^{-1} are sufficient to prevent the sample from shattering.

Sample preparation. When preparing decompression samples for analysis, it is crucial to cut them parallel to the cylinder axis. This approach provides the most comprehensive overview and ensures that all important areas of the sample are analyzed (Preuss et al., 2016). Perpendicular sections at different heights may overlook critical regions, especially the initial stages of vesicle formation, which are often visible only in specific sample volumes (top or bottom).

Appendix B

Table B1. Mean value of microprobe analysis of LLST_1a,b/2a,b,c/3a,b,c/4a,b,c,d,e. LLST_G140 is from Harms et al. (2004). Mean crystal composition of eight measurements in sample LLST_12Hg, equilibrated for 24 h at 1123 K. Note that NBO/T represents non-bridging oxygen per tetrahedron.

	LLST_G140		Mean LLST		LLST_12Hg		LLST_12Hg_cry	
	wt %	mol %	wt %	mol %	wt %	mol %	wt %	mol %
SiO_2	58.41	66.89	59.61	67.16	57.51	68.57	0.15	0.20
TiO_2	0.19	0.16	0.20	0.17	0.18	0.16	1.27	1.25
Al_2O_3	23.09	15.58	23.60	15.67	22.33	15.70	5.12	3.95
FeO	1.66	1.59	1.80	1.69	1.03	1.03	78.21	85.60
MnO	0.38	0.37	0.41	0.39	0.31	0.31	6.45	7.15
MgO	0.08	0.14	0.08	0.13	0.07	0.13	0.84	1.64
CaO	0.7	0.86	0.73	0.88	0.70	0.89	0.03	0.04
Na_2O	9.84	10.92	9.60	10.49	8.44	9.76	0.07	0.07
K_2O	4.78	3.49	4.77	3.42	4.53	3.44	0.09	0.09
Total	99.13	100.00	100.79	100.00	95.11	100.00	92.25	100.00
(mol/100 g)	1.45		1.48		1.40		1.27	
Na_2O/K_2O	2.06	3.13	2.01	3.06	1.86	2.84		
$Al_2O_3/(Na_2O + K_2O + CaO)$	1.51	1.02	1.56	1.06	1.63	1.11		
$(Na_2O + K_2O)/(CaO + MgO)$	18.74	14.48	17.80	13.76	16.84	12.94		
NBO	52.415		39.495		−3.812			
NBO/T	0.036		0.027		−0.003			
NBO/T with 5 wt % H_2O	0.442		0.431		0.395			

	Carroll and Blank (1997)	Schmidt et al. (2013)	Larsen and Gardner (2004)	Schmidt and Behrens (2008)	Iacono-Marziano et al. (2007)
SiO_2	59.38	59.55	57.26	59.55	57.15
TiO_2	0.66	0.19	0.24	0.19	0.30
Al_2O_3	18.92	22.41	23.10	22.41	21.34
FeO		1.24	1.63	1.24	2.70
Fe_2O_3	3.85	0.52		0.52	
MnO	0.2	0.35		0.35	0.14
MgO	0.33	0.07	0.10	0.07	0.39
CaO	0.79	0.71	0.66	0.71	3.26
Na_2O	10.07	9.36	11.21	9.36	5.16
K_2O	5.55	4.75	5.72	4.75	9.46
P_2O_5					0.09
Total	99.75	99.15	99.92	99.15	99.90
Na_2O/K_2O	2.76	2.99	2.98	2.99	0.83
$Al_2O_3/(Na_2O + K_2O + CaO)$	0.79	1.03	0.89	1.03	0.87
$(Na_2O + K_2O)/(CaO + MgO)$	9.94	13.99	16.95	13.99	2.71
NBO	73.8	30.2	104.0	30.2	164.8
NBO/T	0.052	0.021	0.074	0.021	0.12

Appendix C: Review of H_2O_m and OH molar absorption coefficients and H_2O solubility

NIR absorption coefficients related to the absorption bands at 5210 cm^{-1} (molecular H_2O) and 4470 cm^{-1} (OH groups) and total H_2O solubilities were determined for the synthesized LLST composition in this study. Although NIR absorption coefficients for phonolite have been previously reported in the literature (Carroll and Blank, 1997; Larsen and Gardner, 2004; Iacono-Marziano et al., 2007; Schmidt and Behrens, 2008; Schmidt et al., 2013; Fanara et al. (2013); Table C1), certain inconsistencies exist that could lead to significant errors in the evaluation of c_{H_2Ot}. The listed authors are referred to in this section as C&B, L&G, IM et al., S&B, S et al., and F et al., respectively.

The initial differences are evident in the bulk glass composition. L&G, S&B and S et al., used glass compositions based on the analyses by Harms et al. (2004), referred to as G140. The compositions show good agreement to G140 (Table B1). Specifically, the comparison of the alkali-alumina ratios results in values of 1.02 for G140, 1.09 for S&B, 1.03 for S et al. and 1.06 for our composition. However, only S et al. synthesized their composition using oxide and carbonate powders, whereas L&G used natural starting material, which contained several hundreds to thousands of ppm of chlorine, fluorine and P_2O_5 (Harms and Schmincke, 2000), potentially influencing H_2O solubility (e.g. Holtz et al., 1993; Webster et al., 1999). Similarly, C&B used natural starting materials from the IIA subunit of the Montaña Blanca pumice deposit (MBP), Tenerife. In addition to minor deviations in the major element composition compared to G140, these samples also contain several hundreds to thousands of ppm of chlorine, fluorine and P_2O_5 (Ablay et al., 1995). F et al. also synthesized their glass composition, which was based on the composition of the ULST, corresponding to a potassium-rich phonolite melt (Wörner and Schmincke, 1984a).

In addition to the glass composition, the synthesis of the hydrated samples might be an important factor. While C&B and L&G conducted the hydration of their samples in cold-seal pressure vessel (CSPV), with the oxygen fugacity typically close to the nickel / nickel oxide buffer (ΔlogNNO $\pm$1, e.g. Matthews et al., 2003; Martel and Schmidt, 2003), the synthesis of the hydrous glasses used for the determination of ε_{H_2Om} and ε_{OH} is not documented by S et al. The authors only state that the linear absorption coefficients of previously synthesized LSP-II glasses with known H_2O contents were determined. However, based on the hydration of glass cylinders for other experiments in their paper using the IHPV (ΔlogQFM + 3.5), it is assumed that the mentioned samples were also hydrated in the IHPV. Only the samples from F et al. were confirmed to have been synthesized in the IHPV under oxidation conditions identical to those in this study.

Another discrepancy may be the baseline correction used for the evaluation of the measured NIR absorption spectra. The choice of baseline correction can significantly affect the relative H_2O species concentrations (Behrens et al., 1996; Ohlhorst et al., 2001). Various baseline corrections are known, each with different advantages and disadvantages depending on the bulk composition. Common baselines include straight lines at the base of the $\sim$ 5200 and $\sim$ 4500 cm^{-1} bands (Withers and Behrens, 1999), two Gaussians fitted to the iron-related band at $\sim$ 5700 cm^{-1} and the molecular H_2O-related band at $\sim$ 4000 cm^{-1} (Ohlhorst et al., 2001), and (as in our determination) fitting a straight line through the high- and low-frequency minima of the $\sim$ 5200 cm^{-1} peak and extending it below the 4500 cm^{-1} peak (Behrens et al., 1996).

S et al. and F et al. applied two straight lines between the high- and low-frequency minima of the $\sim$ 5200 and $\sim$ 4500 cm^{-1} peaks. This implies that the absorption coefficients are not directly comparable due to the different baseline corrections. Nevertheless, assuming hydration in the IHPV, the coefficients could be applied to our samples if the baseline correction used in both studies were applied to our samples.

In contrast, C&B also determined ε_{H_2Om} and ε_{OH} by FTIR spectroscopy but for the MBP composition. Unfortunately, they did not explain how they performed the baseline correction. However, Fig. 1 in their paper shows an applied baseline correction that resembles the baseline correction using "flexicurves" (Schmidt et al., 1999). Both factors could explain why the values of ε_{H_2Om} and ε_{OH} are inverted, with 1.10 and 1.25, respectively, compared to our coefficients of 1.27 and 1.15 L mol^{-1} cm. Despite these discrepancies, both sets of absorption coefficients agree reasonably well, with our self-determined coefficients lying between the published values of S&B and S et al.

Despite the determination of the linear absorbances of the $\sim$ 5200 and $\sim$ 4500 cm^{-1} peaks, c_{H_2Ot} can also be determined in the mid-infrared region by measuring the absorption of the fundamental OH stretching vibration at $\sim$ 3600 cm^{-1} (ε_{3600}), as applied by L&G and S&B. A significant issue with using ε_{3600}, as noted by S&B, is that the fundamental OH stretching vibration has a very high absorption, necessitating extremely thin samples. Consequently, their sample thicknesses ranged from 9.5 to 36.5 µm, which significantly increased the uncertainties. Furthermore, L&G only mentioned in their paper that they did not calibrate their own coefficient but used an ε_{3600} value of 81 L mol^{-1} cm for this peak in the composition, given by a personal communication. Similarly, S&B used an ε_{3600} value of 67 L mol^{-1} cm from Stolper (1982), which is valid for their analyzed glass compositions of albite, rhyolite, and basalt. Additionally, different baseline corrections were used in S&B and Stolper (1982). Nevertheless, the stated c_{H_2Ot} in S&B should be valid, as they were also determined using thermogravimetry.

Additionally, density measurements of H_2O-undersaturated samples containing $\sim$ 1–8 wt % H_2O were performed by S et al., and samples containing 0.5 wt %–5.5 wt % H_2O by F et al. using the Archimedean principle.

Table C1. Absorption coefficients of H_2O and OH combination bands and the fundamental OH stretch vibration, hydration conditions, and starting material of LLST and phonolite samples. C&B refers to Carroll and Blank (1997), S et al. to Schmidt et al. (2013), L&G to Larsen and Gardner (2004), S&B to Schmidt and Behrens (2008), and IM et al. to Iacono-Marziano et al. (2007). LLST and LSP-II refer to natural G140 (Harms et al., 2004). MBP stands for Montaña Blanca pumice deposit, Tenerife. Albite (Al), rhyolite (Rt), and basalt (B) are given in Stolper (1982).

	$\varepsilon_{H_2Om(5210)}$ [L mol^{-1} cm]	$\varepsilon_{OH(4500)}$ [L mol^{-1} cm]	ε_{3600} [L mol^{-1} cm]	Pressure system	Material
This study	1.27 ± 0.04	1.15 ± 0.07		IHPV	synthetic G140
C&B (1997)	$1.10 \pm 0.12/10$	$1.25 \pm 0.33/22$		CSPV	natural MBP
S et al. (2013)	1.322 ± 0.0471	0.922 ± 0.0931		unknown (IHPV?)	synthetic G140
F et al. (2013)	1.18 ± 0.03	0.94 ± 0.05		IHPV	synthetic ULST
Stolper (1982)			67	unknown	natural Al, Rt, B
L&G (2004)			81	CSPV	natural G140
S&B (2008)			Stolper (1982)	IHPV, CSPV	synthetic G140
IM et al. (2007)	1.18 ± 0.11	1.14 ± 0.09		CSPV	natural VAD79

Density equations were derived for the LSP-II composition with $\rho_{\text{LSP-II}} = (2466.7 \pm 8.9) - (18.6 \pm 1.9) \cdot c_{H_2Ot}$ and for the ULST composition as $\rho_{\text{ULST}} = 2512 - 11.4 \cdot c_{H_2Ot}$. No correction is required for the density equation and should therefore be very similar to our density equation $\rho_{\text{LLST}} = (2485 \pm 11) - (21.9 \pm 2.8) \cdot c_{H_2Ot}$ (Eq. 1). Test calculations using the equations of this study and of S et al. for 1 wt %–6 wt % H_2O show perfect agreement at higher concentrations (6 wt %: $\rho_{\text{LLST}} = 2354 \pm 6\,\text{g L}^{-1}$, $\rho_{\text{LSP-II}} = 2355 \pm 3\,\text{g L}^{-1}$), while at lower H_2O concentrations, such as 1 wt %, the density differs within the range of error (1 wt %: $\rho_{\text{LLST}} = 2463 \pm 8\,\text{g L}^{-1}$, $\rho_{\text{LSP-II}} = 2448 \pm 7\,\text{g L}^{-1}$). These slight deviations may be due to slight variations in the melt composition. However, within the range of error, both equations are consistent. Among the equations analyzed, only that proposed by F et al. exhibits a greater deviation, yielding values of 2443.6 and 2500.6 g L^{-1} for 6 wt % and 1 wt %, respectively. This discrepancy likely correlates with stronger variations in bulk composition.

The H_2O solubility equation (Eq. 5) was derived from solubility experiments conducted at 1323 K using the synthetic LLST glass, representing the equilibrium degassing path during decompression. Comparable experimental data are available from S&B for the same G140 composition (Harms et al., 2004) and from IM et al. using natural K-rich phonolite melt from the Vesuvius "white pumice" AD79 eruption (VAD79) (Table B1). The data relevant to our experimental conditions are presented in Fig. C1. From S&B, only three data points are included, specifically those hydrated in the IHPV at 1273 K between 201 and 50 MPa, to enable a direct H_2O solubility comparison at ~ 1300 K. In contrast, IM et al. provided an extensive dataset of H_2O solubility experiments at 1323 K over a pressure range of 250–30 MPa, with experiments conducted in TZM (titanium–zirconium–molybdenum alloy) CSPV. Notably, although not depicted in the diagram, all datasets consistently indicate a negative temperature dependence of H_2O solubility, meaning that lower temperatures result in higher H_2O solubilities (S&B; IM et al.).

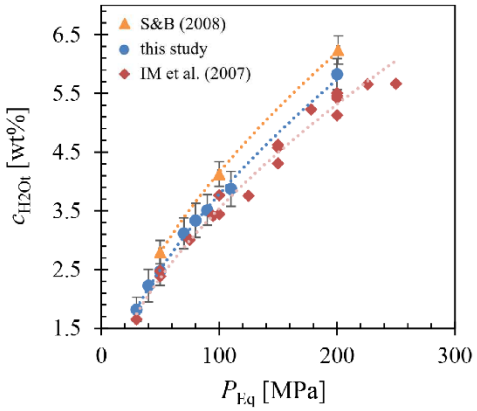

Figure C1. H_2O solubilities corresponding to the G140 composition (Harms et al., 2004) in the IHPV according to Schmidt and Behrens (2008) at 1273 K, this study at 1323 K, and Iacono-Marziano et al. (2007) at 1323 K for the VAD79 composition.

The experiments by S&B utilized glass powder samples. The H_2O content of the glasses was determined by thermogravimetry (TG) using a Setaram™ TGA 92. For samples containing small hydration bubbles, the glass was ground to a fine powder to crack the water-filled vesicles. TG measurements for another MBP composition were verified with KFT measurements, showing good agreement within the error range, expecting similar results with LSP-II. As shown in Fig. C1, the data exhibit slightly increased H_2O solubilities compared to our data. The data differ by ~ 0.5 wt % at 200 MPa, with 6.24 wt % reported by S&B and 5.7 wt % in our dataset. However, this deviation decreases at lower pressures, with a difference of about 0.3 wt % at 50 MPa, where S&B recorded 2.8 wt % and LLST was measured to

2.48 wt %. The slight deviation can be attributed to the small temperature differences of 50 K between S&B at 1273 and 1323 K in this study, as well as differences in absorption coefficients. However, within the scope of the error, the solubilities are in agreement. The solubility equation resulting from the data is given as $c_{H_2Osol(S\&B)} = 0.2931 \cdot P^{0.576}$ [wt %].

Similarly, IM et al. used glass powders and determined the specific absorption coefficients for their melt composition (Tables B1, C1), although they did not detail the baseline correction process. Nevertheless, the H_2O solubility values are in close agreement with those obtained in this study. The data exhibit systematically lower H_2O solubilities, with a slight increase in misfit at higher H_2O solubilities and pressures, reaching up to 0.3 wt % at 200 MPa (5.4 wt %) compared to 5.7 wt % for our LLST composition, but nearly identical values for lower pressures as for 30 MPa with 1.7 wt % at VAD79 compared to 1.8 wt % H_2O for LLST. This discrepancy is within the range of error and could be attributed to differences in starting materials, experimental methods, and absorption coefficients. The solubility equation resulting from the data is given as $c_{H_2Osol(IM)} = 0.2389 \cdot P^{0.5856}$ [wt %].

The well-examined effect of the alkali content and the Na / K ratio may contribute to this discrepancy. The reversed Na / K ratio in VAD79 compared to LLST, specifically the increased K-content and decreased Na-content, led to a decrease in H_2O solubility by approximately 6 % (Schmidt and Behrens, 2008). An additional effect was shown by S&B, where an increase in the $(Na_2O + K_2O)/(CaO + MgO)$ ratio resulted in a roughly 4 % increase in H_2O solubility. A similar effect of alkali content on H_2O solubility was identified in trachytic (Di Matteo et al., 2004) and in rhyolitic melts (Holtz et al., 1995; Allabar et al., 2022), although the effect was more pronounced in those compositions. Therefore, both the reversed Na/K ratio and the significantly higher concentrations of MgO and CaO in the VAD79 composition (Table B1) can explain the slightly lower H_2O solubility values.

Despite these findings, the H_2O solubility curve for the LLST composition in this study falls between the previously published solubility curves. Although there are slight differences in composition, f_{O_2}, and analytical methods, the solubilities agree within an error margin of approximately 0.5 wt %. Therefore, minor experimental deviations do not significantly impact the evaluation of c_{H_2Ot}, and Eq. (5) can be applied in further studies with similar objectives.

Appendix D

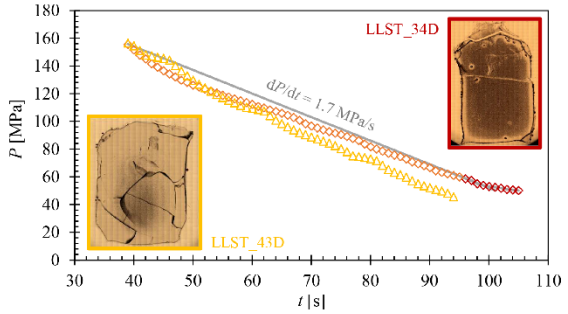

Figure D1. Decompression paths originating from the saturation pressure of ~ 156 MPa are depicted for samples LLST_34D (represented by orange and red diamonds) and LLST_43D (yellow triangles). Additionally, an ideal decompression path of 1.7 MPa s^{-1} is illustrated in gray for comparative analysis. Both samples share similar experimental parameters: c_{H_2Oi} of 5 wt %, P_f of 50 MPa, and quenching rate of 97 K s^{-1}. However, sample 34D experienced a reduction in dP/dt to ~ 0.9 MPa s^{-1} towards the end of decompression, while 43D maintained a constant dP/dt of 1.7 MPa s^{-1}. The variance in dP/dt and the associated longer decompression time caused the complete vesiculation of the sample volume in 34D, while 43D shows the incipient stage of vesicle formation.

Data availability. All data derived from this research are presented in the enclosed tables, figures, and the Supplement.

Supplement. The supplement related to this article is available online at https://doi.org/10.5194/ejm-37-385-2025-supplement.

Author contributions. PLM: conceptualization, sample preparation, experiments, analysis and evaluation, software, visualization, writing of the original draft, organization; MN: conceptualization, supervision, manuscript revision.

Competing interests. The contact author has declared that neither of the authors has any competing interests.

Disclaimer. Publisher's note: Copernicus Publications remains neutral with regard to jurisdictional claims made in the text, published maps, institutional affiliations, or any other geographical representation in this paper. While Copernicus Publications makes every effort to include appropriate place names, the final responsibility lies with the authors.

Special issue statement. This article is part of the special issue "Probing the Earth: experiments on and for our planet". It is a result of the EMPG 2023 conference, Milan, Italy, 12–15 June 2023.

Acknowledgements. We acknowledge the support of the Open Access Publishing Fund of the University of Tübingen. We thank Sebastian Staude for his support during the electron probe microanalysis. We thank Barbara Maier and Annette Flicker for technical support, Simone Schafflick for the high-quality sample preparation and Dennis Eul for support in the laboratory.

Financial support. This research has been supported by the Deutsche Forschungsgemeinschaft (grant no. NO378/15-1).

This open-access publication was funded by the Open Access Publication Fund of the University of Tübingen.

Review statement. This paper was edited by Simone Tumiati and reviewed by Yves Moussallam and one anonymous referee.

References

Ablay, G. J., Ernst, G. G. J., Marti, J., and Sparks, R. S. J.: The ~2 ka subplinian eruption of Montaña Blanca, Tenerife, Bull. Volcanol., 57, 337–355, https://doi.org/10.1007/BF00301292, 1995.

Airy, G. B.: On the Diffraction of an Object-glass with Circular Aperture, Transactions of the Cambridge Philosophical Society, 5, 283–291, 1834.

Allabar, A. and Nowak, M.: Message in a bottle: Spontaneous phase separation of hydrous Vesuvius melt even at low decompression rates, Earth Planet. Sc. Lett., 501, 192–201, https://doi.org/10.1016/j.epsl.2018.08.047, 2018.

Allabar, A. and Nowak, M.: High spatial resolution analysis of H_2O in silicate glass using attenuated total reflection FTIR spectroscopy coupled with a focal plane array detector, Chem. Geol., 556, 119833, https://doi.org/10.1016/j.chemgeo.2020.119833, 2020.

Allabar, A., Dobson, K. J., Bauer, C. C., and Nowak, M.: Vesicle shrinkage in hydrous phonolitic melt during cooling, Contrib. Mineral. Petr., 175, 21, https://doi.org/10.1007/s00410-020-1658-3, 2020a.

Allabar, A., Salis Gross, E., and Nowak, M.: The effect of initial H_2O concentration on decompression-induced phase separation and degassing of hydrous phonolitic melt, Contrib. Miner. Petrol., 175, 22, https://doi.org/10.1007/s00410-020-1659-2, 2020b.

Allabar, A., Petri, P. L., Eul, D., and Nowak, M.: An empirical H2O solubility model for peralkaline rhyolitic melts, Contrib. Mineral. Petr., 177, 52, https://doi.org/10.1007/s00410-022-01915-8, 2022.

Balzer, R., Behrens, H., Waurischk, T., Reinsch, S., Müller, R., Kiefer, P., Deubener, J., and Fechtelkord, M.: Water in alkali aluminosilicate glasses, Front. Mater., 7, 85, https://doi.org/10.3389/fmats.2020.00085, 2020.

Behrens, H., Romano, C., Nowak, M., Holtz, F., and Dingwell, D. B.: Near-infrared spectroscopic determination of water species in glasses of the system MAlSi3O8 (M = Li, Na, K): an interlaboratory study, Chem. Geol., 128, 41–63, https://doi.org/10.1016/0009-2541(95)00162-X, 1996.

Berndt, J., Liebske, C., Holtz, F., Freise, M., Nowak, M., Ziegenbein, D., Hurkuck, W., and Koepke, J.: A combined rapid-quench and H_2-membrane setup for internally heated pressure vessels: Description and application for water solubility in basaltic melts, Am. Mineral., 87, 1717–1726, https://doi.org/10.2138/am-2002-11-1222, 2002.

Blaine, F., Linnen, R., Holtz, F., and Bruegmann, G.: The effect of Cl on Pt solubility in haplobasaltic melt: implications for micronugget formation and evidence for fluid transport of PGEs, Geochim. Cosmochim. Ac., 75, 7792–7805, https://doi.org/10.1016/j.gca.2011.10.010, 2011.

Bondar, D., Zandonà, A., Withers, A.C., Fei, H., Di Genova, D., Miyajima, N., and Katsura, T.: Rapid-quenching of high-pressure depolymerized hydrous silicate (peridotitic) glasses, J. Non-Crystalline Sol., 578, 121347, https://doi.org/10.1016/j.jnoncrysol.2021.121347, 2022.

Brennen, C. E.: Cavitation and Bubble Dynamics, Oxford University Press, Inc., ISBN 0-19-509409-3, 1995.

Bureau, H. and Keppler, H.: Complete miscibility between silicate melts and hydrous fluids in the upper mantle: experimental evidence and geochemical implications, Earth Planet. Sc. Lett., 165, 187–196, https://doi.org/10.1016/S0012-821X(98)00266-0, 1999.

Burnham, C. W. and Davis, N. F.: The role of H_2O in silicate melts, 1: P–V –T relations in the system $NaAlSi_3O_8$–H_2O to 10 kilobars and 1000 °C, Am. J. Sci., 270, 54–79, https://doi.org/10.2475/ajs.270.1.54, 1971.

Cahn, J. W.: Phase separation by spinodal decomposition in isotropic systems, J. Chem. Phys., 42, 93–99, https://doi.org/10.1063/1.1695731, 1965.

Carroll, M. R. and Blank, J. G.: The solubility of H_2O in phonolitic melts, Am. Min., 82, 549–556, https://doi.org/10.2138/am-1997-5-615, 1997.

Cichy, S. B., Botcharnikov, R. E., Holtz, F., and Behrens, H.: Vesiculation and microlite crystallization induced by decompression: a case study of the 1991–1995 Mt Unzen Eruption (Japan), J. Petrol., 52, 1469–1492, https://doi.org/10.1093/petrology/egq072, 2011.

Debenedetti, P. G.: Phase separation by nucleation and by spinodal decomposition: fundamentals, in: Supercritical Fluids, edited by: Kiran, E., Debenedetti, P. G., and Peters, C. J., Nato Science Series E, 366, 123–166, https://doi.org/10.1007/978-94-011-3929-8_5, 2000.

Dubosq, R., Schneider, D. A., Zhou, X., Gault, B., Langelier, B., and Please, P.: Bubbles and atom clusters in rock melts: A chicken and egg problem, J. Volcanol. Geoth. Res., 428, 107574, https://doi.org/10.1016/j.jvolgeores.2022.107574, 2022.

Di Genova, D., Kolzenburg, S., Wiesmaier, S., Dallanave, E., Neuville, D. R., Hess, K. U., and Dingwell, D. B.: A compositional tipping point governing the mobilization and eruption style of rhyolitic magma, Nature, 552, 235–238, https://doi.org/10.1038/nature24488, 2017a.

Di Genova, D., Sicola, S., Romano, C., Vona, A., Fanara, S., and Spina, L.: Effect of iron and nanolites on Raman spec-

tra of volcanic glasses: A reassessment of existing strategies to estimate the water content, Chem. Geol., 475, 76–86, https://doi.org/10.1016/j.chemgeo.2017.10.035, 2017b.

Di Genova, D., Caracciolo, A., and Kolzenburg, S.: Measuring the degree of "nanotilization" of volcanic glasses: Understanding syn-cruptive processes recorded in melt inclusions, Lithos, 318–319, 209–218, https://doi.org/10.1016/j.lithos.2018.08.011, 2018.

Di Genova, D., Brooker, R. A., Mader, H. M., Drewitt, J. W. E., Longo, A., Deubener, J., Neuville, D. R., Fanara, S., Shebanova, O., Anzellini, S., Arzilli, F., Bamber, E. C., Hennet, L., La Spina, G., and Miyajima, N.: In situ observation of nanolite growth in volcanic melt: A driving force for explosive eruptions, Sci. Adv., 6, eabb0413, https://doi.org/10.1126/sciadv.abb0413, 2020.

Di Matteo, V., Carroll, M. R., Behrens, H., Vetere, F., and Brooker, R. A.: Water solubility in trachytic melts, Chem. Geol., 213, 187–196, https://doi.org/10.1016/j.chemgeo.2004.08.042, 2004.

Duan, Z. H. and Zhang, Z. G.: Equation of state of the H_2O, CO_2, and H_2O-CO_2 systems up to 10 GPa and 2573.15 K: molecular dynamics simulations with ab initio potential surface, Geochim. Cosmochim. Ac., 70, 2311–2324, https://doi.org/10.1016/j.gca.2006.02.009, 2006.

Ertel, W., O'Neill, H. S. C., Sylvester, P. J., Dingwell, D. B., and Spettel, B.: The solubility of rhenium in silicate melts: implications for the geochemical properties of rhenium at high temperatures, Geochim. Cosmochim. Ac., 65, 2161–2170, https://doi.org/10.1016/S0016-7037(01)00582-8, 2001.

Fanara, S., Behrens, H., and Zhang, Y.: Water diffusion in potassium-rich phonolitic and trachytic melts, Chem. Geol., 346, 149–161, https://doi.org/10.1016/j.chemgeo.2012.09.030, 2013.

Fiege, A., Holtz, F., and Cichy, S. B.: Bubble formation during decompression of andesitic melts, Am. Mineral., 99, 1052–1062, https://doi.org/10.2138/am.2014.4719, 2014.

Gardner, J. E.: Heterogeneous bubble nucleation in highly viscous silicate melts during instantaneous decompression from high pressure, Chem. Geol., 236, 1–12, https://doi.org/10.1016/j.chemgeo.2006.08.006, 2007.

Gardner, J. E.: Surface tension and bubble nucleation in phonolite magmas, Geochim. Cosmochim. Ac., 76, 93–102, https://doi.org/10.1016/j.gca.2011.10.017, 2012.

Gardner, J. E. and Denis, M.-H.: Heterogeneous bubble nucleation on Fe-Ti oxide crystals in highsilica rhyolitic melts, Geochim. Cosmochim. Ac., 68, 3587–3597, https://doi.org/10.1016/j.gca.2004.02.021, 2004.

Gardner, J. E. and Ketcham, R. A.: Bubble nucleation in rhyolite and dacite melts: temperature dependence of surface tension, Contrib. Miner. Petrol., 162, 929–43, https://doi.org/10.1007/s00410-011-0632-5, 2011.

Gardner, J. E., Hilton, M., and Carroll, M. R.: Experimental constraints on degassing of magma: isothermal bubble growth during continuous decompression from high pressure, Earth Planet. Sc. Lett., 168, 201–218, https://doi.org/10.1016/S0012-821X(99)00051-5, 1999.

Gardner, J. E., Ketcham, R. A., and Moore, G.: Surface tension of hydrous silicate melts: constraints on the impact of melt composition, J. Volcanol. Geoth. Res., 267, 68–74, https://doi.org/10.1016/j.jvolgeores.2013.09.007, 2013.

Gardner, J. E., Wadsworth, F. B., Carley, T. L., Llewellin, E. W., Kusumaatmaja, H., and Sahagian, D.: Bubble Formation in Magma, Annu. Rev. Earth Planet. Sci., 51, 131–154. https://doi.org/10.1146/annurev-earth-031621-080308, 2023.

Giordano, D., Potuzak, M., Romano, C., Dingwell, D. B., and Nowak, M.: Viscosity and glass transition temperature of hydrous melts in the system $CaAl_2Si_2O_8$-$CaMgSi_2O_6$, Chem. Geol., 256, 203–215, https://doi.org/10.1016/j.chemgeo.2008.06.027, 2008.

Gondé, C., Martel, C., Pichavant, M., and Bureau, H.: In situ bubble vesiculation in silicic magmas, Am. Mineral., 96, 111–124, https://doi.org/10.2138/am.2011.3546, 2011.

Gonnermann, H. M. and Gardner, J. E.: Homogeneous bubble nucleation in rhyolitic melt: experiments and nonclassical theory, Geochem. Geophys. Geosyst., 14, 4758–4773, https://doi.org/10.1002/ggge.20281, 2013.

Hajimirza, S., Gonnermann, H. M., Gardner, J. E., and Giachetti, T.: Predicting homogeneous bubble nucleation in rhyolite, J. Geophys. Res.-Sol. Ea., 124, 2395–2416, https://doi.org/10.1029/2018JB015891, 2019.

Hajimirza, S., Gardner, J. E., and Gonnermann, H. M.: Experimental demonstration of continuous bubble nucleation in rhyolite, J. Volcanol. Geoth. Res., 421, 107417, https://doi.org/10.1016/j.jvolgeores.2021.107417, 2021.

Hamada, M., Laporte, D., Cluzel, N., Koga, K. T., and Kawamoto, T.: Simulating bubble number density of rhyolitic pumices from Plinian eruptions: constraints from fast decompression experiments, Bull. Volcanol., 72, 735–746, https://doi.org/10.1007/s00445-010-0353-z, 2010.

Harms, E. and Schmincke, H. U.: Volatile composition of the phonolitic Laacher See magma (12,900 yr BP): implications for syn-eruptive degassing of S, F, Cl and H_2O, Contrib. Miner. Petrol., 138, 84–98, https://doi.org/10.1007/PL00007665, 2000.

Harms, E., Gardner, J. E., and Schmincke, H. U.: Phase equilibria of the Lower Laacher See Tephra (East Eifel, Germany): constraints on pre-eruptive storage conditions of a phonolitic magma reservoir, J. Volcanol. Geoth. Res., 134, 135–148, https://doi.org/10.1016/j.jvolgeores.2004.01.009, 2004.

Hertz, P.: Über den gegenseitigen durchschnittlichen Abstand von Punkten, die mit bekannter mittlerer Dichte im Raume angeordnet sind, Math. Ann., 67, 387–398, https://doi.org/10.1007/BF01450410, 1908.

Higgins, M. D.: Measurement of crystal size distributions, Am. Mineral., 85, 1105–1116, https://doi.org/10.2138/am-2000-8-901, 2000.

Holasek, R. E., Self, S., and Woods, A. W.: Satellite observations and interpretation of the 1991 Mount Pinatubo eruption plumes, J. Geophys. Res., 101, 27635–27655, https://doi.org/10.1029/96JB01179, 1996.

Holtz, F., Dingwell, D. B., and Behrens, H.: Effects of F, B_2O_3 and P_2O_5 on the solubility of water in haplogranite melts compared to natural silicate melts, Contrib. Miner. Petrol., 113, 492–501, https://doi.org/10.1007/BF00698318, 1993.

Holtz, F., Behrens, H., Dingwell, D. B., and Johannes, W.: H_2O solubility in haplogranitic melts: Compositional, pressure, and temperature dependence, Am. Mineral., 80, 94–108, https://doi.org/10.2138/am-1995-1-210, 1995.

Hurwitz, S. and Navon, O.: Bubble nucleation in rhyolitic melts: experiments at high pressure, temperature, and water content, Earth Planet. Sc. Lett., 122, 267–80, https://doi.org/10.1016/0012-821X(94)90001-9, 1994.

Iacono-Marziano, G., Schmidt, B. C., and Dolfi, D.: Equilibrium and disequilibrium degassing of a phonolitic melt (Vesuvius AD 79 "white pumice") simulated by decompression experiments, J. Volcanol. Geoth. Res., 161, 151–164, https://doi.org/10.1016/j.jvolgeores.2006.12.001, 2007.

Keppler, H., Cialdella, L., Couffignal, F., and Wiedenbeck, M.: The solubility of N_2 in silicate melts and nitrogen partitioning between upper mantle minerals and basalt, Contrib. Miner. Petrol., 177, 83, https://doi.org/10.1007/s00410-022-01948-z, 2022.

Larsen, J. F.: Heterogeneous bubble nucleation and disequilibrium H_2O exsolution in Vesuvius K-phonolite melts, J. Volcanol. Geoth. Res., 175, 278–288, https://doi.org/10.1016/j.jvolgeores.2008.03.015, 2008.

Larsen, J. F. and Gardner, J. E.: Experimental study of water degassing from phonolitic melts: implications for volatile oversaturation during magmatic ascent, J. Volcanol. Geoth. Res., 134, 109–124, https://doi.org/10.1016/j.jvolgeores.2004.01.004, 2004.

Le Gall, N. and Pichavant, M.: Homogeneous bubble nucleation in H_2O- and H_2O-CO_2-bearing basaltic melts: results of high temperature decompression experiments, J. Volcanol. Geoth. Res., 327, 604–621, https://doi.org/10.1016/j.jvolgeores.2016.10.004, 2016.

Lorand, J.-P., Alard, O., and Luguet, A.: Platinum-group element micronuggets and refertilization process in Lherz orogenic peridotite (northeastern Pyrenees, France), Earth Planet. Sc. Lett., 289, 298–310, https://doi.org/10.1016/j.epsl.2009.11.017, 2010.

Mallmann, G. and O'Neill, H. S. C.: The effect of oxygen fugacity on the partitioning of Re between crystals and silicate melt during mantle melting, Geochim. Cosmochim. Ac., 71, 2837–2857, https://doi.org/10.1016/j.gca.2007.03.028, 2007.

Mangan, M. and Sisson, T.: Delayed, disequilibrium degassing in rhyolite magma: decompression experiments and implications for explosive volcanism, Earth Planet. Sc. Lett., 183, 441–455, https://doi.org/10.1016/S0012-821X(00)00299-5, 2000.

Marks, P. L. and Nowak, M.: Vesiculation dynamics – Part 2: Decompression-induced H_2O vesicle growth, onset, and progression of coalescence, Eur. J. Mineral., 37, 413–435, https://doi.org/10.5194/ejm-37-413-2025, 2025.

Martel, C. and Schmidt, B. C.: Decompression experiments as an insight into ascent rates of silicic magmas, Contrib. Miner. Petrol., 144, 397–415, https://doi.org/10.1007/s00410-002-0404-3, 2003.

Marxer, H., Bellucci, P., and Nowak, M.: Degassing of H_2O in a phonolitic melt: A closer look at decompression experiments, J. Volcanol. Geoth. Res., 297, 109–124, https://doi.org/10.1016/j.jvolgeores.2014.11.017, 2015.

Matthews, W., Linnen, R. L., and Guo, Q.: A filler-rod technique for controlling redox conditions in cold-seal-pressure vessels, Am. Mineral., 88, 701–707, https://doi.org/10.2138/am-2003-0424, 2003.

McCormick, M. P., Thomason, L. W., and Trepte, C. R.: Atmospheric effects of the Mt. Pinatubo 1991 eruption, Nature, 373, 399–404, https://doi.org/10.1038/373399a0, 1995.

McIntosh, I. M., Llewellin, E. W., Humphreys, M. C. S., Nichols, A. R. L., Burgisser, A., Schipper, C. I., and Larsen, J. F.: Distribution of dissolved water in magmatic glass records growth and resorption of bubbles, Earth Planet. Sc. Lett., 401, 1–11, https://doi.org/10.1016/j.epsl.2014.05.037, 2014.

Mongrain, J., Larsen, J. F., and King, P. L.: Rapid water exsolution, degassing, and bubble collapse observed experimentally in K-phonolitic melts, J. Volcanol. Geoth. Res., 173, 178–184, https://doi.org/10.1016/j.jvolgeores.2008.01.026, 2008.

Morgan, G. and London, D.: Effect of current density on the electron microprobe analysis of alkali aluminosilicate glasses, Am. Mineral., 90, 1131–1138, https://doi.org/10.2138/am.2005.1769, 2005.

Mourtada-Bonnefoi, C. C. and Laporte, D.: Experimental study of homogeneous bubble nucleation in rhyolitic magmas, Geophys. Res. Lett., 26, 3505–3508, https://doi.org/10.1029/1999gl008368, 1999.

Mourtada-Bonnefoi, C. C. and Laporte, D.: Homogeneous bubble nucleation in rhyolitic magmas: an experimental study of the effect of H_2O and CO_2, J. Geophys. Res., 107, 2066, https://doi.org/10.1029/2001JB000290, 2002.

Mujin, M., Nakamura, M., and Miyake, A.: Eruption style and crystal distributions: Crystallization of groundmass nanolites in the 2011 Shinmoedake eruption. Am. Mineral., 102, 2367–2380, https://doi.org/10.2138/am-2017-6052CCBYNCND, 2017.

Murphy, M. D., Sparks, R. S. J., Barkley, J., Carroll, M. R., and Brewer, T. S.: Remobilization of andesite magma by intrusion of mafic magma at the Soufriere Hills Volcano, Montserrat, West Indies, J. Petrol., 41, 21–42, https://doi.org/10.1093/petrology/41.1.21, 2000.

Navon, O. and Lyakhovsky, V.: Vesiculation processes in silicic magmas, in: The Physics of Explosive Volcanic Eruptions, edited by: Gilbert, J. S. and Sparks, R. S. J., Geological Society, London, Special Publications, 145, 27–50, ISBN 1-86239-020-7, 1998.

Nowak, M. and Behrens, H.: An experimental investigation on diffusion of water in haplogranitic melts, Contrib. Miner. Petrol., 126, 365–376, https://doi.org/10.1007/s004100050256, 1997.

Nowak, M., Cichy, S. B., Botcharnikov, R. E., Walker, N., and Hurkuck, W.: A new type of high pressure low-flow metering valve for continuous decompression: First 86 experimental results on degassing of rhyodacitic melts, Am. Mineral., 96, 1373–1380, https://doi.org/10.2138/am.2011.3786, 2011.

Ochs, F. A. and Lange, A. R.: The density of hydrous magmatic liquids, Science, 283, 1314–1317, https://doi.org/10.1126/science.283.5406.1314, 1999.

Ohlhorst, S., Behrens, H., and Holtz, F.: Compositional dependence of molar absorptivities of near-infrared OH^- and H_2O bands in rhyolitic to basaltic glasses, Chem. Geol., 174, 5–20, https://doi.org/10.1016/S0009-2541(00)00303-X, 2001.

Preuss, O., Marxer, H., Ulmer, S., Wolf, J., and Nowak, M.: Degassing of hydrous trachytic Campi Flegrei and phonolitic Vesuvius melts: Experimental limitations and chances to study homogeneous bubble nucleation, Am. Mineral., 101, 859–875, https://doi.org/10.2138/am-2016-5480, 2016.

Reinig, F., Wacker, L., Jöris, O., Oppenheimer, C., Guidobaldi, G., Nievergelt, D., Adolphi, F., Cherubini, P., Engels, S., Esper, J., Land, A., Lane, C., Pfanz, H., Remmele, S., Sigl, M., Sookdeo, A., and Büntgen, U.: Precise date for the Laacher See eruption synchronizes the Younger Dryas, Nature, 595, 66–69, https://doi.org/10.1038/s41586-021-03608-x, 2021.

Sahagian, D. and Carley, T. L.: Explosive volcanic eruptions and spinodal decomposition: A different approach to deciphering

the tiny bubble paradox, Geochem. Geophys. Geosys., 21, 1–9, https://doi.org/10.1029/2019GC008898, 2020.

Scarani, A., Zandonà, A., Di Fiore, F., Valdivia, P., Putra, R., Miyajima, N., Bornhöft, H., Vona, A., Deubener, J., Romano, C., and Di Genova, D.: A chemical threshold controls nanocrystallization and degassing behaviour in basalt magmas, Commun. Earth Environ., 3, 284, https://doi.org/10.1038/s43247-022-00615-2, 2022.

Schmidt, B. C. and Behrens, H.: Water solubility in phonolite melts: Influence of melt composition and temperature, Chem. Geol., 256, 259–268, https://doi.org/10.1016/j.chemgeo.2008.06.043, 2008.

Schmidt, B. C., Holtz, F., and Pichavant, M.: Water solubility in haplogranitic melts coexisting with H_2O-H_2 fluids, Contrib. Miner. Petrol., 136, 213–224, https://doi.org/10.1007/s004100050533, 1999.

Schmidt, B. C., Blum-Oeste, N., and Flagmeier, J.: Water diffusion in phonolite melts, Geochim. Cosmochim. Ac., 107, 220–230, https://doi.org/10.1016/j.gca.2012.12.044, 2013.

Schmincke, H. U., Park, C., and Harms, E.: Evolution and environmental impacts of the eruption of Laacher See Volcano (Germany) 12,900 a BP, Quaternary Int., 61, 61–72, https://doi.org/10.1016/S1040-6182(99)00017-8, 1999.

Shea, T.: Bubble nucleation in magmas: a dominantly heterogeneous process?, J. Volcanol. Geoth. Res., 343, 155–170, https://doi.org/10.1016/j.jvolgeores.2017.06.025, 2017.

Shea, T., Gurioli, L., Larsen, J. F., Houghton, B. F., Hammer, J. E., and Cashman, K. V.: Linking experimental and natural vesicle textures in Vesuvius 79AD white pumice, J. Volcanol. Geoth. Res., 192, 69–84, https://doi.org/10.1016/j.jvolgeores.2010.02.013, 2010.

Stelling, J., Botcharnikov, R. E., Beermann, O., and Nowak, M.: Solubility of H_2O- and chlorine-bearing fluids in basaltic melt of Mount Etna at $T = 1050$–$1250\,°C$ and $P = 200\,MPa$, Chem. Geol., 256, 102–110, https://doi.org/10.1016/j.chemgeo.2008.04.009, 2008.

Stolper, E.: Water in silicate glasses: an infrared spectroscopic study, Contrib. Miner. Petrol., 81, 1–17, https://doi.org/10.1007/BF00371154, 1982.

Tomlinson, E. L., Smith, V. C., and Menzies, M. A.: Chemical zoning and open system processes in the Laacher See magmatic system, Contrib. Miner. Petrol., 175, 19, https://doi.org/10.1007/s00410-020-1657-4, 2020.

Toramaru, A.: BND (bubble number density) decompression rate meter for explosive volcanic eruptions, J. Volcanol. Geoth. Res., 154, 303–316, https://doi.org/10.1016/j.jvolgeores.2006.03.027, 2006.

Van den Bogaard, P. and Schmincke, H. U.: The Eruptive Center of the Late Quaternary Laacher See Tephra, Geologische Rundschau, 73, 933–980, https://doi.org/10.1007/BF01820883, 1984.

Van den Bogaard, P. and Schmincke, H. U.: Laacher See Tephra: A widespread isochronous late Quaternary tephra layer in Central and Northern Europe, Geol. Soc. Am. Bull., 96, 1554–1571, https://doi.org/10.1130/0016-7606(1985)96<1554:LSTAWI>2.0.CO;2, 1985.

Webster, J. D., Kinzler, R. J., and Mathez, E. A.: Chloride and water solubility in basalt and andesite melts and implications for magmatic degassing, Geochim. Cosmochim. Ac., 63, 729–738, 1999.

Withers, A. C. and Behrens, H.: Temperature induced changes in the NIR spectra of hydrous albitic and rhyolitic glasses between 300 and 100 K, Phys. Chem. Mineral., 27, 119–132, https://doi.org/10.1007/s002690050248, 1999.

Wörner, G. and Schmincke, H. U.: Mineralogical and chemical zonation of the Laacher see tephra sequence, J. Petrol., 25, 805–835, https://doi.org/10.1093/petrology/25.4.805, 1984a.

Wörner, G. and Schmincke, H. U.: Petrogenesis of the zoned Laacher See Tephra, J. Petrol. 25, 836–851, https://doi.org/10.1093/petrology/25.4.836, 1984b.

Zhang, Y., Xu, Z., and Behrens, H.: Hydrous species geospeedometer in rhyolite: Improved calibration and application, Geochim. Cosmochim. Ac., 64, 3347–3355, https://doi.org/10.1016/S0016-7037(00)00424-5, 2000.

Manuscript Study II

Titel: Vesiculation dynamics – Part 2: Decompression-induced H_2O vesicle growth, onset, and progression of coalescence

Authors: Patricia Louisa Marks and Marcus Nowak

Published online on July 04, 2025, in European Journal of Mineralogy; special issue: Probing the Earth: experiments on and for our planet, 37, 413–435, https://doi.org/10.5194/ejm-37-413-2025.

Eur. J. Mineral., 37, 413–435, 2025
https://doi.org/10.5194/ejm-37-413-2025

European Journal of Mineralogy
Open Access

Vesiculation dynamics – Part 2: Decompression-induced H_2O vesicle growth, onset, and progression of coalescence

Patricia Louisa Marks and Marcus Nowak

Department of Geosciences, Eberhard Karls University of Tübingen, Tübingen 72074, Germany

Correspondence: Patricia Louisa Marks (patricia.marks@uni-tuebingen.de)

Received: 29 October 2024 – Revised: 31 March 2025 – Accepted: 4 April 2025 – Published: 4 July 2025

Abstract. Supersaturation of H_2O during magma ascent can drive efficient degassing through the formation of fluid vesicles within phonolitic melt, with high vesicle number densities (VNDs) ranging from a logVND of 4 to 6 mm^{-3}. Rapid vesicle formation and growth reduces magma density and may significantly influence eruption style. However, the behavior of vesicle-bearing melt under continued decompression remains poorly understood. This study aims to investigate vesicle growth as well as the onset and progression of vesicle coalescence during decompression in the well-characterized phonolitic Lower Laacher See melt.

Synthetic phonolite melts were hydrated in an internally heated gas pressure vessel at 200 MPa with 5.7 wt % or 5.0 wt % H_2O, establishing conditions of saturation and slight undersaturation prior to decompression. The hydrated melts were continuously decompressed at a superliquidus temperature of 1323 K with rates ranging from 0.064 to 1.7 MPa s^{-1}, reaching final pressures between 70 and 30 MPa before being rapidly quenched to vesiculated glass.

As expected, our results indicate that the pressure range for uniform vesicle formation differs between initially H_2O saturated and undersaturated melts, with coalescence starting at higher pressures in saturated melts. The onset of coalescence is also influenced by the decompression rate, occurring at higher pressures with slower decompression rates. The coalescence process transforms the quenched opaque samples with maximum VND, characterized by nebula of small vesicles sized between 2 and 16 µm into transparent samples with larger vesicles ranging from 37 µm up to ~ 500 µm and VNDs reduced by orders of magnitude, depending on decompression rate, final pressure, and initial H_2O concentration. The sizes of these coalesced vesicles are inversely related to the decompression rate, with larger vesicle sizes occurring at slower decompression rates.

While the maximum logVNDs of initially formed vesicle volumes remain constant across different decompression rates, with high values of 5.1 to 5.7, compatible with the theory of spinodal decomposition, the logVNDs of sample volumes with coalesced vesicles drop markedly by 1.2 to 4.1 log units. The lowest logVNDs, between 0.5 and 0.8, occur at the slowest decompression rate of 0.064 MPa s^{-1}, while the highest logVNDs, between 3.1 and 3.7, are observed at the fastest decompression rate of 1.7 MPa s^{-1}. This coalescence driven pattern mimics the expected decompression rate dependence of initial VND in cases of vesicle nucleation.

These experimental results suggest that significant vesicle coalescence can occur in phonolitic magmas even at relatively fast ascent rates, influencing eruption dynamics. In the case of open-system outgassing, vesicle coalescence creates channel structures with high permeability, allowing fluid to percolate and escape at the top of the magma column. In contrast, in a closed system, vesicles can accumulate as foam with closed porosity at the top of the magma chamber, forming large, gas-pressurized pockets. This buildup may lead to significant disruptions and violent, explosive eruptions. During volcanic activity, transitions between these two systems may occur.

Published by Copernicus Publications on behalf of the European mineralogical societies DMG, SEM, SIMP & SFMC.

1 Introduction

Explosive volcanic eruptions are mainly driven by the rapid vesiculation of supersaturated hydrous melts, primarily releasing H_2O from the melt into fluid vesicles before and during the magma fragmentation process (e.g., Gonnermann and Manga, 2007). As magma ascends, the solubility of volatiles, such as H_2O, decreases with the reduction in pressure. The formation and growth of vesicles in the silicate melt, caused by decompression-induced supersaturation, are crucial for determining the eruption style (e.g., Sparks, 1978; Hurwitz and Navon, 1994; Mourtada-Bonnefoi and Laporte, 2004; Iacono-Marziano et al., 2007; Hamada et al., 2010; Gardner and Ketcham, 2011; Preuss et al., 2016; Shea, 2017; Hajimirza et al., 2019). The vesicle number density (VND), which is the number of vesicles per unit volume of vesicle free melt, determines the distance between vesicles and affects the efficiency of melt degassing (e.g., Cashman and Mangan, 1994; Gardner et al., 1999; Toramaru, 2006; Gonnermann and Manga, 2007; Iacono-Marziano et al., 2007; Allabar and Nowak, 2018). As magma vesiculates and ascends, its total density decreases rapidly, which facilitates sudden volatile expansion and fragmentation (e.g., Kueppers et al., 2006; Genareau et al., 2012).

Despite the potential for high melt porosity at ambient pressure, several volcanic products exhibit lower porosities than expected by the pre-eruptive volatile content, indicating that significant outgassing from the magma is facilitated by vesicle coalescence and percolation (Jaupart and Allègre, 1991; Gardner et al., 1996; Giachetti et al., 2019). The coalescence process is essential for the development of the permeability of vesiculated melts and the dynamics of volcanic eruptions. In a simplistic view, it determines whether eruptions are explosive, when volatiles are retained in the magma, or effusive, when volatiles escape during ascent (Eichelberger et al., 1986; Jaupart, 1998). As vesiculation within the magma continues to increase, the growing network of interconnected vesicles may reach a percolation threshold that enables permeability, allowing fluid to flow through the porous structure (Klug and Cashman, 1996; Sahimi, 1994; Saar and Manga, 1999). The relationship between porosity and permeability, essential for understanding magma degassing and eruption dynamics, depends on the VND, as well as sizes, shapes, and connectivity of vesicles (Saar and Manga, 1999; Blower et al., 2001; Gardner et al., 2006; Gonnermann and Manga, 2007).

Understanding how vesicle numbers and size distributions evolve in silicate melts is of critical importance in understanding eruption behavior and in interpreting pumice and lava textures (Mangan et al., 1993; Cashman et al., 1994; Cashman and Mangan, 1994; Klug and Cashman, 1994, 1996). After vesicle formation and initial growth, Ostwald ripening and vesicle coalescence become the key processes that significantly influence vesicle size distributions in silicate melts. Ostwald ripening involves the diffusive exchange of volatiles between vesicles of different sizes, driven by differences in internal pressure (DeVries, 1958; Sahagian et al., 1989; Proussevitch et al., 1993; Cashman and Mangan, 1994). Vesicle coalescence occurs when the melt film between two adjacent vesicles thins to a critical thickness, leading to rupture and relaxation (Cashman and Mangan, 1994; Klug and Cashman, 1996; Navon and Lyakhovsky, 1998). These processes have been estimated and studied in various melt compositions like basaltic, rhyolitic and phonolitic melts (Sahagian et al., 1989; Proussevitch et al., 1993; Klug and Cashman, 1996; Larsen et al., 2004). Vesicle coalescence rates are influenced by factors such as the approach of neighboring vesicles (Fortelny et al., 1999), the thinning of the melt film to a critical thickness that separates vesicles, the subsequent rupture of this film, and vesicle shape relaxation processes (Cashman and Mangan, 1994; Klug and Cashman, 1996; Navon and Lyakhovsky, 1998). Previous studies have investigated the determination of the critical film thickness in various silicate melts (Proussevitch et al., 1993; Klug and Cashman, 1996) and attempted to estimate the timescales required for film rupture once this critical thickness is attained (Toramaru, 1988; Sahagian et al., 1989; Proussevitch et al., 1993; Klug and Cashman, 1996; Herd and Pinkerton, 1997; Navon and Lyakhovsky, 1998). These estimates typically range from 1 to 10^4 s, contingent upon factors such as melt viscosity, vesicle dimensions, and the critical film thickness (Klug and Cashman, 1996). Coalescence behavior differs depending on whether the vesicle emulsion or foam is "static", maintaining constant external pressure, or "expanding", where vesicles grow during decompression of the melt (Candela, 1991; Navon and Lyakhovsky, 1998). Vesicle coalescence rates can vary significantly between these two scenarios (Barclay et al., 1995; Navon and Lyakhovsky, 1998).

The purpose of this study is to investigate the vesicle coalescence behavior of a phonolite melt during continuous decompression. The phonolite melt is representative of the composition of the Lower Laacher See (Harms et al., 2004). This study complements an existing dataset on vesicle formation in the same phonolite composition under identical decompression rates and experimental conditions (companion paper Part 1; Marks and Nowak, 2025). Therefore, both papers are closely related and provide fundamental data on vesicle formation processes and subsequent coalescence behavior.

2 Experimental and analytical techniques

2.1 Starting material

Synthesized Lower Laacher See Tephra (LLST) glasses were used from a previous synthesis from the study of Marks and Nowak (2025). For the decompression experiments, glass cylinders of 5 mm in diameter and 5.8–7.4 mm in length were placed into Au80Pd20 capsules, with an outer diameter of 5.4 mm and an inner diameter of 5.0 mm. We ensured that

the capsule volume was sufficiently large to accommodate the melt with equilibrium porosity (Φ_{eq}) without rupturing during decompression to low final pressures (P_f). To determine the expected Φ_{eq} at each P_f, the porosity equation from Gardner et al. (1999) was employed. Calculations considered the glass cylinder lengths, H_2O solubility from Marks and Nowak (2025), the hydrous melt density calculations from Ochs and Lange (1999), and the H_2O equation of state (EOS) from Duan and Zhang (2006). These calculations were then used to determine the necessary capsule lengths. Two experimental series were performed, with initial conditions being either saturated or slightly undersaturated, achieved by adding 5.7 wt % or 5.0 wt % H_2O (c_{H_2Oi}) to the capsule, respectively. The top of each capsule was crimped into a trident star and sealed by welding while being cooled with liquid nitrogen to prevent H_2O loss through vaporization. To check for leakage, the capsules were heated in a compartment dryer at 383 K for at least 1 h, pressurized to 200 MPa at ambient temperature in a cold-seal pressure vessel, and reheated to 383 K, with weighing after each step to confirm their integrity.

2.2 Decompression experiments

Combined hydration and decompression experiments were performed using an internally heated argon pressure vessel (IHPV) (Marks and Nowak, 2025). The melts were hydrated at 200 MPa and 1523 K for 96 h. After hydration, the temperature was isobarically reduced at a rate of 10 K min^{-1} to 1323 K, where the samples were thermally equilibrated for 30 min. The hydrous melts were then isothermally decompressed at rates of 1.7, 0.17, and 0.064 MPa s^{-1} to P_f values of 70, 60, 50, 40, and 30 MPa. Upon reaching P_f, the samples were directly quenched isobarically at rates of 150 K s^{-1} (Berndt et al., 2002) or 97 K s^{-1} (Marks and Nowak, 2025) to room temperature. The minimum recorded pressure (P_{min}) is also listed alongside the desired P_f (Table 1). One additional sample (LLST_41D) was isothermally held at P_f for about 20 s and was then quenched at 16 K s^{-1} by turning off the furnace (Allabar et al., 2020b).

The quenched capsules were reweighed to confirm they remained sealed. For subsequent sample analysis, the capsules were prepared as described in Marks and Nowak (2025).

2.3 Analytical methods

The samples were analyzed for residual H_2O concentration in glass (c_{H_2Ot}) using Fourier transform infrared (FTIR) spectroscopy, while vesicle parameters, including vesicle number and size, were quantified through quantitative image analysis (CSDcorrections) and transmission light microscopy (TLM). All measurements were conducted under the same conditions as described in Marks and Nowak (2025).

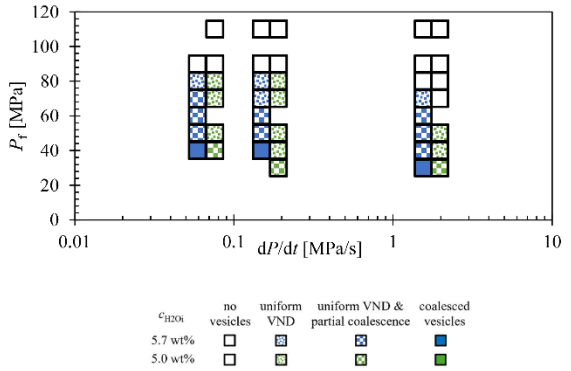

Figure 1. Onset of uniform vesicle observation, partial coalescence, and complete coalescence in decompression samples (data from Marks and Nowak, 2025, are included). Coalescence depends on c_{H_2Oi}, P_f, and on the decompression rate. Open symbols represent samples where no vesicles formed during decompression. Dotted symbols show samples with homogeneous vesicle formation at P_f, while filled square symbols represent samples with both coalesced volumes and pristine vesiculated volumes. Filled symbols indicate samples containing only coalesced vesicles.

3 Results

3.1 Vesicle textures

This study examines the transition from initial vesicle formation to subsequent vesicle growth and the onset of vesicle coalescence during decompression. Textural features and their corresponding conditions are presented in Figs. 1, 2, and 3, incorporating part of the data on initial vesicle formation from Marks and Nowak (2025) to provide a comprehensive overview of both studies. An all-encompassing set of sample images is provided in the Supplement.

The supersaturation pressure (P_{SS}) required for the formation of uniform vesicles depends on c_{H_2Oi} and on the decompression rate (Fig. 1; Marks and Nowak, 2025). In the decompression series (Fig. 2), vesicles are observed within each sample, with P_f ranging from 70 to 30 MPa. The stage of maximal vesiculation in the samples is characterized by a high VND with uniform vesicles sizes, appearing as a milky white opacity in reflection mode under the optical microscope for the embedded sample halves, and as opaque dark areas in thin sections imaged in transmission mode. Decompression samples with P_f lower than that of the maximum vesiculation stage appear transparent with a brownish color in optical microscope images and are characterized by a significantly lower VND. The red colored vesicles in the thin sections are large vesicles that were cut during the preparation process and subsequently filled with glue and epoxy resin (Fig. 2, e.g., 48D, 38D; Fig. S1). As P_f decreases, the proportion of strongly vesiculated volumes declines, while vesicle coalescence progresses. Coalesced vesicles are gen-

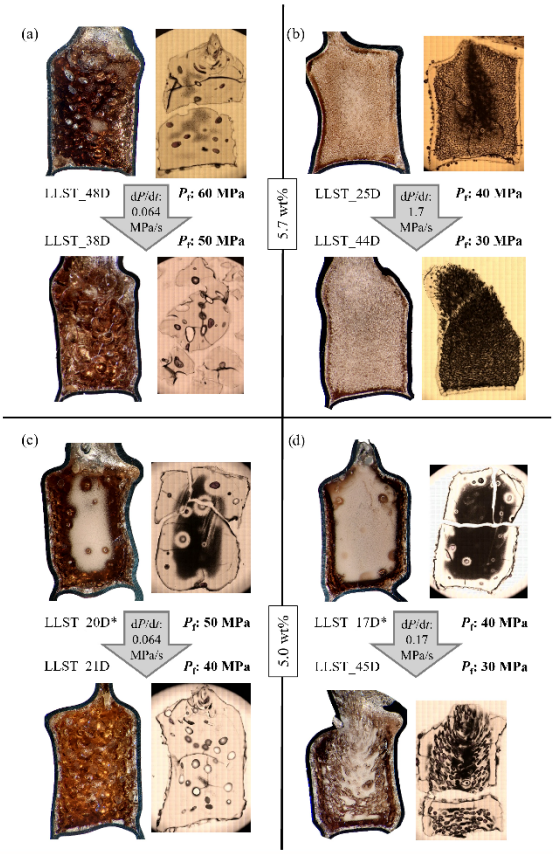

Figure 2. Coalescence behavior of the phonolitic melt during decompression. Hydrous melts with initially ~ 5.7 wt % or 5.0 wt % H_2O were decompressed from 200 MPa with 0.064, 0.17, or 1.7 MPa s^{-1} to P_f of 60, 50, 40, and 30 MPa. Left image of each sample shows the in epoxy embedded sample half, and the right image shows the thin section of ~ 200 µm thickness. Each sample had an original diameter of 5 mm. Samples from Marks and Nowak (2025) are marked with *.

erally characterized by an increased vesicle size and significantly decreased logVNDs. A logVND range of 4 to 5.7 indicates homogeneously distributed small vesicles formed during the initial homogeneous vesicle formation process, while at lower P_f values logVNDs between 3.7 and 0.5 indicate coalesced vesicles (Fig. 3). The logVND values correlate with measured vesicle sizes. High logVNDs correspond to small vesicles sizes, ranging from 2 to 16 µm, depending on the decompression rate, P_f, and c_{H_2Oi}. The onset of coalescence is indicated by increased vesicle sizes, starting at 37 µm and increasing up to ~ 500 µm (Fig. 3, Table 1). The glass porosities correlate with the increasing logVND and vesicle sizes. The glass porosities in Fig. 3 are plotted separately, presenting individual values for both initial uniform vesicles and coalesced vesicles within the same sample. The glass porosity increases with continuing coalescence and P_f.

3.2 Decompression rates

To further analyze the coalescence behavior, the experimental results of the different decompression series are presented individually. Coalescence behavior varies among the three decompression rates, while showing similar behavior at c_{H_2Oi} of 5.7 wt % and 5.0 wt %. A complete overview of all samples from the decompression series, including the samples from Marks and Nowak (2025), is included in the Supplement (Figs. S1 and S2).

3.2.1 dP/dt of 0.064 MPa s^{-1}

Samples decompressed at the slow rate of 0.064 MPa s^{-1} are characterized by the appearance of large vesicles within the initially homogeneously vesiculated volumes during progressing decompression. In the series with 5.7 wt % c_{H_2Oi}, coalescence starts at a P_f of 70 MPa (Fig. 1). The capsule deformed during quenching. This deformation affected all coalesced vesicles, rendering their sizes unanalyzable. However, samples at lower P_f remained nearly undeformed, with vesicle sizes of ~ 300 µm at a P_f of 60 MPa and ~ 500 µm at a P_f of 50 MPa. Despite the presence of large coalesced vesicles, sample volumes with small homogeneous vesicles of 9 µm in diameter are still present in the glass interstices (Fig. 2a). At the lowest P_f of 40 MPa in this series (LLST_39D), homogeneously formed small vesicles are no longer observable, and the vesicle size of the coalesced vesicles can no longer be measured. Due to the large vesicle sizes and partial sample damage during preparation, the sample volume can no longer be evaluated, as the vesicles are no longer individually separated.

In the decompression series with a c_{H_2Oi} of 5.0 wt % (Fig. S2), the sudden appearance of large vesicles also occurs within initially homogeneously formed vesicle volumes. However, in this lower H_2O concentration series, coalescence starts at a lower P_f of 40 MPa. Volumes containing homogeneously formed vesicles with diameters of 13 µm are still present between the large coalesced vesicles, which measure ~ 480 µm. A consistent feature across all coalesced samples is the VND, with low logVND values ranging from 0.83 and 0.56 for the 5.7 wt % series at P_f of 50 and 40 MPa, respectively, and a logVND of 0.53 at P_f of 40 MPa in the 5.0 wt % series.

3.2.2 dP/dt of 0.17 MPa s^{-1}

A different vesicle coalescence behavior is observed in the 0.17 MPa s^{-1} decompression series. Across all coalesced samples at this decompression rate, logVNDs ranging from 1.8 to 0.92 were determined. In the series with 5.7 wt % c_{H_2Oi}, coalescence starts at a P_f between 70 and 60 MPa, with

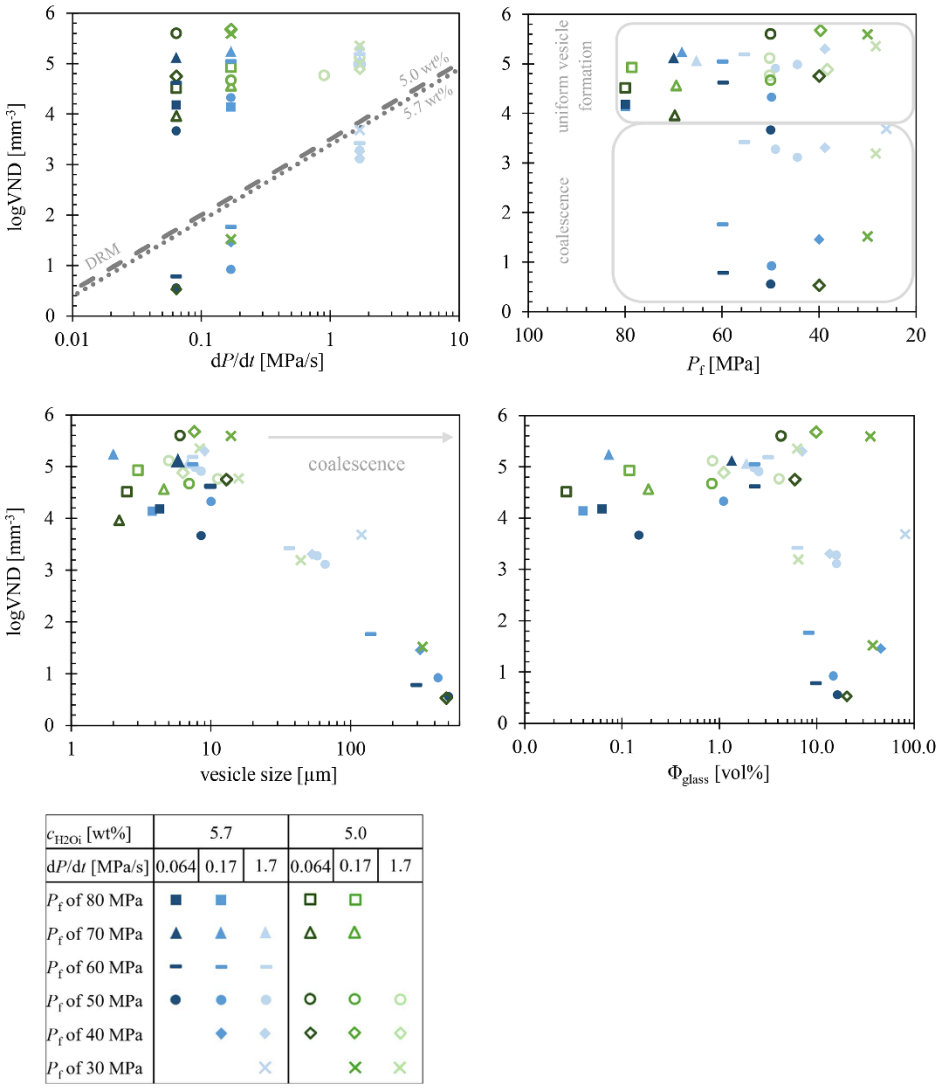

Figure 3. Combined logVND data plots of decompressed and quenched samples (Marks and Nowak, 2025). Data points of the same label correspond to both uniformly distributed vesicles and, if present, coalesced vesicles. The DRM corresponds to the calculated decompression rate meter of Toramaru (2006) (see Sect. 4.4).

large vesicles measuring 140 µm in diameter and smaller homogeneous vesicles of 7 µm in diameter still preserved between the larger vesicles (Fig. 2a). Decompression to a lower P_f of 50 MPa results in increased vesicle sizes of 422 µm for the coalesced vesicles and 10 µm for the preserved homogeneously formed small vesicles (LLST_4D). Upon further decompression to a P_f of 40 MPa, initially homogeneously formed vesicles are erased by coalescence (LLST_26D). However, due to the large size of the coalesced vesicles and their deformation during cooling, accurate diameter measurements could not be obtained. The vesicle size of 314 µm determined using CSDcorrections (Higgins, 2000) is likely incorrect, as the vesicles appear significantly larger at a P_f of 40 MPa compared to 50 MPa based on macroscopic observations. This discrepancy affects the VND, which should not exceed the previous logVND of 0.92 at higher P_f. This discrepancy might relate to the cut number of 61 vesicles in sample LLST_26D which is insufficient for CSDcorrections to generate statistically significant values. Marxer et al. (2015) determined that a minimum of 200 cut vesicles

is required in CSDcorrections analysis to achieve reliable reproducibility. Consequently, the current CSDcorrections data should be handled with caution and regarded only as a preliminary approximation based on the actual vesicle number and size.

In the decompression series with a c_{H_2Oi} of 5.0 wt % (Fig. 2d), the extending coalescence dependence cannot be determined, as coalescence only occurs at the lowest P_f of 30 MPa (LLST_45D). However, an interesting feature of this sample is the preservation of the initial homogeneous vesicle formation stage in the innermost sample center, with a maximum logVND of 5.6, while the outer areas exhibit coalesced vesicles with a logVND of 1.52 and large diameters of $\sim$ 330 µm. Additionally, volumes with small homogeneously formed vesicles are still preserved between the large coalesced vesicles, not only in the innermost part.

3.2.3 dP/dt of 1.7 MPa s^{-1}

The third series, with the fastest decompression rate of 1.7 MPa s^{-1}, reveals a different coalescence behavior. In the 5.7 wt % series, coalescence starts at a P_f of 60 MPa (Fig. 1). In contrast to the other samples, vesicles start to coalesce from the outer part of the sample towards the sample center. The sample centers at P_f of 60, 50, and 40 MPa exhibit uniform and finely vesiculated volumes with consistently high logVNDs of 5.2 to 5.4 and vesicle sizes ranging between 7 and 9 µm in diameter, indicating the preservation of the initial vesicle formation stage (Table 1, Fig. 2b). However, the coalesced volumes expand inward towards the sample center as P_f decreases. At P_f of 60 MPa (LLST_50D), coalesced vesicles have a diameter of 37 µm and a logVND of 3.42. This coalesced volume spans a horizontal width of $\sim$ 600 µm. As P_f decreases, this width extends to an average of about 1000 µm at P_f of 50 MPa and $\sim$ 1200 µm at P_f of 40 MPa (LLST_13D and LLST_25D, respectively). Determining the width at lower P_f is challenging due to slight sample inclination related to preparation, as seen in LLST_13D, and capsule deformation during quenching, as seen in LLST_25D. Nonetheless, an increase in coalescence width is observed with decreasing P_f, showing coalesced vesicle diameters of 53 to 66 µm and logVNDs of 3.31 to 3.11. The final sample in the 5.7 wt % c_{H_2Oi} series exhibits coalescence of the complete sample volume at a P_f of 30 MPa (LLST_44D, Fig. 2b). Only vesicles with diameters of 120 µm remain, but with a relatively high logVND of 3.68.

Similarly, in the 5.0 wt % decompression series at 1.7 MPa s^{-1}, coalescence starts from the outer shell at a P_f of 30 MPa (Fig. S2, LLST_42D). In this sample, the coalescence width extends to $\sim$ 400 µm towards the sample center, with vesicle diameters of 44 µm and a logVND of 3.19, while the inner part of the sample still shows a high logVND of 5.35 with initially homogeneously formed vesicles measuring 8 µm.

3.3 Onset of coalescence

Comparing the vesicle textures across the three series at the onset or completion of coalescence reveals distinct differences in coalescence behavior. In initially H_2O saturated melts, coalescence starts at a higher pressure than in undersaturated melts (Fig. 1). This pressure difference correlates with the difference in H_2O saturation pressures (P_{sat}, from Marks and Nowak, 2025) of 198 and 156 MPa for 5.7 wt % and 5.0 wt %, respectively. Additionally, the onset of coalescence partially depends on the decompression rate, occurring at higher P_f with decreasing rates. The first coalesced vesicles appear in the samples of the 5.7 wt % series at a P_f of 70 MPa at the slowest rate of 0.064 MPa s^{-1} and at a P_f of 60 MPa for the 0.17 and 1.7 MPa s^{-1} rates (Fig. 1). In contrast, coalescence in the samples of the 5.0 wt % series occurs at a P_f of 40 MPa for the 0.064 MPa s^{-1} decompression rate and at a P_f of 30 MPa for the faster rates of 0.17 and 1.7 MPa s^{-1}.

Samples quenched at the onset of coalescence exhibit both pristine homogeneous vesiculated sample volumes and the first coalesced vesicles, represented by two data points in Fig. 3: one for the homogeneous vesiculated volumes with maximum logVNDs of 5.1–5.7 and another for the volumes with coalesced vesicles with significantly lower logVND values between 3.7 and 0.5. It is important to note that the logVND of the pristine homogeneously formed vesicles decreases with the onset of coalescence at the slow decompression rates of 0.064 and 0.17 MPa s^{-1}.

3.4 Special case: equilibration at P_f

A special case regarding the coalescence behavior can be observed when comparing sample LLST_42D and LLST_41D (Fig. 4). Both samples had a c_{H_2Oi} of 5.0 wt % and were decompressed at 1.7 MPa s^{-1} to P_f of 30 MPa. Sample 42D was quenched immediately upon reaching P_f, whereas sample 41D was held at run temperature and P_f for 20 s before quenching. This resulted in different vesicle textures of the two samples. The center of sample 42D is completely filled with small, uniformly distributed vesicles, with sizes $\sim$ 8 µm and a logVND of 5.35, formed during initial vesiculation (Fig. 4). Coalescence is observed only in the intermediate zone between capsule wall and sample center, where vesicle diameters increase to 44 µm and the logVND decreases to 3.19. This represents the regular degassing behavior with the beginning of coalescence during continuous decompression. In contrast, sample 41D shows small, uniformly distributed vesicles only in the innermost sample center, with a reduced logVND of 4.77 and larger vesicle sizes of 16 µm. Between these vesicles, as well as in the outer parts of the sample, coalesced vesicles with large diameters of $\sim$ 100 µm and a low logVND of 2.39 are present. Therefore, as expected, the 20 s equilibration time at P_f of sample LLST_41D led to an in-

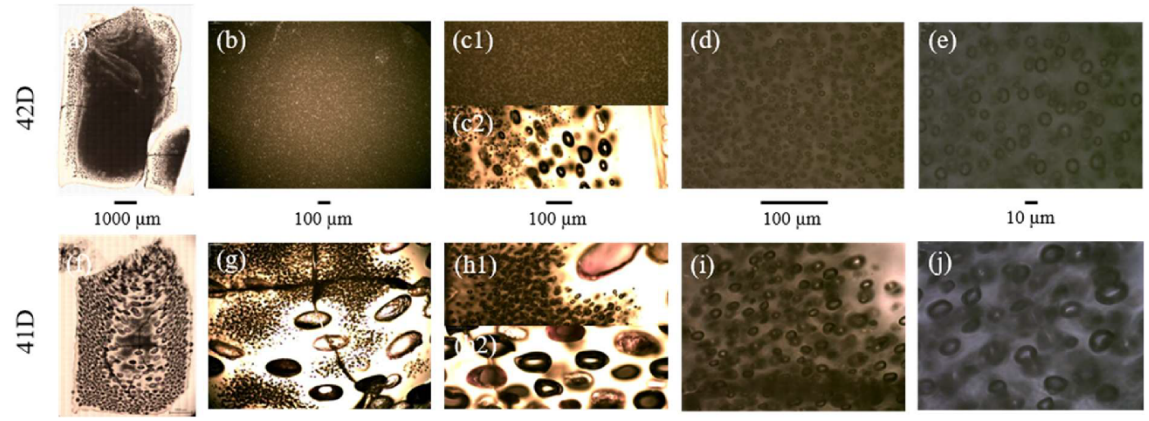

Figure 4. TLM images of samples LLST_42D and LLST_41D. Both samples were decompressed at 1.7 MPa s^{-1} to a P_f of 30 MPa. Sample 42D was quenched immediately upon reaching P_f and shows a homogeneous vesicle appearance throughout the glass (**a–e**). In contrast, sample 41D was held at P_f for 20 s prior to quenching, exhibiting coalescence structures throughout the sample volume with only a few fine homogeneous vesicles remaining in the center (**f–j**). The images were captured from the inner part of the samples, except for (**c**2) and (**h**2), which show the outer and coalesced areas. Scale bars are valid for vertically aligned images.

creased stage of vesicle coalescence and consequently to a decrease in VND.

3.5 c_{H_2Ot}

H_2O concentrations of decompressed samples are presented in Fig. 5. Data of decompression series are plotted separately based on c_{H_2Oi} of 5.7 wt % and 5.0 wt % and the respective decompression rates of 0.064, 0.17, and 1.7 MPa s^{-1}. The data span from the P_f related to the first vesicle observation to the lowest P_f in the series, capturing the onset and full extent of coalescence during continuous decompression applied in this study.

FTIR measurements conducted through pristine, initially vesiculated sample volumes, encompassing both interstitial glass and vesicles in the beam path, show c_{H_2Ot} close to the initial H_2O concentrations (Fig. 5a, b). In samples with a c_{H_2Oi} of 5.7 wt % and dP/dt of 0.064 and 0.17 MPa s^{-1}, the c_{H_2Ot} values through vesiculated sample volumes remain near 5.0 wt % at P_f of 70 and 60 MPa. In contrast, vesicle free interstitial glass measured between coalesced vesicles at P_f of 70–60 MPa shows c_{H_2Ot} reductions to 4.9–4.3 wt %, a decrease of 0.4–1 wt % (Fig. 5a). At lower P_f of 50–40 MPa, c_{H_2Ot} could only be analyzed between coalesced vesicles, yielding values of 4.4 wt %–3.4 wt % as pristine vesiculation was erased by coalescence. This indicates a continuous decrease in c_{H_2Ot} with lower P_f and increased coalescence.

In samples with a c_{H_2Oi} of 5.0 wt % and decompression rates of 0.064 and 0.17 MPa s^{-1}, c_{H_2Ot} measured through pristine vesiculated sample volumes exceeds c_{H_2Oi}, whereas c_{H_2Ot} in interstitial glass between coalesced vesicles remains below c_{H_2Oi}. At P_f values of 50–40 MPa, c_{H_2Ot} through glass with pristine vesicles ranges from 7.9 wt %–4.5 wt %, while glass between coalesced vesicles shows lower values of 4.2 wt %–2.7 wt % (Fig. 5d, e). During continuous decompression to P_f of 30 MPa, c_{H_2Ot} measured through pristine vesiculated sample volumes varies with maximum (c_{H_2Omax}) and minimum (c_{H_2Omin}) H_2O concentrations of 8.2 wt % and 5.2 wt %, respectively, while interstitial glass in zones of coalesced vesicles stabilize at 3.8 wt %.

Samples decompressed at 1.7 MPa s^{-1} exhibit distinct coalescence behavior, with coalescence starting at the outer regions of the vesiculated melt. Cross-sectional concentration profiles reveal significant H_2O variations (Fig. 5c, f). In the 5.0 wt % series (Fig. 5f), the main vesicle formation stage, corresponding to the highest VND, occurs at the lowest P_f of 30 MPa. Three horizontal cross-sections were measured, showing c_{H_2Ot} of 4.1 wt %–4.9 wt % between coalesced vesicles in the outer regions, with c_{H_2Ot} increasing to a maximum of $\sim$ 10 wt % in pristine vesiculated volumes at the sample center.

A similar c_{H_2Ot} distribution is observed in samples with a c_{H_2Oi} of 5.7 wt % decompressed at 1.7 MPa s^{-1}. Partial coalescence is observed at a P_f of 60 MPa. It was not possible to measure interstitial vesicle free glass volumes even in the regions with coalesced vesicles. Here, c_{H_2Ot} slightly increases towards the sample center, reaching c_{H_2Oi} of 5.7 wt %, while decreasing to 5.0 wt % in the outer regions (Fig. 5c). At P_f of 50 and 40 MPa, similar trends appear, with high c_{H_2Ot} of 4.7 wt % in fringe zones near the capsule walls, followed by a decrease to 3.7 wt %–4.3 wt % between coalesced vesicles in outer sample regions. Measurements through glass with pristine vesicles show a steady c_{H_2Ot} increase towards the sample center, reaching a maximum of 6.4 wt %–6.9 wt %. For the sample at P_f of 40 MPa, c_{H_2Ot} rises more steeply towards

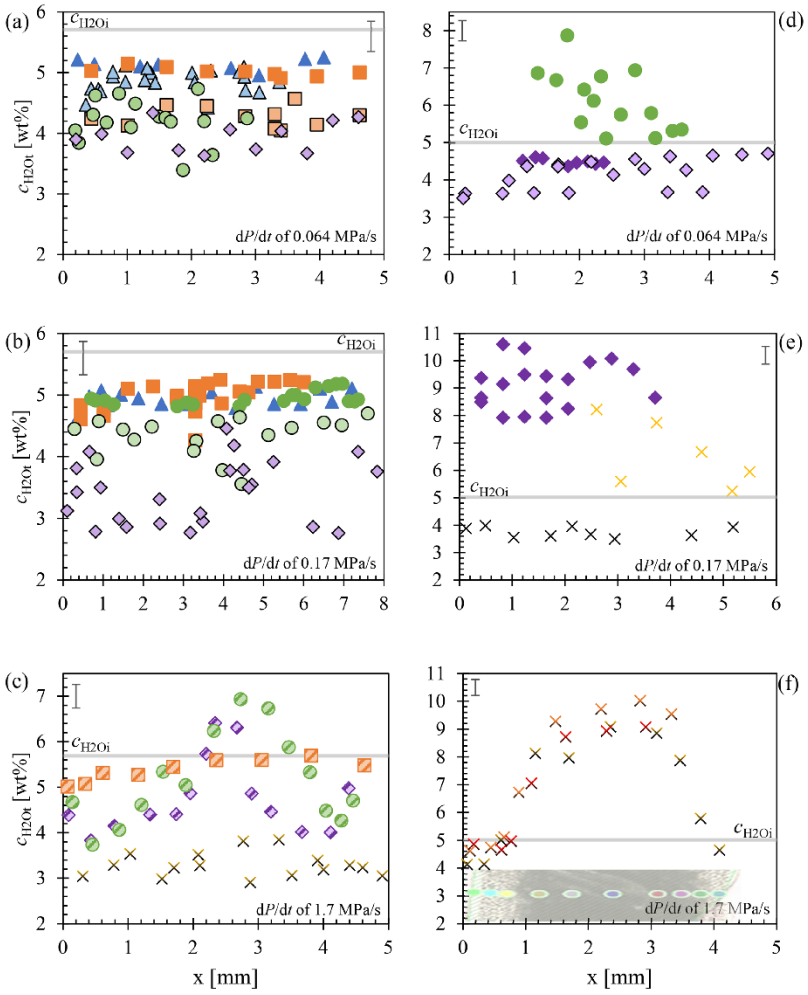

Figure 5. c_{H_2Ot} profiles of decompression samples, supplemented by data from Marks and Nowak (2025): **(a)** c_{H_2Oi} of 5.7 wt % and dP/dt of 0.064 MPa s^{-1}, **(b)** 5.7 wt % and 0.17 MPa s^{-1}, **(c)** 5.7 wt % and 1.7 MPa s^{-1}, **(d)** 5.0 wt % and 0.064 MPa s^{-1}, **(e)** 5.0 wt % and 0.17 MPa s^{-1}, and **(f)** 5.0 wt % and 1.7 MPa s^{-1}. Solid colored symbols represent c_{H_2Ot} through homogeneous vesicles, while pale-colored symbols with black edges represent c_{H_2Ot} in glass between already coalesced vesicles. The two-colored data points in **(c)** and the data in **(f)** correspond to horizontal measurements taken from the left capsule rim, passing through regions with partially coalesced vesicles, homogeneous vesicle areas, and again through coalesced vesicle areas near the right capsule rim. The image in **(f)** represents sample LLST_42D from Fig. 4, with data points corresponding to the measurement points in the image. Error bars are provided for each dataset. c_{H_2Oi} represents the initial H_2O concentration of 5.7 wt % **(a–c)** and 5.0 wt % **(d–f)**.

glass with pristine vesicle volumes, peaking at 6.4 wt % in the profile. Additional measurements in vesiculated volumes show maximum c_{H_2Ot} values of 7.5 wt % (Table 1). The sample decompressed to the lowest P_f of 30 MPa exhibit only coalesced vesicles, with an average c_{H_2Ot} of 3.5 wt % in interstitial glass.

Residual c_{H_2Ot} in interstitial glass of decompressed samples are presented in Fig. A1. Additionally, c_{H_2Oi} of 5.7 wt % and 5.0 wt % were plotted, along with the expected equilibrium H_2O concentration (c_{H_2Oeq}), calculated based on solubility data (Marks and Nowak, 2025). Measurements of samples containing vesicles within the beam path were excluded; only samples where the NIR beam exclusively passed through interstitial glass were included in the plot. The newly added data for coalesced volumes indicate that, even at a low P_f of 30 MPa, no sample achieved the c_{H_2Oeq} predicted by the solubility measurements, irrespective of c_{H_2Oi}. The data consistently show c_{H_2Ot} values approximately 1.5 wt %–

2 wt % higher than the c_{H_2Ocq} calculated using Eq. (5) therein (Fig. A1).

4 Discussion

4.1 VND evolution

In all samples prior to coalescence, a constant VND was observed across various decompression rates, with uniform vesicle sizes within each sample. This feature is an indication of spinodal decomposition, where the critical wavelength of H_2O concentration fluctuations, enhanced by uphill diffusion, and determines the uniform and spontaneous formation of vesicles throughout the melt during decompression (Allabar and Nowak, 2018; Sahagian and Carley, 2020). As a result, spinodal decomposition produces a high, decompression-rate-independent VND along with consistently uniform vesicle sizes (Allabar and Nowak, 2018; Allabar et al., 2020b; Sahagian and Carley, 2020; Gardner et al., 2023).

While the process appears consistent across all samples, a deeper analysis has uncovered specific trends that are now being examined in detail. The evolution of VND with P_f for the decompressed and quenched samples demonstrates at sufficient H_2O supersaturation an apparent initial increase in logVND from ~ 4 to maximum values of 5.1 to 5.7 related to homogeneous vesicle formation, followed by a rapid decrease by orders of magnitude related to progressing coalescence, irrespective of the decompression rate and H_2O content (Fig. 6a, b). Notably, all series start with logVND values of ~ 4 when the first µm-sized vesicles are observable in the quenched glasses, primarily in samples with P_f values of 80 and 70 MPa. The reduced initial VND is suggested to be attributed to quenching of the vesiculated melt, where not all vesicles formed during decompression survived due to minimal size variations (Marks and Nowak, 2025). Quenching of the melt causes shrinkage of the vesicles, possibly to a scale below the optical resolution or complete disappearance related to the reduction in the molar volume of H_2O (Marxer et al., 2015) and the resorption of H_2O from the fluid vesicles into the melt (McIntosh et al., 2014; Allabar et al., 2020a), driven by the increasing solubility of H_2O in phonolite melt with decreasing temperature (Schmidt and Behrens, 2008). However, their presence cannot be entirely ruled out, as they may persist beyond the limits of the applied imaging technique. This step is indicated by number 1 in Fig. 6.

The subsequent increase of logVNDs to maximum values of 5.1–5.7 (Table 1) with decreasing P_f represents the true initial VND of homogeneously formed vesicles due to a sufficient size, allowing them to persist despite the rapid cooling process (number 2 in Fig. 6). The propagating decrease in VND with decompression (number 3 in Fig. 6) is related to the onset and progression of coalescence, showing both volumes of pristine, small and uniform vesicles with high VND as well as volumes with larger coalesced vesicles until the stage of complete coalescence is reached (number 4 in Fig. 6). With the onset of coalescence, the logVND drops drastically by 1.2–4.1 log units to low values depending on the decompression rate (Table 1, Fig. 6).

We emphasize that, particularly in the 1.7 MPa s^{-1} series (Fig. 6a), the transition from the initial appearance of observable vesicles in the glass to the onset of coalescence is achieved within ~ 6 s in the 10 MPa P_f interval. The bimodal stage, characterized by persistent initial VND alongside progressive coalescence, spans a pressure interval of 30 MPa. Complete coalescence is reached at a P_f of 30 MPa, with the logVND decreasing to ~ 2. A more pronounced reduction in logVND, coinciding with the onset of coalescence, is observed in the samples of the 0.17 MPa s^{-1} series (Fig. 6b). With the onset of coalescence, the logVND decreases from 5.1 to a value of 4.3, while the logVND of the coalesced volumes ranges from ~ 1 to 2. The coalesced vesicle volumes exhibit significantly lower logVND values than those observed in the faster-decompressed samples, indicating a more advanced stage of coalescence. At the slowest decompression rate of 0.064 MPa s^{-1}, this process is further intensified, resulting in the lowest logVND values, as low as 0.5. These observations suggest that the logVND of coalesced vesicle volumes is influenced by P_f and the rate and duration of decompression.

4.2 Onset of coalescence: melt porosity

As displayed in Fig. 1, the onset of coalescence is partially dependent on the decompression rate. Within the 10 MPa pressure intervals, it starts at a pressure that is 10 MPa higher at the slowest decompression rate compared to faster rates in both c_{H_2Oi} series. In the 5.7 wt % series, H_2O supersaturation starts almost immediately after decompression begins, as the saturation pressure ($P_{sat} = 198$ MPa) is nearly identical to the starting pressure of 200 MPa. In contrast, samples of the 5.0 wt % series require a pressure drop of ~ 40 MPa before supersaturation initiates ($P_{sat} = 156$ MPa, Marks and Nowak, 2025). This accounts for the observed 30 MPa delay in the onset of coalescence in the 5.0 wt % series compared to the 5.7 wt % series (Fig. 1). Due to the lower P_{sat} in the 5.0 wt % series, only partial coalescence is achieved at the lowest P_f, whereas samples of the 5.7 wt % series undergo full coalescence, reaching a constant VND without residual pristine vesiculated volumes.

At the onset of coalescence, a mean vesicle diameter of 6.7 ± 1 µm and glass porosity (Φ_{glass}) of 2.3 ± 1 vol % for the 5.7 wt % series were measured (Table 1). In contrast, samples of the 5.0 wt % series show higher and more variable values, with vesicle diameters ranging from 8.3–13.9 µm and Φ_{glass} of 6–35.6 vol %. It is important to note that Φ_{glass} does not represent melt porosity prior to quenching, as vesicle shrinkage occurs during cooling related to the decreasing molar volume of H_2O, as well as due to H_2O resorption (McIntosh et al., 2014; Marxer et al., 2015; Allabar and Nowak, 2018;

Table 1. Conditions and results of decompression experiments. Decompression experiments were hydrated at 200 MPa for 96 h at 1523 K and thermally equilibrated for 30 min at 1323 K prior to decompression.

LLST	P_i [MPa]	P_{min} [MPa]	Quenching rate [K s^{-1}]	c_{H_2O}eq at P_f [wt %]	c_{H_2O}max [wt %]	c_{H_2O}t in pure glass [wt %]	c_{H_2O}t in glass through vesicles [wt %]	Vesicle size hom. [µm]	Vesicle size coal. [µm]	l [µm]	τ_{diff}/τ_d	Φ_{glass} hom. [vol %]	Φ_{glass} coal. [vol %]	Φ_{eq} [vol %]	logVND hom. [mm^{-3}]	logVND coal. [mm^{-3}]
dP/dt of 1.7 MPa s^{-1}																
c_{H_2O}i of 5.7 wt %																
50D[a,b]	60	55	MQ	2.66	5.48 ± 0.27		5.26 ± 0.26	7.4	36.5	7.8	0.31	3.2	6.3	38.0	5.19	3.42
13D[b]	50	45	MQ	2.33	6.94 ± 0.27	4.70 ± 0.27	5.00 ± 0.27	7.7	65.5	9.6	0.37	2.3	16.0	43.5	4.99	3.11
13D[b]	50	45	MQ	2.33	6.94 ± 0.27		5.00 ± 0.27	7.4	65.5	9.6	0.37	6.1	16.0	43.5	5.42	3.11
40D[b]	50	49	RQ	2.47	4.43 ± 0.24	4.70 ± 0.27	3.98 ± 0.24	8.5	57.6	10.1	0.45	2.6	16.0	39.4	4.91	3.28
25D[b]	40	39	MQ	2.15	7.46 ± 0.28		4.84 ± 0.28	9.0	53.0	6.1	0.14	7.1	13.6	47.7	5.30	3.31
44D[b]	30	26	MQ	1.69	4.53 ± 0.25		3.29 ± 0.23	119.6	119.6	n.c.	1.76	81.3	81.3	56.0		3.68
c_{H_2O}i of 5.0 wt %																
42D[a,b]	30	28	MQ	1.78	10.02 ± 0.38		7.98 ± 0.33	8.3	44.0	6.0	0.11	6.3	6.5	53.2	5.35	3.19
41D[b]	30	28	NQ	1.77	5.91 ± 0.28	2.88 ± 0.23	4.86 ± 0.26	15.8	102.9	8.0	0.19	10.9	12.4	55.8	4.77	2.39
dP/dt of 0.17 MPa s^{-1}																
c_{H_2O}i of 5.7 wt %																
3D[a]	70	68	MQ	3.01	5.13 ± 0.27		4.95 ± 0.27	2.0		10.1	0.98	0.1		33.5	5.24	
49D[a,b,c]	60	60	MQ	2.79	5.25 ± 0.27		5.08 ± 0.26	7.4	139.2	9.2	0.51	2.3	8.3	31.9	5.05	1.80
4D[b,c]	50	50	RQ	2.49	5.18 ± 0.27	4.36 ± 0.26	4.95 ± 0.27	10.0	422.0	17.4	1.37	1.1	14.8	46.2	4.33	0.92
26D[b,c]	40	40	MQ	2.19	4.46 ± 0.31	3.43 ± 0.30			314.0	n.e.	n.e.		45.8	32.7		1.46
c_{H_2O}i of 5.0 wt %																
17D[a]	40	40	MQ	2.18	10.60 ± 0.33	4.25 ± 0.26	7.67 ± 0.34	7.6		4.1	0.06	9.9		41.9	5.68	
17D[a]	40	40	MQ	2.18	10.60 ± 0.33	4.25 ± 0.26	7.67 ± 0.34	10.8		2.6	0.02	25.3		41.9	5.59	
45D[a,b,c]	30	30	MQ	1.84	8.21 ± 0.32	3.75 ± 0.23	6.57 ± 0.29	13.9	328	1.5	0.01	35.6	37.8	45.8	5.60	1.52
dP/dt of 0.064 MPa s^{-1}																
c_{H_2O}i of 5.7 wt %																
37D[a,b]	70	70	MQ	3.06	5.26 ± 0.27	4.86 ± 0.26	5.14 ± 0.26	5.8	n.c.	9.2		1.3		21.1	5.12	
48D[a,b,c]	60	60	NQ	2.78	5.15 ± 0.27	4.28 ± 0.25	5.02 ± 0.26	9.9	295.5	12.8	2.0	2.3	9.9	27.1	4.62	0.83
38D[b,c]	50	50	MQ	2.50	4.74 ± 0.25	4.20 ± 0.24		8.5	502.0	32.9	7.3	0.1	16.4	28.7	3.67	0.56
39D[b]	40	39	MQ	2.15	4.34 ± 0.24	3.94 ± 0.24		n.e.	n.e.					27.0		
c_{H_2O}i of 5.0 wt %																
20D[a]	50	50	MQ	2.50	7.87 ± 0.28	4.47 ± 0.27	5.34 ± 0.28	6.0				4.3		33.0	5.60	
21D[a,b,c]	40	40	MQ	2.19	4.71 ± 0.28	4.15 ± 0.26	4.49 ± 0.27	12.9	484.0	9.7	1.24	6.0	20.4	36.6	4.75	0.53

Included are data from Marks and Nowak (2023), marked with [a]. Samples with [b] are partially or completely coalesced. [c] determined by CSD; n.c.: not evaluable. P_f = final pressure; P_{min} = recorded minimum pressure during decompression; dP/dt = decompression rate. Quenching rates: MQ = ~ 150 K s^{-1}, NQ = ~ 97 K s^{-1}, RQ = ~ 16 K s^{-1}; c_{H_2O}i = initial H_2O concentration; c_{H_2O}eq = equilibrium H_2O concentration; c_{H_2O}t = measured H_2O concentration in glass; / = inter-vesicle distances; τ_{diff} = diffusion timescale; τ_d = decompression timescale; Φ_{glass} = glass porosity; Φ_{eq} = equilibrium melt porosity; VND: vesicle number density.

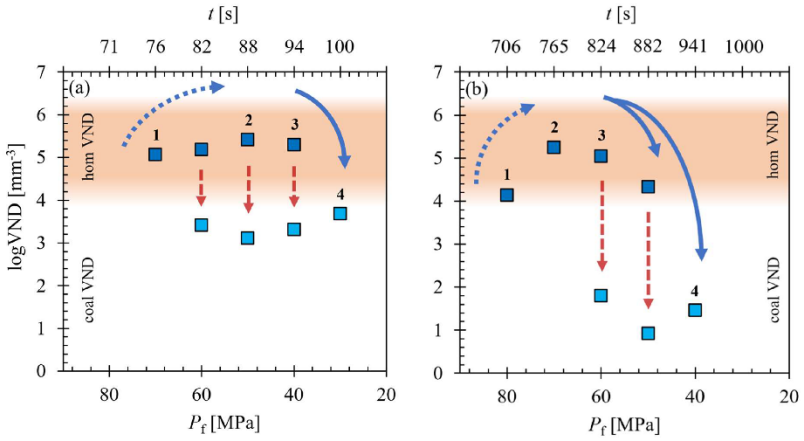

Figure 6. The logVND evolution vs. P_f related to decompression time (t in s). **(a)** Experimental series with 5.7 wt % c_{H_2Oi} and a decompression rate of 1.7 MPa s^{-1}; **(b)** experimental series with c_{H_2Oi} of 5.7 wt % decompressed with 0.17 MPa s^{-1}. Numbers represent the stages of vesicle textures: (1) first vesicle formation observed in quenched glasses influenced by vesicle shrinkage and resorption; (2) samples with vesiculated volumes indicating the highest initial VNDs; (3) Decrease in VND due to the onset and progression of coalescence in sample volumes with pristine vesicles and sample volumes with coalesced vesicles; and (4) complete coalescence stage where volumes with homogeneously formed pristine vesicles are erased. The blue arrows indicate the evolution of the initial VND, while the red arrows highlight the difference within a single sample between the VNDs in the homogeneous and coalesced VND fields.

Allabar et al., 2020b). Equilibrium melt porosities (Φ_{eq}) at P_f were calculated using Eq. (1) (Gardner et al., 1999), incorporating melt density (ρ_{melt}) from Ochs and Lange (1999) and the molar volume of H_2O fluid (V_{mH_2O}) from Duan and Zhang (2006):

$$\Phi_{eq} = \left[\frac{\frac{\rho_{melt}}{M_{H_2O}} \cdot V_{mH_2O} \cdot \left(c_{H_2Oi} - c_{H_2Oeq}\right)}{1 + \left(\frac{\rho_{melt}}{M_{H_2O}} \cdot V_{mH_2O} \cdot \left(c_{H_2Oi} - c_{H_2Oeq}\right)\right)} \right]. \quad (1)$$

Significantly higher porosities were calculated, with a mean Φ_{eq} of 30.3 vol % for the 5.7 wt % series and a mean Φ_{eq} of 46.1 vol % for the 5.0 wt % series (Table 1). Only completely coalesced samples of the 5.7 wt % series exhibit Φ_{glass} values exceeding the predicted Φ_{eq}. This suggests that in the final coalesced stage at low P_f, the CSDcorrections-predicted Φ_{glass} will be close to Φ_{eq}, as the influence of shrinkage due to back diffusion of H_2O into the melt is less pronounced at low VND due to increased vesicle distances.

Vesicle shrinkage can be calculated if the conditions prior and during quenching are known. Resorption shrinkage requires adjusting the H_2O concentration (c_{H_2Oeq}) in the melt prior to cooling (Ryan et al., 2015). Otherwise, if the cooling-induced increase in H_2O solubility does not exceed the level of H_2O supersaturation, no driving force exists for H_2O resorption from the fluid phase back into the melt. As a first approximation, for maximum logVNDs ranging from 5.1 to 5.7 (Table 1, Fig. 3), a mean center of vesicle distance (v_d) of ~ 7 to 9 µm was calculated using Hertz (1908) ($v_d = 5/9 \cdot \mathrm{VND}^{-1/3}$) for a random vesicle distribution. This inter-vesicle distance is sufficiently small to enable c_{H_2Oeq} and Φ_{eq} within seconds via H_2O diffusion from the melt into the vesicles during further decompression, as estimated using the H_2O diffusivity for phonolite melt (Schmidt et al., 2013). To determine the contribution of each vesicle shrinkage mechanism, we first calculate the shrinkage solely due to the Equation of State (EOS, Duan and Zhang, 2006) assuming a constant number of H_2O molecules in the vesicle.

Vesicle deformation is particularly evident in larger vesicles, making the evaluation of coalesced vesicle sizes in sample LLST_37D impossible (Fig. 2). Larger vesicles are more influenced by deformation due to their greater diameter, whereas smaller vesicles tend to maintain their spherical shape during quenching (Fig. 2). The relaxation time for deformed vesicles to return to a spherical shape depends on the vesicle radius (Toramaru, 1988), as well as the melt viscosity, and surface tension. Allabar et al. (2020b) determined this relaxation time to be more than 10 times longer for vesicles with radii of several hundred micrometers compared to vesicles with only a few micrometers in diameter. Assuming the amount of exsolved H_2O in the vesicle remains constant, the decrease in V_{mH_2O} results in a vesicle volume reduction by a shrinkage factor (B_S), corresponding to the ratio of V_{mH_2O} before and after rapid quenching (Marxer et al., 2015):

$$B_S = \frac{V_{mH_2O}[P_{min}, T_{eq}]}{V_{mH_2O}[P_{min}, T_f]}. \quad (2)$$

T_{eq} represents the experimental temperature during decompression. Based on calculations by Allabar et al. (2020b) for Vesuvius AD 79 phonolite, the fictive temperature (T_f), at which vesicle shrinkage ceases is up to 200 K above the

glass transition temperature (T_g) at a cooling rate of 44 K s^{-1}. Marks and Nowak (2025) applied these parameters to their dataset, and determined a T_f of $\sim 965 \pm 20$ K, covering all samples.

The V_{mH_2O} at P_{min} and T_{eq} or T_f was calculated using the EOS of H_2O (Duan and Zhang, 2006). We calculated B_S for samples with a c_{H_2Oi} of 5.7 wt % to range from 2.26 to 1.73 and for samples with a c_{H_2Oi} of 5.0 wt % to range from 2.01 to 1.65. With decreasing P_f and residual c_{H_2Ot}, B_S decreases. This factor can be incorporated into Eq. (3) to calculate melt porosity (Φ_{EOS}) at T_f when shrinkage starts from Φ_{eq} (Marxer et al., 2015):

$$\Phi_{EOS} = \frac{\Phi_{eq}}{\Phi_{eq} - B_s \cdot (\Phi_{eq} - 100)} \cdot 100. \quad (3)$$

The resulting Φ_{EOS} values are between the measured Φ_{glass} and the calculated Φ_{eq}. The calculated Φ_{EOS} ranges from 9 vol % to 43 vol %, with increasing values as P_f decreases. The Φ_{EOS} remains consistently ~ 10 vol %–15 vol % below Φ_{eq} but aligns closely (~ 5 vol %) with CSD-corrected Φ_{glass} in strongly coalesced samples (Table 1).

Allabar et al. (2020b) combined shrinkage by EOS and H_2O resorption, which resulted in a ~ 10 vol % decrease in Φ_{EOS} at a c_{H_2Oi} of 5.3 wt % and a quenching rate of 44 K s^{-1}. It was found that the value of the measured Φ_{glass} is within this determined range. Due to the similar composition and similar c_{H_2Oi}, we assume that a range of ~ 10 vol % with the maximum at Φ_{EOS} is also possible for the samples in this study. The actual melt porosities are therefore between the measured Φ_{glass} and Φ_{EOS}, while the calculation of Φ_{eq} significantly overestimates the porosities.

Returning to melt porosity at the onset of coalescence, the required porosity decreases with decreasing decompression rate but increases with decreasing c_{H_2Oi}. For a c_{H_2Oi} of 5.7 wt %, the Φ_{EOS} values are 23 vol % at a decompression rate of 1.7 MPa s^{-1} and P_{min} of 55 MPa, 17 vol % at 0.17 MPa s^{-1} and P_{min} of 60 MPa, and 11 vol % at 0.064 MPa s^{-1} and P_{min} of 60 MPa. In the c_{H_2Oi} of 5.0 wt % series, the porosity values increase as P_{min} decreases: Φ_{EOS} values are 43 vol % at a decompression rate of 1.7 MPa s^{-1} and P_{min} of 28 MPa, 34 vol % at 0.17 MPa s^{-1} and P_{min} of 30 MPa, and 25 vol % at 0.064 MPa s^{-1} and P_{min} of 40 MPa (Table 2).

4.3 Onset of coalescence in the intermediate zone at dP/dt of 1.7 MPa s^{-1}

The observed onset of coalescence in the intermediate zone of the samples, close to the capsule wall, in the 1.7 MPa s^{-1} series might be related to slight c_{H_2Ot} gradients (Fig. 2). The H_2O solubilities (c_{H_2Oeq}) were calculated in Marks and Nowak (2025). We experimentally determined H_2O solubilities and derived an empirical formula to predict c_{H_2Oeq} between pressures of 200 and 30 MPa at 1323 K. Additionally, we determined c_{H_2Oeq} at the hydration temperature of 1523 K and 200 MPa, which was found to be 5.45 ± 0.26 wt %. At 1323 K, c_{H_2Oeq} increased by ~ 0.4 wt % to 5.83 ± 0.26 wt %. This is consistent with the increased H_2O solubility at lower temperatures observed in phonolite melts (Schmidt and Behrens, 2008). The increase in c_{H_2Oeq} with decreasing temperature is relevant during the 30 min temperature equilibration time after hydration at 1523 K for 96 h. The outer melt volumes are expected to build up a slightly higher H_2O content during the 30 min dwell time compared to the central part of the melt prior to decompression. It is assumed that the excess H_2O of 0.25 wt % at c_{H_2Oi} of 5.7 wt % is evenly distributed between the capsule wall and melt during the hydration at 1523 K. The excess amount of H_2O dissolves in the outer melt volumes during the dwell time at 1323 K. An estimation of D_{H_2O} related to 5.45 wt % H_2O during the 30 min at 1323 K and 200 MPa, without considering the initial onset diffusion during the cooling phase from 1523 to 1323 K, resulted in 651 µm diffusion length by applying the diffusion equation provided by Schmidt et al. (2013). This distance exceeds the width of the coalesced volume at P_f of 60 MPa, which is ~ 600 µm. Therefore, it cannot qualitatively account for the coalescence observed beginning in the outer regions.

At a c_{H_2Oi} of 5.0 wt %, the complete amount of H_2O is homogeneously dissolved throughout the melt already at 1523 K. In this case, the enrichment of H_2O in the outer melt shell fails to explain the onset of coalescence at the sample rim in sample LLST_42D at P_f of 30 MPa. Therefore, we cannot fully explain this unique vesicle coalescence behavior, which warrants further investigation.

4.4 VND adjusted by coalescence follows the decompression rate meter of Toramaru (2006)

The general trend of the VND development with decreasing P_f is consistent across all samples analyzed in this study (Fig. 3). However, the VND of the initially formed (logVND of 5.1–5.7) and partially extinct (logVND of 4.5–5.0) homogeneous vesicles remains constant across all decompression rates, consistently exhibiting uniform vesicle sizes within each sample, suggesting that their initial formation occurs via spinodal decomposition (Allabar and Nowak, 2018; Allabar et al., 2020a; Sahagian and Carley, 2020; Gardner et al., 2023; Marks and Nowak, 2025). This observation supports an alternative degassing mechanism to classical nucleation theory, in which VND depends on the decompression rate, and vesicle formation is limited to the extent necessary to reduce supersaturation. As a result, a range of vesicle sizes is present within a single sample, as new vesicles form only when existing ones are insufficient (Navon and Lyakhovsky, 1998). Upon the onset of coalescence, the VND decreases significantly by several orders of magnitude, 1–2 log units below the predicted VND using the DRM (decompression rate meter) line (Figs. 3, 7), calculated by Eq. (4) according to Toramaru (2006). The DRM is based on nucleation theory, which predicts an increasing nucleation rate with an

Table 2. Samples with volumes showing maximum VND at the onset of coalescence. Data are given for pristine homogeneously vesiculated volumes.

LLST	c_{H_2Oi} [wt %]	dP/dt [MPa s^{-1}]	P_f [MPa]	Vesicle size [µm] Φ_{glass}	Vesicle size [µm] Φ_{EOS}	Φ_{glass} [vol %]	Φ_{eq} [vol %]	Φ_{EOS} [vol %]	l [µm]	logVND [mm^{-3}]
50D	5.7	1.7	55	7.4	15.1	3.2	37.9	23.1	7.8	5.19
42D	5.0	1.7	28	8.3	13.7	6.3	55.8	43.3	6.0	5.35
49D	5.7	0.17	60	7.4	16.5	2.3	31.9	17.4	9.2	5.05
45D	5.0	0.17	30	13.9	23.1	35.6	45.8	33.7	1.5	5.60
37D	5.7	0.064	60	5.8	12.6	1.3	21.1	11	9.2	5.12
21D	5.0	0.064	40	12.9	22.5	6.0	36.6	24.9	9.7	4.75

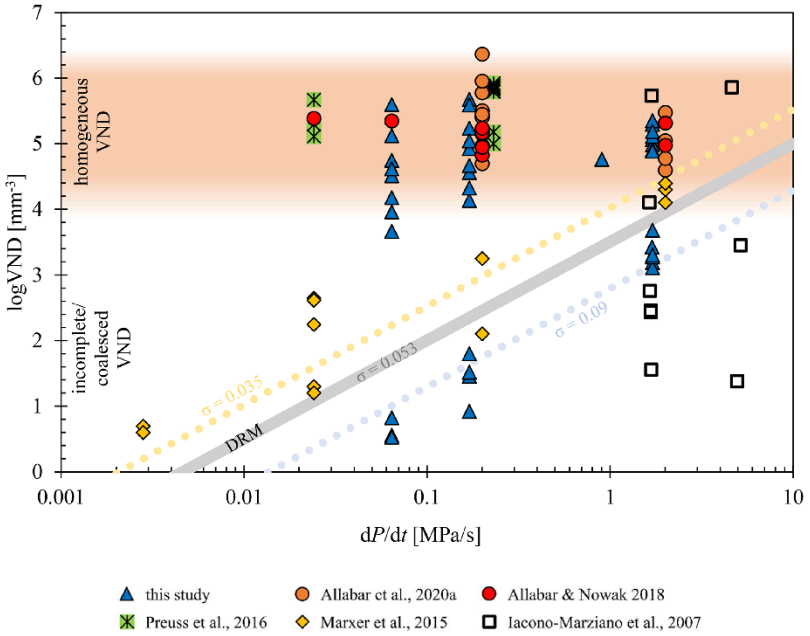

Figure 7. VND vs. decompression rate plot of decompressed samples using hydrous phonolitic or trachytic melt. The samples are presented as follows: this study (including data from Marks and Nowak, 2025) is represented by blue triangles, Allabar and Nowak (2018) by red circles, Allabar et al. (2020b) by orange circles, Preuss et al. (2016) by crossed green squares, Marxer et al. (2015) by yellow diamonds, and Iacono-Marziano et al. (2007) by open squares. For a better overview, data from other authors were slightly shifted in dP/dt by 0.03 at 0.17 MPa s^{-1} and 0.3 at 1.7 MPa s^{-1} to mitigate overlapping. The DRM line is calculated for the LLST composition using the surface tension $\sigma = 0.053$ N m^{-1} calculated by Shea (2017) according to Toramaru (2006). Successful decompression experiments are plotted in the area of homogeneous VND, indicating degassing by spinodal decomposition. Data following the DRM line are influenced by coalescence, due to pre-existing bubbles, or due to an unsuitable capsule design.

increasing decompression rate leading to a decompression-rate-dependent VND of homogeneously nucleated vesicles. This method can be used to derive the magma ascent velocity using VNDs of volcanic ejecta.

$$\mathrm{VND} = 34 \cdot C \cdot \left(\frac{16 \cdot \pi \cdot \sigma^3}{3 \cdot k \cdot T \cdot P_{sat}^2}\right)^{-2} \cdot \left(\frac{V_m \cdot P_{sat}}{k \cdot T}\right)^{-\frac{1}{4}} \cdot \left(\frac{P_{sat}^2 \cdot kT \cdot C \cdot D}{4 \cdot \sigma^2 \cdot (dP/dt)}\right)^{-\frac{3}{2}} \quad (4)$$

C: initial total H_2O concentration (number of molecules per cubic meters [m^{-3}]); σ: surface tension of the vesicle–

melt interface [N m^{-1}]; k: Boltzmann constant (1.38×10^{-23} [J K^{-1}]); T: temperature [K]; P_{sat}: H_2O saturation pressure [Pa]; D: H_2O diffusivity in the silicate melt [m^2 s^{-1}]; V_m: volume of an H_2O molecule in the melt ($= 3 \times 10^{-29}$ m^3) (Burnham and Davis, 1971); dP/dt: decompression rate [Pa s^{-1}]

The model assumes that each H_2O molecule is a potential vesicle nucleation site and that nucleation ceases during decompression when the VND reaches a level where vesicle distances are sufficiently small for a diffusion-controlled decrease in H_2O supersaturation below the threshold necessary for further vesicle nucleation (Toramaru, 2006). Assuming nucleation as the formation process of vesicles, the DRM can be used to calculate the VND as a function of dP/dt by considering the surface tension (σ), H_2O content, and diffusivity defined by the H_2O saturation pressure (Marks and Nowak, 2025). The surface tension was calculated by Eq. (5) according to Shea (2017) and was predicted to be 0.052 N m^{-1} for 5.7 wt % H_2O and 0.053 N m^{-1} for 5.0 wt %. For the parameters σ_{ref}, T_{ref}, P_{ref}, and SiO_{2ref} (surface tension, temperature, pressure, and SiO_2 content), values of a reference melt are chosen and taken to be $\sigma_{ref} = 0.06$ N m^{-1}, $T_{ref} =$ 900 °C, $P_{ref} = 200$ MPa, and $SiO_{2ref} = 66.5$ wt %. The required H_2O diffusivity ($\log D$) (in m^2 s^{-1}) was given in Eq. (6) by Schmidt et al. (2013) with c_{H_2O} (in wt %) and T (in K).

$$\sigma = \sigma_{ref} \cdot \exp\left[\left(-2.2 \times 10^{-2}\right) \cdot \left(SiO_{2_{ref}} - SiO_2\right)\right] - 5 \times 10^{-6} \cdot (T_{ref} - T) + 2 \times 10^{-5} \cdot (P_{ref} - P_{sat}), \quad (5)$$

$$\log D = (-6.001 - 0.277 \cdot c_{H_2Ot}) - (6281 - 565.6 \cdot c_{H_2Ot})/T. \quad (6)$$

While the maximum logVND of the homogeneous vesicle volumes show independence from different decompression rates with consistently high values of 5.1–5.7 (Table 1), the logVNDs of coalesced sample volumes tend to follow the DRM, with the lowest logVNDs of 0.5–0.8 at the lowest decompression rate of 0.064 MPa s^{-1} and the highest logVNDs of 3.1–3.7 at the highest decompression rate of 1.7 MPa s^{-1}. In each series, the onset of coalescence was observed, but complete coalescence – defined in this study as the advanced degassing stage where no pristine homogeneous vesicles remain – was only observed in the c_{H_2Oi} series with 5.7 wt % H_2O. This occurred at a P_f of 40 MPa for rates of 0.064 and 0.17 MPa s^{-1} and at a P_f of 30 MPa for the 1.7 MPa s^{-1} rate.

Therefore, coalescence is a progressive process that results in decreasing VND with P_f. Several decompression experiments with phonolitic and trachytic melts have already been carried out, which both confirm and partially refute the behavior observed here by encompassing both decompression-rate-independent and decompression-rate-dependent VND. However, the decompression-rate-dependent VNDs observed in melts with compositions identical to those exhibiting decompression-rate-independent behavior were produced using an alternative experimental design (Allabar and Nowak, 2018; Allabar et al., 2020a; Preuss et al., 2016; Marxer et al., 2015; Iacono-Marziano et al., 2007).

For example, VAD79 experiments by Iacono-Marziano et al. (2007) and Marxer et al. (2015) revealed that small capsule diameters (2.4–2.5 mm) inhibited uniform vesicle formation due to H_2O diffusional loss towards fringe vesicles at the capsule walls, compounded by coalescence at low P_f. Only the highest decompression rate of 1.7 MPa s^{-1}, presented in the study of Marxer et al. (2015), produced uniformly distributed small vesicles (logVND of $\sim$ 4.3) due to shorter diffusion times. In contrast, Preuss et al. (2016) used larger glass cylinders (5 mm) of Campi Flegrei trachytic and VAD79 phonolitic melts, achieving high logVNDs of $\sim$ 5.6 with decompression-rate-independent VNDs. However, using powdered starting material at the same experimental conditions reduced VNDs significantly due to pre-existing H_2O–N_2 vesicles and degassing by diffusive growth of these pre-existing vesicles. The samples in which powder was used as starting material are therefore not included in Fig. 7. Allabar and Nowak (2018) and Allabar et al. (2020a, b) also observed decompression-rate-independent behavior in hydrous VAD79 melts, with high logVNDs (4.6–6.4) consistent with spinodal decomposition and deviating from the DRM trend (Fig. 7). This underscores that sample geometry, initial starting material, and experimental conditions can critically influence VNDs. Specifically, VNDs can be lower by orders of magnitude if the sample size is too small, if powder is used as the starting material, or if the decompression rate is too slow. A detailed description of the experiments referenced in Fig. 7 is included in Appendix B.

Fitting the DRM to the VNDs related to coalesced samples of this study and to samples of Marxer et al. (2015) result in σ values of 0.09 and 0.035 N m^{-1}, respectively. According to Eq. (4), the slope of the DRM remains constant at 3/2, reflecting its dependency on the diffusion coefficient of H_2O. This relationship allows Eq. (4) to be simplified to Eq. (7):

$$\log\text{VND} = 3/2 \cdot \log(dP/dt) + y, \quad (7)$$

where y represents the intercept on the logVND y axis (Fig. 7). This y-axis intercept is influenced by the surface tension, which in turn depends on both the H_2O concentration and the composition of the melt, leading to a vertical shift of the DRM line.

The question remains why the vesicle coalescence behavior adheres to the DRM line. Vesicle coalescence occurs in three primary stages: (1) the approach of vesicles, facilitated by external and/or internal forces such as vesicle growth (e.g., Maruishi and Toramaru, 2022); (2) the drainage of the melt film between vesicles to a critical thickness until it ruptures; and (3) the relaxation to a spherical shape driven by surface tension (e.g., Eri and Okumura, 2010). Various forces contribute to film drainage in magmas, including gravitational forces (Proussevitch et al., 1993), capillary

forces (Nguyen et al., 2013; Proussevitch et al., 1993), vesicle growth (Castro et al., 2012), and shear deformation in conduit flow (e.g., Caricchi et al., 2011).

In our samples, we observed only the initial and final stages of vesicle coalescence. Only spherical and separated vesicles are observed in the homogeneous vesiculated areas that grew during ongoing decompression (Maruishi and Toramaru, 2022) as well as the final stage of the complete relaxation to spherical shapes in coalesced vesicles (Eri and Okumura, 2010). While evaluating the vesicle shapes in quenched glass, it is important to consider the effects of shrinkage. Most large coalesced vesicles exhibit nearly perfect spherical shapes. Although the VND decreased during coalescence, convergence of vesicles was not observed in the quenched samples.

A recent study by Ohashi et al. (2022) suggests that variations in VND during decompression can be explained by the capillary number ($Ca = \eta R^{\cdot}/\sigma$), which depends on the liquid viscosity (η), the vesicle growth rate ($R^{\cdot}$), and the surface tension (σ). The capillary number represents the interplay between the viscous force arising from vesicle growth and the capillary force. At $Ca \ll 1$, two adjacent vesicles retain their spherical shapes until the film between them ruptures, a process governed by capillary forces. Conversely, at $Ca \gg 1$, vesicles flatten with a constant film thickness, and vesicle growth drives film drainage. This distinction categorizes the coalescence process into capillary-dominated and growth-dominated regimes. An increase in vesicle growth rate and liquid viscosity prolongs the drainage timescale, consequently affecting the percolation threshold, which is defined as the porosity at which the vesiculated magma becomes permeable.

Ohashi et al. (2022) stated that Ca varies significantly with the eruption style of volcanoes. As the viscosity of magma increases due to the exsolution of dissolved H_2O and as vesicle growth accelerates towards the fragmentation depth, Ca varies considerably, spanning multiple orders of magnitude. In high-viscosity melts, a high Ca leads to the development of larger vesicles, which increases the resistance to coalescence. This can elevate the percolation threshold and explain why such magma erupts explosively without significant outgassing. According to Castro et al. (2012), an increase in the ratio of vesicle size also increases the inter-vesicle pressure gradient, resulting in the formation of a dimpled structure. This distinctive geometry may be notable for $Ca \ll 1$, where the Laplace pressure determines the pressure within vesicles.

Ohashi et al. (2022) found a correlation between VND and Ca at the final pressure, where Ca decreases with decreasing VND. The range of Ca where VND changes drastically ($0.1 < Ca < 100$) coincides with the range where the non-dimensional drainage timescale varies steeply. However, they were unable to apply the scaling of Ca to calculate the temporal change of VND. They plan to address this calculation in future studies. Furthermore, their concept does not provide a tool to explain our observed behavior of the VND tendency in the coalesced stage according to the DRM of Toramaru (2006). Based on their investigations, it is evident that variations in viscosity and surface tension during the vesicle growth significantly influence coalescence behavior in the melt.

Numerous models exist to calculate or simulate vesicle growth during decompression or equilibration at specific pressures (e.g., Gardner, 2007; Castro et al., 2012; Huber et al., 2014; Mancini et al., 2016; Giachetti et al., 2019; Coumans et al., 2020; Ohashi et al., 2022). However, no current equations or models can predict a specific VND at which vesicle coalescence will commence. For instance, Mancini et al. (2016) developed a growth-coalescence model based on the coalescence model by Castro et al. (2012). This kinetic model statistically describes vesicle growth due to decompression, volatile exsolution, and coalescence of a polydisperse vesicle population. However, their model assumes steady-state vesiculation processes and does not account for changes in viscosity and H_2O diffusivity during decompression and exsolution of H_2O.

The volatile content in magma significantly influences its bulk density (e.g., Wilson et al., 1980) and bulk viscosity (e.g., Mader et al., 2013). Additionally, H_2O diffusivity and viscosity strongly affect vesicle formation, growth, and coalescence. H_2O diffusivity controls the diffusive growth of vesicles, while the expansion of vesicles due to pressure–volume–temperature (PVT) changes is influenced by melt viscosity (Sparks et al., 1994), which itself is affected by the concentration of dissolved H_2O (e.g., Giordano et al., 2008). Furthermore, $c_{H_2O_t}$ significantly impacts the surface tension of vesicles (Shea, 2017), a critical factor in determining the work required for critically sized vesicle formation in the DRM model proposed by Toramaru (2006). However, the DRM model utilizes only a single value for σ to predict VND across various decompression rates.

To explain and predict the measured VND during ongoing decompression and its dependency on decompression rate, a model that accounts for dynamically evolving parameters such as H_2O content, surface tension, viscosity, vesicle size, and growth rate is required. Specifically, understanding how surface tension changes when vesicles begin to coalesce is crucial. We assert that a substantial amount of experimental work, involving varying melt compositions, decompression rates, and H_2O contents, is essential for developing a comprehensive prediction model for coalescence. This work can contribute to understanding why coalescence is evidently decompression rate-dependent, while the initial number of vesicles is decompression rate-independent.

4.5 The behavior of H_2O during decompression

The evaluation of the absorption spectra of degassed samples reveals further effects of resorption. The H_2O concentrations measured in the glass do not correspond to the $c_{H_2O_t}$ in the melt state. Even if the actual $c_{H_2O_t}$ in the residual melt is un-

known, according to Hajimirza et al. (2019) the relative importance of H_2O diffusion during decompression can be determined by the ratio of the diffusion timescale (τ_{diff}) to the timescale of decompression (τ_d). If the diffusion timescale is shorter than the decompression timescale ($\tau_{diff}/\tau_d \ll 1$), near-equilibrium degassing is facilitated, and degassing is controlled by the decompression rate. For experiments where $\tau_{diff}/\tau_d \gg 1$, H_2O diffusion into vesicles will be too slow to significantly affect saturation within the bulk of the sample. The high logVNDs during the homogeneous vesicle stages are expected to represent near-equilibrium melt degassing due to the rapid reduction of H_2O supersaturation during further decompression from the melt into surrounding vesicles (Marks and Nowak, 2025). In the decompression experiments, vesicles are observed in the glass at P_f ranging from 80 to 50 MPa, depending on the decompression rate and c_{H_2Oi}, so τ_d can be asserted to the time between the pressure at which phase separation occurs and P_f. The τ_{diff} (Eq. 8) is dependent on the characteristic diffusion length l (in mm) and the total H_2O diffusivity (D_{H_2O}) in ($mm^2\,s^{-1}$) (Eq. 6), calculated according to Schmidt et al. (2013) (in $m^2\,s^{-1}$). The l factor is defined by the inter-vesicle distance calculated according to Eq. (9) (Hajimirza et al., 2019).

$$\tau_{diff} = l^2/D_{H_2O}, \tag{8}$$

$$l = \frac{1-\left(\frac{\Phi_{EOS}}{100}\right)^{\frac{1}{3}}}{\left(1-\frac{\Phi_{EOS}}{100}\right)^{\frac{1}{3}}}\left(\frac{4\pi}{3}\mathrm{VND}\right)^{-\frac{1}{3}}. \tag{9}$$

For a consistent calculation, we use Φ_{EOS} as porosity. A conservative estimate of D_{H_2O}, and thus of τ_{diff}, is realized using c_{H_2Oeq} at the P_f of each experiment (Table 1), resulting in the slowest possible H_2O diffusivity. For the onset of vesiculation, we used 80 MPa for both c_{H_2Oi} at rates of 1.7 and 0.17 MPa s^{-1}, 70 MPa for c_{H_2Oi} of 5.7 wt % and 0.064 MPa s^{-1}, and 50 MPa for c_{H_2Oi} of 5.0 wt % and 0.064 MPa s^{-1}. These starting pressures provide a conservative estimate of τ_{diff}/τ_d, as it is likely that vesiculation started earlier at higher P and vesicles were completely resorbed in the high P_f experiments (Allabar et al., 2020b; Marks and Nowak, 2025). The calculated mean l values of ~ 7.2 µm in Table 2 fit very well to the estimated inter-vesicle distances v_d of 7–9 µm according to Hertz (1908). The obtained τ_{diff}/τ_d values, with ratios of < 1, indicate equilibrium degassing in the homogeneously vesiculated melt volumes with high logVNDs > 4.7 and $\Delta P > 20$ MPa for the 1.7 MPa s^{-1} decompression series. In contrast, an increased ΔP of 30 MPa is necessary for the slower decompression rates.

Data from the coalesced volumes have τ_{diff}/τ_d ratios $\gg 1$ (Fig. 8, Table 1), falling within the field of disequilibrium degassing. This is related to an increase in l due to an ongoing decrease in logVND and c_{H_2Ot}, correlated with the D_{H_2O} dependence on c_{H_2Ot} in the melt (Schmidt et al., 2013). As coalescence continues, the supersaturation between the existing vesicles increases, potentially leading to a second degassing process in the residual melt (Allabar et al., 2020a). The H_2O diffusion from the interstitial melt into the large vesicles will not be fast enough to effectively reduce the H_2O supersaturation that builds up during further continuous decompression. This may result in a secondary homogeneous vesicle formation event at $c_{H_2Ot} < c_{H_2Oi}$ and lower P_f compared to the initial vesicle population, resulting in lower Φ_{equ} and lower Φ_{glass}. However, no evidence of a secondary vesicle formation event was observed in the samples of this study. Therefore, if we had decompressed these samples further to lower P_f, a second vesicle formation event would be expected between the large coalesced vesicles, as the diffusion of H_2O would no longer be fast enough in the H_2O-depleted melt. However, most of the capsules are already significantly expanded, so further decompression lower than 30 MPa would not have been feasible as the capsule would burst (Figs. S1 and S2).

In addition to the resorption of H_2O from fluid vesicles back into the melt during quenching, the increasing l with progressing coalescence and decreasing VND contributes to the high c_{H_2Ot} values measured in glasses between coalesced vesicles (Fig. 5). The c_{H_2Ot} measurements in the residual glass are substantially higher than c_{H_2Oeq}, exceeding it by 1 wt %–2 wt %. Measurements through homogeneous vesiculated areas with vesicles in the beam path yielded c_{H_2Ot} values as high as 10 wt % H_2O, which surpass the solubility of the LLST melt by more than 8 wt % (Fig. 5, Table 1). The supercritical H_2O fluid in the vesicles is quenched to water and gas phase at room temperature (Allabar et al., 2020b). Therefore, absorption spectra collected through highly vesiculated volumes should be evaluated using the appropriate absorption coefficients, glass density, and the presence of H_2O-filled vesicles. Absorption coefficients for liquid H_2O are in the range of 5 and 10 L mol^{-1} cm^{-1} in the near-infrared region (Bertie and Lan, 1996), whereas the molar absorption coefficients of LLST glass were determined to $\varepsilon_{H_2Om} = 1.27 \pm 0.04$ and $\varepsilon_{OH} = 1.15 \pm 0.07$ L mol^{-1} cm^{-1} (Marks and Nowak, 2025). Further adjustments to the evaluation of the NIR spectra would be necessary to eliminate the effect of liquid H_2O in the vesicles. For this reason, only measurements in vesicle-free glass volumes should be evaluated.

The samples in Fig. 5 that show almost c_{H_2Oi} were also measured through H_2O vesicles. However, due to the low porosity and small vesicle size, the effect of liquid H_2O captured in vesicles is negligible here. Samples of Fig. 5d, e, and f demonstrate how strongly the measured H_2O content of the samples depends on VND, porosity, and vesicle size. As the proportion of H_2O vesicles in the beam path increases, the measured H_2O content also increases. This case illustrates the importance of accurately analyzing the sample volume to ensure pure glass conditions when assessing the residual melt conditions.

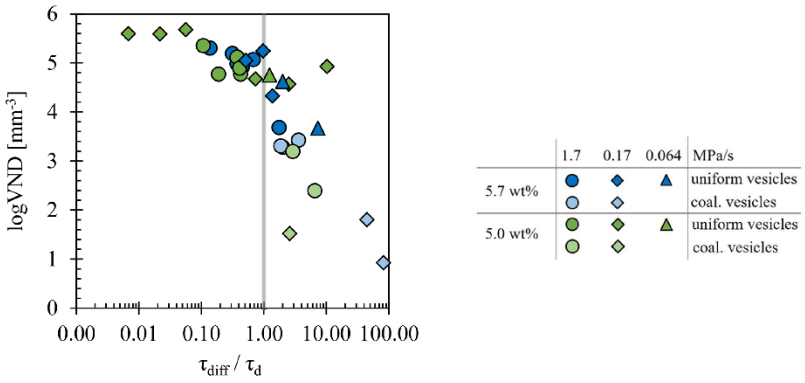

Figure 8. Ratio of diffusion timescale to decompression timescale (τ_{diff}/τ_d) as a function of VND. Blue symbols indicate a c_{H_2Oi} of 5.7 wt %, while green symbols show experiments with c_{H_2Oi} of 5.0 wt %. Decompression rates are represented by circles for 1.7 MPa s^{-1}, diamonds for 0.17 MPa s^{-1}, and triangles for 0.064 MPa s^{-1}. Bright symbols show coalesced volumes, whereas dark symbols represent pristine uniformly vesiculated volumes.

5 Implications for volcanic eruptions

The rapid transformation of initial VND from decompression rate independence with high logVNDs of ∼ 5.5 towards the stage of coalescence, with orders of magnitude lower VNDs that became decompression rate dependent, aligns with the VND prediction according to DRM (Toramaru, 2006). This shift has important implications for understanding magma dynamics during ascent in volcanic conduits. In general, when a homogeneous magma becomes supersaturated in volatiles, vesicle formation occurs through the rapid exsolution of H_2O. High VNDs result in a rapid reduction of the H_2O supersaturation, with vesicle growth proceeding through diffusional H_2O uptake during decompression.

In this study, in the first vesiculation stage high logVNDs of 5.1–5.7 were observed, which align with previous findings of log VNDs of 4–6 in both experimental and natural phonolitic and trachytic samples from Vesuvius and Campi Flegrei (Marxer et al., 2015; Allabar et al., 2018; Gurioli et al., 2005; Mastrolorenzo et al., 2001). At these high VND levels, near-equilibrium degassing from the melt into the vesicles is anticipated. Further vesicle expansion during magma ascent is driven by continued H_2O diffusion into vesicles, facilitated by the reduced solubility of H_2O in the silicate melt and the expansion of the fluid phase under decompression. As vesiculation progresses, decompression rates may increase, driven by buoyancy forces acting on the melt, and decreasing density as vesicles expand (e.g., Wilson et al., 1980). Additionally, vesicles may rise relative to the magma, according to their size and the magma's viscosity, thereby undergoing coalescence and decompressive expansion (Proussevitch et al., 1993).

In open systems, vesicle coalescence can result in high permeability, allowing H_2O to escape at the top of the magma column. Recent experimental studies indicate that the presence of crystals, such as phenocrysts and microlites, promotes vesicle coalescence and reduces the percolation threshold (Cáceres et al., 2022; DeGraffenried et al., 2019). In contrast, in closed systems, vesicles may accumulate as foam at the top of the magma chamber, forming large gas-pressurized pockets that may lead to a final disruption and eruption of the magma. Foams with higher melt viscosity are less likely to disrupt quickly, leading to less frequent but more energetic eruptions compared to lower-viscosity foams, as is typically observed (Proussevitch et al., 1993).

With increasing decompression rates, the time available for vesicle coalescence is reduced, potentially allowing the initially high VND to be preserved up to the surface. Figure 9 illustrates the increase in ϕ_{eq} as final pressure decreases. The porosity values reflect the evolution of the ascending melt. During ascent, the melt becomes supersaturated, without vesicle formation and no reduction in supersaturation (Fig. 9d1). Upon reaching sufficiently low pressures necessary for vesicle formation, the porosity undergoes a rapid increase due to the exsolution of H_2O from the melt over a very brief time interval. This interval decreases with higher decompression rates (Fig. 9d2).

At the highest decompression rate of 1.7 MPa s^{-1} applied in this study (Fig. 9c), porosity increases from 0 vol % to ∼ 35 vol % over a pressure decrease of 10–20 MPa (depending on c_{H_2Oi}), which corresponds to a time span of roughly 6 to 12 s. Although these values are derived from experimental conditions, it is expected that such an extreme increase in porosity, along with the associated buoyant forces, would limit the time available for coalescence and hinder the reduction of magma chamber overpressure. Despite this, if the coalescence stage is reached, ϕ_{eq} increases at a more gradual rate (Fig. 9d3). However, the viscosity of silica-rich melts increases by orders of magnitude as H_2O exsolves (Prous-

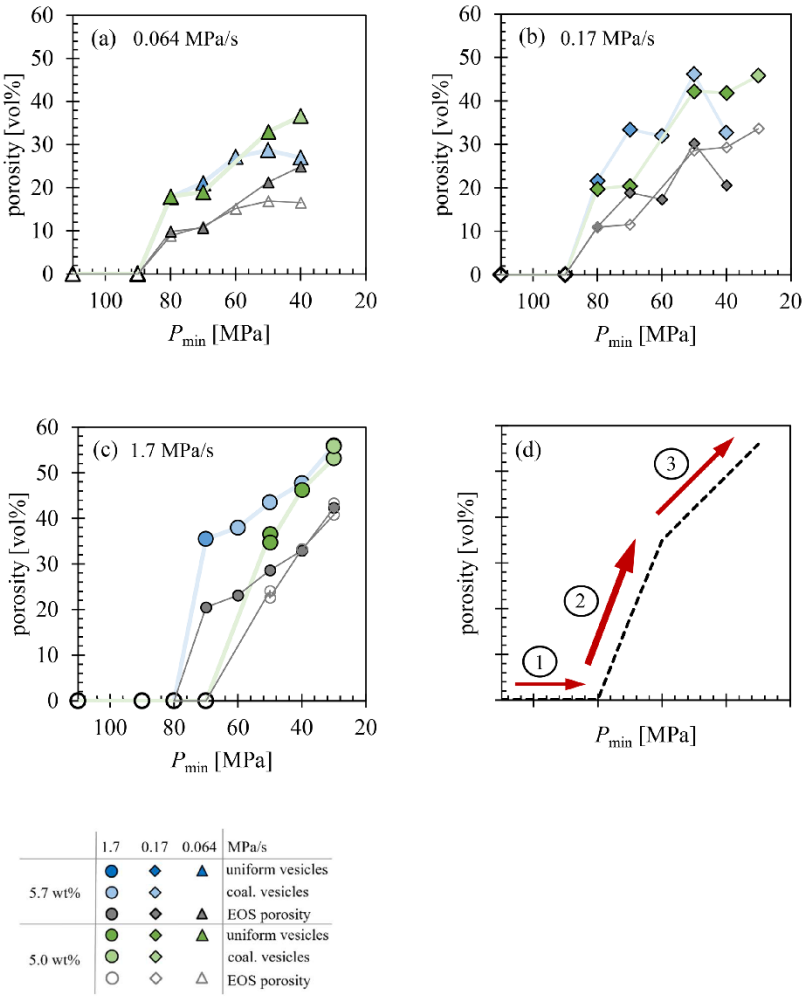

Figure 9. Porosity increases with decreasing final pressure at decompression rates of **(a)** 0.064 MPa s^{-1}, **(b)** 0.17 MPa s^{-1}, and **(c)** 1.7 MPa s^{-1}. The equilibrium melt porosity, calculated according to Eq. (1), is shown in blue for a c_{H_2Oi} of 5.7 wt % and in green for a c_{H_2Oi} of 5.0 wt %. The EOS porosity, calculated according to Eq. (3), is depicted with filled gray symbols for 5.7 wt % and unfilled gray symbols for 5.0 wt %. Panel **(d)** illustrates the general trend of increasing porosity with decreasing final pressure. The numbers indicate: (1) supersaturation of the melt without degassing, where supersaturation continues to increase; (2) onset of degassing, characterized by a rapid increase in porosity and the attainment of maximal VNDs within short timescales; (3) vesicle coalescence, during which porosity increases at a more gradual rate.

sevitch et al., 1993; Sparks, 1978), reducing the ascent rate of vesicles. This observation corresponds with findings by Gardner (2007), where a VND dependence on melt viscosity was noted: in high-viscosity melts, such as rhyolites, the initial high VND tends to be preserved, whereas in lower-viscosity melts like phonolite, coalescence significantly decreases the original VND by one to two orders of magnitude.

Our study supports this VND overprint in low-viscosity phonolitic melt, as similar VND values were observed at various decompression rates during the initial phase of phase separation, followed by significant decrease at the onset of coalescence. Consequently, VND values in natural pumice may not directly correlate with decompression rates, given that VND can vary substantially during magma ascent. Thus, the bulk composition of the melt exerts a substantial influence on the vesiculation process under decompression, and thereby, on ascent dynamics within volcanic conduits.

Appendix A

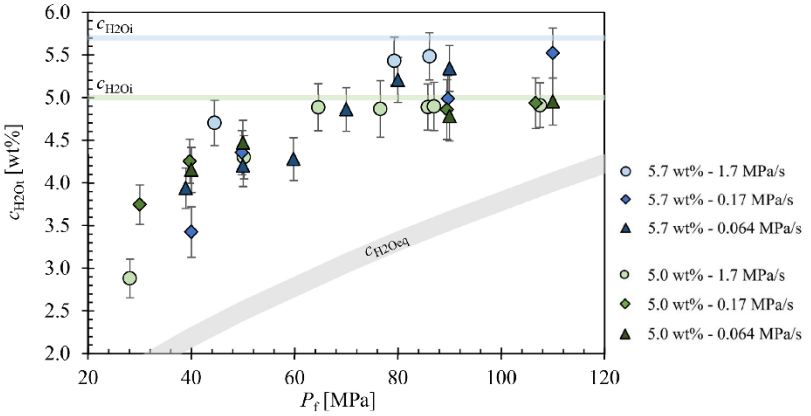

Figure A1. Extended diagram of Marks and Nowak (2025). The residual c_{H_2Ot} in the glass is plotted against the final pressure (P_f) of the decompressed samples. Only samples that were able to be measured undisturbed by vesicles in the beam path are shown. The equilibrium H_2O content (c_{H_2Oeq}) curve was calculated according to Eq. (5) therein.

Appendix B: Description of the experiments in Fig. 7

The first superliquidus decompression experiments using Vesuvius white pumice phonolite (VAD79) were conducted by Iacono-Marziano et al. (2007). Utilizing a similar experimental setup, which employed vertically operating TZM (titanium–zirconium–molybdenum alloy) cold-seal pressure vessels, the initial glass cylinders were subjected to decompression under superliquidus conditions at 1323 K within a pressure range of 200–10 MPa. Although four different decompression rates were tested, only the fastest two rates of 0.17 and 4.8 MPa s^{-1} were applied via continuous decompression and are thus represented in Fig. 7. Their study demonstrated that the experimental investigation of hydrous melt phase separation at low decompression rates (0.0028 and 0.024 MPa s^{-1}) was limited by the capsule size. The small capsule diameter of 2.4 mm inhibited the formation of homogeneously formed vesicles in the sample center due to the diffusional loss of H_2O towards heterogeneously nucleated fringe vesicles at the capsule wall, nucleated at low supersaturation during decompression. However, in samples subjected to rapid decompression, a high logVND of $\sim 5.8\,mm^{-3}$ was observed at a ΔP of 125 to 130 MPa, with no clear dependence of VND on decompression rates ranging from 1.7 to 4.6 MPa s^{-1}. Experiments conducted to lower P_f indicated that vesicles expanded rapidly at a ΔP of about 150 MPa, reaching the process of coalescence at $\Delta P \geq 180$ MPa. This coalescence led to a significant reduction in VND, with values dependent on P_f, resulting in very low VNDs.

While the data from Iacono-Marziano et al. (2007) exhibit a variable VND distribution due to increasing coalescence, the data from Marxer et al. (2015) show a trend similar to the predicted DRM. This trend can be attributed to the capsule design. Marxer et al. (2015) examined the same phonolitic VAD79 composition at the same superliquidus temperature of 1323 K in an IHPV. Capsules with diameters of 2.5 mm and 5.0 mm were used, which were filled with glass cylinders and H_2O to achieve slightly supersaturated and slightly undersaturated melt conditions, respectively. The hydrous melts were decompressed from 200 to 75 MPa at rates ranging from 0.0028 to 1.7 MPa s^{-1}. Only the continuous decompression experiments were included in Fig. 7, as the single-step and multi-step methods do not represent a true decompression pathway (Marxer et al., 2015).

Analysis of the experimental results showed that the 2.5 mm capsules were too small in diameter. Early degassing of the sample due to heterogeneous vesicle nucleation and growth at the capsule-melt interface can prevent homogeneous formation in the sample center if the nominal decompression rate is sufficiently low (Mangan and Sisson, 2000; Iacono-Marziano et al., 2007). H_2O diffusion into heterogeneously nucleated vesicles leads to a depletion of H_2O in the sample center, thereby preventing homogeneous vesicle formation. The samples achieved homogeneous vesicle formation in the central melt volume only at the fastest rate of 1.7 MPa s^{-1}, with logVNDs of ~ 4.3, due to the shorter diffusion time. Therefore, it is essential to clearly distinguish the VND between homogeneous vesicle formation observed at a decompression rate of 1.7 MPa s^{-1} and heterogeneous

nucleation at the capsule melt interface observed at decompression rates of 0.0028, 0.024, and 0.17 MPa s^{-1}, which are too slow for the used capsule diameter. In this case, the VNDs follow the DRM.

Preuss et al. (2016) utilized slightly H_2O-undersaturated trachytic Campi Flegrei and phonolitic VAD79 melts. Decompression experiments in the IHPV with either glass cylinders of 5 mm in diameter or glass powder used as starting material were decompressed at a superliquidus temperature of 1323 K from 200 MPa to P_f of 100, 75, and 60 MPa using continuous decompression rates of 0.024 and 0.17 MPa s^{-1}. Decompression of all samples with glass cylinders as starting material led to homogeneous vesicle formation with high logVNDs of ~ 5.6. The supersaturation pressures for homogeneous vesicle formation were estimated to be < 76 MPa for the trachytic and < 70 MPa for the phonolitic melt. The decompressed samples with powder as starting material resulted in reduced logVNDs by several orders of magnitude due to initially entrapped air in the powder pore space. This led to the formation of tiny H_2O-N_2 vesicles throughout the melts prior to decompression. Degassing of these samples was facilitated by diffusive growth of these pre-existing vesicles. Thus, an H_2O supersaturation of the melt was not achieved. The samples with glass powder used as starting material are therefore not included in Fig. 7. The VNDs observed in samples with glass cylinders as the starting material exhibit degassing behavior similar to the results of this study that is independent of the decompression rate.

Similar observations were made by Allabar and Nowak (2018) and Allabar et al. (2020a). They conducted decompression experiments with hydrous phonolitic melts of VAD79 composition at undersaturated, saturated, and slightly supersaturated H_2O conditions at superliquidus temperatures of 1323 and 1373 K. Samples with glass cylinders with diameters of 5 mm used as starting material were decompressed at rates ranging from 0.024 to 1.7 MPa s^{-1}. They reported high logVNDs, covering a range of 4.6 to 6.4 mm^{-3}, resulting in a mean logVND of ~ 5.3 across the entire dataset. Consequently, the data plotted consistently in the field of homogeneous vesicle formation (Fig. 7) and exhibited a decompression-rate-independent VND, consistent with the concept of spinodal decomposition, deviating significantly from the DRM trend.

Data availability. All data derived from this research are presented in the enclosed tables, figures, and the Supplement.

Supplement. The supplement related to this article is available online at https://doi.org/10.5194/ejm-37-413-2025-supplement.

Author contributions. PLM: conceptualization, sample preparation, experiments, analysis and evaluation, software, visualization, writing of the original draft, organization; MN: conceptualization, supervision, manuscript revision.

Competing interests. The contact author has declared that neither of the authors has any competing interests.

Disclaimer. Publisher's note: Copernicus Publications remains neutral with regard to jurisdictional claims made in the text, published maps, institutional affiliations, or any other geographical representation in this paper. While Copernicus Publications makes every effort to include appropriate place names, the final responsibility lies with the authors.

Special issue statement. This article is part of the special issue "Probing the Earth: experiments on and for our planet". It is a result of the EMPG 2023 conference, Milan, Italy, 12–15 June 2023.

Acknowledgements. We thank Barbara Maier and Annette Flicker for technical support, Simone Schafflick for the high-quality sample preparation and Dennis Eul for support in the laboratory.

Financial support. This research has been supported by the Deutsche Forschungsgemeinschaft (grant no. NO378/15-1).

This open-access publication was funded by the Open Access Publication Fund of the University of Tübingen.

Review statement. This paper was edited by Francois Holtz and reviewed by Mathieu Colombier and Caroline Martel.

References

Allabar, A. and Nowak, M.: Message in a bottle: Spontaneous phase separation of hydrous Vesuvius melt even at low decompression rates, Earth Planet. Sc. Lett., 501, 192–201, https://doi.org/10.1016/j.epsl.2018.08.047, 2018.

Allabar, A., Dobson, K. J., Bauer, C. C., and Nowak, M.: Vesicle shrinkage in hydrous phonolitic melt during cooling, Contrib. Miner. Petr., 175, 21, https://doi.org/10.1007/s00410-020-1658-3, 2020a.

Allabar, A., Salis Gross, E., and Nowak, M.: The effect of initial H_2O concentration on decompression-induced phase separation and degassing of hydrous phonolitic melt, Contrib. Miner. Petr., 175, 22, https://doi.org/10.1007/s00410-020-1659-2, 2020b.

Barclay, J., Riley, R. S., and Sparks, R. S. J.: Analytical models for bubble growth during decompression of high viscosity magmas, Bull. Volcanol., 57, 422–431, https://doi.org/10.1007/BF00300986, 1995.

Berndt, J., Liebske, C., Holtz, F., Freise, M., Nowak, M., Ziegenbein, D., Hurkuck, W., and Koepke, J.: A combined rapid-quench

and H_2-membrane setup for internally heated pressure vessels: Description and application for water solubility in basaltic melts, Am. Mineral., 87, 1717–1726, https://doi.org/10.2138/am-2002-11-1222, 2002.

Bertie, J. E. and Lan, Z.: Infrared Intensities of Liquids XX: The Intensity of the OH Stretching Band of Liquid Water Revisited, and the Best Current Values of the Optical Constants of H_2O(l) at 25 °C between 15,000 and 1 cm^{-1}, Appl. Spectrosc., 50, 1047–1057, https://doi.org/10.1366/0003702963905385, 1996.

Blower, J., Keating, J. P., Mader, H. M., and Phillips, J. C.: Inferring Volcanic Degassing Processes From Vesicle Size Distributions, Geophys. Res. Lett., 28, 347–350, https://doi.org/10.1029/2000GL012188, 2001.

Burnham, C. W. and Davis, N. F.: The role of H_2O in silicate melts, 1: P−V −T relations in the system $NaAlSi_3O_8$–H_2O to 10 kilobars and 1000 °C, Am. J. Sci., 270, 54–79, https://doi.org/10.2475/ajs.270.1.54, 1971.

Cáceres, F., Scheu, B., Colombier, M., Hess, K. U., Feisel, Y., Ruthensteiner, B., and Dingwell, D. B.: The roles of microlites and phenocrysts during degassing of silicic magma, Earth Planet. Sc. Lett., 577, 117264, https://doi.org/10.1016/j.epsl.2021.117264, 2022.

Candela, P. A.: Physics of aqueous phase evolution in plutonic environments, Am. Mineral., 76, 1081–1091, 0003-004X/91/0708−1081, 1991.

Caricchi, L., Pommier, A., Pistone, M., Castro, J., Burgisser, A., and Perugini, D.: Strain-induced magma degassing: Insights from simple-shear experiments on bubble bearing melts, Bull. Volcanol., 73, 1245–1257, https://doi.org/10.1007/s00445-011-0471-2, 2011.

Cashman, K. and Mangan, M.: Physical Aspects of Magmatic degassing II. Constraints on vesiculation processes from textural studies of eruption products, Rev. Mineral., 30, 477–478, https://doi.org/10.1515/9781501509674-018, 1994.

Cashman, K. V., Mangan, M. T., and Newman, S.: S. Surface degassing and modifications to vesicle size distributions in active basalt flows, J. Volcanol. Geoth. Res., 61, 45–68, https://doi.org/10.1016/0377-0273(94)00015-8, 1994.

Castro, J. M., Burgisser, A., Schipper, C. I., and Mancini, S.: Mechanisms of bubble coalescence in silicic magmas, Bull. Volcanol., 74, 10, 2339–2352, https://doi.org/10.1007/s00445-012-0666-1, 2012.

Coumans, J. P., Llewellin, E. W., Wadsworth, F. B., Humphreys, M. C. S., Mathias, S. A., Yelverton, B. M., and Gardner, J. E.: An experimentally validated numerical model for bubble growth in magma, J. Volcanol. Geoth. Res., 402, 107002, https://doi.org/10.1016/j.jvolgeores.2020.107002, 2020.

DeGraffenried, R. L., Larsen, J. F., Graham, N. A., and Cashman, K. V.: The influence of phenocrysts on degassing in crystal-bearing magmas with rhyolitic groundmass melts, Geophys. Res. Lett., 46, 5127–5136, https://doi.org/10.1029/2018GL081822, 2019.

DeVries, A. J.: Foam stability: Part II. Gas diffusion in foams, Delft, the Netherlands, 77, 209–223, https://doi.org/10.1002/recl.19580770302, 1958.

Duan, Z. H. and Zhang, Z. G.: Equation of state of the H_2O, CO_2, and H_2O- CO_2 systems up to 10 GPa and 2573.15 K: Molecular dynamics simulations with ab initio potential surface, Geochim. Cosmochim. Ac., 70, 2311–2324, https://doi.org/10.1016/j.gca.2006.02.009, 2006.

Eichelberger, J. C., Carrigan, C. R., Westrich, H. R., and Price, R. H.: Non-explosive silicic volcanism, Nature, 323, 598–602, https://doi.org/10.1038/323598a0, 1986.

Eri, A. and Okumura, K.: Bursting of a thin film in a confined geometry: Rimless and constant-velocity dewetting, Phys. Rev. E, 8, 1–4, https://doi.org/10.1103/PhysRevE.82.030601, 2010.

Fortelny, I., Ziviny, A., and Juza, J.: Coarsening of the phase structure in immiscible polymer blends: Coalescence or Ostwald ripening?, J. Polymer Sci. B: Polymer Phys., 37, 181–187, https://doi.org/10.1002/(SICI)1099-0488(19990201)37:3<181::AID-POLB1>3.0.CO;2-I, 1999.

Gardner, J. E.: Bubble coalescence in rhyolitic melts during decompression from high pressure, J. Volcanol. Geoth. Res., 166, 161–176, https://doi.org/10.1016/j.jvolgeores.2007.07.006, 2007.

Gardner, J. E. and Ketcham, R. A.: Bubble nucleation in rhyolite and dacite melts: temperature dependence of surface tension, Contrib. Miner. Petrol., 162, 929–943, https://doi.org/10.1007/s00410-011-0632-5, 2011.

Gardner, J., Thomas, R. M. E., Jaupart, C., and Tait, S.: Fragmentation of magma during Plinian volcanic eruptions, Bull. Volcanol., 58, 144–162, https://doi.org/10.1007/s004450050132, 1996.

Gardner, J. E., Hilton, M., and Carroll, M. R.: Experimental constraints on degassing of magma: isothermal bubble growth during continuous decompression from high pressure, Earth Planet. Sc. Lett., 168, 201–218, https://doi.org/10.1016/S0012-821X(99)00051-5, 1999.

Gardner, J. E., Burgisser, A., Hort, M., and Rutherford, M.: Experimental and model constraints on degassing of magma during ascent and eruption, Geol. Soc. Am. Bull. Spec. Pap., 402, 99–114, https://doi.org/10.1130/2006.2402(04), 2006.

Gardner, J. E., Wadsworth, F. B., Carley, T. L., Llewellin, E. W., Kusumaatmaja, H., and Sahagian, D.: Bubble Formation in Magma, Ann. Rev. Earth Planet. Sci., 51, 131–154, https://doi.org/10.1146/annurev-earth-031621-080308, 2023.

Genareau, K., Proussevitch, A. A., Durant, A. J., Mulukutla, G., and Sahagian, D. L.: Sizing up the bubbles that produce very fine ash during explosive volcanic eruptions, Geophys. Res. Lett., 39, L15306, https://doi.org/10.1029/2012GL052471, 2012.

Giachetti, T., Gonnermann, H. M., Gardner, J. E., Burgisser, A., Hajimirza, S., Earley, T. C., Truong, N., and Toledo, P.: Bubble coalescence and percolation threshold in expanding rhyolitic magma, Geochem. Geophys. Geosyst., 20, 1054–1074, https://doi.org/10.1029/2018GC008006, 2019.

Giordano, D., Potuzak, M., Romano, C., Dingwell, D. B., and Nowak, M.: Viscosity and glass transition temperature of hydrous melts in the system CaAl2Si2O8-CaMgSi2O6, Chem. Geol., 256, 203–215, https://doi.org/10.1016/j.chemgeo.2008.06.027, 2008.

Gonnermann, H. M. and Manga, M.: The Fluid Mechanics Inside a Volcano, Annu. Rev. Fluid Mech., 39, 321–356, https://doi.org/10.1146/annurev.fluid.39.050905.110207, 2007.

Gurioli, L., Houghton, B. F., Cashman, K. V., and Cioni, R.: Complex changes in eruption dynamics during the 79 AD eruption of Vesuvius, Bull. Volcanol. 67, 144–159, https://doi.org/10.1007/s00445-004-0368-4, 2005.

Hajimirza, S., Gonnermann, H. M., Gardner, J. E., and Giachetti, T.: Predicting homogeneous bubble nucleation in rhyolite, J. Geophys. Res.-Sol. Ea., 124, 2395–2416, https://doi.org/10.1029/2018JB015891, 2019.

Hamada, M., Laporte, D., Cluzel, N., and Koga, K. T.: Kawamoto T.: Simulating bubble number density of rhyolitic pumices from Plinian eruptions: constraints from fast decompression experiments, Bull. Volcanol., 72, 735–46, https://doi.org/10.1007/s00445-010-0353-z, 2010.

Harms, E., Gardner, J. E., and Schmincke, H. U.: Phase equilibria of the Lower Laacher See Tephra (East Eifel, Germany): constraints on pre-eruptive storage conditions of a phonolitic magma reservoir, J. Volcanol. Geoth. Res., 134, 135–148, https://doi.org/10.1016/j.jvolgeores.2004.01.009, 2004.

Herd, R. and Pinkerton, H.: Bubble coalescence in basaltic lava: Its impact on the evolution of bubble populations, J. Volcanol. Geoth. Res., 75, 137–157, https://doi.org/10.1016/s0377-0273(96)00039-x, 1997.

Hertz, P.: Über den gegenseitigen durchschnittlichen Abstand von Punkten, die mit bekannter mittlerer Dichte im Raume angeordnet sind, Math. Ann., 67, 387–398, https://doi.org/10.1007/BF01450410, 1908.

Higgins, M. D.: Measurement of crystal size distributions, Am. Mineral., 85, 1105–1116, https://doi.org/10.2138/am-2000-8-901, 2000.

Huber, C., Su, Y., Nguyen, C. T., Parmigiani, A., Gonnermann, H. M., and Dufek, J.: A new bubble dynamics model to study bubble growth, deformation, and coalescence, J. Geophys. Res.-Sol. Ea., 119, 216–239, https://doi.org/10.1002/2013JB010419, 2014.

Hurwitz, S. and Navon, O.: Bubble nucleation in rhyolitic melts: experiments at high pressure, temperature, and water content, Earth Planet. Sc. Lett., 122, 267–280, https://doi.org/10.1016/0012-821X(94)90001-9, 1994.

Iacono-Marziano, G., Schmidt, B. C., and Dolfi, D.: Equilibrium and disequilibrium degassing of a phonolitic melt (Vesuvius AD 79 "white pumice") simulated by decompression experiments, J. Volcanol. Geoth. Res., 161, 151–164, https://doi.org/10.1016/j.jvolgeores.2006.12.001, 2007.

Jaupart, C.: Gas loss from magmas through conduit walls during eruption. The physics of explosive volcanic eruptions, Geol. Soc. Lond. Spec. Pub., 145, 73–90, https://doi.org/10.1144/GSL.SP.1996.145.01.05, 1998.

Jaupart, C. and Allègre, C. J.: Gas content, eruption rate and instabilities of eruption regime in silicic volcanoes, Earth Planet. Sc. Lett., 102, 413–429, https://doi.org/10.1016/0012-821X(91)90032-D, 1991.

Klug, K. and Cashmam, K. V.: Vesiculation of May 18, 1980 Mount St. Helens magma, Geology, 22, 468–472, https://doi.org/10.1130/0091-7613(1994)022<0468:VOMMSH>2.3.CO;2, 1994.

Klug, C. and Cashman, K. V.: Permeability development in vesiculating magmas: Implications for fragmentation, Bull. Volcanol., 58, 87–100, https://doi.org/10.1007/s004450050128, 1996.

Kueppers, U., Scheu, B., Spieler, O., and Dingwell, D.B.: Fragmentation efficiency of explosive volcanic eruptions: a study of experimentally generated pyroclasts, J. Volcanol. Geoth. Res., 153, 125–135, https://doi.org/10.1016/j.jvolgeores.2005.08.006, 2006.

Larsen, J. F., Denis, M. H., and Gardner, J. E.: Experimental study of bubble coalescence in rhyolitic and phonolitic melts, Geochim. Cosmochim. Ac., 68, 333–344, https://doi.org/10.1016/S0016-7037(03)00412-5, 2004.

Mader, H. M., Llewellin, E. W., and Mueller, S. P.: The rheology of two-phase magmas: A review and analysis, J. Volcanol. Geoth. Res., 257, 135–158, https://doi.org/10.1016/j.jvolgeores.2013.02.014, 2013.

Mancini, S., Forestier-Coste, L., Burgisser, A., James, F., and Castro, J.: An expansion-coalescence model to track gas bubble populations in magmas, J. Volcanol. Geoth. Res., 313, 44–58, https://doi.org/10.1016/j.jvolgeores.2016.01.016, 2016.

Mangan, M. and Sisson, T.: Delayed, disequilibrium degassing in rhyolite magma: decompression experiments and implications for explosive volcanism, Earth Planet. Sc. Lett., 183, 441–55, https://doi.org/10.1016/S0012-821X(00)00299-5, 2000.

Mangan, M. T., Cashman, K. V., and Newman, S.: Vesiculation of basaltic magma during eruption, Geology, 21, 157–160, https://doi.org/10.1130/0091-7613(1993)021<0157:VOBMDE>2.3.CO;2, 1993.

Marks, P. L. and Nowak, M.: Vesiculation dynamics – Part 1: Decompression-induced H_2O vesicle formation in the Lower Laacher See phonolitic melt, Eur. J. Mineral., 37, 385–412, https://doi.org/10.5194/ejm-37-385-2025, 2025.

Maruishi, T. and Toramaru, A.: Effect of bubble deformation on the coalescence of two ascending bubbles in a viscous liquid, Phys. Fluids, 34, 043302, https://doi.org/10.1063/5.0082506, 2022.

Marxer, H., Bellucci, P., and Nowak, M.: Degassing of H_2O in a phonolitic melt: A closer look at decompression experiments, J. Volcanol. Geoth. Res., 297, 109–124, https://doi.org/10.1016/j.jvolgeores.2014.11.017, 2015.

Mastrolorenzo, G., Brachi, L., and Canzanella, A.: Vesicularity of various types of pyroclastic deposits of Campi Flegrei volcanic field: Evidence of analogies in magma rise and vesiculation mechanisms, J. Volcanol. Geoth. Res., 109, 41–53, https://doi.org/10.1016/S0377-0273(00)00303-6, 2001.

McIntosh, I. M., Llewellin, E. W., Humphreys, M. C. S., Nichols,A. R. L., Burgisser, A., Schipper, C. I., and Larsen, J. F.: Distribution of dissolved water in magmatic glass records growth and resorption of bubbles, Earth Planet. Sc. Lett., 401, 1–11, https://doi.org/10.1016/j.epsl.2014.05.037, 2014.

Mourtada-Bonnefoi, C. and Laporte, D.: Kinetics of bubble nucleation in a rhyolitic melt: an experimental study of the effect of ascent rate, Earth Planet. Sc. Lett., 218, 521–537, https://doi.org/10.1016/S0012-821X(03)00684-8, 2004.

Navon, O. and Lyakhovsky, V.: Vesiculation processes in silicic magmas, in: The Physics of Explosive Volcanic Eruptions, edited by: Gilbert, J. S. and Sparks, R. S. J., Geological Society, London, Special Publications, 145, 27–50, ISBN 1-86239-020-7, 1998.

Nguyen, C. T., Gonnermann, H. M., Chen, Y., Huber, C., Maiorano, A. A., Gouldstone, A., and Dufek, J.: Film drainage and the lifetime of bubbles, Geochem. Geophys. Geosyst., 14, 3616–3631, https://doi.org/10.1002/ggge.20198, 2013.

Ochs, F. A. and Lange, A. R.: The density of hydrous magmatic liquids, Science, 283, 1314–1317, https://doi.org/10.1126/science.283.5406.1314, 1999.

Ohashi, M., Maruishi, T., and Toramaru, A.: Coalescence of growing bubbles in highly viscous liquids, Geochem. Geophys. Geosyst., 23, e2022GC010618, https://doi.org/10.1029/2022GC010618, 2022.

Preuss, O., Marxer, H., Ulmer, S., Wolf, J., and Nowak, M.: Degassing of hydrous trachytic Campi Flegrei and phonolitic Vesu-

vius melts: Experimental limitations and chances to study homogeneous bubble nucleation, Am. Mineral., 101, 859–875, https://doi.org/10.2138/am-2016-5480, 2016.

Proussevitch, A. A., Sahagian, D. L., and Kutolin, V. A.: Stability of foams in silicate melts, J. Volcanol. Geoth. Res., 59, 161–178, https://doi.org/10.1016/0377-0273(93)90084-5, 1993.

Ryan, A. G., Russel, J. K., Nichols, A. R. L., Hess, K. U., and Porritt, L. A.: Experiments and models on H_2O retrograde solubility in volcanic systems, Am. Mineral., 100, 774–786, https://doi.org/10.2138/am-2015-5030, 2015.

Saar, M. and Manga, M.: Permeability-porosity relationship in vesicular basalts, Geophys. Res. Lett., 26, 111–114, https://doi.org/10.1029/1998GL900256, 1999.

Sahagian, D. and Carley, T. L.: Explosive volcanic eruptions and spinodal decomposition: a different approach to deciphering the tiny bubble paradox, Geochem. Geophys. Geosyst., 21, e2019GC008898, https://doi.org/10.1029/2019GC008898, 2020.

Sahagian, D. L., Anderson, A. T., and Ward, B.: Bubble coalescence in basalt flows; comparison of a numerical model with natural examples, Bull. Volcanol., 52, 49–56, https://doi.org/10.1007/BF00641386, 1989.

Sahimi, M.: Applications of percolation theory, London Taylor and Francis, ISBN 0-203-22153-2, https://doi.org/10.1201/9781482272444, 1994.

Schmidt, B. C. and Behrens, H.: Water solubility in phonolite melts: Influence of melt composition and temperature, Chem. Geol., 256, 259–268, https://doi.org/10.1016/j.chemgeo.2008.06.043, 2008.

Schmidt, B. C., Blum-Oeste, N., and Flagmeier, J.: Water diffusion in phonolite melts, Geochim. Cosmochim. Ac., 107, 220–230, https://doi.org/10.1016/j.gca.2012.12.044, 2013.

Shea, T.: Bubble nucleation in magmas: a dominantly heterogeneous process?, J. Volcanol. Geotherm. Res., 343, 155–170, https://doi.org/10.1016/j.jvolgeores.2017.06.025, 2017.

Sparks, R. S. J.: The dynamics of bubble formation and growth in magmas, J. Volcanol. Geoth. Res., 3, 1–37, https://doi.org/10.1016/0377-0273(78)90002-1, 1978.

Sparks, R. S. J., Barclay, J., Jaupart, C., Mader, H. M., and Phillips, J. C.: Chapter 11a. PHYSICAL ASPECTS OF MAGMA DEGASSING I. Experimental and theoretical constraints on vesiculation,Volatiles in Magmas, De Gruyter, Holloway, Berlin, Boston, 1994, 413–446. https://doi.org/10.1515/9781501509674-017, 1994.

Toramaru, A.: Formation of propagation pattern in two-phase flow systems with application to volcanic eruptions, Geophys. J., 95, 613–623, https://doi.org/10.1111/j.1365-246X.1988.tb06707.x, 1988.

Toramaru, A.: BND (bubble number density) decompression rate meter for explosive volcanic eruptions, J. Volcanol. Geoth. Res., 154, 303–316, https://doi.org/10.1016/j.jvolgeores.2006.03.027, 2006.

Wilson, L., Sparks, R. S. J., and Walker, G. P. L.: Explosive volcanic eruptions – IV. The control of magma properties and conduit geometry on eruption column behaviour, Geophys. J. Int., 63, 117–148, https://doi.org/10.1111/j.1365-246x.1980.tb02613.x, 1980.

Publication Study III

Titel: An empirical H_2O solubility model for peralkaline rhyolitic melts

Authors: Anja Allabar, Patricia L. Petri, Dennis Eul, and Marcus Nowak

Published online on April 24, 2022, in Contributions to Mineralogy and Petrology, 177, 52, https://doi.org/10.1007/s00410-022-01915-8.

Calculation scripts (MS Excel and Matlab) are provided in the supplementary material to calculate H_2O solubility in peralkaline rhyolitic melts at 27–500 MPa, 980–1523 K and excess alkali up to 0.0825.

Supplementary Information available at https://doi.org/10.1007/s00410-022-01915-8.

Contributions to Mineralogy and Petrology (2022) 177:52
https://doi.org/10.1007/s00410-022-01915-8

ORIGINAL PAPER

An empirical H_2O solubility model for peralkaline rhyolitic melts

Anja Allabar[1] · Patricia L. Petri[2] · Dennis Eul[2] · Marcus Nowak[2]

Received: 8 September 2021 / Accepted: 30 March 2022

Abstract
The H_2O solubility in peralkaline haplogranitic melts has been experimentally determined as a function of pressure (27–200 MPa) and temperature (1123–1523 K). The compositions were based on $Ab_{38}Or_{34}Qz_{28}$ (AOQ) with 4 and 8 wt% Na_2O in excess. H_2O solubility experiments were performed in an internally heated pressure vessel and quenched to glasses for analysis. For quantification of H_2O contents in the glasses using FTIR analysis, the linear molar absorption coefficients as a function of Na_2O excess with respect to AOQ composition were determined, as well as the glass densities as a function of H_2O concentration. The H_2O solubility increases with increasing pressure, decreasing temperature, and with increasing peralkalinity. A linear dependence between Na_2O excess (wt%) and H_2O solubility (wt%) was found. It has been previously shown that on a molar basis the different alkalis contribute similarly to the H_2O solubility increase so that H_2O solubility increases linearly with excess alkali (difference between mole fractions of alkalis and that of alumina). Thus, the dependence of H_2O solubility on pressure, temperature and excess alkali obtained from the new data of this study allow a simple prediction of H_2O solubility for peralkaline rhyolitic melts based on the excess alkali content. This new empirical model was tested with H_2O solubility data from literature for peralkaline haplogranitic and natural peralkaline rhyolitic melt compositions, yielding good agreement (< 10% deviation) between predicted and observed H_2O solubility, which is an improvement compared to previous models. The model can be applied to natural peralkaline rhyolitic melts that occur, e.g. on Pantelleria, Gran Canaria, or the East African Rift.

Keywords H_2O solubility · Peralkaline melt · Solubility model · Silicate melt

Introduction

Dissolved H_2O influences the physical and chemical properties of silicate melts and magmas, such as melt viscosity, density, liquidus temperature or phase equilibria. H_2O solubility in silicate melts has been experimentally determined for nearly a century (e.g. Goranson 1931; Burnham and Jahns 1962). Since then, numerous studies investigated the H_2O solubility in silicate melts as a function of pressure (P), temperature (T) and melt composition, the variables that influence H_2O solubility. In general, H_2O solubility strongly increases with increasing P, decreases or increases (depending on pressure) with increasing T, whereas the effect of melt composition on H_2O solubility is more complex. Several dependencies of H_2O solubility on chemical parameters have been shown or proposed for silicate melts.

For example in haplogranite melts, a minimum in H_2O solubility was found near metaluminous compositions, where the molar ratio of $M_2O/Al_2O_3 = 1$ (M = Li, Na, K, Rb, Cs) (Behrens 2005; Dingwell et al. 1997). Behrens and Jantos (2001) describe the increase in H_2O solubility towards peraluminous ($M_2O/Al_2O_3 < 1$) and peralkaline ($M_2O/Al_2O_3 > 1$) melts by a parabolic function. However, Dingwell et al. (1997) showed for the peralkaline side that the H_2O solubility increases linearly with peralkalinity. On a weight percent basis, the H_2O solubility decreases with the weight of the added alkali oxide at constant peralkalinity. On a molar basis, however, different alkalis (with Li as an exception) have similar effect on the H_2O solubility at constant peralkalinity (Dingwell et al. 1997). Consequently, the different contribution of alkalis to H_2O solubility on a weight percent basis is an effect of different molar weights. Dingwell et al. (1997) showed the linear

Communicated by Mark S Ghiorso.

✉ Anja Allabar
anja@allabar.de

[1] Karlsruhe, Germany

[2] Department of Geosciences, Eberhard Karls University Tübingen, Wilhelmstraße 56, 72074 Tübingen, Germany

Published online: 24 April 2022

dependence of molar H_2O solubility with excess alkali (difference in mole fraction of alkalis and that of Al) for 50 MPa and their data suggests that this dependence holds up to pressures of 500 MPa. Since then, seven studies were identified that provide H_2O solubility data in peralkaline rhyolitic melts (Linnen et al. 1996; Moore et al. 1998; Gaillard et al. 2001; Behrens and Jantos 2001; Scaillet and Macdonald 2001, 2006; Stabile et al. 2018) but no attempt was made to further systematically investigate H_2O solubility in peralkaline rhyolitic melts as a function of P, T, and composition. Some of the data were, however, used for general solubility models. Over time, various H_2O solubility models have been developed and refined, some for only rhyolitic melts (e.g. Yamashita 1999; Newman and Lowenstern 2002) or mafic melts (Iacono-Marziano et al. 2012; Shishkina et al. 2014) and models accounting for various melt compositions (e.g. Papale et al. 2016; Duan 2014; Ghiorso and Gualda 2015). A probably most recent compilation of existing H_2O solubility data including different melt compositions (and additional CO_2 as volatile) can be found in Ghiorso and Gualda (2015). All these models were recently combined by Iacovino et al. (2021) into a single, easy-to-use model engine.

The aim of this study is to systematically extend the H_2O solubility data for peralkaline rhyolitic melts as a function of P, T and peralkalinity. With these data, existing H_2O models are tested for their accuracy related to peralkaline melts. The new H_2O solubility data are thought to, e.g., help to improve the investigation of peralkaline rhyolite eruption styles that are up to now largely unknown (Clarke et al. 2019) and improving the basis for H_2O-degassing and resorption (bubble growth and bubble shrinkage) considerations during magma ascent.

The density relationship, absorption coefficients and two solubility experiments with AOQ4 composition have been preliminary published in Allabar and Nowak (2020). Detailed descriptions and discussions related to the results are given in this work.

Experimental techniques

Glass synthesis

Peralkaline haplogranitic glasses based on the AOQ composition ($Ab_{38}Or_{34}Qz_{28}$ in wt%; Holtz et al. 1995; Nowak and Behrens 1997) were synthesized for this study. With respect to AOQ composition, glasses with 2, 4 and 8 wt% Na_2O excess (Table 1) were synthesized and are further referred to

Table 1 Theoretical chemical compositions of AOQ and peralkaline haplogranite glasses (bold) and respective results of starting glasses and standard samples determined with EMPA

Composition/ sample name	SiO_2 [wt%]	Al_2O_3 [wt%]	Na_2O [Wt%]	K_2O [wt%]	Excess alkali (mole fraction)
AOQ	**76.14**	**13.53**	**4.65**	**5.68**	**0.0017**
AOQ2	**74.62**	**13.26**	**6.56**	**5.57**	**0.0227**
AOQ2 _01	75.18	12.76	6.56	5.50	0.0253
AOQ4	**73.09**	**12.99**	**8.46**	**5.45**	**0.0435**
AOQ4_1[a]	75.47	11.32	7.97	5.23	0.0471
AOQ4_2	72.84	12.85	8.76	5.55	0.0482
Std_4_0.5(2)[b]	73.71	12.41	8.39	5.49	0.0467
Std_4_1[b]	73.31	12.79	8.18	5.73	0.0438
Std_4_4[b]	73.72	12.55	8.30	5.43	0.0444
AOQ8	**70.05**	**12.45**	**12.28**	**5.23**	**0.0854**
AOQ8 _1[a]	71.03	11.54	12.24	5.19	0.0901
AOQ8 _4a	70.29	12.36	12.12	5.23	0.0842
Std_8_0.5(2)[b]	70.78	11.94	12.03	5.25	0.0859
Std_8_1[b]	70.65	12.00	11.99	5.36	0.0859
Std_8_4[b]	70.87	11.99	11.87	5.27	0.0841

All results are normalized to 100 wt% anhydrous glass composition

The excess alkali value is the difference between mole fractions of alkalis and that of alumina. Measurement conditions are given in the Supplementary material "S1_Tables"

[a]Inhomogeneous glass due to a single synthesis step. The glasses were therefore only used for powder experiments, which were then again checked with EMPA to finally confirm chemical homogeneity

[b]Hydrous glass composition normalized to anhydrous composition. Powder of the inhomogeneous glasses AOQ8_1 and AOQ4_1 were used as starting materials for AOQ4 and AOQ8 standards, respectively. Due to the mixing of the chemically inhomogeneous powder the hydrated samples obtained good agreement with the theoretical AOQ8 composition despite the initial inhomogeneity

as AOQ2, AOQ4 and AOQ8, respectively. Analytical grade oxide and carbonate powder SiO_2, Al_2O_3, Na_2CO_3 and K_2CO_3 were used for synthesis. To provide accurate weight portions, the strongly hygroscopic SiO_2 and Al_2O_3 powders were fired for 18 h at 1073 K and Na_2CO_3 and K_2CO_3 were dried for 24 h at 383 K. The powders were then weighed and mixed. To obtain a chemically homogeneous powder, the mixtures were blended in an overhead shaker for 15 min. Then, each mixture was split up into 4 portions and each portion was milled in a corundum ball mill for 15 min. After the first milling step, each of the two portions were blended, mixed and again split up and milled. This last step was then repeated.

For the first AOQ4 and AOQ8 glass batches (AOQ4_1 and AOQ8_1), 50 g powder was loaded in a Pt90Rh10 crucible. To decarbonize the mixtures, they were heated in a bottom load furnace to 1273 K (1 K/min; 1 h dwell time), subsequently to 1573 K (10 K/min; 3 h dwell time) and finally to 1873 K (10 K/min). At 1873 K, AOQ4_1 was held for 7 h and a dwell time of 3 h was used for the AOQ8_1 batch to drive gas bubbles out of the melt. Subsequently, the melts were air-cooled roughly below T_g and the crucible was then transferred into a furnace preheated to 630 K and 540 K, the calculated glass transition temperatures (T_g^{12}; where the viscosity $\eta = 10^{12}$ Pa s) for nominally dry AOQ4 and AOQ8, respectively (Giordano et al. 2008). The furnace was immediately switched off to maintain a slow cooling rate of ~ 5 K/min. By this method, glasses without tension-induced cracks were obtained (Allabar and Nowak 2020). Electron microprobe analysis (EMPA) of these glasses revealed chemical inhomogeneity with increasing Al_2O_3 concentration towards the bottom of the glass (e.g. 9–14 wt% Al_2O_3 from top to bottom in AOQ8_1). This effect is less pronounced in the AOQ4 composition. It is assumed that during the slow decarbonatization process and formation of partial melt during heating, Al_2O_3 gravitationally sinks towards the bottom of the crucible before complete melting and that the time for diffusional concentration equilibration after complete melting is not sufficient to obtain a chemically homogeneous melt. The resulting inhomogeneous glass was therefore crushed and sieved to < 500 µm and only used for hydration experiments with powder as starting material. EMPA analyses of the standard samples after hydration and equilibration confirm the chemical homogeneity in agreement with the target compositions (Table 1).

Further, AOQ4 and AOQ8 and the AOQ2 glasses were synthesized with the decarbonatization protocol as described above and a 3 h dwell at 1873 K. Then the melts were quenched in water, whereupon the glasses were crushed, milled and reheated to 1873 K. Again, to drive bubbles out of the melts, AOQ4 was held for 10 h and AOQ8 for 7 h at this temperature, which was followed by the same cooling and tempering protocol as described above. AOQ2 was held at 1873 K for 6 h because the time for homogenization was sufficient and the glass was crushed after synthesis. This synthesis protocol yields chemically homogeneous glasses. Furthermore, the synthesis method yields glasses with CO_2 concentrations below the detection limit of < 10 ppm using mid-infrared FTIR spectroscopy (Sierralta et al. 2002; Spickenbom et al. 2010). This is important to note, since small amounts of CO_2 can significantly reduce the H_2O solubility. From the homogeneous AOQ4 and AOQ8 glass charges, cylinders of 3.6 mm diameter were drilled for the H_2O solubility experiments.

Hydration of standard glass samples

The glass samples serving for the determination of near-infrared linear molar absorption coefficients of dissolved hydrous species (molecular H_2O (H_2O_m) and hydroxyl (OH)) are further referred to as "standard samples" and were produced for AOQ2, AOQ4 and AOQ8 compositions. The standard samples are labeled "Std_X_Y", where the X denotes Na_2O excess in wt% and Y denotes the target H_2O concentration in wt% (Table 2).

20 mm long cleaned and annealed Au80Pd20 tubes (4.0 mm OD, 3.6 mm ID) were crimped to three-sided stars on one side and welded. Glass powder sieved to < 500 µm particle size was filled step-by-step into the capsules and densified with a steel piston in between. To obtain glasses with total amounts of dissolved H_2O (H_2O_t, the sum of H_2O dissolved as H_2O_m and OH) of 0.5, 1, 2, 4 and 7 wt %, water was then added to the powder with a digitally controlled Eppendorf micro-pipette. Weighing after each step yields the gravimetrically determined H_2O concentration that was added into the capsule ($c_{H_2O_{grav}}$; Table 2). The upper capsule part was also crimped to a star and welded shut. For AOQ2 one additional sample was prepared with 1.66 wt% H_2O. All capsules were heated in a compartment drier at 383 K for at least 1 h, then compressed to 100 MPa at ambient T and again heated to 383 K with a re-weighing after each step to check for possible leakage.

The samples were hydrated in pairs in an internally heated argon pressure vessel (IHPV) at ~ 1523 K. The pressures (Table 2) were chosen to ensure H_2O undersaturated conditions, for which the H_2O solubility in AOQ melt (Liu et al. 2005) was used as a first proxy. After 24 h, the capsules were quenched isobarically with 16 K/s by switching off the furnace (Allabar et al. 2020).

The H_2O undersaturated hydration of glass powder prevents the formation of hydration vesicles (e.g. Preuss et al. 2016). Hydration vesicles can lead to an underestimation in glass density and an overestimation in H_2O concentration determined by Karl-Fischer-Titration (KFT) because both are bulk sample measurements. Due to the use of powder as starting material, however, part of the inter-particle space is filled with air and part by liquid H_2O, the ratio of

Table 2 Hydration conditions and analytical results for standard samples

Sample #	T_{hom} (K)	P_{hom} (MPa)	Glass density (g/L)	Error	$c_{H_2O\,t}$ grav[a] (wt%)	$c_{H_2O\,t}$ KFT (wt%)	Error	A_{5210}[b]	A_{4470}[b]	Sample thickness [cm][c]
AOQ2 glass	–	–	2317	20		–	–	–	–	–
Std_2_0.5	1516	200	2345	20	0.51	0.48	0.08	0.008	0.070	0.0803
Std_2_1	1516	200	2340	20	1.01	0.91	0.06	0.040	0.110	0.0808
Std_2_1.66	1520	300	2331	24	1.65	1.55	0.05	0.028	0.038	0.0204
Std_2_2	1512	200	2326	22	2.01	1.94	0.06	0.035	0.039	0.0194
Std_2_4	1512	200	2308	33	4.00	3.98	0.07	0.107	0.052	0.0206
Std_2_7	1520	300	2264	20	7.02	6.86	0.09	0.201	0.049	0.0189
AOQ4 glass	–	–	2352	61		–	–	–	–	–
Std_4_0.5(2)	1500	200	2354	19	0.47	0.44	0.03	0.007	0.062	0.0797
Std_4_1	1500	200	2355	20	1.01	0.92	0.06	0.034	0.099	0.0801
Std_4_2	1516	200	2342	18	1.99	1.90	0.07	0.044	0.052	0.0289
Std_4_4	1511	300	2332	18	3.97	3.93	0.07	0.125	0.065	0.0291
Std_4_7	1511	300	2288	18	7.01	7.09	0.12	0.268	0.066	0.0295
AOQ8 glass	–	–	2391	61		–	–	–	–	–
Std_8_0.5(2)	1525	200	2385	25	0.50	0.48	0.03	0.003	0.05	0.0799
Std_8_1	1519	200	2388	23	0.97	0.92	0.06	0.018	0.081	0.0805
Std_8_2	1519	200	2373	21	2.05	2.11	0.06	0.032	0.047	0.0295
Std_8_4	1521	300	2366	19	4.03	4.05	0.06	0.096	0.059	0.0295
Std_8_7	1521	300	2333	20	6.94	7.07	0.1	0.207	0.058	0.0297

All standard samples were hydrated between 23 and 26 h

[a]The gravimetrical c_{H2Ot} is determined from the mass of water inserted into the capsule

[b]The error in peak height is 0.002 absorption units

[c]The error in sample thickness is 0.0003 cm

which depends on the amount of water added into the capsule. Assuming air is mostly represented by N_2, the volatile phase in the experiments will deviate to different degrees from pure water, which can decrease the H_2O solubility (Preuss et al. 2016). However, if at all, only very few vesicles remained in the hydrated glasses (e.g. 5–10 vesicles in a thin section of 500 µm thickness, 3.6 mm diameter) with sizes < 3 µm. Furthermore, during the opening of the capsules, no excess fluid phase was present in the headspace of the capsule, confirming that the H_2O completely dissolved in the melts during synthesis.

H_2O-solubility experiments

For H_2O-solubility experiments, solid glass cylinders of 3.6 mm diameter were used to avoid hydration bubbles at H_2O-supersaturated conditions that would result from the use of powder as starting material and would complicate H_2O concentration analysis. To ensure H_2O saturation of the melt, excess water of 6, 7, 8.5 and 10 wt% H_2O were weighed into 3.6 mm inner diameter Au80Pd20 capsules together with a glass cylinder for the 27, 50, 100, 150 and 200 MPa runs, respectively. The same leakage tests as described for the standard samples were performed on these capsules before the solubility experiments.

The solubility experiment samples are labeled "X_L_Z", where the X denotes Na_2O excess in wt% and Z denotes the sample number (Table 3). All solubility experiments at $T > 1123$ K were performed in the IHPV. Experiments at ~ 1123 K were carried out in a rapid quench cold-seal pressure vessel (CSPV) with H_2O used as a pressure medium. Solubility experiments were performed at 27, 50, 100, 150 and 200 MPa and temperatures of 1523, 1323 and 1123 K. The $T > 1123$ K experiments were held for at least 72 h, while experiments at 1123 K were run at least for 264 h to ensure homogeneous dissolution of H_2O in the melt. Experiments in the IHPV were isobarically quenched with 16 K/s by switching off the furnace. The CSPV experiments were terminated by releasing the external magnet, which holds the sample in the hot zone of the autoclave during the experiment, into the water-cooled part of the autoclave within a time interval of ~ 30 s. Both cooling rates were sufficiently slow to obtain nearly crack-free glasses after sample preparation. At the same time, cooling was fast enough to prevent partial crystallization of the supercooled melts before reaching the glass transition temperature range, which

Table 3 Experimental conditions and analysis results from gravimetrical determination of H_2O concentration and with FTIR-spectroscopy

#	Na_2O excess (wt%)	P (MPa)	T (K)	Gravimetric c_{H_2Ot} [wt%]	c_{H_2Om} FTIR (wt%)	Error (wt%)	c_{OH} FTIR (wt%)	error (wt%)	c_{H_2Ot} FTIR (wt%)	Error (wt%)	Std. dev. (wt%)
4_L_04	4	27	1123	n.d.	1.20	0.04	1.03	0.04	2.23	0.05	0.02
4_L_13	4	50	1520	2.63	1.47	0.04	0.99	0.04	2.46	0.06	0.02
4_L_17	4	50	1323	2.66	1.61	0.05	1.01	0.04	2.61	0.06	0.02
4_L_07	4	50	1123	3.44	1.97	0.06	1.12	0.05	3.09	0.08	0.02
4_L_12	4	100	1509	5.32	2.84	0.12	1.11	0.08	3.95	0.14	0.04
4_L_16	4	100	1324	4.31	3.20	0.08	1.13	0.05	4.33	0.1	0.03
4_L_01	4	100	1123	5.38	3.65	0.08	1.22	0.05	4.86	0.1	0.03
4_L_11	4	150	1508	5.35	4.03	0.14	1.12	0.08	5.16	0.16	0.06
4_L_15	4	150	1325	5.41	4.45	0.12	1.17	0.06	5.61	0.13	0.02
4_L_03	4	150	1123	n.d.	4.90	0.16	1.26	0.08	6.16	0.18	0.06
4_L_10	4	200	1515	6.23	5.27	0.15	1.14	0.07	6.41	0.17	0.05
4_L_14	4	200	1325	6.91	5.53	0.14	1.12	0.06	6.65	0.15	0.07
4_L_05	4	200	1123	n.d.	6.08	0.18	1.28	0.08	7.35	0.21	0.10
8_L_22	8	50	1523	3.70	1.60	0.07	1.32	0.08	2.92	0.1	0.08
8_L_26	8	50	1323	3.12	1.81	0.08	1.37	0.08	3.18	0.11	0.02
8_L_09	8	50	1123	n.d.	2.27	0.08	1.49	0.08	3.76	0.12	0.01
8_L_29	8	100	1523	4.69	2.97	0.10	1.47	0.09	4.43	0.13	0.02
8_L_25	8	100	1325	5.41	3.38	0.11	1.48	0.09	4.85	0.14	0.04
8_L_19	8	100	1123	n.d.	4.04	0.12	1.60	0.09	5.64	0.15	0.04
8_L_28	8	150	1523	6.37	4.43	0.13	1.51	0.09	5.94	0.16	0.06
8_L_20	8	150	1123	7.31	5.69	0.15	1.53	0.09	7.22	0.18	0.08
8_L_27	8	200	1523	7.16	5.93	0.19	1.49	0.11	7.41	0.22	0.04
8_L_23	8	200	1337	7.60	6.37	0.20	1.48	0.11	7.85	0.23	0.04
8_L_21[a]	8	200	1123	8.35	7.20	0.22	1.44	0.11	8.64	0.24	0.09
AOQ2_h1	2	100	1123	4.44	2.97	0.15	1.24	0.13	4.21	0.20	0.09

n.d. not determined

[a]The experiment had an increase in weight after the experiment, but still H_2O in excess in the capsule

was confirmed by inspection of the quenched glasses with a microscope. Before sample preparation, the capsules from solubility experiments were pierced. Some water sparkled out of the capsules ensuring that H_2O still coexisted with the melt at the end of the hydration time, which is required for a successful solubility experiment. Only one experiment (8_L_21; Table 3) had an increased weight after the experiment, possibly due to H_2O (the pressure medium) entering the capsule. Because no big hole was found in the capsule, it can be assumed that no significant fluid exchange between the pressure medium and the fluid in contact with the melt occurred, which could change the melt composition by leaching. Therefore, the experiment was considered successful. The pierced capsules were then dried in a desiccator for ~ 2 days and re-weighed to determine the dissolved H_2O concentration gravimetrically.

Sample preparation

For FTIR spectroscopy glass standard samples, a slice perpendicular to the cylinder axis was cut from the middle of each sample and prepared as a thin section polished on both sides. The thickness of each section (Table 2) was measured with a Mitutoyo digital micrometer (± 3 µm). The residual sample material of the standard samples was used for glass density determination and Karl-Fischer-Titration. The solubility samples were sectioned through the middle of each sample parallel to the cylinder axis and prepared as polished thin section for FTIR spectroscopy.

Analytical techniques

Glass density determination

Glass densities were determined with the buoyancy method using a Sartorius Archimedes precision scale (±0.02 mg). Therefore, the glass pieces were weighed in air and in water. Care was taken that no air bubbles were attached to the sample basket and the sample in the water that could lead to a density underestimation. Via the buoyancy given by the differences of both weights, the glass densities were calculated (Table 2).

Karl-Fischer-titration

The total water concentrations in the hydrous standard glasses were measured by Karl-Fischer-Titration (KFT) at the Institute of Mineralogy, Leibniz University Hannover. A detailed description of this method is given by Behrens et al. (1996). The residual H_2O contents in polymerized glasses after H_2O extraction by heating to 1573 K is 0.1 ± 0.05 wt% (Behrens et al. 1996). Because the samples decomposed to small fragments and powder during the heating process during KFT measurements, the residual H_2O concentrations in the glass after KFT could not be analyzed with FTIR spectroscopy. However, in depolymerized samples the residual H_2O content is negligible (Ohlhorst et al. 2001). Therefore, the KFT data were not corrected for residual H_2O in the glass. KFT results for the standard samples are given in Table 2.

Near-infrared FTIR-spectroscopy

All doubly polished thin sections were analyzed in the near-infrared (NIR) with a Bruker Vertex 80v FTIR spectrometer coupled with a Hyperion 3000 IR microscope. A halogen light source and a CaF_2 beam splitter, a liquid nitrogen cooled InSb single element detector and a 15 × Cassegrain objective were used. Spectra were processed with the OPUS 7 software. Measurement areas of 50 × 50 µm were adjusted by a knife-edge aperture. 50 scans were collected for each spectrum with a spectral resolution of 4 cm^{-1}. Air was measured as reference. Across each sample at least 10 points were measured to confirm the homogeneous distribution of H_2O in the glasses. Peak heights of absorption bands related to molecular H_2O (H_2O_m; ~ 5210 cm^{-1}) and hydroxyl (OH; ~ 4470 cm^{-1}) after linear tangential background correction were used to determine molar NIR absorption coefficients.

The same measurement conditions were applied for the H_2O solubility samples. The measurement points were distributed along two profiles, one perpendicular and one parallel to the cylinder axis to detect a possible H_2O concentration gradient throughout the hydrated cylinder. H_2O_m and OH absorbances were determined after linear tangential background correction. Together with the glass density relationship, linear molar absorption coefficients and sample thickness, the concentration of molecular H_2O (c_{H2Om}) and H_2O dissolved as OH (c_{OH}) were calculated with the Lambert–Beer-Law, the sum of which yields the total amount of H_2O species expressed as dissolved H_2O (c_{H_2Ot}), i.e. the H_2O solubility (Table 3). A detailed description is given in the following sections.

Results and discussion

Glass densities

For all glass compositions, the density linearly decreases with increasing H_2O_t content (Fig. 1). However, the density of the nominally dry glasses is slightly lower than expected by the y-intercept of the linear trend of the corresponding hydrous glasses. The porosity of the anhydrous AOQ2 glasses is ~ 1.3%, ~ 0.02% in the AOQ4 glass and AOQ8 is

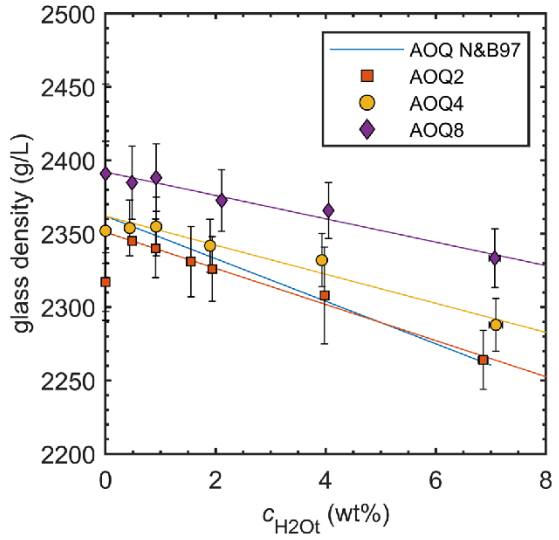

Fig. 1 Glass density as a function of c_{H_2Ot} for AOQ2, AOQ4 and AOQ8 glasses. The density relation for the AOQ glass composition of Nowak and Behrens (1997) (N&B97) is given for comparison. For the data of this study, the regression lines are fitted to hydrous glasses only (for details see text). Errors of the data result from error propagation with weighing errors (±0.2 mg) and the uncertainty in c_{H_2Ot} from KFT measurements (Table 2)

nearly bubble-free. Thus, the low density cannot be attributed to the porosity of the starting material. An explanation for this might be that in contrast to the glasses hydrated at high pressure, dry glasses were synthesized at 1 bar. Behrens et al. (1996) suggest a synthesis pressure dependence on density. Balzer et al. (2020) showed the same effect and compacted anhydrous glasses at high pressure at temperatures in the range of the glass transition which increased the density that is then consistent with the dependence of the high pressure synthesized hydrous glasses. For the data of this study, this means that the air-melted anhydrous glasses synthesized at ambient pressure cannot be directly compared with the hydrous glasses. Therefore, the linear regression lines were fitted to hydrous glasses only (Behrens et al. 1996). The linear relationships (Fig. 1) of density (in g L^{-1}) as a function of c_{H_2Ot} ($=c_{H_2Om}+c_{OH}$; in wt%) are

$$\rho_{AOQ} = (2362) - (14.5) \cdot c_{H_2Ot}, \quad (1)$$

$$\rho_{AOQ2} = (2351 \pm 2) - (12.30 \pm 0.6) \cdot c_{H_2Ot}, \quad (2)$$

$$\rho_{AOQ4} = (2362 \pm 4) - (9.90 \pm 1.2) \cdot c_{H_2Ot}, \quad (3)$$

$$\rho_{AOQ8} = (2392 \pm 3) - (7.96 \pm 0.9) \cdot c_{H_2Ot}, \quad (4)$$

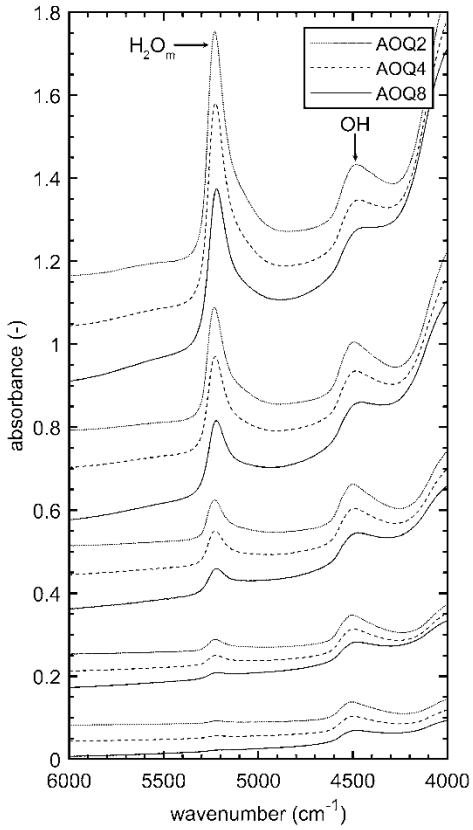

Fig. 2 NIR raw absorption spectra of hydrous AOQ2, AOQ4, and AOQ8 standard glasses normalized to a sample thickness of 500 µm. Each set of 3 spectra is given for the Std_X_0.5, Std_X_1, Std_X_2, Std_X_4 and Std_X_7 samples from bottom to top. The spectra are the mean of 10–13 measurements of each sample. Spectra are shifted in y-direction for illustration purposes. The absorption band at ~ 5210 cm^{-1} is associated with molecular water (H_2O_m) and the band at ~ 4500 cm^{-1} with hydroxyl (OH)

where the AOQ density relationship is from Nowak and Behrens (1997). The density increase with increasing peralkalinity is attributed to increasing depolymerization with the addition of Na_2O, which results in a volume decrease (Bottinga and Richet 1995).

Linear molar absorption coefficients for near-infrared FTIR

The raw mean spectra from 10 to 13 measurements across each sample with c_{H2Ot} between 0.5 and 7 wt% normalized to 500 µm sample thickness are shown in Fig. 2. A standard deviation of ≤ 0.002 absorbance units was determined from single spectra on one and the same sample, demonstrating the homogeneous distribution of H_2O in the samples.

A linear tangent baseline correction identical to the procedure of Behrens et al. (1996) was used to determine peak heights. Therefore, the tangent was anchored at the high wavenumber side of the ~5210 cm^{-1} band and the minimum between the 5210 and 4700 cm^{-1} bands and was then extrapolated towards lower wavenumbers. Consistent with other spectra of peralkaline compositions (Behrens et al. 1996), the tail of the OH band is higher towards lower wavenumbers with an increasing amount of Na_2O excess. This has to be considered for the separation of the combination band from the background (Behrens et al. 1996). The fit of a Gaussian to the 4000 cm^{-1} shoulder (Fig. 3) verifies that the 4470 cm^{-1} peak height is not influenced by the lower frequency band. This justifies the use of the linear tangent baseline correction even for the strongly peralkaline AOQ8 glass. This baseline correction is also preferable because it was also used for AOQ (Behrens and Nowak 2003), allowing a direct comparison of linear molar absorption coefficients with those obtained in this study.

The NIR band intensities of OH (~4470 cm^{-1}) and H_2O_m (~5210 cm^{-1}) were used to calculate the respective concentrations with the Lambert–Beer–Law:

$$c_{H_2O} = \frac{1802 \cdot A_{H_2O}}{d \cdot \rho \cdot \varepsilon_{H_2O}}, \quad (5)$$

$$c_{OH} = \frac{1802 \cdot A_{OH}}{d \cdot \rho \cdot \varepsilon_{OH}}, \quad (6)$$

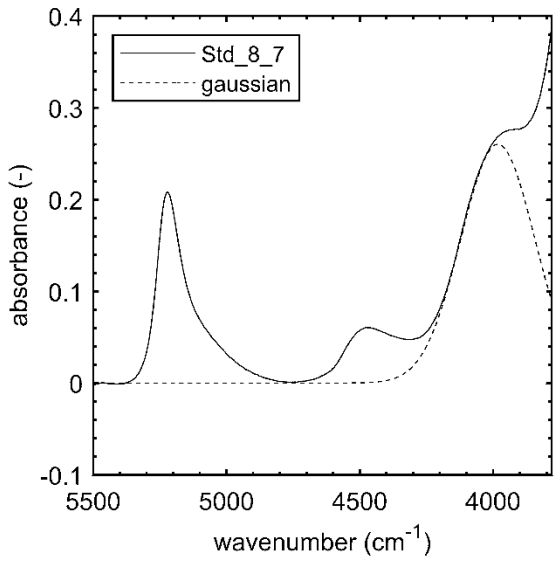

Fig. 3 Linear tangential background-corrected NIR spectrum of Std_8_7. A Gaussian was fitted to the 4000 cm^{-1} shoulder to rule out a possible influence on the peak height of the hydroxyl band

where c_{H_2O} and c_{OH} are the species concentrations expressed as wt% dissolved H_2O, A is the height of the respective absorbance band, d the sample thickness in cm, ρ the density in g L^{-1} and ε the absorption coefficient in L $mole^{-1}$ cm^{-1}. The absorption coefficients were determined for each glass composition using the NIR absorbances of the hydrous glasses with known total c_{H2Ot} from KFT analysis. After the rearrangement of Eqs. 5 and 6, the normalized absorbances (in parentheses) are obtained:

$$\left(\frac{1802 \cdot A_{H_2O}}{d \cdot \rho \cdot c_{H_2O_t(KFT)}}\right) = \varepsilon_{H_2O} - \frac{\varepsilon_{H_2O}}{\varepsilon_{OH}}\left(\frac{1802 \cdot A_{OH}}{d \cdot \rho \cdot c_{H_2O_t(KFT)}}\right). \quad (7)$$

A straight line is obtained by plotting the normalized absorbances where the absorption coefficients of OH and H_2O_m correspond to the intercepts with the x- and y-axis,

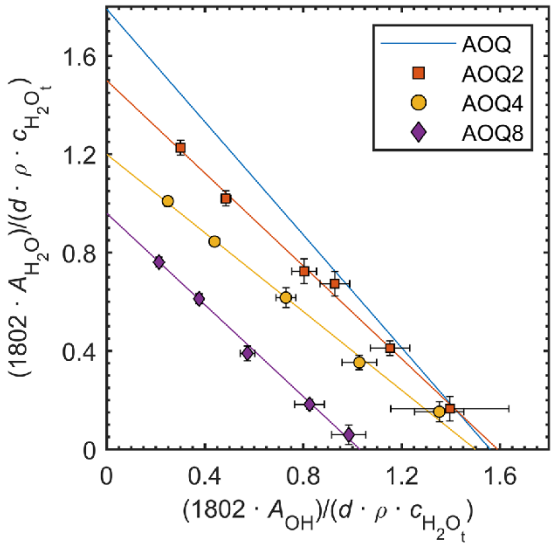

Fig. 4 Normalized absorbances for the hydroxyl and the molecular H_2O absorbance obtained from NIR measurements. The lines are weighted least square regressions. Their x and y-intercepts define the linear molar absorption coefficients for OH and molecular H_2O, respectively. Errors of the data points are derived from an error propagation using errors in d: 0.0003 cm; density and c_{H2O}, see Table 2 and absorbance: 0.002. For comparison the blue line represents the normalized absorbance dependence for AOQ composition determined by Behrens and Nowak (2003) using the same background correction as in this study

respectively (Fig. 4). Absorption coefficients obtained from weighted linear least-squares regression are:

$$\text{AOQ2}: \varepsilon_{OH} = 1.59 \pm 0.04 \text{ and } \varepsilon_{H_2O} = 1.50 \pm 0.02 \text{ L mole}^{-1}\text{cm}^{-1}$$

$$\text{AOQ4}: \varepsilon_{OH} = 1.50 \pm 0.04 \text{ and } \varepsilon_{H_2O} = 1.20 \pm 0.02 \text{ L mole}^{-1}\text{cm}^{-1}$$

$$\text{AOQ8}: \varepsilon_{OH} = 1.03 \pm 0.05 \text{ and } \varepsilon_{H_2O} = 0.96 \pm 0.02 \text{ L mole}^{-1}\text{cm}^{-1}.$$

Compared with AOQ absorption coefficients of ε_{OH}: 1.56 ± 0.021 and ε_{H_2O}: 1.79 ± 0.021 L mole^{-1} cm^{-1} (Behrens and Nowak 2003) the ε_{H_2O} decreases strongly with increasing excess alkali. The ε_{OH} increases slightly from AOQ to AOQ2 but then also decreases towards higher excess alkali, which can be described by the parabolic dependencies given in Fig. 5.

The decrease in absorption coefficients with increasing excess alkali and peralkalinity is consistent with the results of previous studies (Acocella et al. 1984; Behrens et al. 1996). Behrens et al. (1996) attribute this effect to a strong H bonding of the H_2O species to non-bridging oxygens and that only part of the water contributes to the absorption bands. The causes of the ε_{OH} increase for moderate excess alkali addition are unknown, and beyond the scope of this study. However, the dependence of absorption coefficients in Fig. 5 is confirmed by data of Behrens et al. (2009) who determined absorption coefficients using the same baseline procedure for a natural peralkaline rhyolite (NSL) glass composition from New Zealand with similar excess alkali and identical molar Na/(Na+K) proportion of 0.64 as AOQ2. Behrens et al. (1996) showed that the exchange of alkalis (Na, K, Li) changes the absorption coefficients in hydrous alkali feldspar glass. It may be possible that this is also the case for peralkaline rhyolitic glasses. Therefore, the dependence in Fig. 5 may also be affected by the changing Na/(Na+K) ratio increasing from 0.55 to 0.78 from AOQ to AOQ8. Further work is required to determine the influence of different alkalis on the absorption coefficients in peralkaline melts.

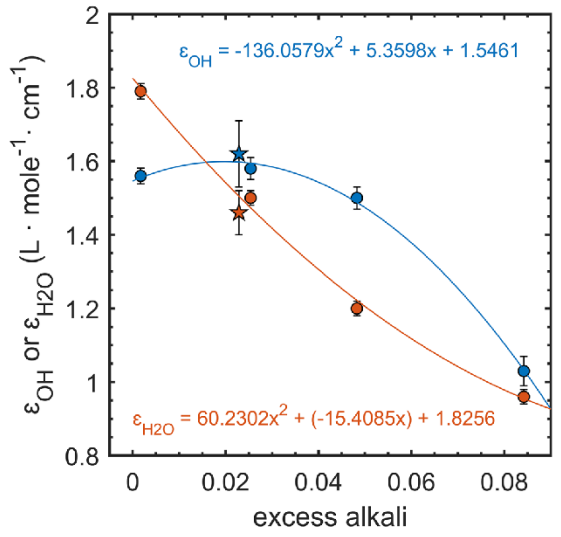

Fig. 5 Dependence of linear molar absorption coefficients with excess alkali (difference between mole fractions of alkalis and that of alumina) obtained from linear tangent baseline correction. The lines are the fits to the data of this study (circles). Stars are absorption coefficients of a natural peralkaline rhyolite composition (NSL) from Behrens et al. (2009) obtained with the same baseline correction

H_2O solubility

H_2O solubilities of haplogranitic melt with Na_2O excess

H_2O solubilities determined with FTIR-spectroscopy are in good agreement with gravimetrically determined H_2O solubilities (Table 3). Similar to other melt compositions, the H_2O solubility in both AOQ4 and AOQ8 melts increases with pressure at constant T and decreases with increasing temperature at constant P (Fig. 6 a-d). Since the empirical solubility equation (Eq. 8) for rhyolitic melts defined by Liu et al. (2005) describes the H_2O solubility as function of P and T for AOQ very well (Fig. 8, data from Holtz et al. (1995) and Liu et al. (2005)), the functional form was adapted to derive solubility equations for AOQ4 and AOQ8. The resulting H_2O solubility (in wt%) equations as a function of P (in MPa) and T (in K) are given by Eqs. 9 and 10. The equations are constrained for in the given P and T ranges. The R^2 is 0.99 for both fits and the root-mean-square error (RMSE) is 0.07 and 0.06 wt% for AOQ4 and AOQ8, respectively.

$$\text{AOQ}: c_{H_2O_t}(\text{wt\%}) = \frac{354.94P^{0.5} + 9.623P - 1.5223P^{1.5}}{T} + 0.001244P^{1.5} \quad [0.1 - 500 \text{ MPa}, 825 - 1423 \text{ K}], \tag{8}$$

$$\text{AOQ4}: c_{H_2O_t}(wt\%) = \frac{337.9P^{0.5} + 28.33P - 2.217P^{1.5}}{T} + 0.001271P^{1.5} \quad [27 - 200 \text{ MPa}, 1123 - 1523 \text{ K}], \tag{9}$$

$$\text{AOQ8}: c_{H_2O_t}(wt\%) = \frac{536.4P^{0.5} + 5.125P - 1.091P^{1.5}}{T} + 0.001323P^{1.5} \quad [50 - 200 \text{ MPa}, 1123 - 1523 \text{ K}]. \tag{10}$$

Results obtained from Eqs. 8–10 reveal that H_2O solubility increases linearly at constant P and T with increasing Na_2O excess from AOQ to AOQ8 (Fig. 7a). At 1323 K

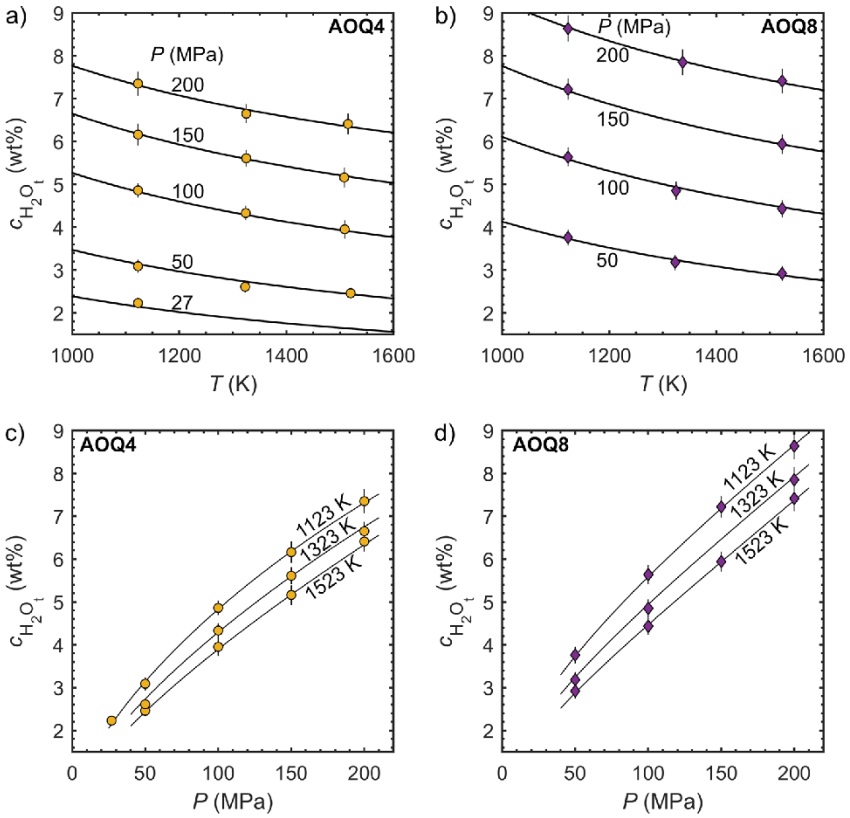

Fig. 6 H_2O solubility in AOQ4 (**a**, **c**) and AOQ8 melts (**b**, **d**) as a function of pressure and temperature. In general, the H_2O solubility increases with increasing Na_2O excess (compare **a** and **b**). For a given composition, the H_2O solubility increases with increasing P and decreasing T. The solubility as calculated by Eq. 9 (for AOQ4) and Eq. 10 (for AOQ8) based on the functional form of Liu et al. (2005) (Eq. 8) are illustrated by the black lines in the investigated P and T ranges

and 50 MPa the H_2O solubility increases by 0.12 wt% per excess wt% Na_2O and at a higher P of 200 MPa solubility increases by 0.3 wt%. As a result of the linear dependence, the solubility of any Na_2O excess value can be calculated by linear interpolation between AOQ and AOQ8 composition at given P and T. This was tested by an additional solubility experiment with AOQ2 melt composition (100 MPa and 1123 K; Fig. 7; Table 3) and data from Dingwell et al. (1997) for haplogranitic melt (HPG8; very similar to AOQ) with 5 (+5Na) and 10 wt% Na_2O (+10Na) (both 50 MPa and 1273 K; Table S1 in the supplement "S1_Tables"). For the experimental P and T conditions of these experiments, the AOQ and AOQ8 solubilities were calculated. Then it was linearly interpolated between 0 and 8 wt% Na_2O excess to obtain the H_2O solubility at the respective Na_2O excess of the desired compositions. The results obtained from interpolation and moderate extrapolation out of the experimentally validated range (in case of the 10 wt% Na_2O excess experiment) yield calculated H_2O solubilities that agree with the experimentally determined values within 6% relative deviation (Fig. 8).

A general H_2O solubility model for peralkaline rhyolitic melts

Dingwell et al. (1997) showed for peralkaline haplogranitic melt at 50 MPa and 1273 K that on a molar basis the solubility increase with peralkalinity is identical for Na_2O, K_2O, Rb_2O and Cs_2O. They also suggest that the same behavior can be expected at P up to 500 MPa. Only the addition of Li_2O affected H_2O solubility to a lower extent compared to the other alkalis, which they explain by a possibly lacking ability of Li_2O to form non-bridging oxygen that would then be accessible for hydrous species. Based on their findings it can be assumed, that on a molar basis, the H_2O solubility dependence between AOQ and AOQ8 as a function of P and T can be applied to haplogranitic compositions with general excess alkali (except for Lithium). The H_2O solubilities of AOQ (data from Holtz et al. 1995 and Liu et al. 2005), AOQ4 and AOQ8 experiments were therefore re-calculated in mol% and new fit parameters were obtained:

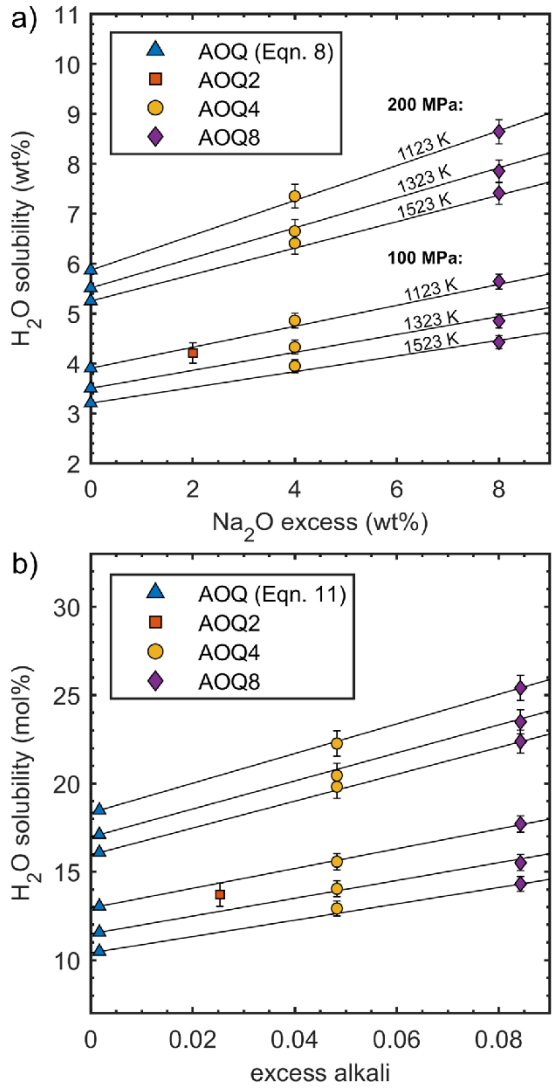

Fig. 7 **a** Linear dependence of H_2O solubility in wt% with increasing Na_2O excess with respect to AOQ composition, exemplarily illustrated for the data experimentally obtained at 200 and 100 MPa and three different temperatures, respectively (Table 3). The AOQ data are calculated from Eq. 8 and the solid lines are the linear interpolations between the results of Eq. 10 (for AOQ8) and Eq. 8. **b** Shows the linear dependence of H_2O solubility in mol% with increasing excess alkali (difference between mole fractions of alkalis and that of alumina) values (derived from EMPA results of the starting glasses, Table 1) for the same P and T conditions. H_2O solubility for AOQ was calculated with Eq. 11 and the solid lines are calculated with Eq. 14

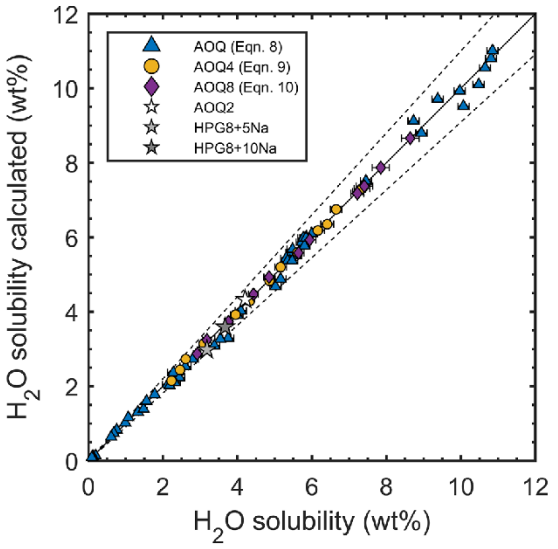

Fig. 8 Comparison of experimentally determined H_2O solubility in AOQ and AOQ + Na_2O excess with the calculated H_2O solubilities. Equations 8–10 accurately predict the H_2O solubility for AOQ to AOQ8 melt compositions, respectively. Since H_2O solubility linearly increases with the amount of Na_2O excess at constant P and T, the solubilities for any haplogranitic melt with Na_2O excess can be calculated by linear interpolation and extrapolation as evidenced by the AOQ2 and HPG8 + 5Na and HPG8 + 10Na datapoints. AOQ data are from Holtz et al. (1995) and Liu et al. (2005), HPG8 + 5Na and + 10Na data are from Dingwell et al. (1997). The dashed lines indicate 10% relative deviation from the 1:1 line (solid line)

$$\mathrm{AOQ}: c_{\mathrm{H_2O_t}}(\mathrm{mol\%}) = \frac{1440P^{0.5} + 3.689P - 3.839P^{1.5}}{T} + 0.003308P^{1.5} \quad [0.1 - 500\ \mathrm{MPa}, 825 - 1423\ \mathrm{K}], \tag{11}$$

$$\mathrm{AOQ4}: c_{\mathrm{H_2O_t}}(\mathrm{mol\%}) = \frac{1249P^{0.5} + 83.59P - 8.523P^{1.5}}{T} + 0.004575P^{1.5} \quad [27 - 200\ \mathrm{MPa}, 1123 - 1523\ \mathrm{K}], \tag{12}$$

$$\mathrm{AOQ8}: c_{\mathrm{H_2O_t}}(\mathrm{mol\%}) = \frac{1896P^{0.5} + 9.01P - 5.518P^{1.5}}{T} + 0.004884P^{1.5} \quad [50 - 200\ \mathrm{MPa}, 1123 - 1523\ \mathrm{K}] \tag{13}$$

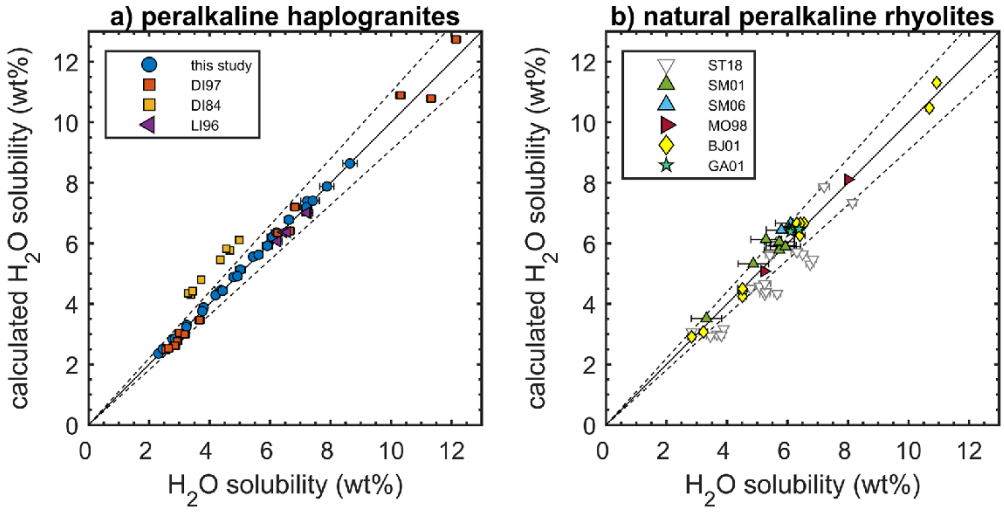

Fig. 9 Results from H_2O solubility calculation compared to the experimentally determined H_2O solubility for synthetic peralkaline haplogranites (**a**) and natural peralkaline rhyolite composition (**b**). For the respective P and T conditions, H_2O solubilities were calculated with Eqs. 11 and 13 for excess alkali values (difference between mole fractions of alkalis and that of alumina) of 0.0017 and 0.0842, respectively. Linear interpolation as a function of excess alkali yields the calculated H_2O solubility (in mol%; Eq. 14) for the excess alkali value of the desired composition. Solubilities were then re-calculated into wt% for comparability with literature data. Data of Stabile et al. (2018) were plotted with white symbols as these data may have to be treated with caution (see Discussion). The dashed lines indicate a 10% deviation from the 1:1 line (solid line). References: DI97: Dingwell et al. (1997); DI84: Dingwell et al. (1984); LI96: Linnen et al. (1996); ST18: Stabile et al. 2018; SM01: Scaillet and Macdonald (2001); SM06: Scaillet and Macdonald (2006); BJ01: Behrens and Jantos (2001); MO98: Moore et al. (1998); GA01: Gaillard et al. (2001)

The equations are constrained for the P and T ranges given in brackets. These equations again reproduce the AOQ data and the data of this study very well (Fig. 9), and the linear dependence of H_2O solubility with increasing excess alkali at constant P and T is also given on a molar basis (Fig. 7b). At 1323 K and 50 MPa the H_2O solubility increases by 0.33 mol% with an increase of 0.01 in excess alkali and by 0.78 mol% at 200 MPa. Therefore, the interpolation between AOQ (excess alkali = 0.0017) and AOQ8 (excess alkali = 0.0842; from EMPA result of the starting glass AOQ8_4a used for the solubility experiments; Table 1) solubility for given P and T should allow H_2O solubility calculation as a function of excess alkali independent of the type of alkali, with Li as an exception:

$$c_{H_2O}(\text{mol\%}) = c_{AOQ8} - \left(\left(c_{AOQ8} - c_{AOQ}\right)/0.0825\right) \times \left(0.0842 - x_{ex}\right), \quad (14)$$

where c_{AOQ8} and c_{AOQ} are the results of Eqs. 11 and 13, respectively for the desired P and T conditions and x_{ex} is excess alkali of the desired composition (difference between mole fractions of alkalis and that of alumina). An MS Excel spreadsheet and Matlab script are provided in the supplementary material ("SolModel_peralk_rhyolite") that calculate the excess alkali and the H_2O solubility in mol% and wt% from the input of P, T and the anhydrous composition in wt%.

Literature data from H_2O solubility experiments with peralkaline haplogranitic melts (Dingwell et al. 1997; Linnen et al. 1996; Dingwell et al. 1997) were collected and the experimentally obtained solubilities were compared with the calculation based on the above-mentioned approach. H_2O solubilities calculated in mol% (Eq. 14) were converted to wt% to be comparable to the experimentally determined solubilities (Fig. 9a). For the haplogranitic melts with different excess alkali values (0.0047–0.0325; alkalis: K and Na) of Linnen et al. (1996), the calculated H_2O solubilities deviate less than 5% from the experimentally determined values. The data of Dingwell et al. (1997), which are haplogranites with a large range of peralkalinity (excess alkali: 0.0074–0.091) with the added alkalis being Na, K, Rb and Cs, can be reproduced with < 10% relative deviation. Only the data of Dingwell et al. (1984) (excess alkali: 0.0009–0.0241; alkalis: Na, K) show a systematic offset, where the calculated H_2O solubility is ~ 1 wt% higher than the experimentally obtained value. The haplogranite of Dingwell et al. (1984) is chemically comparable to the other haplogranites (see supplementary material "S2_data_collection"), so that this systematic deviation cannot be explained. The offset is further discussed later in the text.

Lithium seems to behave differently by affecting H_2O solubility to a lower extent compared to the other alkalis (Dingwell et al. 1997). However, we found that when accounting only for 0.4 times the mole fraction of Li_2O for the calculation of excess alkali, a good agreement for the calculated solubility based on excess alkali with the observed H_2O solubility of Dingwell et al. (1997) is obtained. This could imply that only 40% of the total Li content form non-bridging oxygens that are then accessible for bonding of hydrous species. This factor was implemented into the solubility model (Excel spreadsheet and Matlab script). However, the use of this factor for Li-bearing melts in the solubility model requires further validation as it is so far based on only four data points from Dingwell et al. (1997). Note, that due to this factor, the calculation of the excess alkali value for Li-bearing compositions with the spreadsheet does not give the true but an effective excess alkali value for H_2O solubility calculation.

To further test the developed H_2O solubility model, H_2O solubility data from natural peralkaline rhyolitic melt compositions were used (Scaillet and Macdonald 2001, 2006; Moore et al. 1998; Behrens and Jantos 2001; Gaillard et al. 2001; Stabile et al. 2018). In contrast to the haplogranitic melts, these natural peralkaline compositions contain additionally low amounts of TiO_2 (0–0.36 wt%), MnO (0–0.17), MgO (0–0.02 wt%) and CaO (0.17–0.41 wt%) and higher concentrations of FeO (up to 5.3 wt%; supplementary material "S2_data_collection"). There is good agreement of the modeled H_2O solubilities with the data of Behrens and Jantos (2001), Moore et al. (1998) and Gaillard et al. (2001) with deviations < 7% (Fig. 9b). The excess alkali for these data ranges between 0.0072 and 0.0253. The data of Stabile et al. (2018) (excess alkali: 0.011 – 0.0307) show significant deviation with higher observed solubilities than calculated with the model. However, the data of Stabile et al. (2018) may be treated with caution. This is the only study reporting considerable amounts (~ 30 vol%) of hydration bubbles in the glasses after the solubility experiments due to the use of glass powder as starting material for H_2O supersaturated experiments. The H_2O concentrations have been analyzed with KFT (bulk analysis) without prior crushing of the H_2O bubble-bearing glasses. Therefore, it cannot be excluded that the H_2O solubilities in this study may be overestimated by analyzing the sum of H_2O dissolved in the glass and additional water contained in the bubbles. The data from Scaillet and Macdonald (2001, 2006) are from phase relation studies in peralkaline rhyolitic melts. Scaillet and Macdonald (2006) provide two solubility values that they obtain from H_2O saturated experiments. From Scaillet and Macdonald (2001) we use the H_2O values obtained from crystal-free melt that coexisted with an H_2O vapor phase after equilibration and quench. The data cover a range of excess alkali between 0.0216 and 0.0501. Due to the analysis of H_2O with the by-difference method using the electron microprobe, the errors in H_2O solubility of these two studies are higher compared to those of the other studies. The mean absolute deviation between predicted and observed solubilities for the test data (all data presented in Fig. 9 excluding AOQ8, which is part of the training set of the model) is 8.1% (without Stabile et al. 2018 data: 4.7%).

The good agreement of observed H_2O solubility with the predicted solubilities based only on a single chemical parameter for both Fe-free haplogranites and Fe-bearing natural peralkaline rhyolitic melts suggests that the addition of Fe does not influence the H_2O solubility in peralkaline melts. Gaillard et al. (2001) found that also the Fe^{2+}/Fe^{3+} ratio has no measurable effect on H_2O solubility in their peralkaline melts which is confirmed by the data from Scaillet and Mcdonald (2001) where experiments with iron-bearing melts yield similar H_2O concentrations under reduced and oxidized conditions.

We also tested the calculation of H_2O solubility as a function of the compositional parameter MCLNK-Al/O from Behrens and Jantos (2001) instead of the excess alkali. Behrens and Jantos (2001) developed the MCLNK-Al/O parameter, defined as $100 \times (2\,Mg + 2Ca + Li + Na + K\text{-}Al)$/total oxygen, to describe H_2O solubility for peraluminous to peralkaline melts. For peralkaline melts the parameter corresponds to the ratio of mole percentage of non-bridging and total oxygen. Thus, the parameter would extend the dependence of our model by the contribution of Mg and Ca on the H_2O solubility. The synthetic haplogranites are Mg- and Ca-free, while the melts based on natural compositions have low Mg and Ca concentrations. Therefore, using the MCLNK-Al/O parameter in Eq. 14 instead of excess alkali yields similar H_2O solubilities for the haplogranites. For the natural compositions, the calculated H_2O solubilities using the MCLNK-Al/O parameter are only slightly higher compared to those from excess alkali calculations (supplementary material "S2_data_collection") but still within error. This observation when accounting additionally for Mg and Ca indicates that Mg and Ca in the natural rhyolitic compositions do not influence the H_2O solubility in peralkaline rhyolitic melts to a significant amount.

Comparison with other solubility models

The H_2O solubilities of peralkaline rhyolitic melts were compared to the prediction of the most recent H_2O solubility models—all of which are thermodynamic models—that allow the calculation of solubilities as a function of P, T and melt composition (Papale et al. 2016; Duan 2014; Ghiorso and Gualda 2015). The data of Dingwell et al. (1997) containing Rb and Cs as alkalis cannot be calculated using these models because the models only consider Na and K, the most abundant alkalis in natural melts.

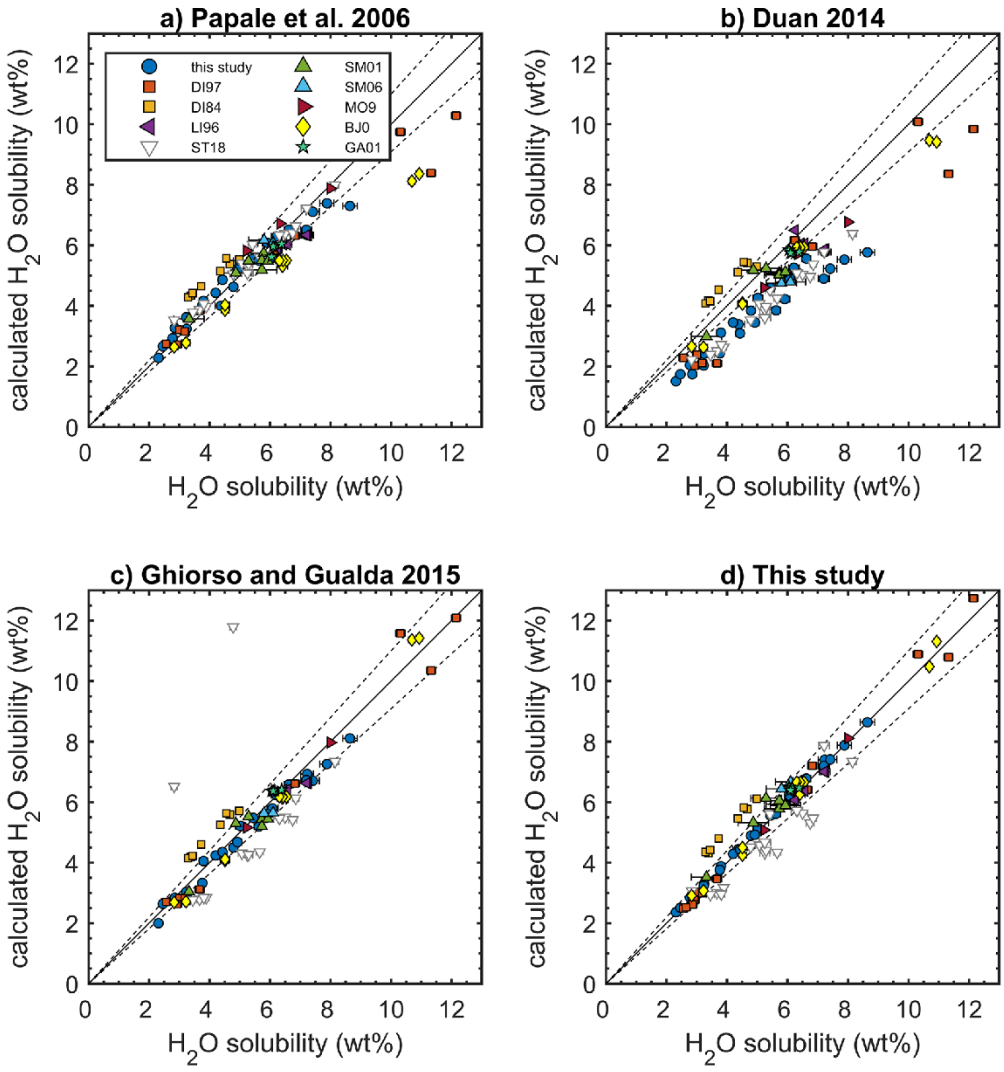

Fig. 10 Available experimentally determined H_2O solubility data for peralkaline rhyolitic melts compared to predicted values from existing H_2O solubility models (**a**–**c**) and the approach of this study (**d**). The legend in **a** is valid for all four graphs. The data in (**d**) are the summary of Fig. 9a, b. The dashed lines indicate a 10% deviation from the 1:1 line (solid line). All datasets together with their chemical composition are available in the supplementary material "S2_data_collection". Data of Stabile et al. (2018) were plotted with white symbols as these data may have to be treated with caution (see discussion). For the Dingwell et al. (1997) data, the melts with alkalis other than Na and K could only be calculated with the model of this study as the other models only account for Na and K. References: DI97: Dingwell et al. (1997); DI84: Dingwell et al. (1984); LI96: Linnen et al. (1996); ST18: Stabile et al. (2018); SM01: Scaillet and Macdonald (2001); SM06: Scaillet and Macdonald (2006); BJ01: Behrens and Jantos (2001); MO98: Moore et al. (1998); GA01: Gaillard et al. (2001)

It was found that the model of Papale et al. (2016) predicts the H_2O solubilities in the haplogranites within 10% deviation at $P < 200$ MPa. The mean absolute deviation of predicted values from observed solubility is 8.4% but the model fails at higher H_2O solubilities where it underestimates the H_2O solubilities significantly (Fig. 10a). The solubilities of Dingwell et al. (1984) are the only ones that are systematically overestimated by the model. For the natural melt compositions also a higher deviation is found at higher H_2O solubilities where the data from Behrens and Jantos (2001) are underestimated. One reason for the deviations can be the sensitivity of the Papale et al. (2016) model to redox

conditions (i.e. Fe^{2+}/Fe^{3+} ratio) as discussed by Wieser et al. (2022). Another reason may be an increasing uncertainty of the model at higher pressures. The Dingwell et al. (1997) melts do not contain iron or other multivalent cations and nevertheless the data show a large discrepancy (Fig. 10a), we suggest that the pressure effect is not negligible.

The Duan (2014) model underestimates H_2O solubilities in peralkaline melts with a mean absolute deviation of 23.7% (Fig. 10b). There is a systematic increase in deviation between modeled and observed solubilities with increasing peralkalinity. At constant P and T, the model predicts nearly constant H_2O solubilities for AOQ4 and AOQ8, indicating that the model does not account for the effect of excess alkalis on H_2O solubility. Again, only the Dingwell et al. (1984) dataset is overestimated.

The Ghiorso and Gualda (2015) model generally predicts most of the data quite well up to high pressure with a mean absolute deviation of 11.8% (Fig. 10c). The Dingwell et al. (1984) data are overestimated and the data of Stabile et al. (2018) are partly underestimated, which is comparable to the model prediction of this study (Fig. 10d). However, for five datapoints (three are out of range of the y-axis) the model predicts unrealistically high solubilities. These are datapoints calculated for compositions where all alkali is present as K_2O, which suggests that the model is not stable towards Na_2O free compositions.

It can be concluded that the new model of this study reproduces the observed solubilities in peralkaline rhyolitic melts most accurately with only two outlier datasets. The model can therefore be considered to be valid within the P and T range of the summarized experiments that are 27–500 MPa and 976–1523 K and excess alkali values up to 0.0825. Concerning the two outlier datasets, it is noteworthy that the Dingwell et al. (1984) data are overestimated by all model predictions. The observed H_2O solubilities contrast especially the overall trend of the Duan (2014) model tends to underestimate H_2O solubility in peralkaline rhyolitic melts. However, the anhydrous melt composition is within the range of the other tested data. Reasons for such a systematic deviation, e.g. a systematic analytical underestimation cannot be excluded but also not be further evaluated.

Conclusion

Existing H_2O solubility models are restricted to Na and K as alkalis present in silicate melts. The approach of this study—calculating the H_2O solubility as a function of excess alkali as a single chemical parameter—allows the prediction of H_2O solubility for melts with all alkali elements except for lithium. Interestingly, the empirical model performs slightly better than the thermodynamic H_2O solubility models. This indicates that the thermodynamic understanding of H_2O solubility in peralkaline melts could be further improved.

The accurate prediction of H_2O solubility in peralkaline melts is a contribution towards better understanding peralkaline rhyolite eruption styles that are up to now largely unknown (Clarke et al. 2019) and to improve the reconstruction of magmatic and volcanic processes related to peralkaline melts that occur e.g. in the East African Rift, Kenyan Rift, Gran Canaria, Turkey and Pantelleria (Lowenstern and Mahood, 1991; Neave et al. 2012; McDonald et al. 2015; Clarke et al. 2019). In the future, the investigation of the effect of peralkalinity on the solubility of other volatiles like CO_2 and mixed volatiles would be interesting.

Summary

- Linear molar absorption coefficients for water species quantification with near-infrared FTIR-spectroscopy were determined for peralkaline melts with the compositions $Ab_{38}Or_{34}Qz_{28}$ (AOQ) + 2, + 4 and + 8 wt% Na_2O excess to allow the determination of the H_2O species concentration.
- H_2O solubilities at high pressures (27–200 MPa) and temperatures (1123–1523 K) were determined for peralkaline haplogranitic melts with 4 and 8 wt% Na_2O excess with respect to AOQ composition. Combined with H_2O solubilities in AOQ melt (Holtz et al. 1995; Liu et al. 2005), a linear dependence of H_2O solubility (wt%) as a function of Na_2O excess (wt%) at constant P and T was found.
- Dingwell et al. (1997) showed that the H_2O solubility (in mol%) can be calculated as a function of excess alkali (difference between alkali and alumina mole fractions). Based on that dependence, a model was developed that describes H_2O solubility (mol%) based on P, T and excess alkali.
- Comparison of the model predictions with the observed H_2O solubilities in peralkaline haplogranitic and peralkaline natural melts yields good agreement. This suggests that H_2O solubility in peralkaline rhyolitic melts, can – besides P and T – be effectively described based on only a single chemical parameter.
- Calculation scripts (MS Excel and Matlab) are provided in the supplementary material to calculate H_2O solubility in peralkaline rhyolitic melts at 27–500 MPa, 980–1523 K and excess alkali up to 0.0825.

Supplementary Information The online version contains supplementary material available at https://doi.org/10.1007/s00410-022-01915-8.

Acknowledgements This project was partially funded by the German Science Foundation (DFG NO378/12-2). We thank Penny Wieser and one anonymous reviewer for their very helpful comments on the manuscript. We thank Barbara Maier and Annette Flicker for technical support and maintenance of the IHPV and the FTIR spectrometer. We acknowledge the high-quality sample preparation by Simone Schafflick. We thank Harald Behrens at the Institute for Mineralogy at the Leibniz University of Hannover to enable us to use the Karl-Fischer-Titration apparatus. We thank Nikolaus Krumrein for performing four solubility experiments within the frame of his bachelor's thesis.

Author contributions AA: conceptualization, glass synthesis, experiments and analysis of AOQ4 and AOQ8, computation, evaluation, and visualization; PP: glass synthesis, experiments, analysis and evaluation of AOQ2; DE: glass synthesis, computation and data collection; MN: conceptualization; AA wrote the original draft of the paper; all authors discussed the results and commented on the draft of the paper.

Data availability statement Tables, supplementary data and information can be found in the electronic supplementary material.

References

Acocella J, Tomozowa M, Watson EB (1984) The nature of dissolved water in sodium silicate glasses and its effect on various properties. J Non Cryst Solids 65:355–372

Allabar A, Nowak M (2020) High spatial resolution analysis of H_2O in silicate glass using attenuated total reflection FTIR spectroscopy coupled with a focal plane array detector. Chem Geol 556:119833

Allabar A, Dobson KJ, Bauer CC, Nowak M (2020) Vesicle shrinkage in hydrous phonolitic melt during cooling. Contrib Mineral Pet 175:21

Balzer R, Behrens H, Waurischk T, Reinsch S, Müller R, Kiefer P, Deubener J, Fechtelkord M (2020) Water in alkali aluminosilicate glasses. Front Mater. https://doi.org/10.3389/fmats.2020.00085

Behrens H (2005) Determination of water solubilities in high-viscosity melts: an experimental study on NaAlSi3O8 and KAlSi3O8 melts. Eur J Mineral 7:905–920

Behrens H, Jantos N (2001) The effect of anhydrous composition on water solubility in granitic melts. Am Mineral 86:14–20

Behrens H, Nowak B (2003) Quantification of H2O speciation in silicate glasses and melts by IR Spectroscopy – in situ versus quench techniques. Phase Transitions 76:45–61

Behrens H, Romano C, Nowak M, Holtz F, Dingwell DB (1996) Near-infrared spectroscopic determination of water species in glasses of the system MAlSi3O8(M=Li, Na, K): an interlaboratory study. Chem Geol 128:41–63

Behrens H, Misiti V, Freda C, Vetere F, Botcharnikov RE, Scarlato P (2009) Solubility of H2O and CO2 in ultrapotassic melts at 1200 and 1250 °C and pressure from 50 to 500 MPa. Am Mineral 94:105–120

Bottinga Y, Richet P (1995) Silicate melts: The "anomalous" pressure dependence of the viscosity. Geochim Cosmochim Acta 59:2725–2731

Burnham CW, Jahns RH (1962) A method for determining the solubility of water in silicate melts. Am J Sci 260:721–745

Clarke B, Calder ES, Dessalegn D, Fontijn K, Cortés JA, Naylor M, Hutchinson W, Yirgu G (2019) Fluidal pyroclasts reveal the intensity of peralkaline rhyolite pumice cone eruptions. Nat Commun 10:2010

Dingwell DB, Harris DM, Scarfe CM (1984) The solubility of H2O in melts in the system SiO2 – Al2O3 – Na2O – K2O – at 1 to 2 kbars. J Geol 92:387–395

Dingwell DB, Holtz F, Behrens H (1997) The solubility of H2O in peralkaline and peraluminous granitic melts. Am Mineral 82:434–437

Duan X (2014) A general model for predicting the solubility behavior of H2O-CO2 fluids in silicate melts over a wide range of pressure, temperature and compositions. Geochim Cosmochim Acta 125:582–609

Gaillard F, Scaillet B, Pichavant M, Bény JM (2001) The effect of water and f_{O2} on the ferric-ferrous ratio of silicic melts. Chem Geol 174:255–273

Ghiorso M, Gualda GAR (2015) An H_2O-CO_2 mixed fluid saturation model compatible with rhyolite-MELTS. Contrib Mineral Pet 169:53

Giordano D, Russell JK, Dingwell DB (2008) Viscosity of magmatic liquids: a model. Earth Planet Sci Lett 271:123–134

Goranson RW (1931) The solubility of water in granitic magmas. Am J Sci 22:481–502

Holtz F, Behrens H, Dingwell DB, Johannes W (1995) H2O solubility in haplogranitic melts: Compositional, pressure, and temperature dependence. Am Mineral 80:94–108

Iacono-Marziano G, Morizet Y, Le Trong E, Gaillard F (2012) New experimental data and semi-empirical parameterization of H2O-CO2 solubility in mafic melts. Geochim Cosemochim Acta 97:1–23

Iacovino et al (2021) VESIcal Part I: An open-source thermodynamic model engine for mixed volatile (H_2O-CO_2) solubility in silicate melts. Earth Space Sci 8:e2020EA001584

Linnen R, Pichavant M, Holtz F (1996) The combined effects of fO2 and melt composition on SnO2 solubility and tin diffusivity in haplogranitic melts. Geochim Cosmochim Acta 60:4965–4976

Liu Y, Zhang Y, Behrens H (2005) Solubility of H2O in rhyolitic melts at low pressures and a new empirical model for mixed H2O–CO2 solubility in rhyolitic melts. J Volcanol Geotherm Res 143:219–235

Lowenstern J, Mahood GA (1991) New data on magmatic H_2O contents of pantellerites, with implications for petrogenesis and eruptive dynamics at Pantelleria. Bull Volcanol 54:78–83

McDonald R, Sumita M, Schmincke HU, Baginski B, White JC, Ilnicki SS (2015) Peralkaline felsic magmatism at the Nemrut volcano, Turkey: impact of volcanism on the evolution of Lake Van (Anatolia) IV. Contrib Mineral Petrol 169:34

Moore G, Vennemann T, Carmichael ISE (1998) An empirical model for the solubility of H2O in magmas to 3 kbars. Am Mineral 83:36–42

Neave DA, Fabbro G, Herd RA, Petrone CM, Edmonds M (2012) Melting, differentiation and degassing at the Pantelleria Volcano, Italy. J Petrol 53:637–663

Newman S, Lowenstern JB (2002) VolatileCalc: a silicate melt–H2O–CO2 solution model written in Visual Basic for excel. Comput Geosci 28:597–604

Nowak M, Behrens H (1997) An experimental investigation on diffusion of water in haplogranitic melts. Contrib Mineral Petrol 126:365–376

Ohlhorst S, Behrens H, Holtz F (2001) Compositional dependence of molar absorptivities of near-infrared OH- and H2O bands in rhyolitic to basaltic glasses. Chem Geol 174:5–20

Papale P, Moretti R, Barbato D (2016) The compositional dependence of the saturation surface of H2O+CO2 fluids in silicate melts. Chem Geol 229:87–95

Preuss O, Marxer H, Ulmer S, Wolf J, Nowak M (2016) Degassing of hydrous trachytic Campi Flegrei and phonolitic Vesuvius melts: experimental limitations and chances to study homogeneous bubble nucleation. Am Mineral 101:859–875

Scaillet B, Macdonald R (2001) Phase relations of peralkaline silicic magmas and petrogenetic implications. J Petrol 42:825–845

Scaillet B, Macdonald R (2006) Experimental constraints on pre-eruption conditions of pantelleritic magmas: Evidence from the Eburru complex, Kenyan Rift. Lithos 91:95–108

Shishkina TA, Botcharnikov RE, Holtz F, Almeev RR, Jazwa AM, Jakubiak AA (2014) Compositional and pressure effects on the solubility of H2O and CO2 in mafic melts. Chem Geol 388:112–129

Sierralta M, Nowak M, Keppler H (2002) The influence of bulk composition on the diffusivity of carbon dioxide in sodium aluminosilicate melts. Am Mineral 87:1710–1716

Spickenbom K, Sierralta M, Nowak M (2010) Carbon dioxide and Argon diffusion in silicate melts: insights into the CO2 speciation in magmas. Geochim Cosmochim Acta 74:6541–6564

Stabile P, Radica F, Bello M, Behrens H, Carroll MR, Paris E, Giuli G (2018) H2O solubility in pantelleritic melts: pressure and alkali effects. J Min Geochem 195(1):1–9

Wieser PE, Iacovino K, Matthews S, Moore G, Allison CM (2022) VESical: 2. Critical approach to volatile solubility modeling using an open-source Python3 engine. Earth Space Sci 9:e2021EA001932

Yamashita S (1999) Experimental study of the effect of temperature on water solubility in natural rhyolite melt to 100 MPa. J Pet 40:1497–1507

Publication Study IV

Titel: H_2O degassing triggered by alkali depletion in bimodal magma injection processes – a new experimental approach

Authors: Patricia Louisa Marks, Anja Allabar, and Marcus Nowak

Published online on August 02, 2023, in European Journal of Mineralogy, 35, 613–633, https://doi.org/10.5194/ejm-35-613-2023.

Eur. J. Mineral., 35, 613–633, 2023
https://doi.org/10.5194/ejm-35-613-2023

European Journal of Mineralogy
Open Access

H_2O degassing triggered by alkali depletion in bimodal magma injection processes – a new experimental approach

Patricia Louisa Marks[1], **Anja Allabar**[2], **and Marcus Nowak**[1]

[1]Department of Geosciences, Eberhard Karls University Tübingen, 72074 Tübingen, Germany
[2]independent researcher

Correspondence: Patricia Louisa Marks (patricia.marks@uni-tuebingen.de)

Received: 1 February 2023 – Revised: 19 June 2023 – Accepted: 30 June 2023 – Published: 2 August 2023

Abstract. The injection of mafic magma into a hydrous felsic magma chamber is a potential trigger mechanism for bimodal explosive volcanism. As H_2O is the most abundant volatile component in magmas, the interaction and the degassing behavior of mildly peralkaline hydrous rhyolitic melt in contact with hydrous basaltic melt were investigated by decompression experiments. Preparatory hydration experiments and bimodal magma decompression experiments, as well as reference experiments, were carried out in an internally heated argon pressure vessel. Pre-hydrated rhyolite and basalt cylinders were perfectly contacted together in a precious-metal capsule, heated to 1348 K at 210 MPa, and thermally equilibrated for 10 min. The initial sample properties were determined by a bimodal reference experiment, quenched immediately after equilibration. To simulate the magma ascent, three bimodal samples and a decompression experiment with two contacted rhyolite cylinders for testing the experimental setup were decompressed with 0.17 or 1.7 MPa s^{-1} to the final pressure of 100 MPa and then quenched.

All decompression experiments resulted in vesiculated samples. The H_2O vesicles observed in the decompressed sample of the monomodal rhyolite–rhyolite reference experiment are homogeneously distributed throughout the sample. The former interface between the contacted glass cylinders is invisible after decompression and quench. This reference experiment proves that the two-cylinder design does not influence the degassing behavior of the hydrous melt, e.g., an increased formation of vesicles at possible nucleation sites at the contact plane of the cylinders.

The undecompressed bimodal rhyolite–basalt sample shows crystal-free rhyolitic glass, whereas 3 µm sized idiomorphic magnetite crystals coexist with glass in the basaltic part of the sample. Within the 10 min run time, a ∼ 300 µm wide hybrid composition zone developed between the hydrous rhyolitic and basaltic endmembers, caused by diffusion-induced mixing processes.

Decompression and quenching of the bimodal melts resulted in vesiculated glass samples. A ∼ 100 µm wide zone of alkali-depleted rhyolitic glass as part of the ∼ 300–560 µm wide hybrid zone is covered with an enhanced number of H_2O vesicles compared to the pristine rhyolitic and basaltic glass volumes. We suggest that this enhanced vesiculated zone forms by a rapid diffusional loss of alkalis from the mildly peralkaline rhyolitic melt into the basaltic melt of the sample. The reduced alkali concentration significantly reduces the H_2O solubility of the rhyolitic melt. This process enhances the H_2O supersaturation necessary for vesicle formation during decompression.

In summary, the new findings imply that convective magma ascent driven by the injection of hot basaltic magma into a hydrous peralkaline rhyolitic melt reservoir leads to enhanced H_2O vesicle formation near the melt interface and thus to efficient degassing. This in turn can accelerate buoyancy-driven magma ascent and mingling and mixing processes that induce further degassing and potentially trigger explosive volcanic eruptions.

Published by Copernicus Publications on behalf of the European mineralogical societies DMG, SEM, SIMP & SFMC.

1 Introduction

Explosive volcanic eruptions are driven by the formation and growth of volatile vesicles, mainly H_2O and subordinate CO_2, in hydrous silicic melts. The formation of fluid vesicles requires supersaturation of volatiles dissolved in the silicate melt. Vesicles in hydrous rhyolitic melt form by nucleation (e.g., Sparks, 1978; Navon and Lyakhovsky, 1998; Gonnermann and Manga, 2007; Hajimirza et al., 2019; Gardner et al., 2022) or, as recently suggested for phonolitic Vesuvius melt composition, by spinodal decomposition (Allabar and Nowak, 2018; Allabar et al., 2020; Sahagian and Carley, 2020; Gardner et al., 2022). However, vesicle formation and growth lead to an overpressure that might burst the ceiling of a magma chamber (e.g., Sparks et al., 1977; Sigurdsson and Sparks, 1981; Miller and Wark, 2008; Spera et al., 2016). The resulting sudden pressure (P) drop enhances the further formation and growth of vesicles, which significantly reduces magma density. Accelerated magma ascent and rapid expansion of vesicles lead finally to magma fragmentation. These fundamental mechanisms hold to small explosive silicic eruptions, such as the 1875 eruption of Askja in Iceland, which produced $\sim 0.2\,km^3$ of rhyolitic magma (Sigurdsson and Sparks, 1981) with a volcanic explosive index (VEI) of 4. They also apply for catastrophic explosions, e.g., the 74 ka supereruption of Toba on Sumatra with a VEI of 8, which ejected $\sim 2800\,km^3$ of rhyolitic magma, equivalent to $\sim 8000\,km^3$ of volcanic ash (Rose and Chesner, 1987; Self and Blake, 2008).

Under the pressure and temperature conditions of subvolcanic magma chambers, silicate melts can dissolve several weight percent (wt %) of the main volatile H_2O. Several processes to achieve volatile supersaturation and vesicle formation are discussed: (1) decompression by magma ascent (e.g., Sparks et al., 1977), (2) sudden pressure drop by earthquakes rupturing hydrous magma chamber roof rocks, (3) enrichment of volatiles that exceed the saturation limit of silicate melt due to partial crystallization (e.g., Bachmann and Bergantz, 2008; Scaillet and Pichavant, 2003), (4) thermal vesiculation induced by the latent heat of partial crystallization and frictional heating (Lavallee et al., 2015), and (5) the injection of hot mafic magma into differentiated volatile-rich silicic magma accompanied by mechanical mingling and chemical mixing processes (Miller and Wark, 2008; Spera et al., 2016; Murphy et al., 1998; Leonard et al., 2002; Druitt et al., 2012; Perugini et al., 2012; Laumonier et al., 2014; Pichavant et al., 2018), as well as (6) dispersion of partially crystallized mafic fragments acting as heterogeneous vesicle nucleation sites in hydrous silicic melts (Paredes-Marino et al., 2017). While the first points have already been extensively studied (e.g., Martel et al., 2017), experimental approaches to the last points are rare. Therefore, this experimental work focuses solely on the effects of magma degassing triggered by magma injection.

1.1 Geological background of explosive volcanic eruptions triggered by magma injection

Bimodal basaltic–rhyolitic volcanism in Iceland was first described by Bunsen (1851). In recent literature partially crystallized mafic streaks, glass fragments, blebs, and enclaves are described as common features in products of explosive felsic volcanic eruptions (e.g., Sparks et al., 1977; Troll et al., 2004; Miller and Wark, 2008; Arienzo et al., 2010; Druitt et al., 2012; Paredes-Marino et al., 2017; Jarvis et al., 2021).

Injection of hot basaltic magma into a rhyolitic magma chamber may induce local temperature differences of up to 500 K that shift the system out of equilibrium (e.g., Sparks et al., 1977; Snyder, 2000; Miller and Wark, 2008). Accompanied mechanical magma mingling significantly increases the contact surface of the two melts (e.g., Perugini et al., 2012; Jarvis et al., 2021). This enhances the transfer of heat and mixing by chemical diffusion. Two important effects are triggered by heat transfer at the interface: (1) volatile-bearing hot basaltic magma cools down and may partially crystallize. The possible exceedance of the volatile saturation limit by sufficient enrichment in the residual melt can lead to vesicle formation and growth. (2) Volatile-rich silicic magma can be superheated. This may lead to the formation and growth of fluid vesicles as H_2O solubility decreases with the temperature at pressures of ≤ 300 MPa (Holtz et al., 1995; Lavallee et al., 2015). In both scenarios, the vesicle formation and growth significantly decrease the magma density, which is controlled by the pressure–volume–temperature (PVT) behavior of H_2O_{fluid}. The decrease in magma density may trigger buoyancy-driven convection and a large-scale overturning of an initially stratified magma chamber within timescales of days or weeks (Sparks et al., 1977; Snyder, 2000; Phillips and Woods, 2002). Further vesicle formation and expansion accelerate magma ascent. The rapid build-up of internal fluid pressure during the growth of bubbles and the increase in melt viscosity induced by H_2O loss may cause melt fragmentation, followed by explosive volcanic eruptions.

1.2 Experimental investigation of the interaction of felsic and mafic magmas

Yoder (1973) investigated experimentally the physicochemical interaction of H_2O-saturated basaltic and rhyolitic melts. The fusion of mixed fine-grained rock powders and H_2O at 100 MPa and 1473 K resulted in complete melt miscibility. In contrast, melting of layered basaltic and rhyolitic rock powders resulted in separated glasses with a narrow diffusion zone with an intermediate (hybrid) composition of $\sim 300\,\mu m$ across the interface after 2 h of fusion and quench. This indicates that silicate melts of different compositions can be maintained in direct contact at least for a short time. Johnston and Wyllie (1988) confirmed these results with coupled hydrous basaltic and rhyolitic melt reaction experiments at

1 GPa and 1193 K. They demonstrated that alkali diffusion is orders of magnitude faster than the diffusion of divalent cations that is limited by the diffusion of the network formers Si and Al (Watson, 1982).

Experimental mingling of basaltic and silicic melts was successfully conducted by the mechanical torsion of two contacted melt disks at 1483 K and ambient P (Kouchi and Sunagawa, 1985). Laumonier et al. (2015) mingled hydrous basaltic and tonalitic magmas by torsion in a Patterson apparatus at 300 MPa and $\leq$ 1293 K. The experimental products show entrainment of mafic crystals into the felsic melt, mafic–felsic banding, and enclave formation similar to the textures observed in bimodal volcanic rocks. Perugini et al. (2012) and Morgavi et al. (2013) used a rotating crucible and a rotating inner cylinder based on the so-called journal bearing system (JBS) to mingle granitic and basaltic melts at 1623–1673 K. The observed chaotic mingling by stretching and folding induces a significant increase in the interface of the silicate melts within hours and enhances diffusional exchange between the two melts. Wiesmaier et al. (2015) demonstrated magma mingling of nominally volatile-free rhyolitic and basaltic melts at ambient P and 1723 K without external forces. Air bubbles were intentionally entrapped at the coarsely ground interface of the two glass cylinders stacked on each other. During the experiment, the initial air bubbles ascended from the melt interface into the overlying rhyolitic melt. The bubbles dragged filament-like mafic melt streaks into the rhyolitic melt. Furthermore, numerical simulations of Montagna et al. (2015) show that the mingling of volatile-rich shoshonitic and partially degassed phonolitic magma develops over a short timescale of hours.

Despite these numerous experimental studies on bimodal melts, experiments to simulate degassing processes driven by magma injection are still lacking. Therefore, this study aims to find an experimental approach to investigate H_2O degassing processes by simulating the injection of volatile-bearing basaltic melt into an H_2O-saturated differentiated felsic melt. The main questions that we try to answer in this study are as follows: how do interdiffusion processes between the rhyolitic and basaltic melt influence the H_2O solubility in the developing intermediate melt composition? Would this further affect the vesicle nucleation? Which zone of bulk melts is influenced by the degassing and mixing processes, dependent on time and decompression rate?

2 Experimental and analytical methods

2.1 Starting material

Rhyolitic and basaltic glasses similar to the bimodal magma compositions of the Askja volcanic complex (Sparks et al., 1977) were synthesized. A modification was implemented on the rhyolitic composition to obtain a simplified and slightly peralkaline haplogranitic composition ($Ab_{38}Or_{34}Qz_{28}$, in wt %; Holtz et al., 1992) with a Na_2O excess of 2 wt %. The modification was chosen to obtain a nearly bubble-free glass and a distinct interface between the intense, dark brown basaltic glass and the iron-free colorless and transparent rhyolitic glass to best visualize the expected bubble textures and possible mixing effects. The basaltic composition was synthesized according to the analyses of Philpotts and Ague (2009) (Table 1). To receive homogeneous starting glasses of rhyolitic and basaltic composition, the glass syntheses were conducted following the experimental protocol of Marxer et al. (2015) and the improvement described in Allabar and Nowak (2018). This procedure ensured crystal- and tension-free homogeneous glasses that are nearly free of air bubbles. Cylinders up to 13 mm in length and 5 mm in diameter were drilled from the glasses. The sharp edges of each glass cylinder were sanded and rounded to prevent capsule damage during pressurization. The glass compositions were confirmed with electron microprobe analysis (EMPA) (Table 1).

2.2 Hydration experiments

Rhyolitic and basaltic glass cylinders were used as starting material for preparatory hydration experiments. Previous studies indicated that hydration experiments at high P and T (temperature) using glass powder induced the formation of numerous small vesicles in the sample volume due to excess H_2O fluid in the case of saturated conditions (e.g., Gardner et al., 1999; Iacono-Marziano et al., 2007) or due to H_2O–N_2 vesicles in the case of H_2O-undersaturated conditions (e.g., Preuss et al., 2016). Annealed and cleaned Au80Pd20 tubes (outer diameter: 5.4 mm; inner diameter: 5.0 mm), with lengths depending on the specific glass cylinder lengths, were closed at the bottom with Au80Pd20 lids while the other side was crimped to a star shape, to stabilize the shape of the capsules at high P and T (Marxer et al., 2015).

To ensure H_2O saturation of the melt during the hydration experiments, 6 wt % to 7 wt % water was welded together with the rhyolite or basalt glass cylinders into the capsules (Fig. 1). Under hydration conditions of 200 MPa and 1523 K, calculated H_2O solubilities are 5.7 wt % H_2O in the mildly peralkaline rhyolitic melt (Allabar et al., 2022) and 4.8 wt % H_2O in the basaltic melt (Berndt et al., 2002). Consequently, the excess water added to the capsules ensured complete H_2O saturation for both melt compositions. To check for possible leakage, the sample capsules were reweighed after heating to 383 K and after pressurization in a cold seal pressure vessel to 100 MPa at room temperature and again after storing at 393 K at ambient pressure. In the case of constant weight, the capsules were used for hydration experiments.

The hydration experiments were performed in an internally heated argon pressure vessel (IHPV) at 1523 K and 200 MPa for 96 h at an intrinsic oxygen fugacity close to $\Delta\log\mathrm{QFM} = +3.5$ (Berndt et al., 2002). After hydration, the

melts were quenched isobarically with a moderate quench rate of $\sim 16\,K\,s^{-1}$ (NQ; Allabar et al., 2020) to room temperature by switching off the IHPV furnace. This ensured the production of crack-free glass cylinders that were used for the magma injection experiments. The capsules were then punctured and heated at 383 K for at least 24 h to gravimetrically determine the amount of released free water to calculate the H_2O content of the glass (Table 2).

2.3 Preparation of hydrated samples

The hydrated glass cylinders were prepared for further decompression experiments and analysis. The cylinders were unwrapped from the capsule material. The 500 µm slices were cut from the middle of the samples perpendicular to the cylinder axis for the preparation of double-sided polished thin sections to be used for sample characterization. The remaining sample halves were ground and polished each on one cylinder face. This procedure enabled an ideal contact surface of two glass cylinders required for the bimodal decompression experiments.

2.4 Bimodal decompression experiments

For each bimodal magma injection (MI) experiment, a hydrated rhyolite cylinder and a hydrated basalt cylinder were inserted into a new Au80Pd20 capsule, oriented as rhyolite on top of basalt or basalt on top of rhyolite (Table 2). The polished faces of both glass cylinders were horizontally aligned to prevent air entrapment between the cylinder faces. Air entrapment could cause the formation of pre-existing vesicles between the two cylinders during the melting process (e.g., Wiesmaier et al., 2015), which may affect the degassing process during subsequent decompression as an experimental artifact. To test this experimental design, a reference sample was prepared where two rhyolite cylinders of one hydrated sample were contacted in a capsule (Fig. 1).

The bimodal experiments were conducted in the IHPV equipped with a rapid quench device (Berndt et al., 2002). Five experiments were performed:

- one decompression reference experiment (rhyolite–rhyolite Rt–Rt: MI_Rt_1) to validate the new experimental procedure
- one bimodal reference experiment (rhyolite–basalt Rt–B: MI_5) to determine the initial melt conditions after thermal equilibration and before decompression
- three bimodal decompression experiments (Rt–B: MI_T_3, MI_6 and MI_7) to study H_2O degassing in a bimodal magma system.

All samples were heated isobarically at the initial pressure (P_i) of 210 MPa at $25\,K\,s^{-1}$ from room temperature to the run temperature (T_r) of 1348 K or 1403 K (Table 2). The P and T conditions ensured H_2O undersaturation to prevent H_2O loss during the temperature equilibration of 10 min. Except for experiment MI_5, the hydrous bimodal melt assemblages and the Rt–Rt melt assemblage were decompressed isothermally, using a high-pressure valve optimized for continuous decompression (e.g., Nowak et al., 2011; Allabar and Nowak, 2018). Decompression rates of 0.17 or $1.7\,MPa\,s^{-1}$ were applied until the final pressure (P_f) of 100 MPa was reached. To minimize partial crystallization of the basaltic melt, all MI samples were quenched at a medium quench rate (MQ) of $\sim 44\,K\,s^{-1}$ (Allabar et al., 2020). Because rhyolitic melt is not as prone to the quench-crystal formation, the Rt–Rt sample was quenched more slowly at $\sim 16\,K\,s^{-1}$ to room temperature by switching off the furnace. After re-weighing the capsules to determine possible H_2O loss due to leakage, the decompressed samples were cut parallel to their cylinder axes. One-half of each sample was embedded in epoxy resin, ground, polished, and sputtered twice with a 5 nm carbon coating for EMPA and scanning electron microscopy (SEM) analysis, while the other half was used for the preparation of double-sided polished thin sections of ~ 200 µm thickness (d; measured with a Mitutoyo digital micrometer (± 3 µm); Table 2) for Fourier transform infrared (FTIR) spectroscopy and optical microscopy.

2.5 Analytical methods

2.5.1 Electron microprobe analysis

The bulk compositions of the nominally dry starting glasses were analyzed with a JEOL JXA 8900 R electron microprobe (EMP). Wavelength-dispersive X-ray spectroscopy analyses were conducted by using an acceleration voltage of 15 kV, a beam current of 3 nA, and a defocused beam with a diameter of 20 µm to optimize for Na analysis (e.g., Morgan and London, 2005; Stelling et al., 2008). Beam counting times were 10 s (Na), 16 s (K, Si, Ca, Al, Mg, Fe), and 30 s (Mn, Ti). To test the homogeneity of the glasses and the agreement with the desired glass composition, 15 points were measured across an entire glass cylinder section of each composition. In sample MI_T_3, one concentration profile was measured across the hybrid zone from the lower basalt to the overlying rhyolite. The samples MI_5, MI_6, and MI_7 were analyzed using a JEOL JXA 8230 electron microprobe under the same conditions but with a beam current of 10 nA. Concentration profiles were measured across the samples, from the initial basaltic composition to the initial rhyolitic composition. EMPA data are given in Table S1 in the Supplement.

2.5.2 Scanning electron microscopy

The experimental samples were examined with a Hitachi TM3030plus Tabletop SEM, an electron beam current of 50 nA, and an acceleration voltage of 15 kV. Backscattered electron (BSE) images of the samples were acquired at up to 5000× magnification (Fig. S1). The overview images of the

Table 1. Glass composition of rhyolite and basalt, measured by EMP, similar to the compositions of the 1875 Askja bimodal eruption (Sparks et al., 1977). Averaged magnetite composition of eight crystals measured in the basalt of MI_T_3. Intermediate melt composition of MI_T_3, MI_7, and MI_6 in the region of enhanced vesicle formation in the hybrid zone. The data of all EMP measurements are given in weight percent (wt %).

Oxides	Rhyolite	Basalt	Magnetite MI_T_3 B	MI_T_3 Hyb[d]	MI_7 Hyb[d]	MI_6 Hyb[d]
SiO_2	75.16	54.75	0.75	71.87	71.06	71.35
TiO_2		1.97	3.64	0.02	0.03	0.01
Al_2O_3	12.76	13.87	2.92	12.24	11.99	12.29
FeO[a]		11.84	80.13	1.53	2.01	1.56
MnO		0.20	0.52	0.11	0.04	0.04
MgO		4.05	5.83	0.58	0.74	0.66
CaO		7.93	0.30	1.48	1.54	1.31
Na_2O	6.54	3.16	0.08	4.70	4.65	4.44
K_2O	5.5	1.46	0.07	4.56	4.18	4.28
Total	99.96	99.23	94.25[c]	97.09[e]	96.24[e]	95.94[e]
x_{ex}^{b}	0.03	−0.04		0.003	0.001	−0.002

[a] Total Fe concentration is given as FeO. [b] x_{ex} is the difference between mole fractions of alkalis and those of alumina ($(Na_2O + K_2O - Al_2O_3) / 100$) (Allabar et al. 2022). [c] FeO converted to FeO and Fe_2O_3 (Carmichael, 1967) gives a total of 100.3 wt % and 100.1 wt % without considering alkali oxides, respectively. [d] Zone where enhanced vesicle formation is observed. [e] Total < 100 wt % due to the H_2O content of the hydrated glass.

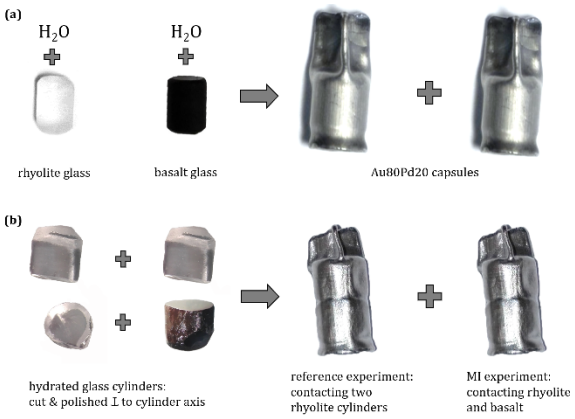

Figure 1. (a) Glass cylinders of rhyolite (Rt_5_h) and basalt (B_4_h), each rounded at the edges, are welded separately into an Au80Pd20 tube (outer and inner diameter: 5.4 and 5.0 mm) with 7 wt % or 6 wt % H_2O, respectively. Hydration experiments were conducted in the IHPV at 200 MPa and 1523 K and equilibrated for 96–168 h. **(b)** The quenched glass cylinders were unwrapped, cut perpendicular to the cylinder axis, and ground and polished at one side of each cylinder face. Contact of a pair of hydrated rhyolite cylinders or a hydrated rhyolite and a hydrated basalt glass cylinder in a new Au80Pd20 tube. Decompression experiments were conducted in the IHPV at 1348 and 1403 K with decompression from 210 to 100 MPa and with rates of 0.17 or 1.7 MPa s^{-1}.

entire samples were generated by adjusting the grey values of individual images and stitching (Fig. 2). BSE images were used to estimate vesicles in the central volume with a number density (VND) using ImageJ and CSD corrections (Higgins, 2000) as described in Marxer et al. (2015) and Preuss et al. (2016).

2.5.3 FTIR spectroscopy

The total H_2O concentrations ($c_{H_2O_t}$) of the hydrated and decompressed rhyolite glasses were determined by FTIR spectroscopy. The samples were analyzed in the near-infrared range (4000–6000 cm^{-1}) with the Bruker Vertex v80 FTIR spectrometer coupled with the HYPERION 3000 IR microscope by using a tungsten halogen light source, a CaF_2 beam splitter, a liquid-N_2-cooled InSb single-element detector, a 15× Cassegrain objective, and the OPUS 7 software package. Overview images of the thin sections were recorded, and the positions of the measuring points were programmed and subsequently automatically measured. With a knife-edge aperture set to 50 × 50 µm, the samples were measured with 50 scans per spectrum in transmission mode at a spectral resolution of 4 cm^{-1}. Air was measured as a reference. Each measurement location was tested to be free of fluid vesicles in the analyzed glass volume by focusing through the thin section. To determine spatial variations in the H_2O concentrations throughout the sample, profiles were measured along the longitudinal and transverse cylinder axes. The infrared data are given in Table S1 in the Supplement.

The $c_{H_2O_t}$ of the hydrated rhyolite samples was determined by measuring the peak heights of the ab-

sorbances (A) of the combination modes of molecular H_2O (H_2O_m) at $\sim 5210\,cm^{-1}$ and hydroxyl groups (OH) at $\sim 4470\,cm^{-1}$. A linear-tangential baseline correction (Behrens et al., 1996) was applied by setting points at ~ 5400 and $\sim 4700\,cm^{-1}$, ensuring that the straight line is tangential to the spectrum between the absorption bands at 5210 and $4470\,cm^{-1}$. For evaluation, the linear molar absorption coefficients ($\varepsilon_{H_2O_m} = 1.50\,L\,mol^{-1}\,cm^{-1}$, $\varepsilon_{OH} = 1.59\,L\,mol^{-1}\,cm^{-1}$) and the density correlation (ρ_{AOQ2} $[g\,L^{-1}] = (2351 \pm 2) - (12.3 \pm 0.6) \cdot c_{H_2O_t}$) from Allabar et al. (2022) were used. Because near-infrared measurements in transmission mode were impossible for basaltic glasses, the total H_2O concentration was determined gravimetrically ($c_{H_2O_g}$) (Table 2).

2.5.4 X-ray diffraction

For the identification of crystals of the partially crystallized basaltic hydration and MI samples, a Bruker D8 Discover μ-XRD (X-ray diffraction) with a VÅNTEC 500 2D detector was used together with a cobalt radiation source ($\lambda = 1.79$ Å), a HOPG primary monochromator, and a 500 µm monocapillary optic. All basaltic samples were measured for 180 s with an acceleration voltage of 30 kV and an electric current intensity of 30 mA. The angle of incidence of the X-ray beam was set to 10° and the detector to 25°. The diffraction patterns of the crystalline phases were evaluated using the Bruker software DIFFRAC.EVA.

2.5.5 Transmitted light microscopy

Vesicles in transparent sample thin sections were quantified using the Zeiss Axio Imager M2M microscope and the software "Trackworks". Each measurement was performed by focusing through the sample in a predefined area, resulting in an analyzed sample volume that was used to normalize the number of vesicles to 1 mm^3 of vesicle-free glass. The errors in the transmitted light microscopy (TLM) analyses were calculated using error propagation, assuming errors of 5 % for vesicle size and vesicle number, as well as ± 3 µm for sample thickness.

3 Results

3.1 Hydration samples

All quenched capsules were punctured after 96–168 h of hydration. Since all samples showed a weight loss after 24 h in the compartment drier (383 K), water in the punctured capsules evaporated, showing that a free H_2O-fluid phase during the entire experiment duration was ensured. The mass of the evaporated excess water was used to calculate by difference the dissolved H_2O concentration in the melt under the given experimental conditions (Table 2).

Table 2. Experimental conditions for hydration and decompression experiments in the IHPV. H_2O solubilities (H_2O sol.) at 200 MPa and 1523 K in rhyolitic melt were calculated according to Allabar et al. (2022) and in basaltic melt according to Berndt et al. (2002).

Sample	Experiment	P_{Eq}, P_i	P_f	T_{Eq}, T_f	t_{Eq}	dP/dt	Quench	H_2O sol.	$c_{H_2O_g}$ max	$c_{H_2O_g}$ min	H_2O loss after puncturing	$c_{H_2O_t}$ in Rt	$\pm H_2O$	d of thin section	Mag in B
		[MPa]	[MPa]	[K]	[h]	[MPa s^{-1}]		[wt %]	[wt %]	[wt %]	[mg]	[wt %]	[wt %]	[mm]	
Rt_1_h^1	Hydr.	200	200	1523	115	–	NQ	5.70	5.20	5.14	4.57	5.67	0.54*	0.072	–
Rt_3_h^2	Hydr.	200	200	1523	96	–	NQ	5.70	5.93	3.99	6.02	5.38	0.19	0.211	–
Rt_4_h^3	Hydr.	200	200	1523	96	–	NQ	5.70	5.14	3.92	10.48	4.35	0.16	0.248	–
Rt_5_h^4	Hydr.	200	200	1523	96	–	NQ	5.70	6.11	5.30	2.58	5.11	0.18	0.232	–
B_2_h^1	Hydr.	200	200	1523	168	–	NQ	4.80	4.88	4.85	4.72			0.279	X
B_3_h^2	Hydr.	200	200	1523	96	–	NQ	4.80	5.41	4.66	10.08			0.210	X
B_4_h^3	Hydr.	200	200	1523	96	–	NQ	4.80	4.00	3.65	9.65			0.245	X
ML_Rt_1	Rt^3 / Rt^3	210	100	1348	10 min	0.17	NQ					4.22	0.14	0.293	–
ML_5	Rt^1 / B^1	210	210	1348	10 min	–	MQ					5.25	0.18	0.229	X
ML_T_3	Rt^2 / B^2	210	100	1348	10 min	0.17	MQ					4.07	0.18	0.210	X
ML_6	Rt^4 / B^3	210	102	1403	10 min	1.7	MQ					4.65	0.20	0.200	X
ML_7	B^3 / Rt^4	210	100	1348	10 min	0.17	MQ					4.53	0.17	0.230	X

P_{Eq} is equilibration/hydration pressure; P_i is initial pressure prior to decompression; P_f is final pressure; T_{Eq} is equilibration/hydration temperature; T_f is run temperature during experiment; t_{Eq} is equilibration/experiment duration; dP/dt is decompression rate; NQ: 16 K s^{-1}; MQ: 44 K s^{-1}; H_2O sol. is H_2O solubility at 200 MPa and 1523 K; d is thickness; Rt is rhyolite; B is basalt; Mag is magnetite. The $c_{H_2O_g}$ max is gravimetrically determined H_2O concentration in the melt if all weight loss of the sample during the experiment, and after piercing and drying was $H_2O \rightarrow$ maximum possible H_2O concentration in melt. The $c_{H_2O_g}$ min is gravimetrically determined H_2O concentration in the melt if all weight loss of the sample during welding, during the experiment, and after piercing and drying was $H_2O \rightarrow$ minimum possible H_2O concentration in melt. The $c_{H_2O_t}$ is total H_2O concentration in rhyolitic glass, determined by FTIR spectroscopy. Hydr. is hydration experiment (7 wt % H_2O added into the capsule for H_2O excess during hydration); Rt / B is Rt on top of B; B / Rt is B on top of Rt; the use of the hydrated samples is assigned by the superscript numbers. * Increased error due to the significantly lower thickness of the thin section of 0.072 mm.

However, during the welding of precious-metal capsules, it may happen that tiny droplets of molten metal form and stick as metal beads to the outside of the welded capsule. At some point, these beads may fall off and cause a weight loss of several milligrams. The associated precious-metal loss cannot be distinguished from any possible water loss during welding. This affects the gravimetric determination of the H_2O content dissolved in the melt. To account for this uncertainty, a maximum ($c_{H_2O_g}$-max) and minimum ($c_{H_2O_g}$-min) H_2O concentration in the melt was calculated under the respective assumption that the weight loss measured after welding is related to total capsule material or total water, respectively.

The lowest $c_{H_2O_g}$ was calculated for the sample Rt_4_h (max: 5.14 wt %; min: 3.92 wt %). FTIR spectroscopic measurements provide a $c_{H_2O_t}$ of 4.35 ± 0.16 wt % H_2O. FTIR measurements of samples Rt_1_h, Rt_3_h, and Rt_5_h result in $c_{H_2O_t}$ of 5.67 ± 0.54 wt %, 5.38 ± 0.19 wt %, and 5.11 ± 0.18 wt % H_2O, respectively. The calculated H_2O solubility of 5.7 wt % under hydration conditions was not reached in samples Rt_3_h, Rt_4_h, and Rt_5_h. This could be related to the longer hydration time of more than 96 h required for the sample cylinder length of 11 mm compared to 6.5 mm (Preuss et al., 2016; Allabar and Nowak, 2018). Nevertheless, FTIR spectroscopic measurements confirmed that a homogeneous H_2O distribution was ensured in the rhyolite glass cylinders (Rt_1/3/4/5_h).

FTIR spectroscopic measurements of basaltic samples were not possible because of the partially crystallized glasses. The samples are opaque to the near-infrared radiation. Even reducing the section thickness of B_3_h to ~ 50 µm does not allow the infrared radiation to penetrate the sample. However, the $c_{H_2O_g}$ calculations of B_2_h with 4.88 wt % (max) and 4.85 wt % (min), as well as sample B_3_h with 5.41 wt % (max) and 4.66 wt % (min), agree sufficiently well with the expected solubility of 4.8 wt % (Berndt et al., 2002). After hydration of sample B_4_h, the capsule had a noticeable weight loss of 9.06 mg, which is attributed to H_2O leaking out during the hydration process. Nevertheless, still some H_2O escaped after puncturing the capsule and during drying in the compartment drier. A calculated $c_{H_2O_g}$ (max–min) of 4.00 wt %–3.65 wt % resulted for this sample. However, the reduced H_2O concentration in the undersaturated basalt samples does not significantly affect the degassing mechanism of the bimodal experiments, as explained in the following discussion.

The investigation of the hydrated samples with XRD showed that all rhyolitic samples were crystal-free, while the basaltic samples contain magnetite and pyroxenes. This crystal analysis was confirmed by investigating the basaltic samples with the SEM. The BSE images also confirm that a significant volume of the basalt samples is partially crystallized. Idiomorphic magnetite crystals up to 2 µm in size are surrounded by dendritic pyroxene quench crystals (Fig. S1).

Optical inspection and SEM analysis confirmed that all hydrated samples were vesicle free. Furthermore, all hydrated rhyolitic and basaltic samples had a cylindrical shape and were therefore ideally suited for the subsequent bimodal decompression experiments.

3.2 Reference experiments

3.2.1 Decompression reference experiment

The reference decompression experiment MI_Rt_1 was intended to validate the new experimental procedure of contacting two hydrous glass cylinders without air entrapment in between. Images of the embedded sample halves and the thin section show heterogeneously nucleated fringe vesicles attached to the capsule wall with a vesicle-free drainage zone (Navon and Lyakhovsky, 1998; Iacono-Marziano et al., 2007). Homogeneously distributed vesicles formed in the entire center sample volume (Fig. 2a). The former interface (indicated by a small kink at the capsule wall) between the two hydrous rhyolite cylinders is no longer visible and enhanced vesicle formation at the former interface is not observed. Therefore, the developed experimental design can be used for further magma injection experiments. The sample contains a VND of 1.8×10^2 mm^{-3} with a mean diameter of ~ 75 µm, determined by TLM. The $c_{H_2O_t}$ was measured as a vertical profile from the sample top to the sample bottom and results in 4.22 ± 0.14 wt %.

3.2.2 Bimodal reference experiment

The bimodal reference experiment MI_5 shows the initial melt conditions after heating and thermal equilibration for 10 min at 1348 K and 210 MPa before decompression. Due to the fast quench rate of 44 K s^{-1}, glass tensions in the sample induced cracking and only a small piece of initially contacted bimodal composition volume was preserved (Fig. 2a). No vesicles formed during the experiment, neither in the rhyolitic nor in the basaltic part of the sample. The basalt is partially crystallized with 1–3 µm sized magnetites. Quench crystals attached to the magnetites as found in hydration samples quenched at 16 K s^{-1} (Fig. S1) are not observed. FTIR measurements of the upper rhyolitic glass result in a mean $c_{H_2O_t}$ of 5.25 ± 0.18 wt % and are therefore slightly lower than the initial $c_{H_2O_t}$ of Rt_1_h with 5.67 ± 0.54 wt %.

The zone between the rhyolitic and basaltic glass that developed during the experiment can be optically characterized by its color transition towards the endmember compositions. While the rhyolitic glass is colorless and transparent, the contact zone turns transparent brownish to nearly black and opaque towards the basaltic part (Figs. 2a, 5). The onset of crystal occurrence corresponds to the black coloration in the optical image. EMP analysis across the sample, parallel to the cylinder axis, shows the development of an intermediate melt composition at the former contact zone of rhyolitic and basaltic melt. The diffusing species are charged ions and complicated multicomponent interdiffusion processes of

oxygen and cations with different charges, as well as different concentrations, and mobilities are expected to maintain charge neutrality (e.g., Watson, 1982; Baker, 1992; Johnston and Wyllie, 1988; Zhang et al., 2010). For a simplified illustration of the interdiffusion processes, we refer to the concentration profiles of oxide components. Figure 3 shows concentrations of oxide components normalized to a range between 0 (lowest concentration) to 1 (highest concentration). This highlights the similarities and differences in the concentration–distance profiles for all measured oxides. Na_2O, K_2O, and SiO_2 concentrations decrease from the rhyolitic glass in the direction to the basaltic glass. Al_2O_3, TiO_2, FeO, MgO, and CaO concentrations decrease from the basaltic glass in the direction to the rhyolitic glass. Na_2O and K_2O show asymmetric concentration profiles and a significantly greater length compared to SiO_2, TiO_2, FeO, MgO, and CaO. The normalized Al_2O_3 concentration is characterized by a strong variation over the entire profile, caused by the small difference in the initial concentration of the starting compositions of 1.11 wt % (Table 1). MnO concentrations are close to the detection limit and are not shown in Fig. 3. For a subsequent assessment of all samples, the SiO_2 concentration profiles of all samples were evaluated to define the length of the mixed hybrid zone. For the reference sample MI_5, the SiO_2 concentration profile extends over 0.3 mm (Table 3, Fig. 3).

To examine a $c_{H_2O_t}$ concentration profile across the hybrid zone, the FTIR spectra were baseline-corrected according to Ohlhorst et al. (2001). Straight lines were fitted through the minima on both sides of the NIR combination bands related to H_2O_m and OH to evaluate the peak heights. As this baseline correction systematically underestimates the OH absorption (Ohlhorst et al., 2001), standard samples of rhyolitic composition (AOQ2, from Allabar et al., 2022) were baseline-corrected according to Behrens et al. (1996) and Ohlhorst et al. (2001) for comparison. The differences in $c_{H_2O_t}$, calculated with the $\varepsilon_{H_2O_m}$ and ε_{OH} of both corrections, are within the error in the $c_{H_2O_t}$ of each sample, except for sample Std_2_7 with the highest H_2O content of 6.9 wt % (Table S1).

Ohlhorst et al. (2001) developed a parabolic equation (Eq. 1) to predict the linear molar absorption coefficients (ε) as a function of the SiO_2 content of the glass, valid for compositions from rhyolite to basalt:

$$\varepsilon = a + b \times {c_{SiO_2}}^2. \quad (1)$$

ε values are given in liters per mole per centimeter ($L\,mol^{-1}\,cm^{-1}$), $a = -0.13$, $b = 0.000257$ (given parameters for the baseline correction used), and c_{SiO_2} is in weight percent (wt %), resulting in rhyolite absorption coefficients of $\varepsilon_{H_2O_m} = 1.57$ and $\varepsilon_{OH} = 1.32\,L\,mol^{-1}\,cm^{-1}$. For the initial basaltic composition, $\varepsilon_{H_2O_m} = 0.76$ and $\varepsilon_{OH} = 0.64\,L\,mol^{-1}\,cm^{-1}$ were calculated. The c_{SiO_2} concentration profile of MI_5 matches with the $c_{H_2O_t}$ profile, since the inflection point of the c_{SiO_2} profile coincides with the first measurement in the color transition from brownish to transparent glass (hereafter referred to as the "midpoint"). To calculate the $c_{H_2O_t}$ of the FTIR-measured profiles across the hybrid zone, each measurement point was assigned the corresponding SiO_2 concentration from the EMP measured profile. For the presented profile of MI_5 (Fig. 4), this corresponds to 73.0 wt % SiO_2 for the first measurement in the rhyolitic part to 60.8 wt % SiO_2 for the midpoint and 55.8 wt % SiO_2 for the last measurement in the basaltic part of the profile (Table S1). Using these concentrations, respectively, absorption coefficients of $\varepsilon_{H_2O_m} = 1.47/0.97/0.80$ and $\varepsilon_{OH} = 1.24/0.82/0.67\,L\,mol^{-1}\,cm^{-1}$ were calculated with Eq. (1). The same procedure was used for all other measurement points.

The glass density, necessary for the calculation of $c_{H_2O_t}$ with the Beer–Lambert law, at the corresponding measurement point was calculated according to the equations of Allabar et al. (2022, Eq. 2), Yamashita (1997, composition no. 43gm, Eq. 3), and Ohlhorst et al. (2001, Eq. 4) for rhyolite, dacite, and basalt, respectively. The equation for the density of dacite was chosen because the hybrid composition at the midpoint is quite similar to the dacite of the Unzen volcano given in Chen et al. (1993):

$$\rho_{Rl} = (2351 \pm 2) - (12.3 \pm 0.6) \cdot c_{H_2O_t}, \quad (2)$$

$$\rho_{D} = (2515 \pm 6) - (11.8 \pm 2.0) \cdot c_{H_2O_t}, \quad (3)$$

$$\rho_{B} = (2819 \pm 13.5) - (20.8 \pm 6.6) \cdot c_{H_2O_t}, \quad (4)$$

where ρ is in grams per liter ($g\,L^{-1}$) and $c_{H_2O_t}$ is in weight percent (wt %). The dependence of the glass density on the H_2O content in the glass required an iterative calculation. As the composition changes over the total profile, Eqs. (2)–(4) were only applied for three data points. Equation (3) was applied to the midpoint. Depending on the length of the hybrid zone determined by EMPA, the measurement points in the hybrid composition were iteratively calculated by interpolating the density between the dacite density of the midpoint and the rhyolite density or the basalt density. This whole procedure was also applied to the other MI samples to be able to determine the H_2O concentrations across the hybrid zone of the samples.

FTIR measurements with absorbance values greater than 1 were excluded from evaluation because less than 10 % of the light penetrates the samples in these measurements, which may result in a nonlinear behavior where the Beer–Lambert law is no longer valid (Mayerhöfer and Popp, 2019). This is especially relevant in the zone with increasing basaltic influence. Such measurements are still displayed in the $c_{H_2O_t}$ profile but marked as open circles (Fig. 4). FTIR measurement points to which no $c_{H_2O_t}$ data point was assigned, as in MI_7 and MI_6, did not yield analyzable NIR spectra due to crystals in the basalt glass.

The $c_{H_2O_t}$ profile in Fig. 4 across the hybrid zone of the undecompressed sample MI_5 shows an increase towards the basaltic composition. The profile starts with a mean $c_{H_2O_t}$ of

5.36 ± 0.20 wt % in the rhyolitic part, followed by a slight decrease in $c_{H_2O_t}$ towards the transition to the hybrid zone down to 5.08 ± 0.21 wt % in the middle of the hybrid data points at 0.38 mm. Further on, $c_{H_2O_t}$ significantly increases up to 6.15 ± 0.30 wt %. With this data point, an H_2O concentration is reached that exceeds the initial H_2O content ($c_{H_2O_i}$) of the rhyolite melt by 0.5 wt %. If the last data points with excessive absorbance (> 1) were included, $c_{H_2O_t}$ up to 6.71 ± 0.37 wt % would be reached, exceeding the initial concentration by 1 wt %. Besides the $c_{H_2O_t}$ profile, the hybrid zone is also characterized by the SiO_2 concentration profile, marked in grey, scaled on the right y axis. The hybrid zone extends over a length of 0.3 mm.

3.3 Bimodal decompression experiments

In samples MI_T_3 and MI_6, a slight indentation of the basalt into the overlying rhyolite can be seen in the central sample area. A gravitationally induced convective movement of the melts is preserved in sample MI_7. The basalt overlying the rhyolite sank into the rhyolite melt, squeezing the rhyolitic melt into the upper part of the capsule. This effect is visually enhanced by cutting the thin section slightly inclined from the cylinder axis (Fig. 2).

The decompressed MI samples (Fig. 2b, c, d) contain in the rhyolitic part heterogeneously nucleated fringe vesicles attached to the capsule walls with a vesicle-free drainage zone (Navon and Lyakhovsky, 1998; Iacono-Marziano et al., 2007) and a homogeneously vesiculated center volume. Vesicles close to the drainage zone are mostly deformed or elliptically shaped, whereas vesicles in the rhyolitic sample center are spheres. The basaltic parts of the samples MI_7 and MI_6 are not vesiculated. The sample MI_T_3 (Fig. 2b) contains vesicles distributed over the whole basaltic part. The vesicles near the capsule wall have small diameters of ~ 25 µm and increase in size towards the center of the sample up to ~ 250 µm, whereas the number of vesicles decreases towards the center. Opposite to the rhyolitic glass part, no vesicles nucleated heterogeneously at the capsule wall in the basaltic part of the sample.

The VND and the mean vesicle diameter of the sectioned vesicles in MI_T_3 were determined using the BSE image as described by Marxer et al. (2015) and Preuss et al. (2016). As the thin section was polished down to 53 µm thickness, each vesicle in the sample was cut and therefore not measurable under uncut conditions with TLM. The VND results in 1.9×10^2 mm^{-3} and ~ 74 µm diameter in the rhyolitic glass and 1.1×10^2 mm^{-3} and ~ 98 µm in the basaltic glass. VNDs and vesicle diameters of MI_7 and MI_6 were determined with TLM. The VND in the rhyolitic part of the samples MI_7 and MI_6 are 2.2×10^2 and 1.2×10^3 mm^{-3}, respectively. The mean diameter of uncut vesicles in MI_7 is ~ 69 µm and in MI_6 ~ 41 µm (Table 3).

FTIR spectroscopic analysis of the central rhyolitic parts results in $c_{H_2O_i}$ of 4.07 ± 0.18 wt % for MI_T_3, 4.53 ± 0.17 wt % for MI_7, and 4.65 ± 0.2 wt % for MI_6 (Tables 2 and S1). Measurements in the basaltic sample parts were not successful.

Minerals detected by X-ray diffraction in the partially crystallized basaltic glasses are magnetites, supported by EMPA. The crystals have sizes of 1–5 µm. Small dendritic quench crystals have grown around the magnetite crystals during quench (Fig. 6). EMP measurements of eight idiomorphic magnetite crystals in MI_T_3 (Table 1) result in a mean concentration of 80.13 wt % FeO* (*total Fe), 5.83 wt % MgO, 3.64 wt % TiO_2, 2.92 wt % Al_2O_3, 0.75 wt % SiO_2, and 0.52 wt % MnO. Very low concentrations of 0.3 wt % CaO, 0.08 wt % Na_2O, and 0.07 wt % K_2O were measured. The total sum of oxides is 94.25 wt %. Calculation of FeO and Fe_2O_3 from FeO* according to Carmichael (1967) results in an oxide sum of 100.3 wt % or 100.1 wt % without the alkali oxides. Based on the main oxide components of the composition, the crystals can be assigned to spinel and are hereafter referred to as magnetite. The quench crystals attached to the magnetite crystals are probably pyroxenes due to the dendritic texture and the depletion of SiO_2 in the residual glass composition. These quench crystals could not be measured with the EMP as they are too small for analysis due to the fast cooling rate of 44 K s^{-1} and are present in concentrations that are too low for XRD analysis.

Hybrid zone

A compositional hybrid zone developed during the experiments between the rhyolitic and basaltic melts (Figs. 2, 3). All decompressed MI samples show an increase in VND or vesicle size near the contact zone of the two compositions. In the upper rhyolitic part of the contact zone of MI_T_3, the still transparent glass is indicated by a series of large vesicles with a mean diameter of ~ 99 µm and a VND of 4.1×10^2 mm^{-3}, elongated along the contact boundary (Fig. 6). The situation is different for samples MI_7 and MI_6, where a ~ 0.2 mm wide vesicle-free zone is observed in MI_7 and a ~ 0.3 mm wide vesicle-free zone is visible in MI_6 at the former contact zone (Fig. 7). In MI_7 and MI_6 the mean vesicle diameter near the contact zone decreases down to ~ 61 and ~ 16 µm, respectively. The VND in MI_7 increases from 2.2×10^2 mm^{-3} in the rhyolite volume to 4.3×10^2 mm^{-3} in the hybrid zone. The VND in MI_6 increases from 1.2×10^3 mm^{-3} in the rhyolite volume to 7.0×10^3 mm^{-3} in the hybrid zone (Table 3). Strikingly, the zone with the enhanced VND occurs in all bimodal decompressed samples in the rhyolite-dominated region of the hybrid zone (Fig. 4).

A color change from nearly opaquely black to semitransparent brownish to transparent colorless shows the development of intermediate melt compositions at the former contact zone of rhyolite and basalt, exemplarily shown for sample MI_7 in Fig. 5. The width of the hybrid zone related to c_{SiO_2} from the initial rhyolitic to the initial basaltic composition is

Table 3. The $c_{H_2O_t}$ measured by FTIR spectroscopy from rhyolite to hybrid zone to basaltic composition. The $c_{H_2O_t}$ values based on measured absorptions (A) > 1 are listed in a separate column. Hyb. signifies hybrid.

Sample	Mean $c_{H_2O_t}$ Rt [wt %]	± [wt %]	Max $c_{H_2O_t}$ hybrid [wt %]	± [wt %]	Max $c_{H_2O_t}$ hyb. incl. $A > 1$ [wt %]	± [wt %]	Max $c_{H_2O_t}$ basalt incl. $A > 1$ [wt %]	± [wt %]
MI_Rt_1	4.22	0.14	–	–	–	–	–	–
MI_5	5.36	0.20	6.15	0.30	6.71	0.37	–	–
MI_T_3	4.02	0.20	5.00	0.30	7.7	0.39	8.48	0.43
MI_7	4.24	0.19	4.93	0.27	5.54	0.31	–	–
MI_6	4.80	0.23	5.55	0.31	6.19	0.35	–	–

Sample	Width of hyb. zone [mm]	VND Rt [mm^{-3}]	VND hyb. [mm^{-3}]	VND B [mm^{-3}]	Vesicle ∅ Rt [µm]	Vesicle ∅ hybrid [µm]	Vesicle ∅ basalt [µm]
MI_Rt_1	–	1.8×10^2	–	–	75	–	–
MI_5	0.30	–	–	–	–	–	–
MI_T_3	0.39	1.9×10^2	4.1×10^2	1.1×10^2	74	99	98
MI_7	0.31	2.2×10^2	4.3×10^2	–	69	61	–
MI_6	0.56	1.2×10^3	7.0×10^3	–	41	16	–

0.39 mm for MI_T_3, 0.31 mm for MI_7, and 0.56 mm for MI_6 (Fig. 3, Table 3).

The $c_{H_2O_t}$ profiles over the hybrid zone of MI_T_3, MI_7, and MI_6 show an increase in $c_{H_2O_t}$ in the transition from the rhyolitic- to the basaltic-dominated composition. Sample MI_T_3 has a mean $c_{H_2O_t}$ of 4.02 ± 0.20 wt % in the rhyolitic part. The $c_{H_2O_t}$ in the hybrid zone starts at 3.89 ± 0.21 wt % and increases up to 5.00 ± 0.30 wt %. The last NIR measurements in the direction of the basaltic composition result in absorptions > 1. An evaluation of the data points with absorbances > 1 provides $c_{H_2O_t}$ up to 7.70 ± 0.39 wt % in the hybrid zone and even a $c_{H_2O_t}$ of 8.48 ± 0.43 wt % in the basaltic-related composition (Table 3). Therefore, the last five measurements are not reliable and were discarded from further discussion. The appearance of the enhanced VND starts at the ∼0.37 mm position in the profile, which corresponds to the onset of the decrease in SiO_2 concentration (Fig. 4).

In sample MI_7, the data points in the rhyolitic composition yield an average $c_{H_2O_t}$ of 4.24 ± 0.19 wt %, while the concentration decreases towards the hybrid zone (Fig. 4). The minimum $c_{H_2O_t}$ of the hybrid zone is 4.03 ± 0.18 wt % and increases up to 4.93 ± 0.27 wt % towards the basaltic part. One data point representing 5.54 ± 0.31 wt % was discarded from further discussion due to an absorption > 1. Two further spectra, one in the hybrid and one in the basaltic composition, were not evaluable because of the magnetite content in the glass. The enhanced vesiculated zone in the sample starts at the 0.64 mm position of the profile, which corresponds to the first third of the SiO_2 concentration profile.

The $c_{H_2O_t}$ profile of sample MI_6 starts with a mean $c_{H_2O_t}$ of 4.80 ± 0.23 wt % in the rhyolitic part and decreases at the beginning of the hybrid zone to 4.63 ± 0.22 wt %. An increase of up to 5.55 ± 0.31 wt % is observed over the hybrid zone towards the basaltic composition. The last measurement (6.19 ± 0.35 wt %) in the hybrid zone was excluded because of the NIR absorption measurements > 1. The zone with the enhanced VND in MI_6 starts at the 0.64 mm position in the profile, which corresponds to the onset of the decrease in c_{SiO_2} (Fig. 4).

4 Discussion

4.1 Initial sample material

The pre-hydrated sample material was examined to evaluate the starting conditions just before decompression. For the evaluation of decompression experiments, the homogeneity and the initial glass porosity are important properties for the degassing and nucleation processes, as shown in Preuss et al. (2016). Using glass cylinders with porosities below the critical value of 6 % (Preuss et al., 2016) excludes the effect of growing pre-existing hydration bubbles by the uptake of H_2O during decompression (Iacono-Marziano et al., 2007). Macroscopic and microscopic examinations of thin sections of hydrated rhyolitic and basaltic glasses yield vesicle-free glasses. This ensures melts without pre-existing vesicles prior to decompression.

While the rhyolitic glasses are crystal free, and the hydrated basaltic glasses quenched at $16\,K\,s^{-1}$ contain magnetite and pyroxene crystals, the basaltic MI samples show only magnetite crystals after quenching at $44\,K\,s^{-1}$. A comparison of the crystal phases in the hydration samples and the MI experiments provides a dissolution of pyroxene during the reheating and the 10 min thermal equilibration of the

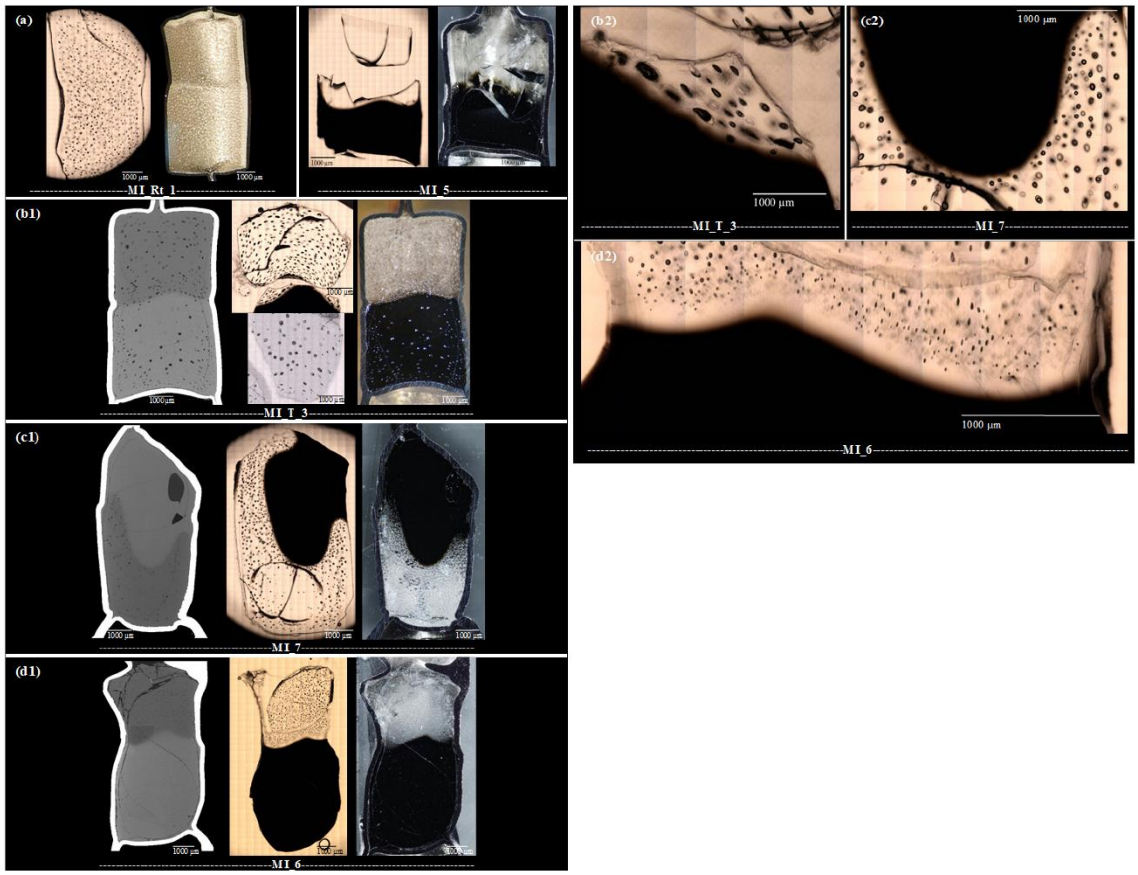

Figure 2. Microscope, BSE, and reflected light images of MI samples, cut and polished along the cylinder axis. BSE and reflected light images were captured from the embedded sample halves, while the microscope images show the IR slides in transmission or reflection mode. All basaltic glasses contain magnetite crystals. The hybrid melt zone of the MI experiments developed between the rhyolitic melt and the basaltic melt. **(a)** The reference experiment MI_Rt_1 with two hydrated rhyolitic glass cylinders was thermally equilibrated at 210 MPa and 1348 K for 10 min and then decompressed with 0.17 MPa s^{-1} to 100 MPa. Vesicles are homogeneously distributed with mean diameters of ~ 75 µm. No enhanced vesicle formation occurred at the previous contact plane. The undecompressed reference sample MI_5 was thermally equilibrated at 210 MPa and 1348 K for 10 min and subsequently quenched to room temperature. A narrow hybrid melt zone formed between the endmember compositions (Table 3). **(b)** The sample MI_T_3 was thermally equilibrated at 210 MPa and 1348 K for 10 min, followed by decompression at 0.17 MPa s^{-1} to 100 MPa. The upper rhyolitic glass is homogeneously vesiculated (mean vesicle diameter of ~ 74 µm). The basaltic glass volume contains vesicles with different sizes ranging from 56 to 224 µm, with an average of 98 µm. The hybrid zone is decorated by a series of ~ 99 µm sized vesicles, elongated along the contact boundary. **(c)** The sample MI_7 with basalt on top of rhyolite was thermally equilibrated at 210 MPa and 1348 K for 10 min and then decompressed with 0.17 MPa s^{-1} to 100 MPa. The basalt is nearly vesicle free, while the rhyolite is highly vesiculated (mean vesicle diameter of ~ 69 µm). Towards the contact zone of rhyolite and basalt, the VND increases, while the vesicle diameter decreases to ~ 61 µm. **(d)** The sample MI_6 was thermally equilibrated at 210 MPa and 1403 K for 10 min and then decompressed with 1.7 MPa s^{-1} to 102 MPa. The rhyolite glass is homogeneously vesiculated with vesicle diameters of ~ 41 µm. The basalt is nearly vesicle free. The images show an increased VND in the hybrid zone, while the vesicle diameter decreases to ~ 16 µm.

melt. This suggests that pyroxene crystallized during quench at the normal quenching rate of ~ 16 K s^{-1} and was therefore not present in the melt before and during decompression. This observation is confirmed by calculations of the phase relations under experimental conditions using the software "Easymelts v.1.2.0". The phase relations of basalt at 210 and 100 MPa, 1550–1050 K, and total H_2O content in the system (H_2O_{sys}) from 0 wt % to 6 wt % are presented in Fig. 8. Calculated but not shown is the phase diagram of basalt at 200 MPa, relevant for the preparatory hydration ex-

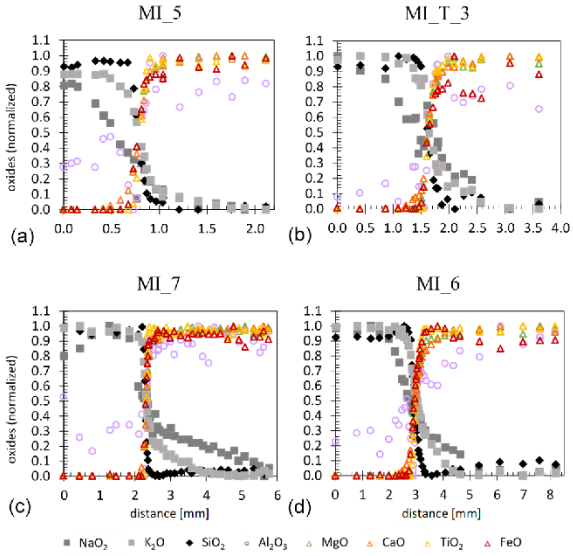

Figure 3. EMPA-measured concentration–distance profiles of oxide components between initial rhyolitic composition (left) and initial basaltic composition (right) of MI_5, MI_T_3, MI_7, and MI_6. The concentrations of the individual oxides were normalized to a range from 0 to 1.

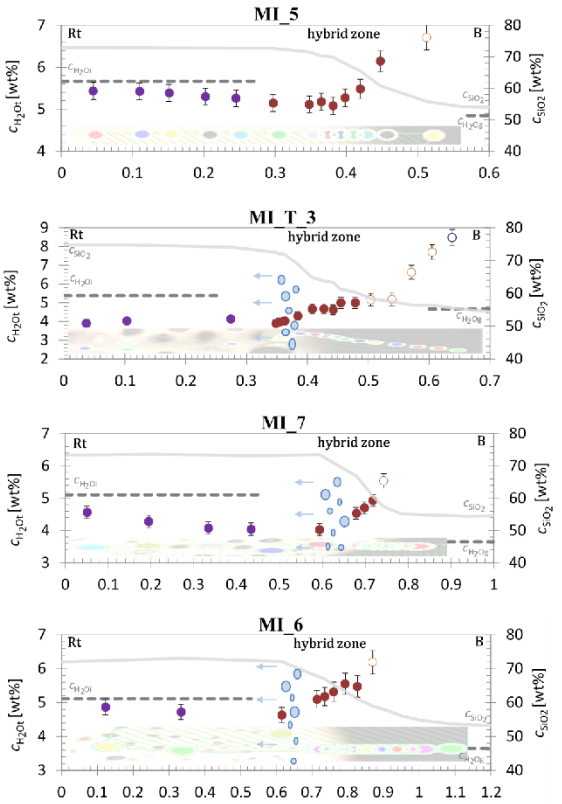

Figure 4. $C_{H_2O_t}$–distance profile from rhyolite to basalt through the hybrid melt zone of bimodal samples MI_5 (undecompressed), MI_T_3, MI_7, and MI_6. The $c_{H_2O_t}$ in rhyolite is colored in violet, measurements in the hybrid melt zone are in red, and $c_{H_2O_t}$ in basalt is shown in blue. Open circles illustrate $c_{H_2O_t}$ based on NIR measurements with absorbances > 1 that were excluded from evaluation. Data points of the concentration–distance profile are visualized in the shaded transmission microscope images of the samples at the bottom of each plot. The initial H_2O concentrations of the hydrated rhyolite ($c_{H_2O_i}$; determined by NIR) and the hydrated basalt ($c_{H_2O_g}$; determined gravimetrically) are displayed by the dashed lines (see Table 2). The hybrid zone is also characterized by the SiO_2 concentration profile (c_{SiO_2}), marked by grey solid lines, scaled on the right y axis. Illustrated by blue ellipsoids is the beginning of the enhanced vesiculated zone of the rhyolite-dominated part of the sample.

periments, since the equilibrium curves of the crystal phases overlap except for a few Kelvin. Under hydration conditions of 200 MPa and 1523 K, spinel (spl) is the only crystal phase that coexists with melt, corresponding to the idiomorphic magnetites observed in all hydrated basaltic samples (Fig. S1). At H_2O concentrations > 5.4 wt %, H_2O would be present in the system as a fluid phase, along with hydrous melt and spinel. This calculated value is above the H_2O solubility of 4.8 wt % given by Berndt et al. (2002), which can be explained by a slightly different melt composition. Thus, it can be concluded that the dendritic pyroxenes in the hydration samples crystallized during the cooling process. This is unavoidable due to the melt composition and the cooling rate of 16 K s^{-1} since an intact sample cylinder is essential for the subsequent contact with a rhyolitic glass cylinder for the MI experiments.

From the phase diagram in Fig. 8, H_2O_{sys} can be confined under decompression starting conditions of 1348 K and 210 MPa to a range of 2.65 wt %–5.2 wt %, since neither pyroxene nor H_2O fluid coexisted with hydrous basaltic melt and spinel. This accounts for the reference sample MI_5. For sample MI_T_3 it can be inferred from Fig. 8 that at least 3.2 wt % H_2O was dissolved in the basaltic melt system (B_3_h), since a significant number of H_2O vesicles formed during decompression to 100 MPa. This is consistent with the equilibrium degassing of basaltic melt experimentally demonstrated by Le Gall and Pichavant (2016). As in sample MI_7, only a few vesicles formed near the drainage zone, and in MI_6 only one vesicle is present in the decompressed glass, so the range of possible H_2O content in the basalt cylinder (B_4_h) can be assigned less clearly. At least 2.25 wt % H_2O was dissolved in the melts, as neither pyroxene nor feldspar crystallized. Possibly the H_2O_{sys} was at a maximum of 3.2 wt % so that a free fluid phase could not develop, as the equilibrium H_2O content of

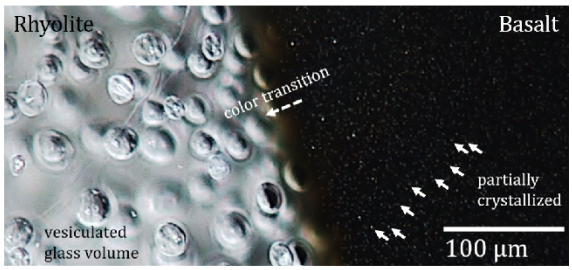

Figure 5. Microscope image of sample MI_7. Alignment of the image is identical to the capsule during the experiment. The basaltic glass is partially crystallized by magnetite (arrows). The hybrid zone is characterized by a color transition from opaquely black (basalt) to semitransparent brownish to transparent colorless (rhyolite).

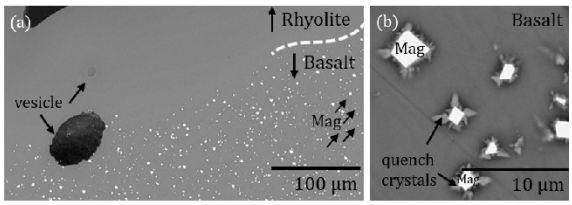

Figure 6. (a) Hybrid zone of MI_T_3 with a sharp boundary of the magnetite crystals (Mag) in the basaltic-dominated volume towards the rhyolitic-dominated glass. **(b)** BSE image of dendritic growth of quench crystals on idiomorphic magnetite (Mag).

3.3 wt % at 100 MPa final pressure, corresponding to Berndt et al. (2002), is higher than the actual dissolved H_2O content of the basaltic melt. Hence, the basaltic melts of MI_6 and MI_7 were not supersaturated with H_2O during decompression, and thus no vesicles formed in the basaltic melt volume.

4.2 MI decompression experiments

4.2.1 Vesicle formation

The images of the decompressed samples (Fig. 2) show similar textures of the vesicles. The sample volumes can be divided into four different zones: (1) the peripheral zone containing vesicles at the contact of the capsule wall with rhyolite, referred to as fringe vesicles (Navon and Lyakhovsky, 1998; Iacono-Marziano et al., 2007); (2) partially crystallized basaltic glass with vesicles in the central volume; (3) rhyolite glass with vesicles in the central volume (Navon and Lyakhovsky, 1998); and (4) the hybrid zone with an increased VND compared to the rhyolite volume (Table 3), with a smaller or larger vesicle diameter, depending on the $c_{H_2O_i}$ of the pre-hydrated rhyolitic and basaltic glasses (Table 2).

Based on classical nucleation theory (e.g., Navon et al., 1998), vesicles nucleate from H_2O-supersaturated melt by

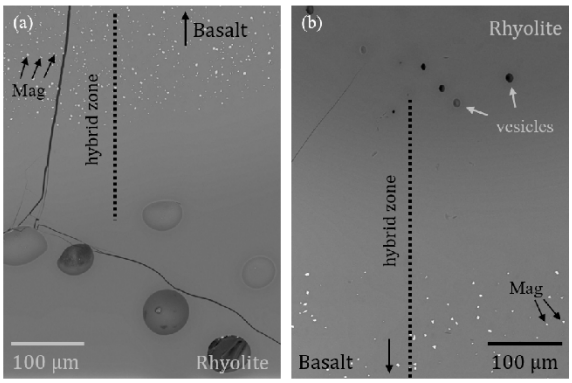

Figure 7. BSE images of the hybrid zones of MI_7 **(a)** and MI_6 **(b)**. A ∼ 200 µm wide vesicle-free zone developed in MI_7 and a ∼ 300 µm wide vesicle-free zone developed in MI_6 as part of the hybrid zone (marked by the dotted line). In the rhyolitic-dominated part, vesicles of ∼ 61 µm in MI_7 and vesicles of ∼ 16 µm in MI_6 formed.

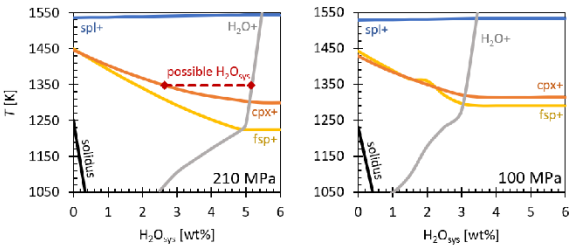

Figure 8. Phase relations of basalt at 210 and 100 MPa as a function of T and H_2O_{xys}, calculated using the software Easymelts v.1.2.0. spl+, cpx+, fsp+, and H_2O+ are the spinel, clinopyroxene, feldspar, and H_2O in curves. The oxygen fugacity was set to $\log f_{O_2} = \mathrm{QFM} + 3$, corresponding to the intrinsic conditions in the IHPV (Berndt et al., 2002). Further phases occurring at lower temperatures were excluded.

exceeding the critical size of molecular clusters and grow into vesicles. Diffusion of additional H_2O molecules into the existing vesicles reduces the energy of the entire system, which further drives the diffusion process during decompression (Hurwitz and Navon, 1994). Diffusion-driven H_2O transfer from the H_2O-supersaturated melt volumes through the depleted melt–vesicle interface into the vesicles leads to an increase in vesicle size. The four vesiculated zones may have been the result of different nucleation mechanisms.

Numerous fringe vesicles in the rhyolitic melt form heterogeneously at the interface between the capsule and the melt due to a low wettability of hydrous rhyolitic melt. This reduces the required energy to form vesicles at a low degree of supersaturation during decompression (e.g., Mangan and Sisson, 2000; Iacono-Marziano et al., 2007). Due to the diffusion of H_2O from the melt into the fringe vesicles, homo-

geneously nucleated vesicles can no longer form in the H_2O-depleted melt zone, which is referred to as the drainage zone (Mangan and Sisson, 2000). The observation that only a few vesicles nucleated at the capsule wall in the basaltic part of sample MI_T_3 may be due to good wettability of Au80Pd20 capsule material with hydrous basaltic melt. In this case, energy required to nucleate vesicles is not reduced (e.g., Gualda and Ghiorso, 2007; Edmonds et al., 2015).

Images of sample MI_T_3 show magnetite crystals in direct contact with vesicles in the basaltic part of the sample (Fig. 6). During hydration, magnetite crystals formed in the basaltic melt. This suggests that, during reheating followed by decompression within the stability field of magnetite, these crystals served as nucleation sites for the formation of the H_2O vesicles in the melt. The reduction in energy required for heterogeneous vesicle nucleation on magnetites was observed in hydrous rhyolitic melt (Hurwitz and Navon, 1994; Mangan and Sisson, 2000, 2005; Gardner and Denis, 2004; Gardner, 2007; Gardner and Ketcham, 2011), as well as in andesitic and basaltic melts (Edmonds et al., 2015).

Vesicle nucleation in the basaltic part was not observed in the samples MI_7 and MI_6 due to the initially H_2O-undersaturated basaltic melts (Table 2). Despite the magnetite nucleation seeds, the supersaturation pressure was not yet reached for the lower H_2O contents during the decompression to final pressure of 100 MPa.

As the rhyolite melts in the experiments of this study were free of pre-existing crystals or inhomogeneities, homogeneous vesicle nucleation has occurred in the central volume of the rhyolitic melts. According to nucleation theory, the VND increases strongly with the decompression rate $\mathrm{d}P/\mathrm{d}t$ (Toramaru, 2006). This is confirmed by the MI samples where the rhyolitic part of MI_6 at the fastest decompression rate of $1.7\,\mathrm{MPa\,s^{-1}}$ has the highest VND of $1.2 \times 10^3\,\mathrm{cm^{-3}}$ compared to MI_T_3 and MI_7 decompressed with $0.17\,\mathrm{MPa\,s^{-1}}$ and having similar VNDs of 1.9×10^2 and $2.2 \times 10^2\,\mathrm{cm^{-3}}$, respectively (Table 3).

All decompressed MI samples differ in their vesicle textures and VNDs in the hybrid zone from the initial rhyolitic central melt volume. It can be excluded that vesicles, nucleated heterogeneously at magnetite crystals, have ascended from the basalt into the hybrid zone. This is proven by experiment MI_7, where the basalt was placed on top of the rhyolite. Due to the difference in density, the basalt has sunk into the rhyolite, but the zone with the enhanced VND is clearly contained in the lower rhyolite-dominated region of the hybrid zone and is therefore positioned below the partially crystallized basalt.

The position and the size of vesicles in the hybrid zone may depend on the initial $c_{H_2O_i}$ conditions. In the hybrid zone of MI_T_3, the vesicles of $\sim 99\,\mu\mathrm{m}$ are bigger than in the rhyolitic melt center (Table 3) but positioned in the vicinity of the previous contact plane of the two cylinders. This can be attributed to H_2O-saturated rhyolitic and basaltic melt conditions before decompression. This was different for MI_6 and MI_7. Since the basalt of both samples was H_2O-undersaturated, H_2O diffused from the rhyolitic melt via the developing hybrid melt into the basaltic region of the sample. This H_2O depletion resulted in an extended vesicle-free zone in the hybrid region of samples MI_6 and MI_7, as shown in Fig. 7. Compared to MI_T_3, however, a higher ΔP (reduced pressure during decompression) was required to form vesicles, related to the lower $c_{H_2O_i}$ in the melt. This resulted in a smaller vesicle size observed in the hybrid zone compared to the rhyolitic melt volumes. The later onset of the vesicle nucleation process during decompression did not allow the vesicles to grow as much as in MI_T_3, which explains the reduced vesicle size in MI_7 of $\sim 61\,\mu\mathrm{m}$. The vesicle size of MI_6 with a decompression rate of $1.7\,\mathrm{MPa\,s^{-1}}$ may not be directly comparable to that of MI_T_3 and MI_7 with decompression rates of $0.17\,\mathrm{MPa\,s^{-1}}$ due to the higher VND related to the faster decompression rate in the case of nucleation (Toramaru, 2006).

4.2.2 Concentration profiles of melt components

The melt between rhyolite and basalt developed as an intermediate composition through multicomponent interdiffusion processes of ions, depending on their concentrations, charges, specific diffusion coefficients, and the requirement to maintain charge neutrality over the sample. The alkalis Na^+ and K^+ diffuse orders of magnitudes faster than other network-modifying cations like Ca^{2+}, Mg^{2+}, Fe^{2+}, Fe^{3+}, and Ti^{4+} and network formers with the lowest mobility like Si^{4+} and Al^{3+} coupled to O^{2-} diffusion (e.g., Watson, 1982; Baker, 1992; Johnston and Wyllie, 1988; Zhang et al., 2010). In particular, the cations Na^+ and K^+ diffused much faster than Si^{4+} in the direction of the basalt, resulting in a significant depletion of Na_2O and K_2O components in the rhyolite-dominated hybrid area. Counter flux Ca^{2+}, Mg^{2+}, Ti^{4+}, Fe^{2+}, Fe^{3+}, and Al^{3+} diffused towards the rhyolitic composition. The asymmetric concentration profile of Na_2O with a greater length on the rhyolitic profile side is suggested to be caused by different Na^+ diffusion coefficients in basalt and rhyolite melt, as Na^+ has a higher diffusivity in rhyolitic composition (Zhang et al., 2010). This effect is enhanced by the higher H_2O content in the rhyolite, since the mobility increases with increasing H_2O content in the melt (Watson, 1981). Except for the alkalis, the other oxide components show concentration profiles with a symmetric pattern in the hybrid zone (Fig. 3).

The SiO_2 concentration profiles were evaluated for their length to compare the hybrid zones of the different samples. The differences in the length of the hybrid zones are striking when comparing samples MI_T_3 and MI_7 with sample MI_6. The higher temperature of $\sim 50\,\mathrm{K}$ during thermal equilibration and decompression of MI_6 caused an increase in diffusivities of components (Zhang et al., 2010). Based on experiments on the self-diffusion of Si^{4+} in dry dacitic melts, Tinker and Lesher (2001)

show that the diffusion coefficient of Si doubles at 1 GPa between 1628 and 1683 K, from $1.45 \times 10^{-14} \pm 0.45$ to $3.75 \pm 1.13 \times 10^{-14}$ m^2 s^{-1}. This corresponds to the T difference of 50 K between MI_T_3 and MI_7 and that of MI_6. The linear trend of $\ln D$ with the reciprocal of T provides a first estimate of the differences in the Si^{4+} diffusion coefficients for the experiments shown here, via extrapolation of the data of Tinker and Lesher (2001) with the equation of Zhang et al. (2010, Eq. 37 therein). Despite the longer diffusion time of MI_T_3 and MI_7 (1247 s) compared to MI_6 (665 s) related to the slower decompression rate, the higher T of MI_6 of 1403 K results in a slightly higher diffusion coefficient of $2.5(+0.9/-0.6) \times 10^{-17}$ m^2 s^{-1} compared to $5.5(+1.9/-1.4) \times 10^{-18}$ in MI_T_3 and MI_7 at 1348 K. These calculations demonstrate that the 50 K temperature difference did indeed result in a longer diffusion distance. However, this corresponds only to the assumption of dry melts. Due to the influence of H_2O on the Si^{4+} diffusion coefficient (up to a factor of 10; Baker and Bossanyi, 1994) and the multidimensional behavior of the interacting melt components, further decomposition of the temperature dependence of the diffusion of Si^{4+} cannot be presented within the scope of this project.

4.2.3 The $c_{H_2O_t}$ profiles

The H_2O concentrations measured between the vesicles of the zone with high VNDs are generally slightly higher than the calculated equilibrium solubility at final pressure. Due to increasing H_2O solubility with decreasing T at P<300 MPa (Holtz et al., 1995), part of the H_2O fluid diffused from vesicles back into the melt during quench, causing vesicle shrinkage (McIntosh et al., 2014; Allabar et al., 2020). As a result, resorption halos formed with increased H_2O concentrations in the melt surrounding the vesicles, recorded in the glasses (McIntosh et al., 2014; Allabar et al., 2020). Vesicle shrinkage is reinforced by the decrease in the molar volume of H_2O fluid during the isobaric quench (Marxer et al., 2015; Allabar et al., 2020). The size of the halos around the vesicles depends on the cooling rate and is therefore comparable in all bimodal decompression samples. A high VND favors fast H_2O resorption during cooling due to the high number of H_2O fluid sources per melt volume. Due to an increased VND in the hybrid melt zone within a decompressed sample, it can be assumed that H_2O resorption was most efficient in the hybrid melt zones.

Resorption of H_2O from vesicles back to the melt might also be an explanation for the high $c_{H_2O_t}$ in the hybrid area with dacitic composition. It could be possible that vesicles also nucleated in the basaltic-dominated hybrid zone during decompression. Assuming similar temperature dependence of H_2O solubility in dacite, already formed vesicles in the basaltic-dominated hybrid region might have dissolved again during cooling due to resorption of H_2O from vesicles into the melt. Therefore, hybrid melt that resorbed H_2O indicates a much higher $c_{H_2O_t}$ in the glass than in the rhyolite-dominated vesiculated hybrid regions (Fig. 4). Based on the EMPA data, the hybrid melt evolved to a dacitic composition, comparable to that of the Unzen dacite (Chen et al., 1993). Sato et al. (1999) showed experimentally that 5.7 wt % H_2O is soluble at 98 MPa and 1303 K, which is quite similar to our final experimental conditions of 100 MPa and 1348 K. Therefore, at P_f the solubility of H_2O in dacitic melt is much higher than in rhyolitic or basaltic melt, with 3.8 wt % and 3.3 wt %, respectively (Allabar et al., 2022; Berndt et al., 2002). This may explain the increase of $\sim$ 1 wt % H_2O in each hybrid $c_{H_2O_t}$ profile.

However, the evaluation of $c_{H_2O_t}$ is prone to errors. A crucial point is the use of Eq. (1) of Ohlhorst et al. (2001) for the determination of the absorption coefficients. The composition and the structure of the glasses are decisive factors for the application of the calibration. Liu et al. (2004) found that Eq. (1) given by Ohlhorst et al. (2001) is only applicable to the rhyolitic, dacitic, andesitic, and basaltic compositions that were also used for calibration due to the Fe^{2+} / Fe^{3+} ratio on the calibration. In our case, the bulk compositions of the individual measurement points differ from those used by Ohlhorst et al. (2001). The bimodal compositions are in the compositional range between the rhyolite and dacite of Ohlhorst et al. (2001). Nevertheless, due to the continuous change in composition, the method of Ohlhorst (2001) is appropriate for calculating approximations of the actual H_2O content. Gaussian background correction was also tested to evaluate the spectra, as described in Ohlhorst et al. (2001), Yamashita et al. (1997), and in Liu et al. (2004). However, the required punctual overlap of the spectrum with the Gaussian curve between $\sim$4500 and $\sim$5200 cm^{-1} is not possible for all NIR spectra collected along the hybrid zone. Due to the changing bulk composition, the slope of the spectra changes (Supplement Fig. S2). For the rhyolitic composition, it is not possible to tangent the minimum between 4500 and 5200 cm^{-1}. Similarly, in the dacite zone, the minimum between 4500 and 5200 cm^{-1} cannot be reached. Only for spectra with significant basaltic influence is it possible to tangent to the minimum and thus to perform the Gaussian background correction as proposed by Ohlhorst et al. (2001) and Yamashita et al. (1997). Since the same background correction must be applied for the use of absorption coefficients like for the determination of absorption coefficients, they cannot be used if the Gaussian correction cannot be applied on the spectra. Thus, the background correction according to Ohlhorst et al. (2001) with the straight lines under the bands of 4500 and 5200 cm^{-1} is useful to determine the absorptions of OH and H_2O_m, even if the Fe^{2+} / Fe^{3+} ratio of the bimodal decompressed samples does not exactly match the calibration.

Another problem is that the error in the absorption coefficients calculated according to Ohlhorst et al. (2001) increases with $c_{H_2O_t}$ (Table S1). The slight decrease in $c_{H_2O_t}$ between the rhyolite and the hybrid region is probably caused by the

density interpolation between the two compositions, as the density changes more than the SiO_2-dependent absorption coefficients along the rhyolite-dominated region. However, since there is no c_{SiO_2}-dependent density formula for hydrous rhyolitic to basaltic glasses, the interpolation of density between two known compositions is the simplest way to evaluate $c_{H_2O_t}$ trends.

For a first check of the validity of the $c_{H_2O_t}$ profiles calculated by the NIR absorption spectra, an uncalibrated "by-difference" method was performed on the EMPA bulk concentration profiles (Devine et al., 1995). The difference in the sum of the oxides to 100 wt % was considered H_2O content. Although this is a semiquantitative method for determining the H_2O content in the glasses, the data show a systematic increase in $c_{H_2O_t}$ in the hybrid zone towards the basaltic compositions (Table S1). Data of the mean, minimum, and maximum $c_{H_2O_t}$ of each sample in rhyolite, hybrid composition, and basalt data correlate remarkably well with the H_2O contents determined from the absorption spectra. The maximum $c_{H_2O_t}$ in dacitic composition, measured by FTIR spectroscopy and EMPA, differs by 3 % (MI_5), 34 % (MI_T_3), and 6 % each for MI_7 and MI_6.

Despite the errors in determining H_2O contents with both methods, the increase in the H_2O contents across the hybrid zone towards basalt may be possible. However, H_2O contents up to ~ 6 wt % in the zone with dacitic composition are surprising and need further investigation. An improvement for the determination of H_2O contents with NIR spectroscopy would be the synthesis of hydrous glass standards with intermediate compositions in several mixing steps between rhyolite and basalt that match bulk compositions of the hybrid zone. However, this procedure is very time-consuming and considerably beyond the scope of this paper. The H_2O contents in the hybrid range shown here can therefore be regarded as a first approximation of the actual values.

4.2.4 Alkali depletion as the crucial factor for enhanced vesicle nucleation in the hybrid zone

The enhanced VND occurs in all decompressed bimodal samples in the rhyolite-dominated region of the hybrid zones, as presented in Figs. 2 and 4. As a new approach to vesicle nucleation investigated for the first time, alkali diffusion and the accompanying alkali depletion in the rhyolite-dominated region of the evolving hybrid zone between rhyolite and injected basalt are now discussed. We suggest that the enhanced vesiculated zone forms due to rapid diffusive loss of alkalis, from the mildly peralkaline rhyolitic part into the basaltic part of the sample (Fig. 3). The decreased Na_2O concentration significantly reduces the H_2O solubility of the rhyolite and promotes H_2O supersaturation in the alkali-depleted rhyolitic melt near the contact zone during decompression. Dingwell et al. (1997) showed that H_2O solubility depends on alkali excess ($x_{ex} = (Na_2O + K_2O - Al_2O_3) / 100$), which is the difference between mole fractions of alkalis and those of alumina. The effect of the peralkalinity on the H_2O solubility in silicate melts was recently confirmed and refined by Allabar et al. (2022). They found a linear increase in the H_2O solubility with increasing Na_2O excess or, in general, for alkali excess. Based on the provided calculation tool by Allabar et al. (2022), the alkali excess was calculated for the melt composition of the hybrid zone in the bimodal samples with enhanced VND. The glass composition of each sample in the region of enhanced vesicle formation is presented in Table 1. While the initial x_{ex} content in mildly peralkaline rhyolite was 0.03, x_{ex} decreased during the decompression experiments by more than 90 % close to the H_2O solubility minimum at $x_{ex} = 0$. This reduced the H_2O solubility of the melt by ~ 0.4 wt % so that a lower ΔP was required to induce vesicle formation in the contact region of the developing hybrid melt compared to the pristine rhyolite. Further decompression allowed these vesicles to grow, whereas in the pristine rhyolitic melt the vesicles formed and grew at a higher ΔP (Fig. 9), resulting in VNDs about half the size of those in the hybrid melt zones (Table 3). From this, it can be concluded that besides P and T, also the alkali concentration is a decisive factor for the H_2O solubility and thus for the vesicle nucleation in silicate melts.

5 Implications and examples for natural bimodal volcanism

The injection of a mafic melt into a hydrous rhyolitic magma chamber cannot be directly observed in nature at the time of its occurrence. However, experiments can give insight into such processes. This experimental study is based on the basic melt compositions of the Askja volcano in Iceland (Sparks et al., 1977), considering the composition of basalt enclaves and a slightly simplified rhyolite composition. To relate these results to other natural alkaline volcanic systems, further natural bimodal compositions were analyzed for their alkali content using the method of Allabar et al. (2022) to calculate x_{ex}, as well as the classical molar alkali oxides ($Na_2O + K_2O$) to alumina oxide (Al_2O_3) ratio. Nine further natural bimodal systems of rhyolitic and basaltic to andesitic compositions were analyzed – De Rosa et al. (2002) (Salina Island: rhyolite and andesite); Smithies et al. (2015) (Mount Palgrave: rhyolite (187 077, 195 670) and basalt (194 662, 195 640)); Sparks et al. (1977) (Askja: rhyolite and basalt); Saito et al. (2002) (Satsuma-Iwojima: rhyolite (S-1–S-4) and basalt to basalt–andesite (SM-1b, SM-2, SM-3)); Leat et al. (1986) (Parys Mountain: rhyolite (P5) and basalt (P2)); Lacasse et al. (2007) (Katla Caldera: rhyolite (KAT02-18) and basalt (KAT02-17)); Pritchard et al. (2013) (Yellowstone: rhyolite (GR-1-R) and basalt (GR-1-B)); Jahn et al. (2009) (eastern Central Asian Orogenic Belt: basalt and rhyolite); and Ngounouno et al. (2000) (Kapski plateau: rhyolite and basalt) (Table S1) – all resulting in higher x_{ex} and alkali / alumina ratios of the rhyolitic composition compared to the more mafic

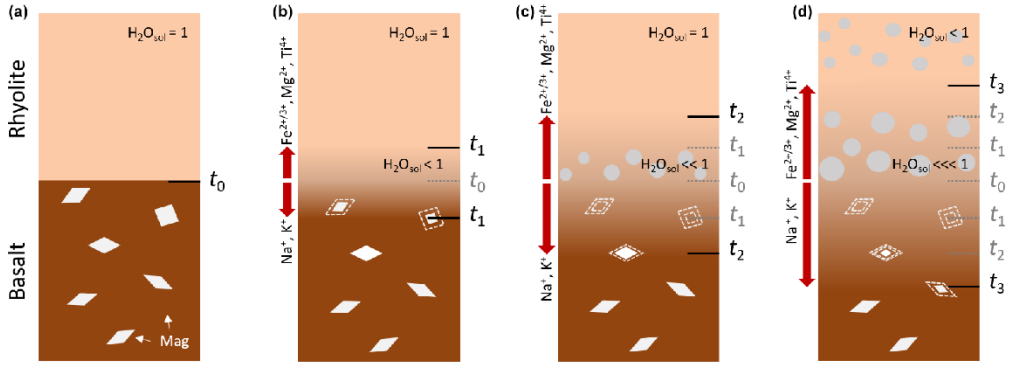

Figure 9. Schematic illustration of the development at the contact surface of the melts during magma injection. **(a)** (t_0): intrusion of a partially crystallized basaltic melt into a peralkaline rhyolitic magma chamber. The rhyolitic melt is saturated in H_2O. **(b)** (t_1): interdiffusion processes start. A hybrid melt forms at the contact area. The rhyolitic melt becomes rapidly depleted in alkalis (Na^+ and K^+ diffuse into basalt), while cations such as Mg^{2+}, Ca^{2+}, Fe^{2+}, Fe^{3+}, and Ti^{4+} diffuse slowly from the basalt into the rhyolite melt, leading to an incipient dissolution of magnetite crystals (Mag) in the basalt. H_2O solubility decreases in the alkali-depleted zone. **(c)** (t_2): during magma-ascent-induced decompression vesicles form in the rhyolite-dominated region of the hybrid melt because the solubility of H_2O is significantly reduced due to alkali depletion. The dissolution of magnetite in the basaltic-dominated melt is progressing. **(d)** (t_3): vesicles in the hybrid zone grow and accelerate buoyancy-driven magma ascent and mingling and mixing processes that induce further vesicle nucleation.

compositions (x_{ex} ratio Rt / B: 0–0.8; alkali / alumina ratio Rt / B: 1.3–3.6). Although, according to the model of Allabar et al. (2022), the peralkalinity of the melts is not ensured, as x_{ex} <0, we suspect from the distinct ratio of alkalis in rhyolite and basalt in each natural example that, in the case of injection of mafic melt, alkalis will diffuse from the felsic toward the mafic melt. It has been shown that the depletion of alkalis in the rhyolitic region of the contact zone reduces the solubility of H_2O. Moreover, this concept is not limited to peralkaline rhyolitic compositions only. Other bimodal volcanic systems with compositions of rhyodacite, dacite, and andesite – e.g., Gertisser et al. (2009) (Santorini: rhyodacite and basalt); Di Muro et al. (2008) (Mount Pinatubo: dacite and andesite); and Sigmundsson et al. (2010) (Eyjafjallajökull; trachyandesite and basalt) (Table S1) – show a ratio of x_{ex}, as well as the alkali to alumina ratio, on the felsic magma composition side (x_{ex} ratio Rt / B: 0.4–0.8; alkali / alumina ratio Rt / B: 1.3–1.7). It can therefore be assumed that in these cases, the alkalis also diffuse from the felsic melt into the mafic melt and thus lead to rapid depletion in the felsic part of the contact zone. The depleted melts become supersaturated in H_2O because the H_2O solubility decreases strongly with the decreasing alkali concentration of the melt (Dingwell et al., 1997; Allabar et al., 2022). Vesicles form in the hybrid zone at an early stage during the injection of mafic melt, leading to an increased contrast in density and viscosity compared to the pristine rhyolitic magma. The density contrast and the viscosity contrast between rhyolitic and basaltic melt are crucial for magma mingling and therefore enlarge the contact zone and thus the chemical magma mixing processes (Huppert et al., 1982). The resulting vesicle formation in the contact zone can accelerate buoyancy-driven magma ascent and mingling as shown by Wiesmaier et al. (2015). Extensive magma mingling could increase the possibility of mafic crystals being entrained into the felsic melt (e.g., Laumonier et al., 2015; Paredes-Marino et al., 2017), which would then act as nucleation sites and trigger further heterogeneous vesicle nucleation processes. Therefore, it can be generally considered that injection of a mafic melt into a felsic magma chamber can trigger explosive volcanic eruptions. The experimental results presented here and their compatibility with natural bimodal volcanic systems demonstrate the importance of alkali diffusion for H_2O solubility and the resulting H_2O supersaturation of melts in the contact region. Consideration of this aspect could open new perspectives on degassing behavior in such complicated volcanic systems.

Data availability. All data derived from this research are presented in the enclosed tables, figures, and the Supplement.

Supplement. The supplement related to this article is available online at: https://doi.org/10.5194/ejm-35-613-2023-supplement.

Author contributions. PLM: sample preparation, experiments, analysis and evaluation, visualization, writing of the original draft; AA: supervision, validation, software; MN: conceptualization, supervision.

Competing interests. The contact author has declared that none of the authors has any competing interests.

Special issue statement. This article is part of the special issue "Probing the Earth: magma and fluids, a tribute to the career of Michel Pichavant". It is a result of the Magma & Fluids workshop, Orléans, France, 4–6 July 2022.

Acknowledgements. We acknowledge the support of the Open Access Publishing Fund of the University of Tübingen. We thank Monika Rusiecka and one anonymous reviewer for their very helpful comments on the manuscript. We thank the DFG for financial support for the acquisition of the electron microprobe (grant: INST 37/1026-1 FUGG) and Thomas Wenzel and Sebastian Staude for their support during the sample measurements. We thank Barbara Maier and Annette Flicker for technical support and maintenance of the IHPV and the FTIR spectrometer, as well as Simone Schafflick for the high-quality sample preparation.

Financial support. This open-access publication was funded by the University of Tübingen.

Review statement. This paper was edited by Francois Holtz and reviewed by Monika Rusiecka and one anonymous referee.

References

Allabar, A. and Nowak, M.: Message in a bottle: Spontaneous phase separation of hydrous Vesuvius melt even at low decompression rates, Earth Planet. Sc. Lett., 501, 192–201, https://doi.org/10.1016/j.epsl.2018.08.047, 2018.

Allabar, A., Dobson, K. J., Bauer, C. C., and Nowak, M.: Vesicle shrinkage in hydrous phonolitic melt during cooling, Contrib. Mineral. Petr. 175, 21, https://doi.org/10.1007/s00410-020-1658-3, 2020.

Allabar, A., Petri, P. L., Eul, D., and Nowak, M.: An empirical H_2O solubility model for peralkaline rhyolitic melts, Contrib. Mineral. Petr., 177, 52, https://doi.org/10.1007/s00410-022-01915-8, 2022.

Arienzo, I., Moretti, R., Civetta, L., Orsi, G., and Papale, P.: The feeding system of Agnano–Monte Spina eruption (Campi Flegrei, Italy): Dragging the past into present activity and future scenarios, Chem. Geol., 270, 135–147, https://doi.org/10.1016/j.chemgeo.2009.11.012, 2010.

Bachmann, O. and Bergantz, G.: The Magma Reservoirs That Feed Supereruptions, Elements, 4, 17–21, https://doi.org/10.2113/GSELEMENTS.4.1.17, 2008.

Baker, D. R.: Estimation of diffusion coefficients during interdiffusion of geologic melts: Application of transition state theory, Chem. Geol., 98, 11–21, https://doi.org/10.1016/0009-2541(92)90089-N, 1992.

Baker, D. R. and Bossanyi, H.: The combined effect of F and H_2O on interdiffusion between peralkaline dacitic and rhyolitic melts, Contrib. Mineral. Petr., 117, 203–214, https://doi.org/10.2138/rmg.2010.72.8, 1994.

Behrens, H., Romano, C., Nowak, M., Holtz, F., and Dingwell, D. B.: Near-infrared spectroscopic determination of water species in glasses of the system $MAlSi_3O_8$ (M = Li, Na, K): an interlaboratory study, Chem. Geol., 128, 41–63, https://doi.org/10.1016/0009-2541(95)00162-X, 1996.

Berndt, J., Liebske, C., Holtz, F., Freise, M., Nowak, M., Ziegenbein, D., Hurkuck, W., and Koepke, J.: A combined rapid-quench and H_2-membrane setup for internally heated pressure vessels: Description and application for water solubility in basaltic melts, Am. Mineral., 87, 1717–1726, https://doi.org/10.2138/am-2002-11-1222, 2002.

Bunse, R. W.: Ueber die Processe der vulkanischen Gesteinsbildung Islands, Annu. Rev. Phys. Chem., 83, 197–272, https://doi.org/10.1002/andp.18511590602, 1851.

Carmichael, I. S. E. and Nicholls, J.: Iron-Titanium Oxides and Oxygen Fugacities in Volcanic Rocks, J. Geophys. Res., 72, 4665–4687, https://doi.org/10.1029/JZ072i018p04665, 1967.

Chen, C. H., DePaolo, D. J., Nakada, S., and Shieh, Y. N.: Relationship between eruption volume and neodymium isotopic composition at Unzen volcano, Nature, 362, 831–834, https://doi.org/10.1016/j.jvolgeores.2008.03.042, 1993.

De Rosa, R., Donato, P., and Ventura, G.: Fractal analysis of mingled/mixed magmas: an example from the Upper Pollara eruption (Salina Island, southern Tyrrhenian Sea, Italy), Lithos, 65, 299–311, https://doi.org/10.1016/S0024-4937(02)00197-4, 2002.

Devine, J. D., Gardener, J. E., Brack, H. P., Layne, G. D., and Rutherford, M. J.: Comparison of microanalytical methods for estimating H_2O contents of silicic volcanic glasses, Am. Mineral., 80, 319–328, https://doi.org/10.2138/am-1995-3-413, 1995.

Di Muro, A., Pallister, J., Villemant, B., Newhall, C., Semet, M., Martinez, M., and Mariet, C.: Pre-1991 sulfur transfer between mafic injections and dacite magma in the Mt. Pinatubo reservoir, J. Volcanol. Geoth. Res., 175, 517–540, https://doi.org/10.1016/j.jvolgeores.2008.02.025, 2008.

Dingwell, D. B., Holtz, F., and Behrens, H.: The solubility of H2O in peralkaline and peraluminous granitic melts, Am. Mineral., 82, 434–437, https://doi.org/10.2138/AM-1997-3-421, 1997.

Druitt, T. H., Costa, F., Deloule, E., Dungan, M., and Scaillet, B.: Decadal to monthly timescales of magma transfer and reservoir growth at a caldera volcano, Nature, 482, 77–97, https://doi.org/10.1038/nature10706, 2012.

Edmonds, M., Brett, A., Herd, R. A., Humphreys, M. C. S., and Woods, A.: Magnetite-bubble aggregated at mixing interfaces in andesite magma bodies, in: The Role of Volatiles in the Genesis, Evolution and Eruption of Arc Magmas, Geol. Soc. Sp., 410, 95, https://doi.org/10.1144/SP410.7, 2015.

Gardner, J. E., Hilton, M., and Carroll, M. R.: Experimental constraints on degassing of magma: isothermal bubble growth during continuous decompression from high pressure, Earth Planet. Sc. Lett., 168, 201–218, https://doi.org/10.1016/S0012-821X(99)00051-5, 1999.

Gardner, J. E. and Denis, M.-H.: Heterogeneous bubble nucleation on Fe-Ti oxide crystals in high-silicia rhy-

olitic melt, Geochim. Cosmochim. Ac., 68, 3587–3597, https://doi.org/10.1016/j.gca.2004.02.021, 2004.

Gardner, J. E.: Heterogeneous bubble nucleation in highly viscous silicate melts during instantaneous decompression from high pressure, Chem. Geol., 236, 1–12, https://doi.org/10.1016/j.chemgeo.2006.08.006, 2007.

Gardner, J. E. and Ketcham, R. A.: Bubble nucleation in rhyolite and dacite melts: temperature dependence of surface tension, Contrib. Mineral. Petr., 162, 929–943, https://doi.org/10.1007/s00410-011-0632-5, 2011.

Gardner, J. E., Wadsworth, F. B., Carley, T. L., Llewellin, E. W., Kusumaatmaja, H., and Sahagian, D.: Bubble Formation in Magma, Annu. Rev. Earth Pl. Sc., 51, 131–154, https://doi.org/10.1146/annurev-earth-031621-080308, 2022.

Gertisser, R., Preece, K., and Keller, J.: The Plinian Lower Pumice 2 eruption, Santorini, Greece: Magma evolution and volatile behavior, J. Volcanol. Geoth. Res., 186, 387–406, https://doi.org/10.1016/j.jvolgeores.2009.07.015, 2009.

Gonnermann, H. M. and Manga, M.: The Fluid Mechanics Inside a Volcano, Annu. Rev. Fluid Mech., 39, 321–356, https://doi.org/10.1146/annurev.fluid.39.050905.110207, 2007.

Gualda, G. A. R. and Ghiorso, M. S.: Magnetite scavenging and the buoyancy of bubbles in magmas, Part 2: Energetics of crystal-bubbles attachment in magmas, Contrib. Mineral. Petr., 154, 479–490, https://doi.org/10.1007/s00410-007-0206-8, 2007.

Hajimirza, S., Gonnermann, H. M., Gardner, J. E., and Giachetti, T.: Predicting homogeneous bubble nucleation in rhyolite, J. Geophys. Res.-Sol. Ea., 124, 2395–2416, https://doi.org/10.1029/2018JB015891, 2019.

Higgins, M. D.: Measurement of crystal size distributions, Am. Mineral., 85, 1105–1116, https://doi.org/10.2138/am-2000-8-901, 2000.

Holtz, F., Behrens, H., Dingwell, D. B., and Taylor, R. P.: Water solubility in aluminosilicate melts of haplogranite composition at 2 kbar, Chem. Geol., 96, 289–302, https://doi.org/10.1016/0009-2541(92)90060-I, 1992.

Holtz, F., Behrens, H., Dingwell, D. B., and Johannes, W.: H_2O Solubility in Haplogranitic Melts – Compositional, Pressure, and Temperature-Dependence, Am. Mineral., 80, 94–108, https://doi.org/10.2138/am-1995-1-210, 1995.

Huppert, H. E., Sparks, R. S. J., and Turner, J. S.: Effects of volatiles on mixing in calc-alkaline magma systems, Nature, 297, 554–557, https://doi.org/10.1038/297554a0, 1982.

Hurwitz, S. and Navon, O.: Bubble Nucleation in Rhyolitic Melts – Experiments at High-Pressure, Temperature, and Water-Content, Earth Planet. Sc. Lett., 122, 151–164, https://doi.org/10.1016/0012-821X(94)90001-9, 1994.

Iacono-Marziano, G., Schmidt, B. C., and Dolfi, D.: Equilibrium and disequilibrium degassing of a phonolitic melt (Vesuvius AD 79 "white pumice") simulated by decompression experiments, J. Volcanol. Geoth. Res., 161, 151–164, https://doi.org/10.1016/j.jvolgeores.2006.12.001, 2007.

Jahn, B. M., Litvinovsky, B. A., Zanvilevich, A. N., and Reichow, M.: Peralkaline granitoid magmatism in the Mongolian–Transbaikalian Belt: Evolution, petrogenesis and tectonic significance, Lithos, 113, 521–539, https://doi.org/10.1016/j.lithos.2009.06.015, 2009.

Jarvis, P. A., Pistone, M., Secretan, A., Blundy, J. D., Cashman, K. V., Mader, H. M., and Baumgartner, L. P.: Crystal and Volatile Controls on the Mixing and Mingling of Magmas, Geoph. Monog. Ser., 264, 125–150, https://doi.org/10.1002/9781119564485.ch6, 2021.

Johnston, A. D. and Wyllie, P. J.: Interaction of granitic and basic magmas: experimental observations on contamination processes at 10 kbar with H_2O, Contrib. Mineral. Petr., 98, 352–362, https://doi.org/10.1007/BF00375185, 1988.

Kouchi, A. and Sunagawa, I.: A Model for mixing basaltic and dacitic magmas as deduced from experimental data, Contrib. Mineral. Petr., 89, 17–23, https://doi.org/10.1007/BF01177586, 1985.

Lacasse, C., Sigurdsson, H., Carey, S. N., Johannesson, H., Thomas, L. E., and Rogers, N. W.: Bimodal volcanism at the Katla subglacial caldera, Iceland: insight into the geochemistry and petrogenesis of rhyolitic magmas, Bull. Volcanol., 69, 373–399, https://doi.org/10.1007/s00445-006-0082-5, 2007.

Laumonier, M., Scaillet, B., Pichavant, M., Champallier, R., Andujar, J., and Arbaret, L.: On the conditions of magma mixing and its bearing on andesite production in the crust, Nat. Commun., 5, 5607, https://doi.org/10.1038/ncomms6607, 2014.

Laumonier, M., Scaillet, B., Arbaret, L., Andujar, J., and Champallier, R.: Experimental mixing of hydrous magmas, Chem. Geol., 418, 158–170, https://doi.org/10.1016/j.chemgeo.2015.10.031, 2015.

Lavallée, Y., Dingwell, D. B., Johnson, J. B., Cimarelli, C., Hornby, A.J., Kendrick, J. E., von Aulock, F. W., Kennedy, B. M., Andrews, B. J., Wadsworth, F. B., Rhodes, E., and Chigna, G.: Thermal vesiculation during volcanic eruptions, Nature, 528, 544–547, https://doi.org/10.1038/nature16153, 2015.

Leat, P. T., Jackson, S. E., Thorpe, R. S., and Stillman, C. J.: Geochemistry of bimodal basalt-subalkaline/peralkaline rhyolite provinces within the Southern British Caledonides, J. Geol. Soc. Lond., 143, 259–273, https://doi.org/10.1144/gsjgs.143.2.0259, 1986.

Le Gall, N. and Pichavant, M.: Homogeneous bubble nucleation in H_2O- and H_2O-CO_2-bearing basaltic melts: Results of high temperature decompression experiments, J. Volcanol. Geoth. Res., 327, 604–621, https://doi.org/10.1016/j.jvolgeores.2016.10.004, 2016.

Leonard, G. S., Cole, J. W., Nairn, I. A., and Self, S.: Basalt triggering of the c. AD 1305 Kaharoa rhyolite eruption, Tarawera Volcanic Complex, New Zealand, J. Volcanol. Geoth. Res., 115, 461–486, https://doi.org/10.1016/S0377-0273(01)00326-2, 2002.

Liu, Y., Behrens, H., and Zhang, Y.: The speciation of dissolved H_2O in dacitic melt, Am. Mineral., 89, 277–284, https://doi.org/10.2138/am-2004-2-304, 2004.

Mangan, M. and Sisson, T.: Delayed, disequilibrium degassing in rhyolite magma: decompression experiments and implications for explosive volcanism, Earth Planet. Sc. Lett., 183, 441–455, https://doi.org/10.1016/S0012-821X(00)00299-5, 2000.

Mangan, M. and Sisson, T.: Evolution of melt-vapor surface tension in silicic volcanic systems: Experiments with hydrous melts, J. Geophys. Res., 110, B01202, https://doi.org/10.1029/2004JB003215, 2005.

Martel, C., Brooker, R. A., Andújar, J., Pichavant, M., Scaillet, B., and Blundy, J. D.: Experimental Simulations of Magma Storage and Ascent, in: Volcanic Unrest, edited by: Gotts-

mann, J., Neuberg, J., and Scheu, B., Adv. Volcanol., 101–110, https://doi.org/10.1007/11157_2017_20, 2017.

Marxer, H., Bellucci, P., and Nowak, M.: Degassing of H_2O in a phonolitic melt: A closer look at decompression experiments, J. Volcanol. Geoth. Res, 297, 109–124, https://doi.org/10.1016/j.jvolgeores.2014.11.017, 2015.

Mayerhöfer, T. G. and Popp, J.: Beer's Law – Why Absorbance Depends (Almost) Linearly on Concentration, Chemphyschem, 20, 511–515, https://doi.org/10.1002/cphc.201900103, 2019.

McIntosh, I. M., Llewellin, E. W., Humphreys, M. C. S., Nichols, A. R. L., Burgisser, A., Schipper, C. I., and Larsen, J. F.: Distribution of dissolved water in magmatic glass records growth and resorption of bubbles, Earth Planet. Sc. Lett., 401, 1–11, https://doi.org/10.1016/j.epsl.2014.05.037, 2014.

Miller, C. F. and Wark, D. A.: Supervolcanoes and their explosive supereruptions, Elements, 4, 11–15, https://doi.org/10.2113/GSELEMENTS.4.1.11, 2008.

Montagna, C. P., Papale, P., and Longo, A.: Timescales of mingling in shallow magmatic reservoirs, Geol. Soc. Lond. Spec. Publ., 422, 131–140, https://doi.org/10.1144/SP422.6, 2015.

Morgan, G. and London, D.: Effect of current density on the electron microprobe analysis of alkali aluminosilicate glasses, Am. Mineral., 90, 1131–1138, https://doi.org/10.2138/am.2005.1769, 2005.

Morgavi, D., Perugini, D., De Campos, C. P., Ertel-Ingrisch, W., and Dingwell, D. B.: Time evolution of chemical exchanges during mixing of rhyolitic and basaltic melts, Contrib. Mineral. Petr., 166, 615–638, https://doi.org/10.1007/s00410-013-0894-1, 2013.

Murphy, M. D., Sparks, R. S. J., Barclay, J., Carroll, M. R., Lejeune, A.-M., Brewer, T. S., Macdonald, R., Black, S., and Young, S.: The role of magma mixing in triggering the current eruption at the Soufriere Hills Volcano, Montserrat, West Indies, Geophys. Res. Lett., 25, 3433–3436, https://doi.org/10.1029/98GL00713, 1998.

Navon, O. and Lyakhovsky, V.: Vesiculation processes in silicic magmas, Geol. Soc. Spec. Publ., 145, 27–50, https://doi.org/10.1144/GSL.SP.1996.145.01.03, 1998.

Navon, O., Chekhmir, A., and Lyakhovsky, V.: Bubble growth in highly viscous melts: theory, experiments, and autoexplosivity of dome lavas, Earth Planet. Sc. Lett., 160, 763–776, https://doi.org/10.1016/S0012-821X(98)00126-5, 1998.

Ngounouno, I., Déruelle, B., and Demaiffe, D.: Petrology of the bimodal Cenozoic volcanism of the Kapsiki plateau (northernmost Cameroon, Central Africa), J. Volcanol. Geoth. Res., 102, 21–44, https://doi.org/10.1016/S0377-0273(00)00180-3, 2000.

Nowak, M., Cichy, S. B., Botcharnikov, R. E., Walker, N., and Hurkuck, W.: A new type of high pressure low-flow metering valve for continuous decompression: First 86 experimental results on degassing of rhyodacitic melts, Am. Mineral., 96, 1373–1380, https://doi.org/10.2138/am.2011.3786, 2011.

Ohlhorst, S., Behrens, H., and Holtz, F.: Compositional dependence of molar absorptivities of near-infrared OH- and H_2O bands in rhyolitic to basaltic glasses, Chem. Geol., 174, 5–20, https://doi.org/10.1016/S0009-2541(00)00303-X, 2001.

Paredes-Marino, J., Dobson, K. J., Ortenzi, G., Kueppers, U., Morgavi, D., Petrelli, M., Hess, K.-U., Laeger, K., Porreca, M., Pimentel, A., and Perugini, D.: Enhancement of eruption explosivity by heterogeneous bubble nucleation triggered by magma mingling, Sci. Rep.-UK, 7, 16897, https://doi.org/10.1038/s41598-017-17098-3, 2017.

Perugini, D. and Poli, G.: The mixing of magmas in plutonic and volcanic environments: analogies and differences, Lithos, 153, 261–277, https://doi.org/10.1016/j.lithos.2012.02.002, 2012.

Perugini, D., De Campos, C. P., Ertel-Ingrisch, W., and Dingwell, D. B.: The space and time complexity of chaotic mixing of silicate melts: Implications for igneous petrology, Lithos, 155, 326–340, https://doi.org/10.1016/j.lithos.2012.09.010, 2012.

Phillips, J. C. and Woods, A. W.: Suppression of large-scale magma mixing by melt-volatile separation, Earth Planet. Sc. Lett., 204, 47–60, https://doi.org/10.1016/S0012-821X(02)00978-0, 2002.

Philpotts, A. R. and Ague, J. J.: Principles of Igneous and Metamorphic Petrology, Cambridge University Press, 700 pp., https://doi.org/10.1017/9781108631419, 2009.

Pichavant, M., Poussineau, S., Lesne, P., Solaro, C., and Bourdier, J. L.: Experimental Parametrization of Magma Mixing: Application to the AD 1530 Eruption of La Soufrière, Guadeloupe (Lesser Antilles), J. Petrol., 2, 257–282, https://doi.org/10.1093/petrology/egy030, 2018.

Preuss, O., Marxer, H., Ulmer, S., Wolf, J., and Nowak, M.: Degassing of hydrous trachytic Campi Flegrei and phonolitic Vesuvius melts: Experimental limitations and chances to study homogeneous bubble nucleation, Am. Mineral., 101, 859–875, https://doi.org/10.2138/am-2016-5480, 2016.

Pritchard, C. J., Larson, P. B., Spell, T. L., and Tarbert, K. D.: Eruption-triggered mixing of extra-caldera basalt and rhyolite complexes along the East Gallatin–Washburn fault zone, Yellowstone National Park, WY, USA, Lithos, 175/176, 163–177, https://doi.org/10.1016/j.lithos.2013.04.022, 2013.

Rose, W. I. and Chesner, C. A. : Dispersal of ash in the great Toba eruption, 7 KA, Geology, 15, 913–917, https://doi.org/10.1130/0091-7613(1987)15<913:DOAITG>2.0.CO;2, 1987.

Sahagian, D. and Carley, T. L.: Explosive Volcanic Eruptions and Spinodal Decomposition: A different Approach to Deciphering the Tiny Bubble Paraox, Geochem. Geophy. Geosy., 21, 6, https://doi.org/10.1029/2019GC008898, 2020.

Saito, G., Stimac, J. A., Kawanabe, Y., and Goff, F.: Mafic-felsic magma interaction at Satsuma-Iwojima volcano, Japan: Evidence from mafic inclusions in rhyolites, Earth Planet. Space, 54, 303–325, https://doi.org/10.1186/BF03353030, 2002.

Sato, H., Nakada, S., Fujii, T., Nakamura, M., and Suzuki-Kamata, K.: Groundmass pargasite in the 1991–1995 dacite of Unzen volcano: phase stability experiments and volcanological implications, J. Volcanol. Geoth. Res., 89, 197–212, https://doi.org/10.1016/S0377-0273(98)00132-2, 1999.

Scaillet, B. and Pichavant, M.: Experimental constraints on volatile abundances in arc magmas and their implications for degassing processes, in: Volcanic degassing, edited by: Oppenheimer, C., Pyle, D., and Barclay, J., Geol. Soc. Lond. Spec. Publ., 213, 23–52, https://doi.org/10.1144/GSL.SP.2003.213.01.03, 2003.

Self, S. and Blake, S.: Consequences of explosive supereruptions, Elements, 4, 41–46, https://doi.org/10.2113/GSELEMENTS.4.1.41, 2008.

Sigmundsson, F., Hreinsdóttir, S., Hooper, A., Árnadóttir, T., Pedersen, R., Roberts, M. J., Óskarsson, N., Auriac, A., Decriem, J., Einarsson, P., Geirsson, H., Hensch, M., Ófeigsson, B. G., Sturkell, E., Sveinbjörnsson, H., and Feigl, K. L.: Intrusion trig-

gering of the 2010 Eyjafjallajökull explosive eruption, Nature, 468, 426–430, https://doi.org/10.1038/nature09558, 2010.

Sigurdsson, H. and Sparks, R. S. J.: Petrology of rhyolitic and mixed magma ejecta from the 1875 eruption of Askja, Iceland, J. Petrol., 22, 41–84, https://doi.org/10.1093/petrology/22.1.41, 1981.

Smithies, R. H., Howard, H. M., Kirkland, C. L., Korhonen, F. J., Medlin, C. C., Maier, W. D., Quentin de Gromard, R., and Wingate, M. T. D.: Piggy-back Supervolcanoes – Long-Lived, Voluminous, Juvenile Rhyolite Volcanism in Mesoproterozoic Central Australia, J. Petrol., 56, 735–763, https://doi.org/10.1093/petrology/egv015, 2015.

Snyder, D.: Thermal effects of the intrusion of basaltic magma into a more silicic magma chamber and implications for eruption triggering, Earth Planet. Sc. Lett., 175, 257–273, https://doi.org/10.1016/S0012-821X(99)00301-5, 2000.

Sparks, R. S. J.: The dynamics of bubble formation and growth in magmas: a review and analysis, J. Volcanol. Geoth. Res., 3, 1–37, https://doi.org/10.1016/0377-0273(78)90002-1, 1978.

Sparks, R. S. J., Sigurdsson, H., and Wilson, L.: Magma mixing: a mechanism for triggering acid explosive eruptions, Nature, 267, 315–318, https://doi.org/10.1038/267315a0, 1977.

Spera, F. J., Schmidt, J. S., Bohrson, W. A., and Brown, G. A.: Dynamics and thermodynamics of magma mixing: Insights from a simple exploratory model, Am. Mineral., 101, 627–643, https://doi.org/10.2138/am-2016-5305, 2016.

Stelling, J., Botcharnikov, R. E., Beermann, O., and Nowak, M.: Solubility of H_2O- and chlorine -bearing fluids in basaltic melt of Mount Etna at $T = 1050$–$1250\,°C$ and $P = 200\,MPa$, Chem. Geol., 256, 102–110, https://doi.org/10.1016/j.chemgeo.2008.04.009, 2008.

Tinker, D. and Lesher, C. E.: Self diffusion of Si and O in dacitic liquid at high pressures, Am. Mineral., 86, 1–13, https://doi.org/10.2138/am-2001-0101, 2001.

Toramaru, A.: BND (bubble number density) decompression rate meter for explosive volcanic eruptions, J. Volcanol. Geoth. Res., 154, 303–316, https://doi.org/10.1016/j.jvolgeores.2006.03.027, 2006.

Troll, V. R., Donaldson, C. H., and Emeleus, C. H.: Pre-eruptive magma mixing in ash-flow deposits of the Tertiary Rum Igneous Centre, Scotland, Contrib. Mineral. Petr., 147, 722–739, https://doi.org/10.1007/s00410-004-0584-0, 2004.

Watson, B.: Basalt Contamination by Continental Crust: Some Experiments and Models, Contrib. Mineral. Petr., 80, 73–87, https://doi.org/10.1007/BF00376736, 1982.

Wiesmaier, S., Morgavi, D., Renggli, C. J., Perugini, D., De Campos, C. P., Hess, K.-U., Ertel-Ingrisch, W., Lavallée, Y., and Dingwell, D. B.: Magma mixing enhanced by bubble segregation, Solid Earth, 6, 1007–1023, https://doi.org/10.5194/se-6-1007-2015, 2015.

Yamashita, S., Kitamura, T., and Kusakabe, M.: Infrared spectroscopy of hydrous glasses of arc magma compositions, Geochem. J., 31, 169–174, https://doi.org/10.2343/geochemj.31.169, 1997.

Yoder, H. S.: Contemporaneous basaltic and rhyolitic magmas, Am. Mineral., 58, 153–171, 1973.

Zhang, Y., Ni, H., and Chen, Y: Diffusion Data in Silicate Melts, Rev. Mineral. Geochem., 72, 311–408, https://doi.org/10.2138/rmg.2010.72.8, 2010.